Design of surface chemical reactivity and optical properties in glasses

Antoine Lepicard

▶ **To cite this version:**

Antoine Lepicard. Design of surface chemical reactivity and optical properties in glasses. Other. Université de Bordeaux; University of Central Florida (Orlando), 2016. English. NNT : 2016BORD0162 . tel-01424212

HAL Id: tel-01424212
https://theses.hal.science/tel-01424212

Submitted on 2 Jan 2017

HAL is a multi-disciplinary open access archive for the deposit and dissemination of scientific research documents, whether they are published or not. The documents may come from teaching and research institutions in France or abroad, or from public or private research centers.

L'archive ouverte pluridisciplinaire **HAL**, est destinée au dépôt et à la diffusion de documents scientifiques de niveau recherche, publiés ou non, émanant des établissements d'enseignement et de recherche français ou étrangers, des laboratoires publics ou privés.

THÈSE PRÉSENTÉE

POUR OBTENIR LE GRADE DE

DOCTEUR DE

L'UNIVERSITÉ DE BORDEAUX

ET DE L'UNIVERSITÉ DE FLORIDE CENTRALE (UCF)

ÉCOLE DOCTORALE DES SCIENCES CHIMIQUES

SPÉCIALITÉ PHYSICO-CHIMIE DE LA MATIÈRE CONDENSÉE

Par Antoine LEPICARD

Design of surface chemical reactivity and optical properties in glasses

Sous la direction de : Vincent RODRIGUEZ
(co-directeur: Marc DUSSAUZE et Kathleen RICHARDSON)

Soutenue le 4 octobre 2016

Membres du jury:

M. NEUVILLE Daniel	Directeur de Recherche, IPGP, Sorbonne Paris Cité	Président/Rapporteur
M. QUIQUEMPOIS Yves	Professeur, Université de Lille I	Rapporteur
M. BOULANGER Benoit	Professeur, Institut Néel, Université Grenoble Alpes	Examinateur
Mme. RICHARDSON Kathleen	Professeur, University of Central Florida, USA	Directrice de thèse
M. RODRIGUEZ Vincent	Professeur, Université de Bordeaux	Directeur de thèse
M. DUSSAUZE Marc	Chargé de Recherche, Université de Bordeaux	Directeur de thèse

A mes parents,

RÉSUMÉ

La photonique est un domaine qui a connu un fort essor ces dernières années et qui est désormais omniprésent dans notre quotidien. Ce domaine scientifique se focalise sur l'étude de la lumière et plus particulièrement sur l'étude et la fabrication de systèmes permettant de générer, contrôler, convertir et détecter des signaux lumineux. Les applications de la photonique sont variées et incluent les communications optiques, la défense, la détection dans des processus biochimique, l'imagerie, etc… Cette liste n'est en aucun cas exhaustive et une multitude d'autres applications sont également accessibles.

Ce domaine de la science est relativement récent. Sa genèse remonte aux années 1960 avec les premières LED développées par Holonyak. [1] Dans les années 1970, le domaine a connu un fort essor suite à l'invention par Corning de la première fibre optique à faible perte optique. [2] Le développement de cette nouvelle branche de la science n'a ensuite pas cessé, et plus récemment, un nouveau domaine a émergé : la *microphotonique*. La microphotonique est centrée sur le contrôle de la lumière à l'échelle micrométrique dans l'idée de remplacer la microélectronique, ce qui permettrait de gagner en rapidité dans l'échange d'information. Pour cela, la réalisation de circuit photonique intégré est nécessaire. Elle permettrait d'associer diverses fonctions optiques sur un seul composant à petite échelle en utilisant des propriétés optiques, à la fois linéaire et non linéaire (ONL).

Le travail effectué au cours de cette thèse s'est focalisé sur deux aspects essentiels de la microphotonique : (i) le développement de nouveaux matériaux pour de telles applications et (ii) le développement d'une technique pour contrôler précisément diverses propriétés du matériau à

diverses échelles. Notre travail ne s'est pas focalisé seulement sur les propriétés optiques mais sur l'ensemble des propriétés de surface du substrat (mouillabilité, réactivité, …) ainsi que les propriétés d'optique linéaire et non linéaire. Pour introduire ces modifications en surface du verre, un traitement particulier au verre a été utilisé : le *poling thermique*.

Le poling thermique est une technique qui consiste à appliquer un fort champ électrique (DC) entre deux électrodes situées de chaque côté d'un substrat de verre chauffé sous sa température de transition vitreuse (Tg). Au cours du traitement thermique les charges présentent dans le verre, essentiellement les cations alcalins, vont gagner en mobilité et ensuite migrer vers la cathode sous l'effet du champ électrique. Typiquement, une fois le champ électrique appliqué au verre chauffé, un phénomène de dissociation de charge se met en place et le courant parcourant le verre atteint rapidement un maximum. Une zone de déplétion de ces porteurs de charges se crée alors au cours du traitement de poling thermique entrainant l'augmentation de la résistivité de la zone située sous l'anode. Au fur et à mesure que la résistivité augmente, le courant parcourant le verre diminue jusqu'à ce qu'il atteigne un plateau. La température est ensuite rabaissée à température ambiante et le voltage appliqué entre les deux électrodes est coupé seulement à cet instant. En procédant de cette manière les charges déplacées au cours du traitement sont « gelées » à leurs positions et un fort champ électrique interne est induit au sein de la matrice vitreuse. Le substrat de verre est alors dit *« polarisé »*. Sous l'anode, après le départ des cations, la charge est localement négative. Il est important de noter que le verre est seulement chargé localement et que des charges positives sont distribuées dans le reste de l'échantillon afin de garder une charge globale nulle et de satisfaire la loi de Gauss.

Le champ électrique induit dans le verre se rapproche facilement de la tension de claquage au sein du diélectrique (10^8 - 10^9 V/m). [3-6] Au vu du nombre de charges positives déplacées au cours du traitement thermique d'un verre riche en alcalins (tel qu'un verre sodo-calcique), il apparait évident qu'un système de compensation de charges prend place au cours du traitement. Le déplacement des charges positives a été bien décrit dans la littérature par le départ de cations alcalins ou alcalino-terreux au cours du traitement vers la cathode. [3, 7, 8] Concernant le mouvement de charges négatives vers l'anode pour compenser le départ de charges positives, la description du phénomène est plus complexe. Il a été mis indirectement en évidence, par des études structurelles, qu'une migration d'anions oxygène pouvait se mettre en place et être suivi d'une réaction d'oxydation et de la formation d'oxygène moléculaire au sein de la matrice vitreuse. [9-11] Un potentiel rôle de la conduction électronique au cours du traitement ne peut pas être écarté [12-15] et il est difficile de trouver des preuves expérimentales répondant aux questions sur la nature des charges négatives en mouvement. Enfin, pour compenser le départ de cations mobiles de la zone proche de l'anode, un phénomène, d'injection de charges positives de l'atmosphère vers la matrice vitreuse peut prendre place, on parle alors *d'anode ouverte*. Pour éviter cette injection, il est possible de travailler en *anode partiellement fermée* en réalisant le traitement sous atmosphère inerte.

Ce traitement de polarisation thermique a été utilisé pour la première fois afin de coller un substrat de verre à un métal dans l'industrie de la microélectronique à la fin des années 1960 par Wallis et Pomerantz. [16] Quelques décennies plus tard et après l'essor de la photonique, le poling thermique a trouvé une nouvelle utilité. Le verre a toujours été un matériau de prédilection pour l'optique ; notamment, un de ses nombreux avantages pour l'optique est le peu de perte optique dû à l'absence

de joint de grains au sein de la matrice vitreuse. Cette particularité est dû au fait que le verre est un matériau non-cristallin caractérisé par un désordre dans sa structure. Le matériau est donc isotrope et est caractérisé par la présence d'un centre d'inversion. Ainsi, pour chaque point de l'espace de coordonnées (x, y, z), il existe un autre point de coordonnées (-x, -y, -z) indissociable du premier point. Bien qu'avantageux en optique linéaire, la présence de ce centre d'inversion, rend toutes propriétés d'optique non linéaire du second ordre totalement impossible dans ce milieu. Néanmoins, après poling thermique, la présence du fort champ électrique induit va permettre de briser cette centrosymétrie et de donner accès à ces propriétés tel que la génération de second harmonique (GSH), [17] normalement impossible dans un matériau centrosymétrique. Il s'agit d'un effet électrooptique de génération de seconde harmonique induite par champ électrique ou « *Electric field induced second harmonic (EFISH)* ». Cet effet est dû à l'interaction entre la susceptibilité non linéaire d'ordre 3 ($\chi^{(3)}$) du matériau et du champ électrique induit. Ces propriétés d'optique non linéaire du second ordre sont très importantes en photonique, et un phénomène tel que la GSH est constamment utilisé en optique pour la conversion de fréquence. Des matériaux, tel que des cristaux, sont déjà accessibles pour ces applications mais présentent certains désavantages en comparaison des verres. Notamment, les monocristaux nécessaires à de telles applications sont couteux et difficile à préparer. Un substrat de verre avec des propriétés de GSH présenterait donc un avantage certain pour l'industrie.

Plus récemment, de nouvelles applications au poling thermique ont émergé et ont motivé plusieurs parties de ce travail de thèse. En particulier, le rôle de ce champ dans la réactivité de surface de bioverre polarisé a été mis en avant par Mariappan et al.. [18, 19] Ces verres, développés pour la première fois par Hench à la fin des années 1960, [20] sont fait pour réagir avec le corps humain au

contact de ce dernier. Le verre est alors peu à peu assimilé par le corps et permet la création d'hydroxyapatite qui est un des éléments constitutifs des os. Dans le cas de bioverre polé, la présence du champ électrique enterré sous la surface permet alors d'accélérer ce processus de formation de l'hydroxyapatite à la surface du verre.

Le traitement de polarisation thermique a également été développé en tant que traitement d'impression assisté sous champ électrique dans de multiples travaux. [21-23] Il a été démontré qu'en utilisant une électrode structurée en lieu d'une électrode plane à l'anode, le traitement permet d'imprimer la topologie de l'électrode à la surface de l'échantillon polarisé. L'anode peut alors être vu comme un tampon. Ce traitement permet donc de modifier localement la topologie d'un verre mais également de structurer l'information de seconde harmonique induite à la surface du verre. [24] Pour aller plus loin, en maitrisant le motif à imprimer sur le verre, des systèmes optiques tels que des réseaux de diffraction peuvent être imprimés. [25]

Ce travail de thèse s'est donc focalisé sur ces multiples aspects du poling thermique en tant que traitement de modification des propriétés de surface d'un verre. Néanmoins, afin de maitriser les multiples phénomènes et changement de propriétés prenant place au cours du traitement, notre travail s'attache à donner une description complète des mécanismes se déroulant au cours du traitement.

La première partie de notre travail s'est intéressée à l'étude des verres d'oxydes, largement décrit dans la littérature du poling thermique. Le premier système vitreux présenté dans ce travail est un verre de borophosphate de niobium (BPN), une référence à l'université de Bordeaux pour le poling thermique.[9, 26-28] Du fait de sa forte polarisabilité, ce verre se prête tout particulièrement à des

applications en optique non linéaire du second ordre et a permis d'obtenir des valeurs de $\chi^{(2)}$ induit parmi les plus fortes jamais mesurées dans un système vitreux. Notre travail s'est donc focalisé sur le contrôle de ces propriétés ONL du 2nd ordre à l'échelle du micromètre, ce qui pourrait s'avérer essentiel dans le but de créer des systèmes microphotoniques. Afin de contrôler les propriétés de GSH à l'échelle du micromètre, l'usage d'une électrode structurée est nécessaire. Cette approche est similaire aux travaux de structuration de topologie par poling thermique qui ont employé des électrodes métalliques structurées. [21] De telles électrodes permettent de modifier l'intensité du champ électrique appliqué à la surface du verre au cours du traitement mais le traitement reste effectif sur l'ensemble de la surface présente sous l'anode. Après traitement, la zone polarisée présentera seulement une inhomogénéité dans la réponse de GSH. Ici, nous souhaitons induire un contraste plus drastique, quasiment binaire en termes de propriété de GSH induite. Pour cela, le matériau choisi à l'anode est une lame de microscope avec un dépôt d'ITO (Indium Tin Oxide) conducteur à la surface. Cette couche d'ITO, de 500 nm d'épaisseur, est localement ablaté par irradiation laser. Des motifs peuvent donc être inscrits aisément à la surface de l'électrode, de telle zones sont dites « *structurées* ». L'électrode résultante est donc formée de zone conductrice (où le dépôt est toujours en place) et de zone non-conductrice (où le dépôt a été ablaté) qui ne vont pas prendre part de la même manière au traitement de polarisation. Nous avons montré, par microsonde, qu'au cours du traitement, la migration de cations mobiles prenait place essentiellement sous les zones en contact avec le dépôt d'ITO. Cette migration est également associée à un changement de structure, mis en évidence par spectroscopie vibrationnelle Raman. Il en résulte un contrôle de la composition et de la structure à l'échelle micrométrique qui suit parfaitement le potentiel appliqué à la surface du verre au cours du traitement (le potentiel de

surface étant directement lié à la présence d'ITO ou non à la surface de l'électrode). En ce qui concerne les propriétés de GSH, il a été observé, par microscopie de seconde harmonique, que les zones actives se retrouvent localisées à l'interface des zones structurées sur l'électrode. Un effet de confinement de charges induites au sein de la matrice vitreuse est donc observé à ces interfaces. Cet effet permet de contrôler précisément, à l'échelle du micron, la géométrie et la localisation du champ électrique induit et donc des propriétés de GSH. Ce premier résultat permet donc d'envisager la possibilité de réaliser des systèmes photoniques où des conditions de quasi-accord de phase seraient réunies, ce qui permettraient d'augmenter considérablement le taux de conversion de la lumière.

Dans la deuxième partie de notre travail sur les verres d'oxydes, nous nous sommes intéressés à une autre problématique, à savoir le contrôle de la réactivité de surface d'un verre par poling thermique. Plus particulièrement, nous avons tenté d'exacerber l'affinité d'une zone du verre pour l'eau atmosphérique et de créer des zones fortement réactives à côté de zone non-réactive. Plusieurs possibilités s'offraient à nous pour réaliser un tel système. Bien évidemment, d'autres techniques sont déjà connues pour modifier la réactivité de surface d'un verre (activation par UV-ozone, etc…) mais la possibilité d'avoir ce champ électrique induit au sein de la matrice nous permettait d'envisager une possible exaltation de cet effet. De même, en utilisant le traitement de poling thermique, plusieurs approches étaient envisageables. Pendant le traitement de poling thermique, il est possible d'introduire des hydroxyles au sein de la matrice vitreuse si le traitement est effectué en électrode ouverte. Un tel système sera alors fortement hydrophile. Néanmoins, nous avons choisi une autre approche, basé sur un effet de changement de la structure du verre associé au fort champ induit. Le traitement de poling thermique permet de modifier la structure du verre

suite au départ des espèces mobiles au cours du traitement. Nous avons voulu montrer que la compréhension de la structure du verre associée à un contrôle des conditions de poling thermique permettent d'obtenir la nouvelle structure désirée, associé à un champ électrique fort. Le verre utilisé au cours de ce travail est un borosilicate, fortement chargé en bore, se situant au sein de l'anomalie du bore. Cette anomalie se manifeste pour un ratio de modificateur (ici Na_2O) sur bore (B_2O_3) inférieur à 0.2. [29] Pour un tel ratio, tout modificateur du réseau ajouté à la matrice vitreuse va s'associer au réseau borate, laissant le réseau silicate entièrement réticulé et formé de tétraèdre SiO_4. L'ajout d'un sodium au réseau du bore va permettre la transformation d'une entité triangulaire BO_3 en un tétraèdre BO_4^- au voisinage d'un sodium pour compenser la charge locale. Le verre obtenue est un verre stable dans l'atmosphère. Le traitement de polarisation thermique est ensuite effectué sous atmosphère contrôlée afin d'empêcher tout injection d'espèce de l'atmosphère au sein du verre. Au cours du traitement de polarisation, les cations sodium vont migrer vers la cathode, forçant la structure vitreuse à se réarranger. Ce changement de structure a été clairement mis en évidence par spectroscopie infrarouge. Le réseau silicate n'est pas impacté par ce départ, tandis que le réseau borate va être forcé à se restructurer et à former des triangles BO_3 interconnectés formant une structure proche d'anneau boroxol. En plus de cette nouvelle structure, la microscopie de génération de seconde harmonique nous a permis de mettre en avant la présence de ce champ électrique statique induit, localisé dans les zones ayant subi ce changement de structure. Il en résulte une nouvelle structure après traitement que l'on qualifiera de structure borate chargée. Pour mettre en avant l'augmentation de la réactivité de surface du verre, celui-ci est exposé à l'atmosphère du laboratoire. En l'espace de quelques minutes, la zone où est présente la structure borate chargée est le lieu de la formation d'une couche hydratée. La spectroscopie

infrarouge a permis de mettre en avant ce caractère hydraté et, associé à la spectroscopie Raman, il nous a été permis de mettre en avant la formation d'acide borique en surface. Cette formation d'acide borique permet de mettre en évidence un processus de lixiviation à la surface du verre. Le déroulement de la réaction peut être simplement résumé. Suite à la formation de cette structure chargée au cours du traitement, l'eau atmosphérique est fortement attirée sur celle-ci. S'en suit une réaction préférentielle avec le réseau borate au travers d'un processus de lixiviation, entrainant la formation d'acide borique et la destruction partielle de la nouvelle structure chargée. Il a enfin été démontré que l'utilisation d'une électrode structurée à l'anode permet le contrôle de ce phénomène à l'échelle micrométrique. Un tel contrôle de la chimie de surface d'un verre s'avère particulièrement intéressant dans l'optique de créer des systèmes de type : « laboratoire sur puce ». De tels systèmes permettraient la réalisation de réaction chimique confinée dans de petits volumes une éventualité particulièrement intéressante lorsque les réactifs sont peu abondants. Un laboratoire sur puce performant devrait permettre à la fois la réalisation de réaction chimique en son sein mais devrait également permettre de monitorer ces réactions. La fenêtre infrarouge de la lumière étant la zone comprenant les signatures vibrationnelles de la vaste majorité des espèces organique, la spectroscopie infrarouge représente alors la meilleure solution analytique. Il est donc indispensable d'avoir des systèmes vitreux transparent dans l'infrarouge afin de réaliser les systèmes optiques permettant l'analyse de ces composés. La dernière partie de ce travail de thèse s'est donc centrée sur l'étude de verre de chalcogénures (transparent dans l'infrarouge).

Les verres de chalcogénures ont souvent été présentés comme des candidats idéaux pour les applications de poling thermique pour la génération de seconde harmonique. Du fait de leur très forte polarisabilité, leur susceptibilité optique non linéaire d'ordre 3 ($\chi^{(3)}$) est la plus forte de toutes

les familles de verres. Cette propriété intrinsèque du verre entre directement dans la réponse d'optique non linéaire du second ordre induite après traitement de poling thermique. Il a donc été envisagé qu'un verre présentant un fort $\chi^{(3)}$ permettrait d'obtenir un fort $\chi^{(2)}$ induit. Cependant, les premiers résultats n'ont pas été à la hauteur des attentes. Notamment, la réponse induite après poling a très souvent souffert d'une faible stabilité au cours du temps, avec des temps de décroissance pouvant s'approcher de la journée ou semaines. Il est alors difficile d'envisager d'utiliser ces verres pour des applications concrètes. Enfin, du fait de leur composition particulière (absence d'oxygène, absence de cations mobiles), leur comportement au cours du poling thermique diffère des compositions d'oxydes largement étudiées et les mécanismes prenant place au cours du traitement de polarisation thermique n'ont pas pu être complétement décrit dans ces systèmes vitreux. La première partie de notre travail sur les chalcogénures s'est donc attachée à la compréhension des mécanismes de formation de la charge d'espace au sein du verre, et plus particulièrement à la stabilité de cette dernière. Ces verres ont la particularité de présenter des faibles températures de transition vitreuse et sont connus pour leur capacité à relaxer sous celle-ci. Il a donc été décidé de réaliser quatre compositions de verre dans le ternaire Ge-Sb-S en partant de la composition $Ge_{25}Sb_{10}S_{65}$, bien connu de la littérature et qui présente, à ce jour, le meilleur résultat de poling thermique d'un verre de chalcogénure (en termes d'intensité du $\chi^{(2)}$ induit).[30, 31] En partant de cette composition, trois verres additionnels, de taux en soufre croissant, ont été réalisé. L'ajout de soufre s'est fait au détriment du germanium, en gardant un taux d'antimoine constant. Les quatre compositions obtenues sont : $Ge_{25}Sb_{10}S_{65}$ (A), $Ge_{22.5}Sb_{10}S_{67.5}$ (B), $Ge_{20}Sb_{10}S_{70}$ (C) et $Ge_{17.5}Sb_{10}S_{72.5}$ (D). Cette sur-stœchiométrie en soufre permet d'introduire des ponts S-S au sein de la matrice vitreuse, rendant celle-ci plus « flexible ». Cet effet se traduit par

une baisse de la température de transition vitreuse. Le but étant ici d'observer si une augmentation de cette flexibilité du réseau entrainerait une baisse de la stabilité de l'effet induit. Un second aspect essentiel du traitement de polarisation thermique se devait d'être étudié, à savoir le rôle des porteurs de charges positifs au sein de la matrice vitreuse. Pendant le traitement de polarisation thermique des verres d'oxydes, le rôle primordial des cations positifs (notamment des espèces alcalines) dans la formation de la charge d'espace ont été amplement documenté. Les verres de chalcogénures ne dérogent pas à cette règle et, malgré l'absence théorique d'alcalin de leur composition, il a été suggéré que leur présence, sous la forme d'impureté, jouait un rôle similaire dans la création de la charge d'espace. [32] Il a donc été décidé de doper ces verres en alcalin, par l'ajout de Na_2S, afin d'avoir un cation mobile en quantité non-négligeable, facilitant son suivi après le traitement. Les verres préparés ont donc été dopés avec 1 et 3 mol% de sulfure de sodium. Au cours du poling thermique, une première différence a été observée entre les verres dopé et non-dopé. En effet, les verres dopés en sodium présentaient une conduction cationique non-négligeable. Après poling thermique, la création sous l'anode d'une zone vidée en sodium a été observée seulement dans les verres dopés. Ce changement de composition a été accompagné d'un réarrangement structural observé en spectroscopie vibrationnel Raman dans ces verres dopés. La structure du verre polé se rapprochant alors de son analogue sans sodium. Afin d'étudier le champ électrique induit au cours du traitement de polarisation thermique, la technique des *franges de Maker*, une technique d'ellipsométrie de seconde harmonique, a été utilisée. Cette technique permet de mesurer la réponse de seconde harmonique du matériau en faisant varier l'angle d'incidence et/ou la polarisation du faisceau indicent. Les franges mesurées permettent alors de remonter à la symétrie de l'anisotropie à l'origine du signal et, dans le cas d'un verre polarisé, cela

revient donc à étudier le champ électrique induit au sein de la matrice vitreuse. L'étude de ces franges a permis de mettre en évidence une réponse inhabituelle, le premier jour après traitement, dans les verres dopés et non-dopés. Les franges mesurées ne pouvaient pas être décrites par un champs électrique induit perpendiculairement à la surface du verre (selon l'axe z), comme attendu dans un verre polarisé. De plus, les verres présentaient une contribution au signal de seconde harmonique à incidence normale, mettant ainsi en évidence une contribution au signal de seconde harmonique dans le plan de la surface du verre (selon les axes x et y). La décroissance du signal mesuré était présente, comme typiquement observé dans les verres de chalcogénures. Concernant les verres non-dopés, après une semaine, aucun signal ne pouvait être mesuré. Les verres dopés en sodium ont également présenté une décroissance du signal de seconde harmonique. Néanmoins, après un mois, ce signal s'est stabilisé et les franges mesurées présentaient alors une réponse typique d'un champ électrique induit perpendiculairement à la surface et la composante à incidence normale était alors absente. Pour expliquer l'évolution du signal et une telle différence entre les verres dopés et non-dopés, plusieurs hypothèses ont été proposée. Tout d'abord, la composante du signal de seconde harmonique présente dans le plan de l'échantillon se devait d'être expliquée. La possibilité de la cristallisation de cristaux non-centrosymétrique au cours du poling a été écartée car aucun signe de cristallisation n'a été mesuré par spectroscopie vibrationnelle ou par diffraction des rayons X. De plus, la décroissance de cette composante au cours du temps ne concorde pas avec l'hypothèse de cristaux qui seraient, eux, particulièrement stable. Il a donc été envisagé que ce signal provenant du plan de la surface pouvait être lié à un champ électrique induit, non pas selon l'axe z, mais selon les axes x et y (dans le plan de la surface). Des franges de Maker ont donc été mesurées à incidence normale (fixe) en faisant varier la polarisation du faisceau indicent. Une

telle démarche permet de supprimer la contribution éventuelle provenant de l'axe z et de se focaliser sur celle contenu dans le plan de la surface. Un modèle simple et fortement contraint a ensuite été mis en place, décrivant la réponse attendu pour une GSH provenant d'un effet électro-optique induit selon les axes x et y. Les franges mesurées sur le verre ont pu être parfaitement décrites par ce modèle. Le premier jour après poling, le signal mesuré pour les verres dopés et non-dopés peut donc être décrit par une réponse électro-optique induite par des champs selon les axes x, y et z. Les composantes selon x et y diminuent néanmoins grandement au cours du temps pour finir par ne laisser que la composante selon l'axe z, typique d'un verre polarisé par traitement de poling thermique. Pour expliquer cette différence de stabilité dans les champs induits, un parallèle a été fait avec le modèle présenté par Shimakawa dans les années 1990 sur la création de défauts dans les verres de chalcogénures par irradiation laser. Il a présenté un modèle de création de défauts chargés de deux types. Le premier correspond à la création de *« self trapped exciton »*, défaut chargé présentant une faible stabilité et étant à des niveaux d'énergies leurs permettant de se réarranger facilement pour revenir à leur état fondamental. Le second type de défaut chargé présenté est la création de *« Random pairs »* qui correspondent à une stabilisation de ces défauts par réarrangement structural. Les défauts se retrouvent donc dans un état métastable. Nous avons donc émis l'hypothèse que le premier type de défaut était fortement présent après poling, sans directionnalité préférentiel, expliquant donc le caractère erratique des franges mesurées. Ces défauts se réarrangent ensuite pour revenir à leur état fondamental. Cela explique la disparition du signal mesuré dans les verres non-dopés et le changement dans les franges mesurées sur les verres dopés. Dans ces derniers, nous émettons l'hypothèse que la migration de sodium qui est associée à des réarrangements structuraux permet la création du second type de défaut et la stabilisation de

ceux-ci. La migration de sodium se fait préférentiellement selon l'axe z pour compenser le champ électrique extérieur appliqué entre les deux électrodes. Les *« random pairs »* stabilisées se trouvent donc stabilisé selon l'axe z et la signature d'un effet électro-optique provenant d'un champ électrique induit selon l'axe z est donc la seule restante. Ce travail a donc permis de mieux comprendre les mécanismes prenant place au cours du traitement de polarisation thermique et de trouver une façon d'améliorer la stabilité des nouvelles propriétés induites en favorisant les réarrangements structuraux. Une meilleure compréhension des mécanismes nous permet désormais d'essayer de trouver des applications concrètes à ce traitement de polarisation thermique dans les verres de chalcogénures.

La dernière partie du travail sur les chalcogénures s'est donc intéressée à l'application du poling employant une électrode structurée. Il a été démontré qu'il était possible de transférer les motifs de l'électrode à la surface du verre sur les compositions dopées. Nous avons également montré que ces électrodes permettaient de contrôler la répartition du sodium à la surface du verre, permettant ainsi de faire varier localement la composition du verre. Cette variation de composition a permis d'obtenir des variations d'indices importantes, jusqu'à une diminution de 0.05 de l'indice optique. Nous avons également démontré qu'il était possible de faire varier la composition/indice graduellement, permettant ainsi de créer des lentilles à gradient d'indice au sein du verre. Les caractéristiques optiques de ces lentilles peuvent être contrôlées en faisant varier la structuration de l'électrode, la composition du verre ainsi que les conditions de poling. De tels microlentilles présentent un réel intérêt pour l'industrie et peuvent être réalisées sur tout type de verre, à la condition qu'il contienne un cation mobile. Ce dernier travail a conduit au dépôt d'un brevet européen.

Ce travail de thèse a permis d'appliquer le traitement de poling thermique sur une large variété de verre. L'accent mis sur la compréhension des mécanismes au cours du traitement a permis ensuite de prédire les changements de propriétés attendus et de les contrôler à différentes échelles (macro ou micrométrique). Il a permis de mettre en avant le potentiel de la technique de poling pour la réalisation de système où diverses propriétés sont contrôlées à l'échelle micrométrique, ce qui présente un potentiel certain pour la microphotonique.

References

(1) Holonyak, N.; Bevacqua, S. F. Coherent (Visible) Light Emission from Ga(As1−xPx) Junctions. *Appl. Phys. Lett.* **1962**, *1*, 82-83.

(2) Maurer, R. D.; Schultz, P. C. Fused Silica Optical Waveguide. **1972**.

(3) Carlson, D. E.; Hang, K. W.; Stockdale, G. F. Electrode "Polarization" in Alkali-Containing Glasses. *J. Am. Ceram. Soc.* **1972**, *55*, 337-341.

(4) Mukherjee, N.; Myers, R. A.; Brueck, S. R. J. Dynamics of Second-Harmonic Generation in Fused Silica. *J Opt Soc Am B* **1994**, *11*, 665-669.

(5) Liu, X. -.; Zhang, M. -. Theoretical Study for Thermal/Electric Field Poling of Fused Silica. *Japanese Journal of Applied Physics, Part 1: Regular Papers and Short Notes and Review Papers* **2001**, *40*, 4069-4076.

(6) Dussauze, M.; Cremoux, T.; Adamietz, F.; Rodriguez, V.; Fargin, E.; Yang, G.; Cardinal, T. Thermal Poling of Optical Glasses: Mechanisms and Second-Order Optical Properties. *Int. J. Appl. Glass Sci.* **2012**, *3*, 309-320.

(7) Carlson, D. E. Anodic Proton Injection in Glasses. *J. Am. Ceram. Soc.* **1974**, *57*, 461-466.

(8) Carlson, D. E.; Hang, K. W.; Stockdale, G. F. Ion Depletion of Glass at a Blocking Anode - 1, 2. *J Am Ceram Soc* **1974**, *57*, 291-300.

(9) Dussauze, M.; Kamitsos, E. I.; Fargin, E.; Rodriguez, V. Structural Rearrangements and Second-Order Optical Response in the Space Charge Layer of Thermally Poled Sodium-Niobium Borophosphate Glasses. *J. Phys. Chem. C* **2007**, *111*, 14560-14566.

(10) Dussauze, M.; Rodriguez, V.; Velli, L.; Varsamis, C. P. E.; Kamitsos, E. I. Polarization Mechanisms and Structural Rearrangements in Thermally Poled Sodium-Alumino Phosphate Glasses. *J. Appl. Phys* **2010**, *107*.

(11) Dussauze, M.; Rodriguez, V.; Lipovskii, A.; Petrov, M.; Smith, C.; Richardson, K.; Cardinal, T.; Fargin, E.; Kamitsos, E. I. How does Thermal Poling Affect the Structure of Soda-Lime Glass? *Journal of Physical Chemistry C* **2010**, *114*, 12754-12759.

(12) Krieger, U. K.; Lanford, W. A. Field Assisted Transport of Na+ Ions, Ca2+ Ions and Electrons in Commercial Soda-Lime Glass I: Experimental. *J. Non Cryst. Solids* **1988**, *102*, 50-61.

(13) Lipovskii, A. A.; Melehin, V. G.; Petrov, M. I.; Svirko, Y. P.; Zhurikhina, V. V. Bleaching Versus Poling: Comparison of Electric Field Induced Phenomena in Glasses and Glass-Metal Nanocomposites. *J. Appl. Phys.* **2011**, *109*.

(14) Mariappan, C. R.; Roling, B. Mechanism and Kinetics of Na+ Ion Depletion Under the Anode during Electro-Thermal Poling of a Bioactive Glass. *J. Non Cryst. Solids* **2010**, *356*, 720-724.

(15) Redkov, A. V.; Melehin, V. G.; Lipovskii, A. A. How does Thermal Poling Produce Interstitial Molecular Oxygen in Silicate Glasses? *J. Phys. Chem. C* **2015**, *119*, 17298-17307.

(16) Wallis, G.; Pomerantz, D. I. Field Assisted Glass-Metal Sealing. *J. Appl. Phys.* **1969**, *40*, 3946-3949.

(17) Myers, R.; Mukherjee, N.; Brueck, S. R. Large Second-Order Nonlinearity in Poled Fused Silica. *Opt. Lett.* **1991**, *16*, 1732-1734.

(18) Mariappan, C. R.; Roling, B. Investigation of Bioglass-Electrode Interfaces After Thermal Poling. *Solid State Ionics* **2008**, *179*, 671-677.

(19) Mariappan, C. R.; Yunos, D. M.; Boccaccini, A. R.; Roling, B. Bioactivity of Electro-Thermally Poled Bioactive Silicate Glass. *Acta Biomaterialia* **2009**, *5*, 1274-1283.

(20) Hench, L.; Splinter, R.; Allen, W.; Greenlee, T. Bonding Mechanisms at the Interface of Ceramic Prosthetic Materials. *J. Biomed. Mater. Res.* **1972**, *5*, 117-141.

(21) Lipovskii, A. A.; Kuittinen, M.; Karvinen, P.; Leinonen, K.; Melehin, V. G.; Zhurikhina, V. V.; Svirko, Y. P. Electric Field Imprinting of Sub-Micron Patterns in Glass-Metal Nanocomposites. *Nanotechnology* **2008**, *19*.

(22) Sokolov, K.; Melehin, V.; Petrov, M.; Zhurikhina, V.; Lipovskii, A. Spatially Periodical Poling of Silica Glass. *J. Appl. Phys.* **2012**, *111*.

(23) Chou, S. Y.; Liang, X. Method and Apparatus of Electrical Field Assisted Imprinting. **2014**

(24) Yang, G.; Dussauze, M.; Rodriguez, V.; Adamietz, F.; Marquestaut, N.; Deepak, K. L. N.; Grojo, D.; Uteza, O.; Delaporte, P.; Cardinal, T.; Fargin, E. Large Scale Micro-Structured Optical Second Harmonic Generation Response Imprinted on Glass Surface by Thermal Poling. *J. Appl. Phys.* **2015**, *118*.

(25) Fleming, L. A. H.; Goldie, D. M.; Abdolvand, A. Imprinting of Glass. *Optical Materials Express* **2015**, *5*, 1674-1681.

(26) Dussauze, M.; Bidault, O.; Fargin, E.; Maglione, M.; Rodriguez, V. Dielectric Relaxation Induced by a Space Charge in Poled Glasses for Nonlinear Optics. *Journal of Applied Physics* **2006**, *100*.

(27) Dussauze, M.; Fargin, E.; Malakho, A.; Rodriguez, V.; Buffeteau, T.; Adamietz, F. Correlation of Large SHG Responses with Structural Characterization in Borophosphate Niobium Glasses. *Optical Materials* **2006**, *28*, 1417-1422.

(28) Dussauze, M.; Fargin, E.; Rodriguez, V.; Malakho, A.; Kamitsos, E. Enhanced Raman Scattering in Thermally Poled Sodium-Niobium Borophosphate Glasses. *J. Appl. Phys.* **2007**, *101*.

(29) Shelby, J. E.; Lopes, M. In *Introduction to Glass Science and Technology;* The Royal Society of Chemistry: 2005, pp X001-X004.

(30) Guignard, M.; Nazabal, V.; Smektala, F.; Adam, J. -.; Bohnke, O.; Duverger, C.; Moréac, A.; Zeghlache, H.; Kudlinski, A.; Martinelli, G.; Quiquempois, Y. Chalcogenide Glasses Based on Germanium Disulfide for Second Harmonic Generation. *Advanced Functional Materials* **2007**, *17*, 3284-3294.

(31) Guignard, M.; Nazabal, V.; Troles, J.; Smektala, F.; Zeghlache, H.; Quiquempois, Y.; Kudlinski, A.; Martinelli, G. Second-Harmonic Generation of Thermally Poled Chalcogenide Glass. *Optics Express* **2005**, *13*, 789-795.

(32) Guignard, M. Verres et vitrocéramiques infrarouge à base de chalcogénures pour l'optique non linéaire du second ordre, Université de Rennes I, Rennes, 2005.

ACKNOWLEDGMENTS

Ce travail de thèse a été réalisé en co-tutelle entre deux continents. Je tiens donc à remercier tout d'abord le directeur de l'Institut des Sciences Moléculaires (ISM) de Talence, Monsieur Philippe Garrigue et celui du CREOL (College of Optics and Photonics) d'Orlando, Monsieur Bahaa Saleh pour m'avoir permis de travailler au sein de ces deux laboratoires.

Je souhaite ensuite exprimer mes plus sincères remerciements à Monsieur Daniel Neuville et Monsieur Yves Quiquempois qui ont accepté de juger ce travail de thèse en tant que rapporteur. De plus, je tiens à remercier à nouveau Monsieur Daniel Neuville pour avoir accepté à la dernière minute de présider mon jury de thèse. Je tiens à remercier également Monsieur Benoit Boulanger, Monsieur Yannick Petit et Monsieur Thierry Cardinal qui ont accepté de faire partie de ce jury de thèse.

Je souhaite remercier tout particulièrement mes trois directeurs de thèse, Monsieur Vincent Rodriguez, Monsieur Marc Dussauze et Madame Kathleen Richardson. Je tiens à vous remercier pour votre disponibilité, votre soutien et vos précieux conseils tout au long de ces trois années. Dr. Richardson, je souhaite vous remercier de m'avoir donné l'opportunité de venir étudier et travailler aux Etats-Unis. Vincent, je te remercie pour les discussions et le temps que tu m'as consacré pour m'initier au monde merveilleux de l'optique non linéaire. Marc, je tiens à te remercier pour toute l'énergie que tu as dépensée pendant cette thèse. J'ai énormément appris grâce à toi dans des domaines qui m'étaient parfois complétement inconnus au début de ma thèse. Je te remercie pour ta patience, ta pédagogie et ta bonne humeur. Tu as été un réel mentor pour moi et se fut un réel plaisir que de travailler avec toi jour après jour.

Je tiens à remercier Thierry Cardinal de l'ICMCB qui m'a accueilli au sein de son groupe pour la synthèse de mes verres d'oxydes et qui a accepté de partager son savoir-faire avec moi.

Je souhaite également remercier tous les membres permanents ou non-permanents du GSM. Ce fut un réel plaisir que de vous côtoyer au cours de ces trois ans. J'ai réellement apprécié la bonne humeur générale et les conversations animées autour d'un café. Tout particulièrement, je souhaite remercier Frédéric Adamietz sans qui bon nombre de résultats de cette thèse n'aurait pu être obtenus. Merci à toi de m'avoir toujours aidé au cours de mon travail et merci surtout pour ta bonne humeur et pour les sorties plage/montagne avec le reste du labo ! Un grand merci également à Flavie avec qui j'ai apprécié collaborer et qui a supporté l'humour de Fred et de moi-même. Je souhaite remercier les stagiaires qui ont participé au travail de cette thèse et tout particulièrement Matthieu Chafer qui a très fortement contribué au travail sur les BPN. Je souhaite également remercier Margot qui a commencé sa thèse en même temps que moi et qui a également connu les joies de la co-tutelle ! Je te remercie tout particulièrement d'avoir fait le voyage depuis la Belgique pour assister à ma soutenance. Je tiens enfin à remercier l'ensemble des étudiants du groupe pour les moments passés ensemble.

Un très grand merci aux membres du GPCL à Orlando, Benn, James, Andy, Charmayne, Jason, Devon, Spencer, Erick, Laura, Karima, Spencer, Becca et tous les autres. J'ai apprécié pouvoir travailler dans la bonne humeur à vos côtés et je vous remercie de m'avoir fait découvrir la vie américaine, notamment les burgers de chez Oblivion et les pizzas de Lazy Moon. Je souhaite également remercier Heidi et Taylor qui m'ont parfois accueilli chez eux au cours de mes multiples aller-retours entre Bordeaux et Orlando.

Je souhaite également dire à quel point je suis reconnaissant à mon frère Romain et mes sœurs Marguerite et Clémentine pour leur soutien au cours de cette thèse mais également au cours des 23 années qui l'ont précédée. Je suis heureux de vous avoir à mes côtés et, même de loin, vous avez toujours su me remotiver et m'encourager. Bien entendu, rien n'aurait été possible sans mes parents qui m'ont donné le goût du travail et m'ont permis d'arriver là où je suis.

Enfin, je ne peux finir ces remerciements sans un paragraphe pour Elise. La thèse m'a permis de te rencontrer et rien que pour cela je ne regrette pas mon choix. Tu as toujours été là pour moi au cours de ces trois années et je te remercie d'avoir supporté mes multiples voyages de l'autre côté de l'Atlantique. Il me tarde de pouvoir commencer un nouveau chapitre à notre histoire commune, cette fois ancré sur un seul continent !

TABLE OF CONTENTS

LIST OF FIGURES

LIST OF TABLES

CHAPTER 1: INTRODUCTION

Today, photonics have become ubiquitous in our daily life. This scientific domain focuses on the study of light – more specifically on the study and fabrication of devices to generate, process (by modulating or amplifying), convert and detect optical signals. It covers the entire light spectrum but is mostly focused on visible and infrared light. The range of applications of photonics is broad and includes optical communication, information and computing, defense, bio-chemical sensing, image processing. This list is not exhaustive and other applications are possible.

Photonics is a relatively new scientific domain that started its growth after the development of the first semiconductor light emitting devices (LED) developed in the early 1960s in the USA by Holonyak. [1] Holonyak is considered as the father of the LED but its principle was first observed by Round in 1907 [2] and discussed by Losev in the 1920s in a series of paper. [3] However, the 1960s and the 1970s, with the development at Corning of the first optical fiber having low enough optical losses to be used in telecommunication (as low as 20 dB/km), [4] were the two decades which started the burst of photonics.

Recently efforts have been made to reduce device sizes and a subdomain of photonics has emerged that is microphotonic. Microphotonic deals with light at a microscopic scale and ultimately aims to replace microelectronics devices as the use of light would accelerate the flow of transmitted information. To replace microelectronics, Photonic Integrated Circuit, also known as PIC, are developed. These devices are similar to electronic integrated circuit in that on a compact chip, several components are present with various role. The photonic functions present on these devices are more and more relying on non-linear optics (NLO). However, challenges remain in the

development of new materials and new fabrication technique to improve the efficiency of such components.

The study presented in this PhD work is centered on these issues of developing new materials for microphotonic and integrated circuits. Our main interest is focused on engineering materials to tailor their optical properties (linear and non-linear). This focus is not only limited to the optics themselves, as we aim to tailor the functionality of the components. Here, we examine chemical functionality, i.e., surface properties (such as surface reactivity, wettability...) to design devices which could be used as Lab-on-a-chip or PICs, as well as the creation of nonlinear functionality and its stability. This modification to the base glass' behavior is introduced to the optical material through a process of thermal poling.

Materials which have been used so far for non-linear optics are typically inorganic crystals which present a strong non-linear response. However, these materials present major drawbacks as they are difficult to manufacture and induce important intensity losses as light propagates. Optical glasses present a good alternative to crystal as they are easy to manufacture and present a good transmission of light with low losses. The main issue with amorphous materials is due to their centrosymmetry which forbid them to exhibit Second Order Non-Linear Properties (SONL) such as Second Harmonic Generation (SHG). Several techniques have been developed to bypass this difficulty and to break the centrosymmetry of the glass. The major available techniques to break a glass's centrosymmetry are thermal poling, optical poling and corona discharge which will be described later on in this introductory chapter.

Our work is focused on the study of thermal poling as a mean to tailor not only a glass second order non-linear response but also to tailor its linear optical properties, its structure and stability and the resulting surface reactivity at both macro- and micrometric scales.

The approach to this topic was to first find suitable glass compositions in two glass systems (oxide glasses and chalcogenide glasses) and to then find the appropriate thermal poling conditions to treat these samples. During the poling step, efforts were made to tailor the glass's properties at a micrometric scale and to understand the underlying mechanisms of such a thermal poling process.

This work has been conducted in close collaboration with several teams in France with the Institut of Molecular Science (ISM) and the Institut de Physico-Chimie de la Matière Condensée (ICMCB) of the University of Bordeaux, and in the USA in the Glass Processing and Characterization Laboratory (GPCL) at CREOL the College of Optics and Photonics at the University of Central Florida.

The dissertation is divided in five chapters. Discussed below is an introduction to the poling method, providing necessary background on the techniques and mechanisms used to break a glass's centrosymmetry for SONL properties as well as a brief introduction to nonlinear optics. It also gives an extensive literature review on prior efforts on thermal poling.

The second chapter gives a description of the main techniques used to prepare and characterize the glasses before and after poling.

The third chapter discusses results obtained in sodium borophosphate niobium glasses, which are a well-studied, reference glass system for thermal poling. The work presented therein uses this

system to evaluate and demonstrate the use of structured electrodes to micro- (µ-)pattern optical properties of the surface during thermal poling.

The fourth chapter focuses on thermal poling to induce a change of surface reactivity in a borosilicate glass at both macro- and micrometric scale by first using a classical thermal poling and then by using thermal poling using structured electrode, introduced in the third chapter. This technique has allowed us to evaluate and understand the chemical mechanism in the glass which gives rise to the resulting post-poled, spatially selective chemical surface modification.

Lastly, the fifth chapter focuses on thermal poling as a means to tailor chalcogenide optical properties (linear and non-linear), using a classical thermal poling technique and structured electrodes. Here, our work addresses several fundamental issues including the mechanism of glass structure modification in the non-oxide network, the effect of glass stoichiometry and most importantly, the inter-relationship between the poling conditions and glass network's chemistry on the long-term stability in the post-poled glass network and the resulting *induced* modification to the material's optical properties. A mechanism is proposed which illustrates the improvement in stability that has resulted in this study, as compared to prior efforts to pole infrared glasses.

1.1 How to break a glass's centrosymmetry?

Glasses are amorphous materials which present the phenomenon of glass transition temperature. Due to their lack of long range order, an amorphous medium is perfectly centrosymmetric. A medium is said to be centrosymmetric when it possesses an inversion center. In such a point group, for every point with coordinates (x, y, z) in the unit cell, there is an indistinguishable point with coordinates (-x, -y, -z). The presence of an inversion center makes it impossible for the medium to

exhibit certain properties such as Second Order Non-Linear Optical properties. For a glass to exhibit such properties, it is therefore necessary to break its centrosymmetry. Two families of techniques can be used. The first one relies on the use of an electric field and the various available techniques are regrouped under the name of poling. The second one disrupt the glass centrosymmetry by controlling the growth of non-centrosymmetric crystals inside the glass matrix to form glass-ceramics. The second family will not be detailed here but we will briefly define the various poling techniques available to break a glass's centrosymmetry.

1.1.1 Optical poling

Optical poling is a technique which employs an intense laser light to irradiate a glass sample. The electric field is thus applied without a direct contact but through the laser light. The first reported use of this technique was made in the 1986 by irradiation of a silica fiber with a high intensity light. [5] Following this pioneer work, lots of studies followed to try to improve the efficiency of the optically poled fibers. [6-9] Optical poling is a photo-induced effect which is based on the photogalvanic effect, a phenomenon by which a current appears in a homogeneous medium under illumination. [10, 11] More precisely, the process taking place in glasses is a third-order coherent photogalvanic effect. [12] The recorded non-linearity is rather low in glasses using that technique, of the order of 10^{-3} pm/V but have a great advantage in that this technique allows for a self-assembly of the induced electric field permitting to meet phase matching conditions, an important concept which will be defined in a section to follow.

1.1.2 Corona poling

Corona poling or Corona discharge is a technique which involves the partial breakdown of air or nitrogen atmosphere. The sample to be poled is placed on a grounded plate which can be used as

a heating plate. A needle is suspended above the sample and a high voltage (5 to 10 kV) is applied on the needle causing ionization of the surrounding atmosphere. Ions will move towards the cathode and encounter the dielectric. The charge continues to increase at the surface of the sample until an equilibrium is reached. During the process, molecules (in case of a polymer) will orientate as dipoles and will keep their orientation after poling unless the sample is heated. This technique has been used extensively in poling of polymer films [13] but has also been successfully used on glasses. [14]

1.1.3 Thermal poling

Thermal poling was first developed in the late 1960s by Wallis and Pomerantz [15, 16] and is the technique used throughout this PhD. The process is conducted on a glass slide placed between two electrodes (usually silicon) in a cell with controlled atmosphere (air, argon, nitrogen…). The assembly is then heated below the glass transition temperature of the glass, and once a homogeneous temperature is reached, a strong DC electric field is applied across the sample.

Upon heating the sample, charges (mostly alkali and alkaline-earth cations) have their mobility increased. The DC bias is then applied between the two electrodes thus promoting charge separation through cationic migration towards the cathode. The cation departure can be seen as an electric field assisted migration. As cations leave the vicinity of the anode, a layer of the order of few microns is left entirely depleted of them underneath the surface. The depleted layer is formed of negative charges originating from non-bridging oxygens (NBO) in oxide glasses following cation departure. The conductivity in the alkali-depleted layer then dropped and most of the applied DC voltage is effectively distributed solely on this layer, resulting in an internal field that can reach values up to 10^8 - 10^9 V/m. [17-20] Depending on the nature of the glass and the type of poling

(blocking anode conditions or open anode conditions), charge rearrangements can take place and the thickness of the layer can vary. The sample is then brought back to room temperature and only then is the applied DC electric field removed. The charges are said to be “frozen in” the glass matrix resulting in a strong static electric field in the near anode surface. The direction of this static electric field is opposite to the electric field applied during poling as charge separation in the medium was intended to compensate that applied electric field. The principle of thermal poling is summarized in figure 1.1.

At this point it is important to make a difference between the term poling used in glasses as opposed to poling as used in poling of ferroelectric ceramics. In the latter case, a polycrystalline ceramic is heated above its Curry temperature making the structure centrosymmetrical. A large electric field is subsequently applied to the ceramic as the sample is cooled down. By doing this, the dipoles align with the electric field thus breaking the centrosymmetry. Back at room temperature, the electric field is removed and the ferroelectric domains keep their new orientation leading to a permanent polarization of the ceramic. In thermal poling of glasses, cation migration is known to be involved and is responsible of the creation of a space charge in the vicinity of the anode. Charges are then frozen inside the glass matrix leading to the creation of a static electric field inside the glass and to the polarization of the sample.

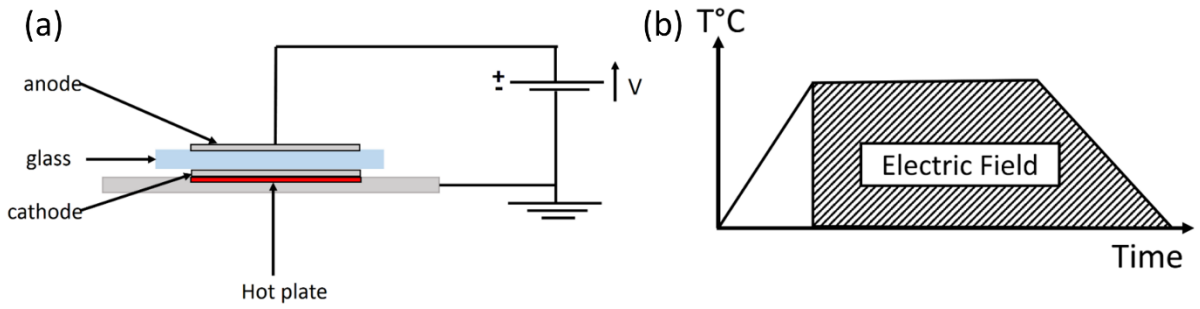

Figure 1.1. Principle of thermal poling: thermal poling assembly (a), heat treatment and electric field as a function of time (b)

1.2 Introduction to second order nonlinear optics

1.2.1 Light to matter interaction and the concept of polarization

To better understand the various phenomenon involved in this induced Second Order Nonlinear response of the medium, it is necessary to do a basic overview of nonlinear optics (for further details on Second Order Nonlinear Optical Properties and characterization techniques, the book by Verbiest et al. is more detailed [21]). Two important things need to be first described: light and matter as the phenomenon described here deal with light to matter interaction.

Light is an electromagnetic wave described by an electric (E) and a magnetic field (B). The axis perpendicular to these two fields gives the direction of light propagation and Maxwell's equations allows one to fully describe this propagating wave. In the work presented here, the magnetic field part of light will be neglected as its effect on dielectric medium (such as glasses) is considered negligible. Only the electric field remains and can be written as:

$$E(r,t) = E_0(e^{(ik.r-i\omega t)}) \quad (1.1)$$

With ω being the pulsation of the electromagnetic field also equals to 2πν (ν being the frequency), ω.t a time-dependent phase term and k.r a space-dependent phase term. k is the wave vector that

indicates the direction of light propagation, it is equal to $2\pi n/\lambda$ (n being the refractive index, λ being the wavelength).

Matter is described as being made up of atoms comprised of a positive point charge (core) surrounded by a cloud of negative charges (electrons). This assembly of core and electrons can be approximate as a dipole which is characterized by its *dipole moment* M. The dipole moment is a vector which describes the separation of the positive and negative charges. In absence of an exterior electric field, the dipole moment is null, this is the classical approach of a dielectric medium. However, once an electric field is applied, it will interact with the charged particles. Typically, the core tends to move in the direction of the field and the electrons will move in the opposite direction. The movement of the electrons is usually more significant, as their considerably lower mass leads to a faster response. This interaction will cause a charge separation that can be seen as a deformation of the cloud of electrons, characterized by *induced microscopic dipole moments* μ. Under illumination with a *low intensity light*, the induced microscopic dipole moments oscillate with the same frequency as the incident electric field. The formation of dielectric dipole moments at the microscopic scale results in the apparition of a macroscopic polarization which is the sum of all microscopic dipoles. This is the classical linear light to matter interaction. Nevertheless, in the case of illumination of a material with a *high intensity light*, i.e. of the order of the atomic cohesion forces, the cloud of electrons oscillate with a higher amplitude and cannot be described by a harmonic oscillation and it is necessary to develop the resulting polarization in series as a function of the local electric field. The induced dipole moment at the microscopic scale is written as:

$$\mu_{ind}(\omega) = \mu^{(1)}(\omega) + \mu^{(2)}(\omega) + \mu^{(3)}(\omega) + \cdots$$
$$= \alpha F(\omega) + \beta F(\omega)F(\omega) + \gamma F(\omega)F(\omega)F(\omega) \quad (1.2)$$
$$+ \cdots$$

With α the molecular first order polarizability or linear polarizability while β and γ are respectively the second and third order polarizability terms which described the nonlinear induced polarization and F the local field. In this expression (ω) refers to the frequency of the electro-magnetic wave as in expression (1). For the sake of clarity, this term will be omitted in most of the expressions of this thesis but one should keep in mind that this argument is implicit and that polarizability is frequency-dependent. To better describe the interactions at the microscopic scale, it is important to define the local field F. At the microscopic scale, the local field F is not perfectly equal to the electric field E of the incident light due to the interactions between the dipoles. A local field factor (f) is thus necessary to account for interactions between neighboring dipoles. A common form of the local field factor is given by the Lorentz-Lorentz approximation [22] and takes into account these interactions. The local field F can be written as

$$\vec{F} = f\vec{E} \quad (1.3)$$

As stated earlier, at the macroscopic scale, the polarization can be seen as the sum of all the induced microscopic dipole moment. The material polarization is thus similarly described at the macroscopic scale by

$$P = \epsilon_0[\,\chi^{(1)}E + \chi^{(2)}EE + \chi^{(3)}EEE + \cdots\,] \quad (1.4)$$

where ϵ_0 is the vacuum permittivity, $\chi^{(1)}$ the linear susceptibility, $\chi^{(2)}$and $\chi^{(3)}$ respectively the second and third order nonlinear susceptibilities and E the electric field. The field of nonlinear optics (NLO) consists in studying the behavior of light in a nonlinear medium and thus to focus on the higher order terms.

The quantities at the base of the second-order nonlinear optical properties of a medium are the second order polarizability (microscopic scale) and the second order susceptibility (macroscopic scale). These two quantities can be linked together and, in the case of a system made up of N oscillators, can be written as

$$\chi^{(2)} = Nf\beta \tag{1.5}$$

With N the number density and f a local field factor. β and $\chi^{(2)}$ are both tensors of rank 3 containing 27 components in a 3x3x3 matrix. In this work, only second order nonlinear properties are studied and we will focus on the second order nonlinear susceptibility $\chi^{(2)}$. Our main focus will be on the $P^{(2)}$ term which varies quadratically with the electric field (therefore refers to as the quadratic polarization) and is equal to

$$\mathrm{P}^{(2)} = \epsilon_0 \chi^{(2)}\ \mathrm{EE} \tag{1.6}$$

Which is equivalent to

$$P_i^{(2)} = \epsilon_0 \sum_{j,k} \chi_{ijk}^{(2)} E_j E_k \tag{1.7}$$

where ikj referring to the Cartesian coordinates (x,y and z), $P_i^{(2)}$ is a component of the polarization vector, E_j and E_k components from the electric field vector and $\chi_{ijk}^{(2)}$ the terms of the rank 2 tensor. If we now write this expression explicitly, for the case of type I SHG, we obtain:

$$\begin{bmatrix} P_x^{(2)} \\ P_y^{(2)} \\ P_z^{(2)} \end{bmatrix} = \epsilon_0 \begin{bmatrix} \chi_{xxx}^{(2)} & \chi_{xyy}^{(2)} & \chi_{xzz}^{(2)} & \chi_{xyz}^{(2)} & \chi_{xzy}^{(2)} & \chi_{xzx}^{(2)} & \chi_{xxz}^{(2)} & \chi_{xxy}^{(2)} & \chi_{xyx}^{(2)} \\ \chi_{yxx}^{(2)} & \chi_{yyy}^{(2)} & \chi_{yzz}^{(2)} & \chi_{yyz}^{(2)} & \chi_{yzy}^{(2)} & \chi_{yzx}^{(2)} & \chi_{yxz}^{(2)} & \chi_{yxy}^{(2)} & \chi_{yyx}^{(2)} \\ \chi_{zxx}^{(2)} & \chi_{zyy}^{(2)} & \chi_{zzz}^{(2)} & \chi_{zyz}^{(2)} & \chi_{zzy}^{(2)} & \chi_{zzx}^{(2)} & \chi_{zxz}^{(2)} & \chi_{zxy}^{(2)} & \chi_{zyx}^{(2)} \end{bmatrix} \begin{bmatrix} E_x^2 \\ E_y^2 \\ E_z^2 \\ E_y E_z \\ E_z E_y \\ E_z E_x \\ E_x E_z \\ E_x E_y \\ E_y E_x \end{bmatrix} \quad (1.8)$$

In the specific case of Second Harmonic Generation, $\chi_{ijk}^{(2)} = \chi_{ikj}^{(2)}$, as the susceptibility tensor is invariant to the permutation of j and k, this tensor can be simplified and written with a 3x6 matrix.

In the case of SHG, another formalism is usually used to represent the susceptibility tensor, that is the tensor d_{ijk} which is equal to $\chi_{ijk}^{(2)}/2$. The tensor d_{ijk} is usually written as d_{il}, where i=1 corresponds to the x axis, i=2 to the y axis and i=3 to the z axis. As for l, it takes values from 1 to 6 which corresponding values are shown in Table 1.1.

Table 1.1. Corresponding values between l and jk

l	**1**	**2**	**3**	**4**	**5**	**6**
jk	xx	Yy	zz	yz = zy	xz = zx	xy = yx

Equation (1.8) can thus be rewritten for the case of Second Harmonic Generation as

$$\begin{bmatrix} P_x^{(2)}(2\omega) \\ P_y^{(2)}(2\omega) \\ P_z^{(2)}(2\omega) \end{bmatrix} = \epsilon_0 \begin{bmatrix} d_{11} & d_{12} & d_{13} & d_{14} & d_{15} & d_{16} \\ d_{21} & d_{22} & d_{23} & d_{24} & d_{25} & d_{26} \\ d_{31} & d_{32} & d_{33} & d_{34} & d_{35} & d_{36} \end{bmatrix} \begin{bmatrix} E_x^2(\omega) \\ E_y^2(\omega) \\ E_z^2(\omega) \\ 2(E_y(\omega)E_z(\omega)) \\ 2(E_x(\omega)E_z(\omega)) \\ 2(E_x(\omega)E_y(\omega)) \end{bmatrix} \quad (1.9)$$

1.2.2 The effect of symmetry on the $\chi^{(2)}$ tensor

The $\chi^{(2)}$ tensor has specific properties link to symmetries which are necessary to discuss to understand nonlinear optics. These various types of symmetries are permutation symmetry, time-reversal symmetry and symmetry in space. The first two types of symmetry are fundamental properties of the susceptibilities while spatial symmetry is linked to the nonlinear medium. To illustrate the importance of symmetry, let's take the case of glass, i.e. a centrosymmetric medium. As defined earlier, a centrosymmetric medium has a center of inversion, Neumann's principle [23] states that if a medium is invariant to certain symmetry operations, its physical properties must be invariant too. Therefore, the electric field E must be equal to –E and the polarization P equal to –P. For second order nonlinear optical properties, we have written the term $P^{(2)}$ as $P^{(2)} = \chi^{(2)}EE$. By applying Neumann's principle, the previous expression is equivalent to $-P^{(2)} = \chi^{(2)}(-E)(-E)$ which therefore gives $\chi^{(2)}$ equals to zero. Using Neumann's principle, it is then possible to evaluate the influence of a symmetry operation on a term of the tensor. To makes this easier, one can use the direct inspection method developed by Fumi [24] which states that following a symmetry operation, if the index ijk of a term of the tensor changes sign, this term is equal to zero. A good example to understand the importance of symmetry on the rank two tensor is the one of quartz crystal which is used as a reference for SHG in this work. Quartz crystal belongs to the 32 (international notation

or D_3 with the Schoenflies notation) point group, its second order nonlinear susceptibility tensor can thus be written as

$$\begin{bmatrix} d_{11} & -d_{11} & 0 & d_{14} & 0 & 0 \\ 0 & 0 & 0 & 0 & -d_{14} & d_{11} \\ 0 & 0 & 0 & 0 & 0 & 0 \end{bmatrix} \quad (1.10)$$

1.2.3 Origin of the induced SONL properties in poled glasses

As stated earlier, second order nonlinear optical activity is forbidden in glasses. However, during thermal poling, a strong internal static electric field E_{int} is induced inside the glass matrix in the cation depleted region. The presence of this internal electric field breaks the glass centrosymmetry which gives rise to an electro-optical effect called Electric Field Induced Second Harmonic or EFISH. The second harmonic generation then originates from the interaction between the third order nonlinear susceptibility $\chi^{(3)}$ and the static electric field. The second order nonlinear susceptibility can then be written as

$$\chi^{(2)} = 3\,\chi^{(3)} E_{(int)} \quad (1.11)$$

The glass no longer belongs to the point group $\bar{1}$ (international notation, C_i in Schoenflies), but now belongs to the $C_{\infty v}$ (Schoenflies, ∞mm in the International notation) as the electric field acts as a rotation axis of infinite order, the glass now also possesses an infinite number of mirror planes which include the static electric field. The $\chi^{(2)}$ tensor can thus be written as

$$\begin{bmatrix} 0 & 0 & 0 & 0 & d_{31} & 0 \\ 0 & 0 & 0 & d_{31} & 0 & 0 \\ d_{31} & d_{31} & d_{33} & 0 & 0 & 0 \end{bmatrix} \quad (1.12)$$

The origin of the SHG can be due a dipole re-orientation or to the static electric field. To discriminate between these two possible origins, it is useful to study the ratio d_{33}/d_{31}. In the case of a dipole orientation, this ratio increases as the orientation increases. However, in the case of a static electric field, the ratio is strictly equal to 3.

To optimize the SONL response of the glass, two factors are important (i) a high $\chi^{(3)}$ value or (ii) the presence of a strong induced electric field. The first parameter is linked to the intrinsic properties of the material and its constituent elements, for instance chalcogenide, highly polarizable elements (Nb, Ti, …) and elements with a lone pair (Te…) allow an enhancement of the medium's polarization. The second parameter is linked to the presence of mobile species in the glass and to the poling conditions. To obtain a large value of the electric field, it is necessary to obtain a large alkali depletion and to concentrate it over a small thickness. The parameters and conditions of the poling such as nature of the electrodes, atmosphere, treatment duration, thickness of the glass sample (which is linked to resistivity), intensity of the applied electric field are all important to control the thickness of the depleted layer and will be discussed throughout this chapter.

1.2.4 Phase matching conditions

Various parametric processes in nonlinear phenomenon need to meet phase matching conditions to be efficient. These phenomena rely on the interaction of two waves with different frequency. In the medium, due to the chromatic dispersion, the two waves are going to propagate at two different speed and the medium will have two refractive indices n_ω and $n_{2\omega}$. In the case of frequency doubling, like SHG, the intensity of the signal is then dependent of these two indices and of the difference between the magnitude of the two wave vector (k), given by

$$\Delta k = k_2 - 2k_1 \quad (1.13)$$

If the two waves interfere constructively, meaning the medium is non-dispersive (no chromatic dispersion, $n_\omega = n_{2\omega}$), then Δk is null and the transfer is optimum, *phase matching conditions* are met.

Out of phase matching conditions, meaning the medium is dispersive ($n_\omega \neq n_{2\omega}$) the two waves are travelling at two different speeds, the contributions from the two waves do not add up constructively. Interferences between the two waves induce oscillations of the amplitude of the second harmonic signal.

Phase matching conditions can be obtained in nonlinear crystals by playing with the birefringence of the crystals which permits to eliminate the phase mismatch. Another technique can be also used that is *quasi-phase matching* (QPM). [25-27] This technique is the one used in glasses (but not only) as it is not possible to employ birefringence properties. In that case, real phase match does not occur but it is possible to reach high conversion by making a periodical array of nonlinear active layers. In crystals, the sign of the nonlinearity will then vary along the light path. This configuration is achieved by periodic poling which can be done in two ways, *(i)* local erasure of the poled region and by *(ii)* the use of a periodically structured electrode.

To understand how to design a periodically polled glass or crystals with opposite sign of nonlinearity, it is necessary to define the notion of coherence length. In nonlinear optics the coherence length corresponds to the length over which the phase difference between the two waves (the fundamental and the harmonic wave) is equal to π. The coherence length is defined as

$$L_c = \left|\frac{\pi}{\Delta k}\right| \tag{1.14}$$

It should not be mistaken with the coherence length in optics used to quantify the degree of temporal coherence over which coherence drops down in a significant manner.

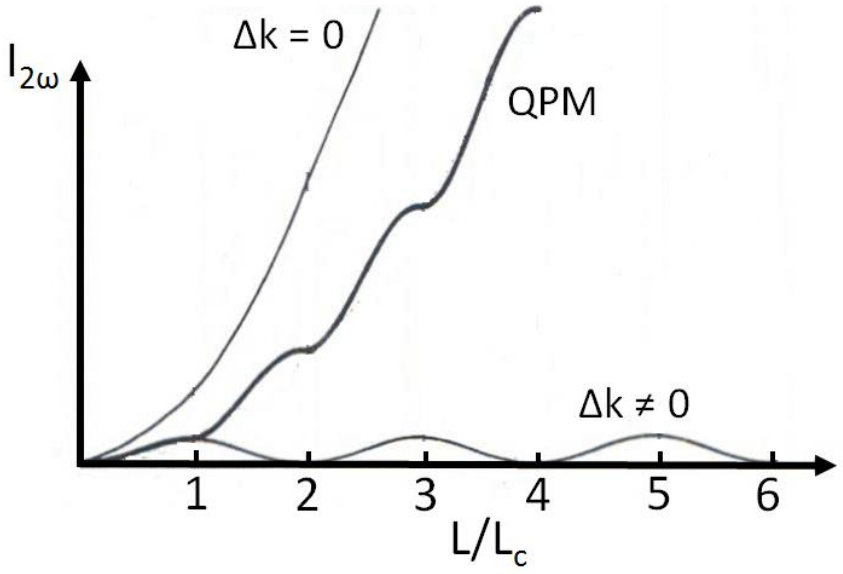

Figure 1.2. Representation of the evolution of the $I_{2\omega}$ intensity as a function of the length L of the medium

When designing a periodically poled crystal or glass, the length of the period should be equal to the coherence length. By doing so, the amplitude of the harmonic wave continues to grow instead of dropping however not as fast as in real phase-matching conditions.

Figure 1.2 presents the three cases defined earlier: phase matching conditions, quasi-phase matching and no phase matching conditions. It is plotted as a function of L/L_c with L being the distance over which the light is propagating in the medium.

1.3 Second Harmonic Generation in Silica glass

In 1991, Myers [18, 28] recorded second harmonic generation in silica for the first time. He proceeded similarly to the procedure described at the beginning of this chapter. The experiment aimed at polarizing a polymer film deposited on a glass substrate but he noticed that the treatment had an effect on the substrate. The recorded non-linearity was up to 1 pm/V. [28] Following this work, it was noticed that the static electric field could be linked to the presence of an alkali depleted layer under the anode. Poling of silica glasses was then thoroughly studied by the scientific community. [18, 28-31]

The impact of various parameters (atmosphere, voltage, electrodes, time) of the treatment were studied and it was possible to control the size of the non-linear layer, its intensity and its position in the sample. [20] The SHG response is studied using quantifying Maker fringes technique while the position of the non-linear active layer can be found using micro-SHG imaging, acid etching and/or backscatter ion mass spectrometry (to find the alkali-depleted layer). These studies helped to better described the mechanisms of thermal poling and to predict the resulting NLO properties. Especially, the work of Quiquempois et al. showed the strong dependence of the SHG intensity with the applied voltage. [32] Upon poling of an Infrasil 301® glass slide, he proved the existence of a voltage threshold as well as a linear dependence of the square root of the SHG signal with voltage intensity. In this particular glass, they found rather large SHG response and a thin space charge region (5 μm). Their work is of the utmost importance as they proposed a model which matched and could explain their observations. Their model was broader than the ones preceding that were only taking into account the migration of the cations to estimate the non-linear response induced in the medium. [18, 33] These previous attempts were limited as they took into account only few

charge carriers with strict limiting conditions thus only matching experimental results for very specific cases. The model of Quiquempois et al. however took into account charge dissociations and recombination as well as the effect of the heating on the diffusion of the moving species. They then applied and adapted the model by Proctor and Sutton [34] to thermal poling to evaluate the charge distribution in a glass under an electric field. An expression for the electric field as a function of the distance from the anode could be obtained.

The study which was conducted by Quiquempois et al. was made on a particular silica glass which contains mostly alkali cations and has a low content in OH impurities. The role of the various impurities present in silica glasses (both alkali and OH) was studied in an article by Dussauze et al. [20] and proved their importance on post-poling properties. Three silica glasses were studied: Infrasil ®, Suprasil 2B ® and Suprasil 300 ®. Their impurity content is shown in Table 1.2.

In this effort, three glasses were poled under the same conditions, i.e. 90 min at 300 °C with a DC bias of 5 kV but had Maker fringes presenting widely different profiles. All glasses presented a purely EFISH contribution but dissimilarities are worth discussing.

Table 1.2. Impurities content in various silica glasses, from M. Dussauze et al.[20]

Impurities concentration in ppm	Infrasil ®	Suprasil 2B ®	Suprasil 300 ®
OH	≤ 8	≤ 1000	≤ 1
Na	1	≤ 0.01	≤ 0.01
Li	1	≤ 0.001	≤ 0.001
K	0.8	≤ 0.01	≤ 0.01

Both Suprasil ® glasses showed more complicated patterns with the appearance of multiple fringes. In addition, in Suprasil ® glasses, both $\chi^{(2)}$ and electric field were lower. This could be explained by a larger alkali depleted layer (up to 100 μm) and by a non-negligible contribution from the bulk glass. The low alkali content makes necessary for the depleted layer to spread out across the glass to be able to screen the applied voltage. In the Infrasil ® glass, to screen the applied voltage of 5 kV, thanks to the higher alkali concentration (10^{23} ions/m^3), a depleted layer of 1 micron gives a static electric field close to 10^9 V/m (so 10^3 - 10^4 C/m^3). In Suprasil ® glasses, as fewer alkali are available (10^{-2} ppm), the maximum charge density is 10^2 C/m^3, two order of magnitude lower than in Infrasil ®, thus requiring a thickness twice larger to screen the applied electric field. This then leads to a lower response of the induced SHG, two order of magnitude lower than in the case of Infrasil ®.

The contribution from the bulk can be theoretically predicted following the zero-potential condition, the electric field distribution across the glass sample can be described as on the following figure with the $\chi^{(2)}$ coefficients of the alkali depleted layer and the bulk, respectively being positive and negative. [35]

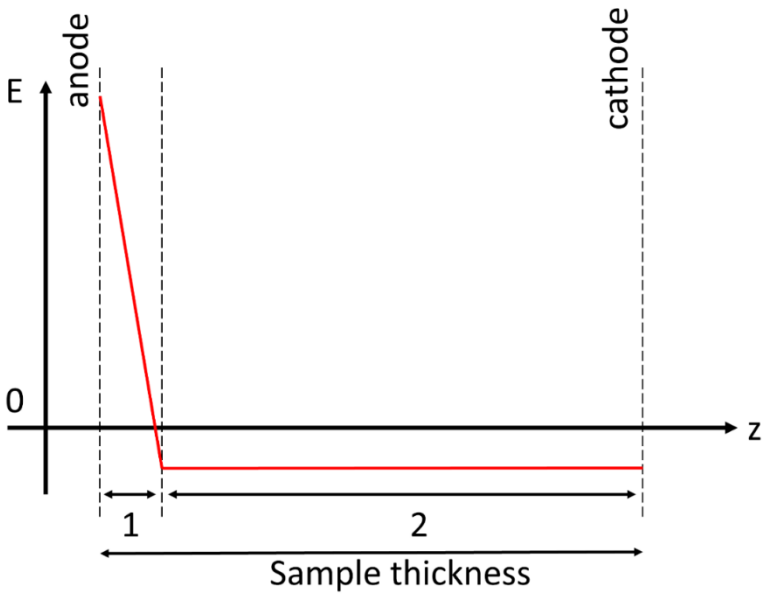

Figure 1.3. Evolution of the electric field in a poled sample (blocking anode and open cathode) First zone correponds to the cation depleted layer, second zone corresponds to the bulk

Voltage, temperature, impurities content are all parameters directly influencing the post-poling properties. For instance, in the literature, poling effective on scale ranging from few microns to hundreds of microns [36, 37] are reported depending on the parameters and glass matrix used during the procedure.

From all of these studies, thermal poling of silica glasses is now well understood, the important parameters have been identified allowing for a good control of the post-poling properties. Researchers then moved on to more complicated glass compositions which are going to be discussed in sections to follow.

1.4 Thermal poling of alkali-rich glasses

The preponderant role of cationic conductions in the formation of the static electric field in the glass was shown in silica glass. Owing to their higher ionic conductivity, alkali-rich glasses should

therefore exhibit additional changes directly linked to cations displacement. Thermal poling of alkali-rich glasses has been studied mainly for two applications, *(i) anodic bonding* in microelectronic applications [16] and (*ii) glass poling for nonlinear optical properties*. [38] These two communities have tried to describe the mechanisms taking place during thermal poling but so far did not manage to agree on a description of the charges involved, especially regarding the nature of negative species. In 1974, Carlson et al. [17, 39, 40] gave a first description of the mechanisms taking place in the process which is still a reference today. Carlson studied polarization of glasses and demonstrated the appearance of an alkali depleted layer under the anode. Depending on the poling conditions, blocking electrode or open electrode conditions, different mechanisms were proposed. Blocking electrodes cannot supply charges to inject into the glass, therefore species moving during poling only originate from the glass matrix; whereas under open electrode conditions, injections of species from the surrounding atmosphere (mostly H^+ and H_3O^+) or from the electrode can take place. It is important to note that it is almost impossible to meet perfectly blocking electrode conditions. The electrode will be considered blocking at the anode if no charges can be injected to the glass from its surroundings. However, exchange between the glass and the atmosphere can still occur through departure of species from the glass. Carlson showed that following the formation of the alkali-depleted layer, almost all of the voltage applied on the sample is effectively applied on the alkali free region. The electric field building up in that region can reach values so large that dielectric breakdown should occur in the alkali-depleted region. As dielectric breakdown does not occur, it is therefore necessary to take into account compensation processes. Carlson suggests that following cation departure, negative species start to move towards the anode to compensate the charges. The depleted layer contains can be seen as formed of a large amount of non-bridging

oxygens (NBO) and the electric field in that region is high enough to dissociate the NBOs which then migrate towards the anode. He also pointed out that the depleted region densified and that the poled region is subjected to topography changes.

As in silica glasses, the SHG response varies depending on the parameters and compositions used during poling. As shown by Dussauze in his study above, all silica is not identical, and processing methods used to produce high purity silica impact the residual, trace levels of impurities (OH-, hydride, and low quantities of cationic species). Under open electrode conditions, charges are injected inside the glass matrix. The space charge created is believed to be compensated for by the hydroxyl groups injected inside the glass and the depleted layer can be formed over longer distances. Whereas under blocking anode conditions, no injection is possible therefore resulting in thinner depleted layer.

Scientists agreed on the creation of the alkali-depleted layer and on the injection of positively charged species at the anode. The process can then be seen as an electric field assisted ionic exchange. Two main mechanisms occur during poling, (i) a compensation mechanism coming from the material itself by network rearrangement, [41] (ii) a compensation mechanism based on the ionic exchange. [42]

However, the debate on the nature of the negative charges moving in the glass is still topical with some papers suggesting a displacement of electrons and others suggesting displacement of the NBOs. [43, 44] The presence of an oxygen depleted layer in the glass following thermal poling was demonstrated by NMR measurements [45] and ion-beam analysis. [46] Thorough study of structural rearrangements and the necessity of charge equilibrium also highlighted the possible deficit of

oxygen in anodic region following poling. [20, 41-43, 47, 48] These last studies used vibrational spectroscopy to highlight structural changes in the near surface region and helped solidify the understanding of the mechanism of charge migration in alkali-containing oxide glasses. For instance, when poling soda-lime glasses, departure of the alkali from the subanodic region change the structure from a Q_3 containing network to a Q_4 network. Q_3 and Q_4 are notations used in glass science to respectively refer to a SiO_4 tetrahedra with one non-bridging oxygen (NBO) and one tetrahedra without any non-bridging oxygen. The glass structure is then closer to the one of pure silica. [42] Similarly in sodium-alumino phosphate glasses, following poling the connectivity of the phosphate network increases. [41] In borosilicate glasses, structural rearrangements associated with sodium migrations are mostly linked to the conversion of $B\emptyset_4^-$ with a neighboring sodium cations to $B\emptyset_3$ units. [48] All of these results indirectly indicate the primordial role of oxygen in the compensation process and that exchanges taking place in the glass can be described through oxidation-reduction (redox) reactions.

On the other hand, some authors describe reactions taking place upon thermal poling as purely electronic. The role of electronic conductivity in poling was studied by Krieger, [49] by Lipovskii [50] when poling silver particles containing glasses and by Mariappan et al. [51] when poling bioactive phospho-silicate glasses containing 50 % of sodium and calcium. Krieger disagreed with the possible oxygen motion considered by Carlson and others. [17] Krieger and colleagues thought that the current was carried by electrons as they observed fluctuations in their current measurements, a signed of a relaxation process that could be self-healing dielectric breakdown; plus, they did not observe motion of oxygen ions. In Lipovskii's work, electrons originate from metal nanoparticles and are only emitted in the presence of the external electric field. The electrons then drift towards

the anode. Mariappan et al. observed that the depletion layer formed during poling was created on a shorter time scale than its resistance. They made the hypothesis that following sodium departure (even with few hundreds of ppm) the created electric field is of the order of the breakdown voltage. Such a high voltage is sufficient to make the electrons mobile in the glass and compensation of negative charges can take place via electron extraction. This would result in the diminution of the internal electric field, allowing for migration of even more sodium cations without going above the breakdown voltage. More recently, Redkov et al. [52] discussed the mechanisms of molecular oxygen formation during thermal poling and proposed an interesting new theory. Their work disagreed on the oxygen anions motion in the glass as they stated that oxygen migration should only occur at higher temperatures, close to the glass transition temperature. Instead they proposed that following alkali departure, the electric field reaches value high enough for the remaining negatively charged NBOs to discharge, creating electrons that migrate to the anode. During thermal poling, peroxide radicals, $\equiv Si - O^{\cdot}$ (where the dot denotes an unpaired electron and the three lines to three bridging bonds), are formed through breakage of B-O-Si bonds which is accompanied by the release of one electron. Here, mechanical stresses between the depleted region and the bulk glass increase, thus deforming the network and promoting polymerization of the glass matrix through the combination of two of these peroxides which can result in the creation of molecular oxygen.

While many advances have been made to better understand the mechanisms of the thermal poling, the large number of variables in the process and the composition-specific response of the glass network to the process, have led to ongoing questions on the use of the method in glasses. These variables have to date prevented the community from enabling a singular, complete description of

the process for all materials. The lack of a complete description of all processes involved has not prevented researchers from obtaining good results in modifying the optical properties in thermally poled alkali-rich glasses. Among the families tested for Second Harmonic Generation, one particularly stood out, that is niobium borophosphate glasses (BPN). Glasses belonging to this family showed the highest post-poling induced second harmonic generation with an induced $\chi^{(2)}$ susceptibility of 5 pm/V. [53]

1.5 Second Harmonic Generation in chalcogenide glasses

Inorganic optical glasses can be distinguished by their non-linear refractive indices. The non-linear refractive index of fused silica, often used as a reference, is known to be equal to 2.2 10^{-20} m^2/W. [54] The non-linear refractive index can be related to the third-order non-linear susceptibilities with the following equation [55]

$$n_2 = \frac{12}{n}\pi Re\chi^{(3)}_{111}(-\omega,\omega,\omega,-\omega) \qquad (1.15)$$

As discussed earlier, $\chi^{(3)}$ plays an important role in thermal poling as shown in equation (1.11). Thus, a glass with a high non-linear refractive index should be more suitable for thermal poling. Figure 1.4 illustrates a classification of glasses depending on their nonlinear refractive indices. [20] Chalcogenide glasses exhibit the highest nonlinear refractive index which should lead to strong SHG response after polarization. Chalcogenide glasses are usually used for their good transparency in the mid-IR region. Among glasses transparent in the infrared, we find fluoride glasses, tellurite glasses and chalcogenides. Fluoride cannot present an interesting material as they have the lowest $\chi^{(3)}$ among glasses. Tellurite have higher $\chi^{(3)}$ than oxide but are still one order of magnitude lower

than chalcogenide. Hence chalcogenide represent the appropriate candidate for an effective thermal poling associated with infrared transparency.

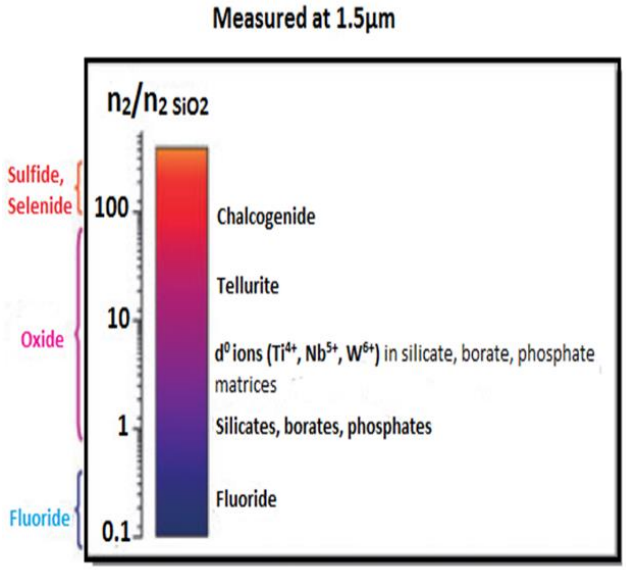

Figure 1.4. Classification of the nonlinear refractive index of several glass families, Dussauze [20]

Several studies on poling of chalcogenide glasses have been conducted. One of the first recorded second-order non-linear susceptibility in arsenic sulfide thin films has been found by Quiquempois et al. [56] and was obtained both by thermal poling and optical poling. Using the Maker fringes technique with a pump wavelength of 1550 nm they were able to record magnitude up to 0.6 pm/V.

Optical poling was used by Qiu et al. [57] in $Ge_{20}As_{20}S_{60}$ glasses by shining both ω and 2ω laser beam (1064 nm and 532 nm) on the sample at room temperature under no electric field. Photo-induced SHG properties seem to remain stable overtime and was four order larger than in the tellurite glass $15Nb_2O_5$-$85TeO_2$ and seven times larger than for a 1 mm thick Y-cut quartz crystal. Liu et al. [58] used electron beam irradiation (from a SEM) in Ge-As-S glasses and obtained a value of up to 0.8 pm/V of the second order non-linear susceptibility. The proposed mechanism at the

origin of SHG signal is due to formation of secondary electrons in the glass associated with the absorption of the incident electrons, creating a space charge in the glass as well as a rearrangement of the polar bonds under that field. More recently, the poling of arsenic-germanium sulfide glasses have also been investigated by Shoulders et al.[59] A glass of composition $As_{36}Ge_6S_{58}$ was chosen for its known photosensitivity and structural reorganization upon irradiation. This glass was then doped with sodium to increase ionic conductivity. $\chi^{(2)}$ of the order of 5.10^{-2} pm/V was obtained.

Dussauze et al. [60] worked on the binary arsenic – sulfur, doped with sodium. Using Raman spectroscopy, they were able to study the photo-induced structural changes over time. During poling, soda-lime glasses were placed between the glass and the anode, allowing for the injection of sodium into the glass matrix, responsible for the SHG signal. Here, formation of sulfur-sulfur homopolar bonds and structural rearrangements appear in the glass, due to its photosensitivity and tendency to photo-structural rearrangement. These two contributions were shown to contribute to the resulting SHG signal.

The most meaningful studies on chalcogenides from the standpoint of magnitude of the resulting induced $\chi^{(2)}$ were performed by Guignard et al. [61] and Jing et al. [62] obtaining values of $\chi^{(2)}$ equal to 8 pm/V in $Ge_{25}Sb_{10}S_{65}$ and 7pm/V in $60GeS_2$-$20Ga_2S_3$-20KBr, respectively. While impressive in their magnitude, these works shared a common drawback, which is the poor stability (retention of induced field effects) over time for the resulting SHG response.

Guignard showed the importance of electronic conductivity and ionic conductivity during poling. [63] She proposed two different mechanisms, depending on the conductivity of the glass. She showed that for gallium-containing glasses, formation of thermally activated defects will occur. These

defects might result from breakage of chemical bonds which accompany the induced SONL response. However electronic defects relax easily after poling recombining in hours to days, as compared to more (meta)-stable structural changes or ionic migration. Ionic migration still plays a role in poling of chalcogenide, mostly in the form of sodium ions which are usually present as an impurity in the compositions studied in the literature.

The role of defects, either naturally occurring or induced in chalcogenides is not uncommon. Two different ways of creating defects, i.e. charge defects or structural rearrangements, was first described in chalcogenides by Shimakawa in the early 1990's in the study of photoinduced changes in chalcogenide films. [64] This work, built on earlier work by Mott, [65, 66] Ovshinsky [67] and Anderson [68] in evaluating metastable structural configurations of 'abnormal' bonding configurations that deviated from traditional stoichiometric configurations (which follow the traditional 8-n rule). Here, over- or under-coordinated species, usually 'clusters' of bonded atoms shown to occur in chalcogen-containing glasses, can possess localized charges that typically exist as charge-neutral pairs, referred to as defect coordination pairs (DCPs). When structural re-arrangements occur due to an induced optical field, the random pairs (negative and positive) are well separated, dropping the energy, thus being more stable. The following figure present the difference in energy and stability between charge defects (self-trap excitons) and structural re-arrangements (random pairs). To obtain a stable electric field inside the glass, it is more interesting to go towards structural changes.

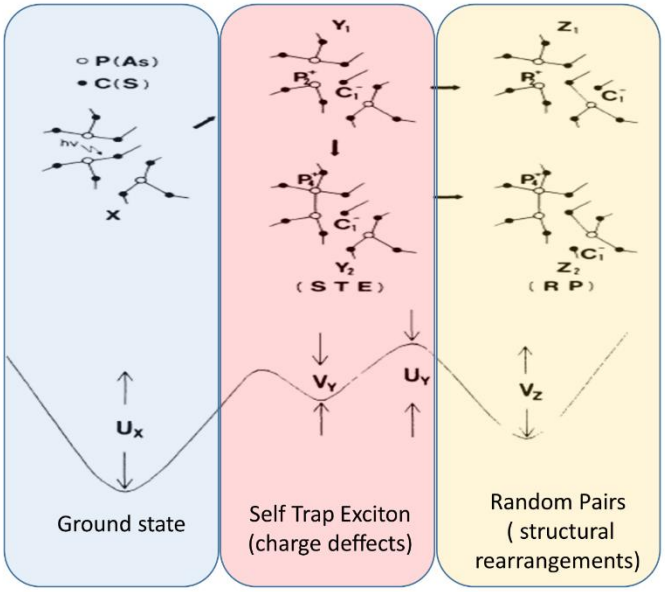

Figure 1.5. Difference in energy and stability between charge defects and structural re-arrangements

Even though poling of chalcogenide glasses seems promising to achieve large second order nonlinearities making them adequate for applications as active photonics materials, they still present lots of limitations. Most of the poled glasses did not produce a large second order nonlinearities, plus, the implemented $\chi^{(2)}$ was usually not stable over time. Few work have been conducted on that matter. Zeghlache et al. [69] studied the stabilization of the $\chi^{(2)}$ in sulfide glasses subjected to poling. They showed by cycling poling on $Ga_5Ge_{20}Sb_{10}S_{65}$ they could obtain a signal of 4 to 5 pm/V stable over several months. They attributed the enhanced stability to a burying of the SHG active layer accompanied by an increase in thickness of this layer following cycling.

1.6 Applications of thermal poling

So far we have discussed the principle of thermal poling and its major application in Second Harmonic Generation. Apart from the obvious use in nonlinear optics, thermal poling has found applications in a variety of domains ranging from microelectronics, [16] to electro-optics, [70] to

surface reactivity enhancement, [71] to changes of mechanical properties, [72] as well as glass formation. [73]

In this section, we will discuss some of the applications-oriented work that can be found in the literature.

1.6.1 Microelectronics: the first use of thermal poling

Thermal poling found its first application in microelectronics for metal to glass sealing. The first description of direct bonding in the literature was made by Wallis and Pomerantz in 1969. [16] This publication was made after Pomerantz patented anodic bonding in 1968.[15] In their paper they described how sealing of metals to glass could be achieved in less than a minute by applying a DC voltage between the two, without the need to use adhesive. Upon heating of a Pyrex® and silicon assembly to 400°C under an applied voltage of 300 V, fringes are observed under an optical microscope. These fringes are the evidence of an air gap between silicon and the glass, which vanish rapidly as the glass and metal are sealed together. The optical image then presents a gray interface, evidence of perfect bonding, without air pockets. Before discovering this methodology, sealing of glasses to metals was obtained by a heating treatment called fusion seal. The treatment was long and more expensive than poling, plus, thermal expansion mismatch between the two layers could be a problem. Following this early work, anodic bonding was thoroughly studied by the scientific community.

Recently, anodic bonding moved away from microelectronics and found new applications. Authors work on development of pressure sensors, [74, 75] micro-fluidic devices, with possible applications in separation of DNA molecules [76-78] and in biocompatible glass-silicon sealed packages. [79, 80]

1.6.2 Electro-optics

Following thermal poling, several changes are going to occur in the glass which can then change the properties of the glass. The most straightforward change is the appearance of the frozen in electric field inside the glass matrix. As stated earlier, the introduction of the static electric field efficiently breaks the centrosymmetry of the glass, allowing for second order nonlinear optical properties which opens up applications in electro-optics.

1.6.2.1 Planar waveguides

Optical waveguides are systems used to guide light and to confine it in a delimited region of propagation. They are usually comprised of two regions with different refractive indices, the core has a higher refractive index than the cladding (corresponding to the surrounding medium). Two principle configurations of waveguide can be found, the planar waveguide and the channel waveguide. The main difference between the two is that the light is propagated only in one dimension with a planar waveguide, contrary to a channel waveguide where the light is propagated along two dimensions. An example of a planar waveguide would be a thin film of high refractive index deposited on a substrate of smaller refractive index (cladding). For the channel waveguide, a typical example would be an optical fiber where the core with higher refractive index is surrounded by the cladding of lower refractive index. A representation of these two waveguides is given in the following figure.

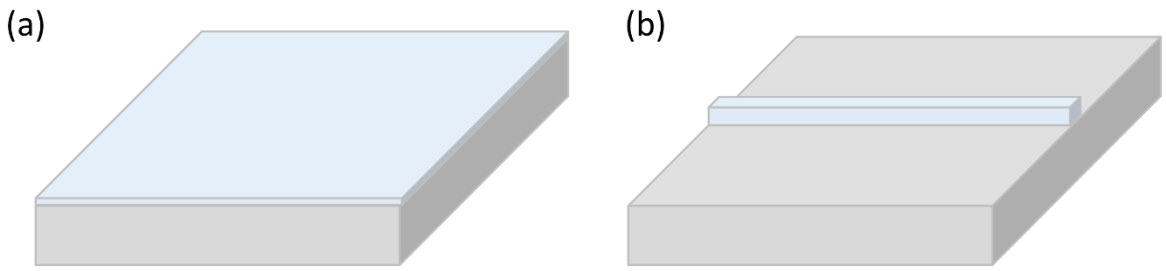

Figure 1.6. Representation of a planar waveguide (a) and a channel waveguide (b)

Upon thermal poling of a glass, cations migrate towards the cathode, leaving a zone depleted of cations. Hence the poled area usually presents a lower refractive index than that of the unpoled region. It is therefore possible to create waveguides in a glass by mean of thermal poling and several studies have been conducted on that matter. Making waveguide in thermally poled glasses is particularly interesting as the light which propagate inside this waveguide could interact with the poled region to make a nonlinear active waveguide.

Formation of waveguide in glasses by thermal poling is not limited to planar waveguide and channel waveguide have also been formed. The work of Margulis et al. [70] has shown the possibility to make single mode channel waveguides in soda lime glass using a periodic electrode at the anode. An aluminum film was deposited on the surface of the glass to be used as anode and channels where open in it. As the poling efficiently takes place under the remaining aluminum electrode, the poled area underwent a reduction of their refractive index by 1.5 % following cations migration. Waveguides were formed under the aluminum free area on the electrode. Waveguides were buried several microns under the surface which shows that the cladding correspond to the sodium depleted region of lower refractive index. As only the cladding is poled, the optical nonlinearity induced in the glass can only interact with the guided light through the evanescent field.

Other works have followed and have helped to better understand the mechanisms taking place in the formation of such waveguides in glasses containing more than one cation susceptible to drift under the electric field. In 2002, Brennand et al. [81] have studied the fabrication of planar waveguide by thermal poling of soda-lime glasses and showed it was necessary to not only take into account the sodium drift but also the displacement of the less mobile alkaline and alkaline-earth cations present in the glass. When a glass containing several mobile cations, two regions are going to be formed under the anodic surface. As in all poling procedures, a layer depleted in sodium cations is formed but at the interface between the depleted layer and the bulk glass, an accumulation region is formed and made of the less mobile cations (Ca^{2+}, $Mg^{2+,}$ K^{+}). These cations are also going to drift under the action of the electric field but cannot go further than the sodium depleted region as the electric field driving sodium migration in the bulk is too low to move Ca^{2+} and Mg^{2+}. The presence of this accumulation region was also demonstrated before by Lepinsky. [82] The refractive index in the sodium depleted region is higher than that of the substrate (cladding) and the position of the waveguide was found to be in the accumulation region under the glass surface. The cation distribution profile and position of the waveguide are represented in Figure 1.7.

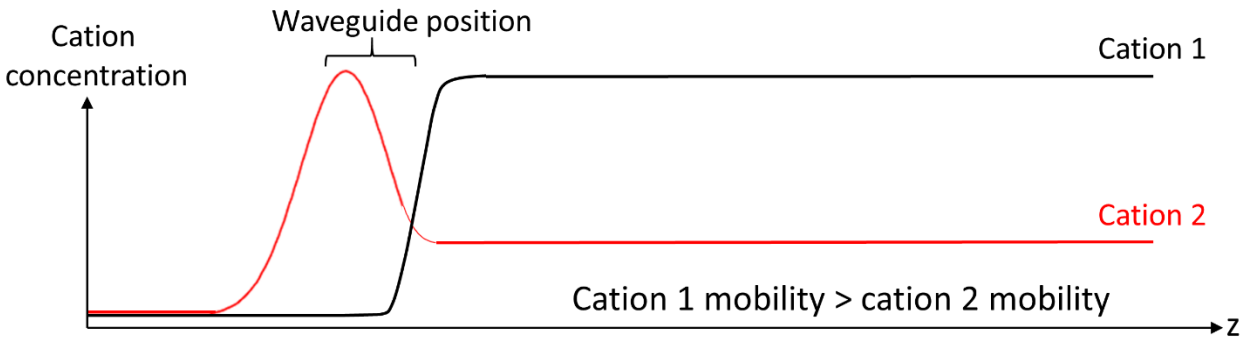

Figure 1.7. Concentration profile of mobile cations as well as waveguide position

More recently, Ng et al. [83] have demonstrated the combined use of femtosecond laser writing of waveguides and thermal poling to create to obtain nonlinear waveguide interaction in fused silica. Of note, they developed a double poling to increase the efficiency of the induced nonlinearity into the waveguide. This work opened new possibilities for development of new active devices in glasses.

These previous studies have focused on the fabrication of waveguides through the use of thermal poling but did not focus on the conversion efficiency of the fundamental wave to the harmonic waves. Other studies have focused on this particular point and described techniques to obtain quasi-phase matching conditions in waveguides.

Quasi-Phase Matching (QPM) was obtained in fused silica by Chao et al. [84] Waveguides were created by Ge-ion implantation using lithography technique. Following this step, thermal poling was performed to obtain SHG in the waveguides. The SHG signal is then locally erase by mean of UV light exposure with a periodic mask applied on the waveguide. The system showed a first-order quasi-phase-matching SHG from 1064 to 532 nm with a conversion efficiency of 6.1×10^{-4} %/W/cm^2 associated with a $d_{Q,eff}$ of 0.03 pm/V.

Li et al. studied QPM in channel waveguide in fused silica. [85] The sample was uniformly poled and waveguides were inscribed on the thermally poled sample with a femtosecond laser. A silicon grating was placed on top of the poled sample with grating groves perpendicular to the waveguides. The $\chi^{(2)}$ was then erased periodically by placing the sample in an e-beam evaporator deposition system. The underlying erasure mechanism is thought to be due to X-ray irradiation. The

conversion efficiency of such a system is of $2x10^{-5}$ %/W/cm^2 with an effective nonlinear coefficient of 0.0075 pm/V.

The use of periodic electrodes was made by Fadge-Pedersen, [86] where they demonstrated fabrication of a device allowing for a normalized conversion efficiency of $1.4x10^{-3}$ %/W/cm^2 with an associated nonlinearity of about 0.13 pm/V.

1.6.2.2 Optical fibers

Strauß et al. [87] showed that similarly to planar waveguide, poling with periodic electrodes could be performed on silica fibers. By using a periodic gold electrode as an anode on the side of the fiber to pole the sample, they were able to obtain quasi-phase matching conditions for conversion of 1064 nm laser beam to a 532 nm wavelength. However, the conversion efficiency was rather small, being only of 10^{-6} %/W/cm^2. The work by Pruneri et al. [88] was even more promising as they showed that by fabricating a grating on a D-shaped germane silicate fiber, they were able to obtain peak conversion efficiency as high as 20% for a 1532 nm wavelength.

Margulis and his team in Sweden have studied thermal poling in optical fibers with the aim to prepare fibers with an efficient second order optical nonlinearity, for instance for applications in fiber lasers. They filled twin-hole fibers with metal to serve as electrodes. They were able to study several electrodes configurations and found that using a so-call “charging” process (without the use of a cathode) yields a higher induced static electric field and better stability of the post-poling properties. [89] Similar studies of thermally poled twin-hole fibers have been conducted by L. Huang et al., [90-92] Camara [93] and D. Huang et al.. [94] The literature of thermally poled twin-hole fibers present extensive theoretical studies of various poling configurations which is then compared to

experimental results. The important parameters have been well discussed and controlled these rendered the resulting thermal poling more efficient. The models to explain these mechanisms still present some limitations as all activation energy of the cations are not known, the exact concentrations of these species as well as their distributions and how these glass-specific attributes impact the resulting post-poled properties is still not completely understood. However, we observe that these studies are more applications-oriented compared to studies of thermal poling in the past which were more mechanisms-oriented. The thermal poling community has now enough understanding of the process to move towards more concrete applications. In the domain of thermally poled optical fibers, projects such as the CHARMING project: Components for Highly Advanced time-Resolved fluorescence Microscopy based on Nonlinear Glass fibers, [95] show that the scientific community is now ready to use thermal poling for concrete applications.

1.6.3 Thermal poling as an imprinting process

New efforts have been undergone to control the optical properties of a glass at smaller scales. To do that, thermal poling was proved useful, especially as an imprinting process. Using patterned electrodes, an electric field assisted imprinting process can take place. Several approaches have been studied in the literature on several glass compositions.

Lipovskii used an anode with a relief to imprint phase and amplitude onto silver containing glasses. Detailed patterned with features below a resolution of a micron [96] can be imprinted and diffraction grating can be formed as the bulk glass and depleted layer present variation of refractive index of 0.02. [97] A similar approach using silver was used by Delestre et al. [98] to micro-pattern a glass's surface. The glass surface is first coated with silver which is then locally ablated using a femtosecond laser and the sample is finally poled. A constant SHG is recorded outside the ablated

line which corresponds to the typical EFISH recorded on poled samples while the ablated lines are also SHG efficient but belong to another class of symmetry C_s instead of $C_{\infty v}$. Using a profiled anode, Chervinskii et al. were able to form silver nanoisland in silver-sodium ion exchanged glasses. [99] Metal island films (MIF) were thus formed on the glass following complex patterns with spatial resolution up to 200 nm. The use of profiled electrodes allows to directly realized fragile MIF at the glass's surface, thus avoiding potentially damageable manipulations.

Thermal poling as an imprinting process was well studied and proved useful to create diffraction gratings in soda-lime glasses, [100] to structure the 2nd order nonlinear response of the glass [101] and to record patterns on the glass surface, solely as an imprinting process. [102-104] However, this technique still has a great potential and new applications which could use all the effects observed here, i.e. patterning, refractive index change, etc… , are still to be developed.

1.6.4 Use of the electric field to enhance chemical properties

1.6.4.1 Enhance bioactivity

The applications presented so far are the most common and represent the most straightforward use of thermal poling but applications can go beyond these fields. Our interest in changing surface reactivity of glasses was triggered partially by publications showing changes of surface reactivity in bioactive glasses following thermal poling. Bioactive glasses were first developed in the late 60s by Hench and the first article was published in 1972. [105] Hench defines bioactive materials as designed to "replace diseased or damaged tissues". [106] Bioglasses are typically alkali rich glasses made of SiO_2, CaO, Na_2O and P_2O_5. As bioactive glasses are alkali-rich, they are suitable candidates for thermal poling. Several teams studied the potential beneficial effect of thermal poling on the bio-activity of ceramic and glass materials.[71, 107, 108] They noticed that due to the

strong electric field underneath the surface, cations were more rapidly adsorbed at the surface, accelerating the bone growth on the implant. Mariappan et al. [51, 71, 109] studied the effect of thermal poling on bioglasses and noticed fast growth of a negatively-charged silica layer on top of the glass, promoting adsorption of calcium and phosphate ions leading to the growth of crystalline apatite. It seems that surface charges on both bioceramics [108] and bioglasses [71] positively influence the growth of calcium phosphate layer when immersed in simulated body fluids (close to human plasma). This interesting result shows that by using thermal poling, it is possible to locally change the reactivity of a glass. In that case the polarized glass allows for a faster crystallization of hydroxyapatite-like crystals. This reaction is only possible on specific glasses composition. With this in mind, it is expected that thermal poling of carefully chosen glass compositions would allow to tailor surface reactivity and properties.

1.6.4.2 Self-assembly of nanoparticles using electrostatic forces

Thermal poling allows for the creation of a strong electric field in the near surface of the glass, of the order of 10^9 V/m. This electric field presents the advantage of allowing for creation of second-harmonic generation. However, an interesting possibility is to have this electric field interact with charged molecules. The self-assembly of nanoparticles is a vast field of research and give rise to multiple techniques to control the assembly of nanoparticles. [110] In the late 60s, Iler presented a way of constructing multilayer films of alternating positively and negatively charged colloidal particles, [111] the electrostatic self-assembly. Various materials were developed using this technique and it was possible to make layers of colloidal particles, [112] polymers [113] and dendrimers. [114, 115]

In the same philosophy, Palleau et al. [116] used AFM nanoxerography to inject charges onto a surface to attract nanoparticles (silver and gold). At first a PMMA thin film is charged with an

AFM tip. The sample is then immerged in the colloidal dispersion of charged nanoparticles and finally dried under a nitrogen flow. They were able to obtain assemblies of various geometries with various type of charged particles (organic, inorganic and metallic). They finally showed that it was possible to elaborate a pattern of positive and negative charges as it can be seen on Figure 1.8.

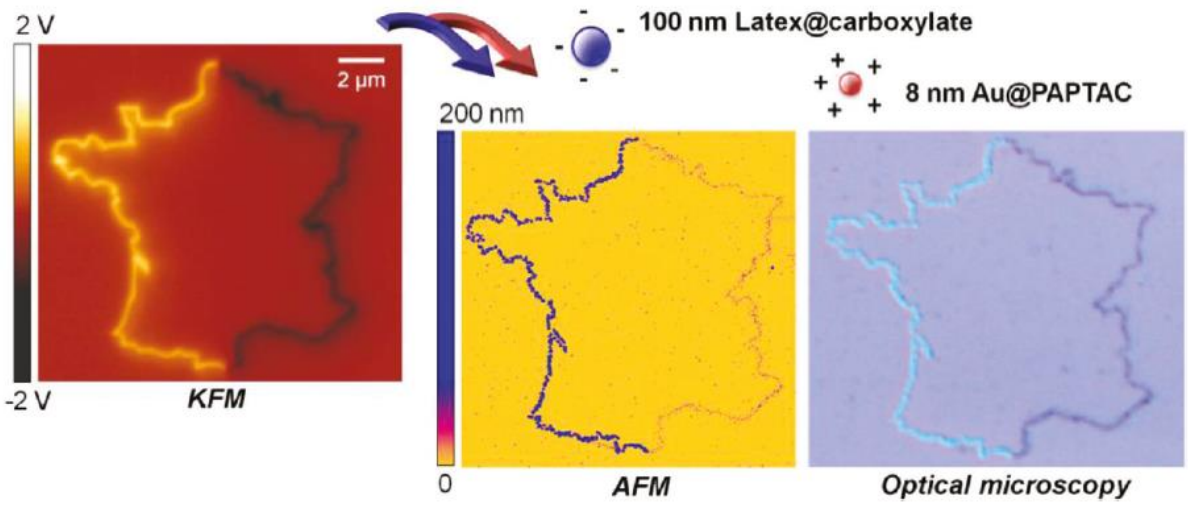

Figure 1.8. Pattern of positive and negative charges elaborated with nanoxerography by Palleau et al. [116]

All these works did not use thermal poling to obtain these results but they present strong similarity with thermal poling. Electric charges are at the base of these processes and the electric field induced during thermal poling is theoretically strong enough to give similar results. A control of the localization of the induced electric field could thus be used to attract charged particles at the surface of a glass substrate.

1.7 References

(1) Holonyak, N.; Bevacqua, S. F. Coherent (Visible) Light Emission from Ga(As1−xPx) Junctions. *Appl. Phys. Lett.* **1962**, *1*, 82-83.

(2) Round, H. J. A Note on Carborundum. *Electrical World* **1907**, *19*, 309-310.

(3) Losev, O. V. Luminous Carborundum [Silicon Carbide] Detector and Detection with Crystals. *Telegrafiya i Telefoniya bez Provodov (Wireless Telegraphy and Telephony)* **1927**, *44*, 485-494.

(4) Maurer, R. D.; Schultz, P. C. Fused Silica Optical Waveguide. **1972**, .

(5) Osterberg, U.; Margulis, W. Dye Laser Pumped by Nd YAG Laser Pulses Frequency Doubled in a Glass Optical Fiber. *Opt. Lett.* **1986**, *11*, 516-18.

(6) Vogel, E. M. Glasses as Nonlinear Photonic Materials. *J Am Ceram Soc* **1989**, *72*, 719-724.

(7) Vogel, E. M.; Weber, M. J.; Krol, D. M. Nonlinear Optical Phenomena in Glass. *Physics and Chemistry of Glasses* **1991**, *32*, 231-254.

(8) Margulis, W.; Laurell, F.; Lesche, B. Imaging the Nonlinear Grating in Frequency-Doubling Fibres. *Nature* **1995**, *378*, 699-701.

(9) Margulis, W.; Garcia, F. C.; Hering, E. N.; Guedes Valente, L. C.; Lesche, B.; Laurell, F.; Carvalho, I. C. S. Poled Glasses. *MRS Bull* **1998**, *23*, 31-35.

(10) Dianov, E. M.; Sokolov, V. O.; Sulimov, V. B. Theory of Polarization Dependence of Coherent Photocurrent and its Application to the Photogalvanic Model of Second-Harmonic Generation in Silica Fibres. *Sov Lightwave Commun* **1992**, *2*, 133-140.

(11) Dianov, E. M.; Starodubov, D. S. Photoinduced Second-Harmonic Generation in Glasses and Glass Optical Fibers. *Optical Fiber Technology* **1994**, *1*, 3-16.

(12) SOKOLOV, V. O.; SULIMOV, V. B. Theory of 3rd-Order Nonlinear Photoconductivity and 3rd-Order Photogalvanic Effect in Glass. *PHYSICA STATUS SOLIDI B-BASIC RESEARCH* **1995**, *187*, 189-204.

(13) Singer, K. D.; Kuzyk, M. G.; Holland, W. R.; Sohn, J. E.; Lalama, S. J.; Comizzoli, R. B.; Katz, H. E.; Schilling, M. L. Electro-optic Phase Modulation and Optical Second-harmonic Generation in Corona-poled Polymer Films. *Appl. Phys. Lett.* **1988**, *53*, 1800-1802.

(14) Okada, A.; Ishii, K.; Mito, K.; Sasaki, K. Phase-Matched Second-Harmonic Generation in Novel Corona Poled Glass Waveguides. *Applied Physics Letters* **1992**, *60*, 2853-2855.

(15) Pomerantz, D. United States of America Patent , 1968.

(16) Wallis, G.; Pomerantz, D. I. Field Assisted Glass-Metal Sealing. *J. Appl. Phys.* **1969**, *40*, 3946-3949.

(17) Carlson, D. E.; Hang, K. W.; Stockdale, G. F. Electrode "Polarization" in Alkali-Containing Glasses. *J. Am. Ceram. Soc.* **1972**, *55*, 337-341.

(18) Mukherjee, N.; Myers, R. A.; Brueck, S. R. J. Dynamics of Second-Harmonic Generation in Fused Silica. *J Opt Soc Am B* **1994**, *11*, 665-669.

(19) Liu, X. -.; Zhang, M. -. Theoretical Study for Thermal/Electric Field Poling of Fused Silica. *Japanese Journal of Applied Physics, Part 1: Regular Papers and Short Notes and Review Papers* **2001**, *40*, 4069-4076.

(20) Dussauze, M.; Cremoux, T.; Adamietz, F.; Rodriguez, V.; Fargin, E.; Yang, G.; Cardinal, T. Thermal Poling of Optical Glasses: Mechanisms and Second-Order Optical Properties. *Int. J. Appl. Glass Sci.* **2012**, *3*, 309-320.

(21) Verbiest, T.; Clays, K.; Rodriguez, V. In *Second-Order Nonlinear Optical Characterization Techniques: An Introduction;* Taylor & Francis Group, Ed.; Boca Raton, 2009; .

(22) Lorentz, H. A. In *Theory of electrons and its applications to the phenomena of light and radiant heat;* Stechert: 1909; .

(23) Lalena†, J. N. From Quartz to Quasicrystals: Probing Nature's Geometric Patterns in Crystalline Substances. *Crystallography Reviews* **2006**, *12*, 125-180.

(24) Fumi, F. The Direct-Inspection Method in Systems with a Principal Axis of Symmetry. *Acta Crystallogr.* **1952**, *5*, 691-694.

(25) Armstrong, J. A.; Bloembergen, N.; Ducuing, J.; Pershan, P. S. Interactions between Light Waves in a Nonlinear Dielectric. *Phys.Rev.* **1962**, *127*, 1918-1939.

(26) Franken, P. A.; Ward, J. F. Optical Harmonics and Nonlinear Phenomena. *Rev.Mod.Phys.* **1963**, *35*, 23-39.

(27) Fejer, M. M.; Magel, G. A.; Jundt, D. H.; Byer, R. L. Quasi-Phase-Matched Second Harmonic Generation: Tuning and Tolerances. *IEEE J. Quant. Electron.* **1992**, , 2631.

(28) Myers, R. A.; Mukherjee, N.; Brueck, S. R. J. Large Second-Order Nonlinearity in Poled Fused Silica, . *Optics Letters* **1991**, *16*, 1732-1734.

(29) Quiquempois, Y.; Martinelli, G.; Duthérage, P.; Bernage, P.; Niay, P.; Douay, M. Localization of the Induced Second-Order Non-Linearity within Infrasil and Suprasil Thermally Poled Glasses. *Optics Communications* **2000**, *176*, 479-487.

(30) Alley, T. G.; Brueck, S. R. J.; Wiedenbeck, M. Secondary Ion Mass Spectrometry Study of Space-Charge Formation in Thermally Poled Fused Silica. *J. Appl. Phys.* **1999**, *86*, 6634-6640.

(31) Alley, T. G.; Brueck, S. R. J.; Myers, R. A. Space Charge Dynamics in Thermally Poled Fused Silica. *J. Non Cryst. Solids* **1998**, *242*, 165-176.

(32) Quiquempois, Y.; Godbout, N.; Lacroix, S. Model of Charge Migration during Thermal Poling in Silica Glasses: Evidence of a Voltage Threshold for the Onset of a Second-Order Nonlinearity. *Physical Review A. Atomic, Molecular, and Optical Physics* **2002**, *65*, 438161-4381614.

(33) Kazansky, P. G.; Russel, P. S. J. Thermally Poled Glass: Frozen-in Electric Field Or Oriented Dipoles? *Opt.Commun.* **1994**, *110*, 611-614.

(34) Proctor, T. M.; Sutton, P. M. Static Space-Charge Distributions with a Single Mobile Charge Carrier. *J. Chem. Phys.* **1959**, *30*, 212-220.

(35) Quiquempois, Y.; Kudlinski, A.; Martinelli, G. Zero-Potential Condition in Thermally Poled Silica Samples: Evidence of a Negative Electric Field Outside the Depletion Layer. *J Opt Soc Am B* **2005**, *22*, 598-604.

(36) Pruneri, V.; Samoggia, F.; Bonfrate, G.; Kazansky, P. G.; Yang, G. M. Thermal Poling of Silica in Air and Under Vacuum: The Influence of Charge Transport on Second Harmonic Generation. *Appl. Phys. Lett.* **1999**, *74*, 2423-2425.

(37) Qiu, M.; Egawa, S.; Horimoto, K.; Mizunami, T. The Thickness Evolution of the Second-Order Nonlinear Layer in Thermally Poled Fused Silica. *Opt. Commun.* **2001**, *189*, 161-166.

(38) Garcia, F. C.; Carvalho, I. C. S.; Hering, E.; Margulis, W.; Lesche, B. Inducing a Large Second-Order Optical Nonlinearity in Soft Glasses by Poling. *Appl. Phys. Lett.* **1998**, *72*, 3252-3254.

(39) Carlson, D. E. Anodic Proton Injection in Glasses. *J. Am. Ceram. Soc.* **1974**, *57*, 461-466.

(40) Carlson, D. E.; Hang, K. W.; Stockdale, G. F. Ion Depletion of Glass at a Blocking Anode - 1, 2. *J Am Ceram Soc* **1974**, *57*, 291-300.

(41) Dussauze, M.; Rodriguez, V.; Velli, L.; Varsamis, C. P. E.; Kamitsos, E. I. Polarization Mechanisms and Structural Rearrangements in Thermally Poled Sodium-Alumino Phosphate Glasses. *J. Appl. Phys* **2010**, *107*.

(42) Dussauze, M.; Rodriguez, V.; Lipovskii, A.; Petrov, M.; Smith, C.; Richardson, K.; Cardinal, T.; Fargin, E.; Kamitsos, E. I. How does Thermal Poling Affect the Structure of Soda-Lime Glass? *Journal of Physical Chemistry C* **2010**, *114*, 12754-12759.

(43) Dussauze, M.; Kamitsos, E. I.; Fargin, E.; Rodriguez, V. Structural Rearrangements and Second-Order Optical Response in the Space Charge Layer of Thermally Poled Sodium-Niobium Borophosphate Glasses. *J. Phys. Chem. C* **2007**, *111*, 14560-14566.

(44) Ziemath, E. C.; Araújo, V. D.; Escanhoela Jr., C. A. Compositional and Structural Changes at the Anodic Surface of Thermally Poled Soda-Lime Float Glass. *J. Appl. Phys.* **2008**, *104*.

(45) Schmidt, B.; Nitzsche, P.; Lange, K.; Grigull, S.; Kreissig, U.; Thomas, B.; Herzog, K. In Situ Investigation of Ion Drift Processes in Glass during Anodic Bonding. *Sens Actuators A Phys* **1998**, *67*, 191-198.

(46) Nitzsche, P.; Lange, K.; Schmidt, B.; Grigull, S.; Kreissig, U.; Thomas, B.; Herzog, K. Ion Drift Processes in Pyrex-Type Alkali-Borosilicate Glass during Anodic Bonding. *J. Electrochem. Soc.* **1998**, *145*, 1755-1762.

(47) Guimbretìre, G.; Dussauze, M.; Rodriguez, V.; Kamitsos, E. I. Correlation between Second-Order Optical Response and Structure in Thermally Poled Sodium Niobium-Germanate Glass. *Appl. Phys. Lett.* **2010**, *97*.

(48) Möncke, D.; Dussauze, M.; Kamitsos, E. I.; Varsamis, C. P. E.; Ehrt, D. Thermal Poling Induced Structural Changes in Sodium Borosilicate Glasses. *Phys. Chem. Glasses: Eur. J. Glass Sci. Technol. B* **2009**, *50*, 229-235.

(49) Krieger, U. K.; Lanford, W. A. Field Assisted Transport of Na+ Ions, Ca2+ Ions and Electrons in Commercial Soda-Lime Glass I: Experimental. *J. Non Cryst. Solids* **1988**, *102*, 50-61.

(50) Lipovskii, A. A.; Melehin, V. G.; Petrov, M. I.; Svirko, Y. P.; Zhurikhina, V. V. Bleaching Versus Poling: Comparison of Electric Field Induced Phenomena in Glasses and Glass-Metal Nanocomposites. *J. Appl. Phys.* **2011**, *109*.

(51) Mariappan, C. R.; Roling, B. Mechanism and Kinetics of Na+ Ion Depletion Under the Anode during Electro-Thermal Poling of a Bioactive Glass. *J. Non Cryst. Solids* **2010**, *356*, 720-724.

(52) Redkov, A. V.; Melehin, V. G.; Lipovskii, A. A. How does Thermal Poling Produce Interstitial Molecular Oxygen in Silicate Glasses? *J. Phys. Chem. C* **2015**, *119*, 17298-17307.

(53) Dussauze, M.; Fargin, E.; Lahaye, M.; Rodriguez, V.; Adamietz, F. Large Second-Harmonic Generation of Thermally Poled Sodium Borophosphate Glasses. *Opt. Express* **2005**, *13*, 4064-4069.

(54) Stegeman, G. I.; Torruellas, W. E. Nonlinear Materials for Information Processing and Communications. *Philosophical Transactions of the Royal Society A: Mathematical, Physical and Engineering Sciences* **1996**, *354*, 745-756.

(55) Weber, M. J.; Milam, D.; Smith, W. L. Nonlinear Refractive Index of Glasses and Crystals. *Optical Engineering* **1978**, *17*, 463-469.

(56) Quiquempois, Y.; Villeneuve, A.; Dam, D.; Turcotte, K.; Maier, J.; Stegeman, G.; Lacroix, S. Second-Order Nonlinear Susceptibility in As2S3 Chalcogenide Thin Glass Films. *Electronics Letters* **2000**, *36*, 733-734.

(57) Qiu, J.; Si, J.; Hirao, K. Photoinduced Stable Second-Harmonic Generation in Chalcogenide Glasses. *Opt. Lett.* **2001**, *26*, 914-16.

(58) Liu, Q.; Zhao, X.; Tanaka, K.; Narazaki, A.; Hirao, K.; Gan, F. Second-Harmonic Generation in Ge-as-S Glasses by Electron Beam Irradiation and Analysis of the Poling Mechanism. *Optics Communications* **2001**, *198*, 187-192.

(59) Shoulders, W. T.; Novak, J.; Dussauze, M.; Musgraves, J. D.; Richardson, K. Thermal Poling Behavior and SHG Stability in Arsenic-Germanium Sulfide Glasses. *Optical Materials Express* **2013**, *3*, 700-710.

(60) Dussauze, M.; Zheng, X.; Rodriguez, V.; Fargin, E.; Cardinal, T.; Smektala, F. Photosensitivity and Second Harmonic Generation in Chalcogenide Arsenic Sulfide Poled Glasses. *Optical Materials Express* **2012**, *2*, 45-54.

(61) Guignard, M.; Nazabal, V.; Smektala, F.; Adam, J. -.; Bohnke, O.; Duverger, C.; Moréac, A.; Zeghlache, H.; Kudlinski, A.; Martinelli, G.; Quiquempois, Y. Chalcogenide Glasses Based on Germanium Disulfide for Second Harmonic Generation. *Advanced Functional Materials* **2007**, *17*, 3284-3294.

(62) Jing, R.; Guang, Y.; Huidan, Z.; Guorong, C.; Tanaka, K.; Fujita, K.; Murai, S.; Tsujiie, Y. Second-Harmonic Generation in Thermally Poled Chalcohalide Glass. *Opt. Lett.* **2006**, *31*, 3492-3494.

(63) Guignard, M. Verres et vitrocéramiques infrarouge à base de chalcogénures pour l'optique non linéaire du second ordre, Université de Rennes I, Rennes, 2005.

(64) Shimakawa, K.; Inami, S.; Elliott, S. R. Reversible Photoinduced Change of Photoconductivity in Amorphous Chalcogenide Films. *Physical Review B* **1990**, *42*, 11857-11861.

(65) Mott, N. F.; Davis, E. A.; Street, R. A. States in the Gap and Recombination in Amorphous Semiconductors. *Philosophical Magazine* **1975**, *32*, 961-996.

(66) Street, R. A.; Mott, N. F. States in the Gap in Glassy Semiconductors. *Phys. Rev. Lett.* **1975**, *35*, 1293-1296.

(67) Ovshinsky, S. R.; Adler, D. Local Structure, Bonding, and Electronic Properties of Covalent Amorphous Semiconductors. *Contemporary Physics* **1978**, *19*, 109-126.

(68) Anderson, P. W. Model for the Electronic Structure of Amorphous Semiconductors. *Phys. Rev. Lett.* **1975**, *34*, 953-955.

(69) Zeghlache, H.; Guignard, M.; Kudlinski, A.; Quiquempois, Y.; Martinelli, G.; Nazabal, V.; Smektala, F. Stabilization of the Second-Order Susceptibility Induced in a Sulfide Chalcogenide Glass by Thermal Poling. *J. Appl. Phys.* **2007**, *101*.

(70) Margulis, W.; Laurell, F. Fabrication of Waveguides in Glasses by a Poling Procedure. *Appl. Phys. Lett.* **1997**, *71*, 2418-2420.

(71) Mariappan, C. R.; Yunos, D. M.; Boccaccini, A. R.; Roling, B. Bioactivity of Electro-Thermally Poled Bioactive Silicate Glass. *Acta Biomaterialia* **2009**, *5*, 1274-1283.

(72) He, H.; Luo, J.; Qian, L.; Pantano, C. G.; Kim, S. H. Thermal Poling of Soda-Lime Silica Glass with Nonblocking Electrodes—Part 2: Effects on Mechanical and Mechanochemical Properties. *J Am Ceram Soc* **2016**, *99*, 1231-1238.

(73) McLaren, C.; Heffner, W.; Tessarollo, R.; Raj, R.; Jain, H. Electric Field-Induced Softening of Alkali Silicate Glasses. *Appl. Phys. Lett.* **2015**, *107*.

(74) Abeysinghe, D. C.; Dasgupta, S.; Boyd, J. T.; Jackson, H. E. A Novel MEMS Pressure Sensor Fabricated on an Optical Fiber. *IEEE Photonics Technology Letters* **2001**, *13*, 993-995.

(75) Abeysinghe, D. C.; Dasgupta, S.; Jackson, H. E.; Boyd, J. T. Novel MEMS Pressure and Temperature Sensors Fabricated on Optical Fibers. *J Micromech Microengineering* **2002**, *12*, 229-235.

(76) Han, J.; Craighead, H. G. Separation of Long DNA Molecules in a Microfabricated Entropic Trap Array. *Science* **2000**, *288*, 1026-1029.

(77) Kutchoukov, V. G.; Laugere, F.; Van Der Vlist, W.; Pakula, L.; Garini, Y.; Bossche, A. Fabrication of Nanofluidic Devices using Glass-to-Glass Anodic Bonding. *Sens Actuators A Phys* **2004**, *114*, 521-527.

(78) Kutchoukov, V. G.; Pakula, L.; Parikesit, G. O. F.; Garini, Y.; Nanver, L. K.; Bossche, A. Fabrication of Nanofluidic Devices in Glass with Polysilicon Electrodes. *Sensors and Actuators, A: Physical* **2005**, *123-124*, 602-607.

(79) Harpster, T. J.; Najafi, K. In *In Long-term testing of hermetic anodically bonded glass-silicon packages;* 2002; , pp 423-426.

(80) Harpster, T. J.; Nikles, S. A.; Dokmeci, M. R.; Najafi, K. Long-Term Hermeticity and Biological Performance of Anodically Bonded Glass-Silicon Implantable Packages. *IEEE Transactions on Device and Materials Reliability* **2005**, *5*, 458-465.

(81) Brennand, A. L. R.; Wilkinson, J. S. Planar Waveguides in Multicomponent Glasses Fabricated by Field-Driven Differential Drift of Cations. *Opt. Lett.* **2002**, *27*, 906-908.

(82) Lepienski, C. M.; Giacometti, J. A.; Leal Ferreira, G. F.; Freire Jr., F. L.; Achete, C. A. Electric Field Distribution and Near-Surface Modifications in Soda-Lime Glass Submitted to a Dc Potential. *J. Non Cryst. Solids* **1993**, *159*, 204-212.

(83) Ng, J. C. 1.; Qian1, L.; Herman, P. R. 1. Thermal Poling of Femtosecond Laser-Written Waveguides in Fused Silica. *Opt. Lett.* **2016**, *41*, 1022-1025.

(84) Chao, S.; Chen, H. -.; Yang, Y. -.; Wang, Z. -.; Shih, C. T.; Niu, H. Quasi-Phase-Matched Second-Harmonic Generation in Ge-Ion Implanted Fused Silica Channel Waveguide. *Optics Express* **2005**, *13*, 7091-7096.

(85) Li, G.; Winick, K. A.; Said, A. A.; Dugan, M.; Bado, P. Quasi-Phase Matched Second-Harmonic Generation through Thermal Poling in Femtosecond Laser-Written Glass Waveguides. *Optics Express* **2009**, *17*, 9442-9453.

(86) Fage-Pedersen, J.; Jacobsen, R.; Kristensen, M. Planar Glass Devices for Efficient Periodic Poling. *Optics Express* **2005**, *13*.

(87) Strauß, A.; Jauernig, U.; Reichel, V.; Bartelt, H. Generation of Green Light in a Thermally Poled Silica Fiber by Quasi-Phase-Matched Second Harmonic Generation. *Optik* **2010**, *121*, 490-493.

(88) Pruneri, V.; Bonfrate, G.; Kazansky, P. G.; Richardson, D. J.; Broderick, N. G.; De Sandro, J. P.; Simonneau, C.; Vidakovic, P.; Levenson, J. A. Greater than 20%-Efficient Frequency Doubling of 1532-Nm Nanosecond Pulses in Quasi-Phase-Matched Germanosilicate Optical Fibers. *Opt. Lett.* **1999**, *24*, 208-210.

(89) Margulis, W.; Tarasenko, O.; Myrén, N. Who Needs a Cathode? Creating a Second-Order Nonlinearity by Charging Glass Fiber with Two Anodes. *Optics Express* **2009**, *17*, 15534-15540.

(90) Huang, L.; Ren, G.; Gao, Y.; Zhu, B.; Peng, W. Design of Thermally Poled Twin-Core Fiber Coupler with Electrical Tunability. *IEEE Photonics Technol Lett* **2015**, *27*, 919-922.

(91) Huang, L.; Ren, G.; Sun, X. In *In Evolution of two-dimensional electric field in poled twin-hole optical fiber;* 2014; .

(92) Huang, L.; Ren, G.; Gao, Y.; Zhu, B.; Sun, X. Hindering Effect of the Core-Cladding Interface in Thermally Poled Optical Fibers. *Appl. Opt.* **2015**, *54*, 5771-5776.

(93) Camara, A.; Tarasenko, O.; Margulis, W. Study of Thermally Poled Fibers with a Two-Dimensional Model. *Opt. Express* **2014**, *22*, 17700-17715.

(94) Huang, D.; De Lucia, F.; Healy, N.; Corbari, C.; Sazio, P. J. A. In *In Who needs contacts?: Optical fiber poling by induction;* 2014; .

(95) EU funded project CHARMING: Components for Highly Advanced time-Resolved fluorescence Microscopy based on Nonlinear Glass fibers. *http://www.charming-project.eu/* (accessed 04/22, 2016).

(96) Lipovskii, A. A.; Kuittinen, M.; Karvinen, P.; Leinonen, K.; Melehin, V. G.; Zhurikhina, V. V.; Svirko, Y. P. Electric Field Imprinting of Sub-Micron Patterns in Glass-Metal Nanocomposites. *Nanotechnology* **2008**, *19*.

(97) Lipovskii, A. A.; Rusan, V. V.; Tagantsev, D. K. Imprinting Phase/Amplitude Patterns in Glasses with Thermal Poling. *Solid State Ionics* **2010**, *181*, 849-855.

(98) Delestre, A.; Lahaye, M.; Fargin, E.; Bellec, M.; Royon, A.; Canioni, L.; Dussauze, M.; Adamietz, F.; Rodriguez, V. Towards Second-Harmonic Generation Micropatterning of Glass Surface. *Appl. Phys. Lett.* **2010**, *96*.

(99) Chervinskii, S.; Sevriuk, V.; Reduto, I.; Lipovskii, A. Formation and 2D-Patterning of Silver Nanoisland Film using Thermal Poling and Out-Diffusion from Glass. *J. Appl. Phys.* **2013**, *114*.

(100) Fleming, L. A. H.; Goldie, D. M.; Abdolvand, A. Imprinting of Glass. *Optical Materials Express* **2015**, *5*, 1674-1681.

(101) Yang, G.; Dussauze, M.; Rodriguez, V.; Adamietz, F.; Marquestaut, N.; Deepak, K. L. N.; Grojo, D.; Uteza, O.; Delaporte, P.; Cardinal, T.; Fargin, E. Large Scale Micro-Structured

Optical Second Harmonic Generation Response Imprinted on Glass Surface by Thermal Poling. *J. Appl. Phys.* **2015**, *118*.

(102) Sokolov, K.; Melehin, V.; Petrov, M.; Zhurikhina, V.; Lipovskii, A. Spatially Periodical Poling of Silica Glass. *J. Appl. Phys.* **2012**, *111*.

(103) Ikutame, N.; Kawaguchi, K.; Ikeda, H.; Sakai, D.; Harada, K.; Funatsu, S.; Nishii, J. Low-Temperature Fabrication of Fine Structures on Glass using Electrical Nanoimprint and Chemical Etching. *J. Appl. Phys.* **2013**, *114*.

(104) Chou, S. Y.; Liang, X. Method and Apparatus of Electrical Field Assisted Imprinting. **2014**, .

(105) Hench, L.; Splinter, R.; Allen, W.; Greenlee, T. Bonding Mechanisms at the Interface of Ceramic Prosthetic Materials. *J. Biomed. Mater. Res.* **1972**, *5*, 117-141.

(106) Hench, L. L. The Story of Bioglass®. *J. Mater. Sci. Mater. Med.* **2006**, *17*, 967-978.

(107) Yamashita, K.; Oikawa, N.; Umegaki, T. Acceleration and Deceleration of Bone-Like Crystal Growth on Ceramic Hydroxyapatite by Electric Poling. *Chem. Mater.* **1996**, *8*, 2697-2700.

(108) Nakamura, S.; Kobayashi, T.; Nakamura, M.; Itoh, S.; Yamashita, K. Electrostatic Surface Charge Acceleration of Bone Ingrowth of Porous Hydroxyapatite/ß-Tricalcium Phosphate Ceramics. *J. Biomed. Mater. Res. A.* **2010**, *92*, 267-275.

(109) Mariappan, C. R.; Roling, B. Investigation of Bioglass-Electrode Interfaces After Thermal Poling. *Solid State Ionics* **2008**, *179*, 671-677.

(110) Huie, J. C. Guided Molecular Self-Assembly: A Review of Recent Efforts. *Smart Mater. Struct.* **2003**, *12*, 264-271.

(111) Iler, R. K. Multilayers of Colloidal Particles. *J. Colloid Interface Sci.* **1966**, *21*, 569-594.

(112) Kumar, A.; Mandale, A. B.; Sastry, M. Sequential Electrostatic Assembly of Amine-Derivatized Gold and Carboxylic Acid-Derivatized Silver Colloidal Particles on Glass Substrates. *Langmuir* **2000**, *16*, 6921-6926.

(113) Decher, G. Fuzzy Nanoassemblies: Toward Layered Polymeric Multicomposites. *Science* **1997**, *277*, 1232-1237.

(114) Bliznyuk, V. N.; Rinderspacher, F.; Tsukruk, V. V. On the Structure of Polyamidoamine Dendrimer Monolayers. *Polymer* **1998**, *39*, 5249-5252.

(115) Tsukruk, V. V.; Rinderspacher, F.; Bliznyuk, V. N. Self-Assembled Multilayer Films from Dendrimers. *Langmuir* **1997**, *13*, X-2176.

(116) Palleau, E.; Sangeetha, N. M.; Viau, G.; Marty, J. -.; Ressier, L. Coulomb Force Directed Single and Binary Assembly of Nanoparticles from Aqueous Dispersions by AFM Nanoxerography. *ACS Nano* **2011**, *5*, 4228-4235.

CHAPTER 2: INSTRUMENTS AND EXPERIMENTAL TECHNIQUES

2.1 Glass synthesis

2.1.1 Borosilicate glasses

Bulk glass with composition SiO_2 39 mol%, B_2O_3 51 mol%, Na_2O 10 mol% was prepared from high purity materials SiO_2 (Sigma Aldrich, 99,99 %), $Na_2B_4O_7 - 10H_2O$ (Sigma Aldrich, > 99%), and H_3BO_3 (Alfa Aesar, 99.9995 %). Hygroscopic powders were first dried in an oven overnight. Raw materials were then mixed, ground and poured into platinum crucible. The batch was melted at 1100°C and quenched by dipping the bottom of the crucible in water. The glass was then ground in a fine powder and melted two additional time. In the final step of the melting process, the glass was quenched between two brass plates to maximize the quenching rate as the glass tends to phase separate. The glass was then visually inspected for sign of extensive phase separation, which typically gives an opalescent glass. In absence of signs of phase separation, the glass was annealed overnight, 40°C below the glass transition temperature (T_g ~ 450°C). One-millimeter-thick samples were then cut and optically polished on both sides.

2.1.2 Chalcogenide glasses

Chalcogenide glasses require special care during preparation to avoid contamination with oxygen and water. All base glasses were prepared from high purity elemental Ge, Sb and S (Alfa Aesar, 99.999 % purity), and sodium was added to the matrix by introduction of sodium sulfide (purity unspecified). Raw materials were weighed out under nitrogen in a glove box to prevent any atmosphere contamination and inserted in a quartz ampule. Glasses were prepared in 15 or 30 grams' batches. A closed connector is placed at the end of the tube while in the glove box and the batch is only open when the tube is connected to the vacuum pump. The batch is then subjected to

a mild vacuum for 30 minutes. Larger batches require the sulfur to be melted under vacuum to allow enough space at the end of the tube for the following sealing step. The evacuated ampule is then sealed with an oxygen-methane torch. The tube is placed in a rocking furnace (Barnstead Thermolyne 21100) which assures better homogeneity during the melting process. The homogenization temperature was set-up to 850°C, with a heating rate of 1°C/min. The ampule stays at the homogenization temperature overnight and the temperature is lowered to 750°C before quenching the tube with forced air. The lowering of the temperature before quenching is necessary to prevent the ampule from shattering as the glass goes through T_g and retracts. Glasses are then place in a furnace (Barnstead Thermolyne 48000) and annealed at T_g-40°C overnight to lower the internal constraints.

Once the annealing step completed, glasses were removed from the silica tube. The glass rod was then sliced and optically polished in 1 mm thick samples. The grinding and polishing process is performed in 4 steps to ensure best optical quality. All samples were then controlled by optical microscope until surfaces with the smaller amount of scratches and pits were obtained. Part of the glass batch was finely ground using a mortar and pestle for differential scanning calorimetry (DSC) analysis and for X-ray diffraction (XRD).

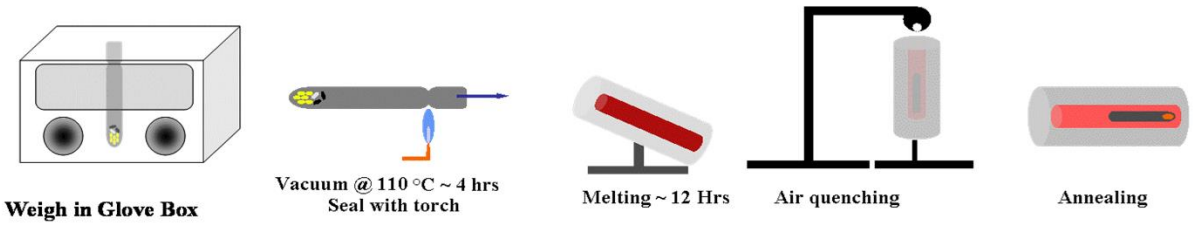

Figure 2.1. Preparation steps of a chalcogenide glass

2.2 Differential Scanning calorimetry

Differential Scanning Calorimetry, abbreviated as DSC, is a technique which measures difference in heat flow between a reference and the sample. The sample is ground in a fine powder and placed in an aluminum crucible. The crucible is mechanically sealed and a hole is poked in the lid. A reference is prepared by sealing an empty crucible. The two crucibles are then placed together in the furnace and a heat treatment, typically a ramp to an elevated temperature (550°C) at 10 K/min, is performed. The apparatus measures the heat flow required to keep the two crucibles at the same temperature during the ramp. The heat flow is then plotted as a function of temperature; such a plot is called a thermogram. The two signals are then compared to obtain thermal properties such as glass transition temperature (T_g), crystallization temperature (T_x) and melting temperature (T_m).

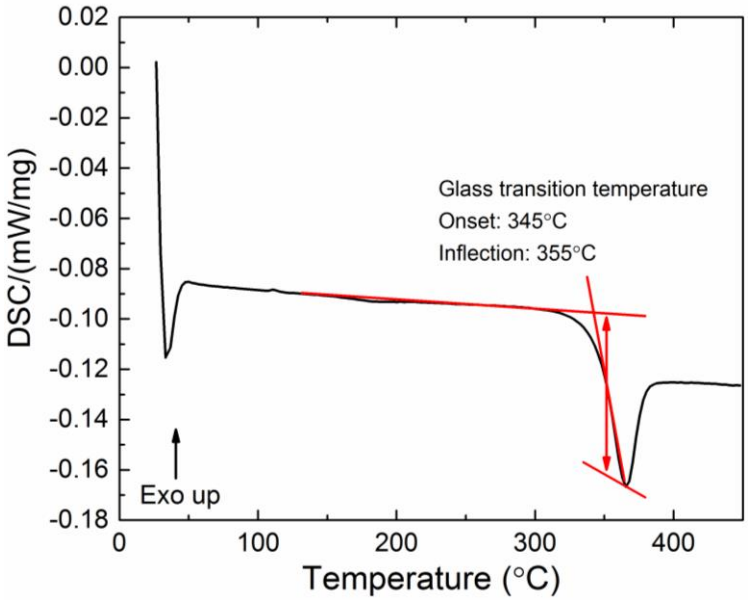

Figure 2.2. Thermogram showing the measurement of a glass transition temperature

The glass transition temperature does not correspond to a fixed temperature in glasses, therefore, there are several ways to measure it from a DSC thermogram. The glass temperature is the first endothermic phenomenon measured on a glass sample. It can be defined as the onset of this endothermic phenomenon or the inflection point of the endothermic peak. The second way of measuring the glass transition temperature is more reproducible and is obtained by taking the first derivative of the heat flow. The glass transition temperature then corresponds to the minimum of this derivative. Figure 2.2 presents the two accepted ways of determining T_g.

2.3 Density measurements

Density measurement is one essential characterization of a glass. It is more precisely defined as the volumetric mass density and corresponds to the mass of a sample per unit volume, i.e. the mass occupying a unit volume of material. Density of glasses are measured using the Archimedes method. Samples are first measured in air and then immersed in deionized water with an Aaron

balance (AE Adams PGW Balance). Several samples are measured for each composition to minimize the error on the measurements. The density of deionized water is precisely known and the density of the glass is then easily determined.

2.4 Measurements of the refractive index using Brewster's angle and the M-lines

Refractive index measurements are especially important when making glasses for optics and are also needed when fitting the 2^{nd} order nonlinear response of the poled glass. During this PhD work, two set-ups were used to measure refractive indices, the Brewster angle technique and the M-lines technique.

The Brewster angle measurement technique was used to measure the indices for wavelengths in the visible and near-IR. The following wavelength are available: 405, 532, 639, 785, 940, 1310 and 1550 nm.

This technique utilizes the principle of the Brewster angle which corresponds to a particular angle of incidence for which a polarized light is perfectly transmitted through a sample without any reflection. In the case of an unpolarized light, the reflected light is then perfectly polarized. It is necessary to define the polarization of light to explain the phenomenon. Light polarization is decomposed into two perpendicular components S and P. The P polarization (from the German parallel) represents the electric field component parallel to the plane of incidence, while the S polarization (from German senkrecht, meaning perpendicular) represents the electric field component perpendicular to the plane of incidence.

Figure 2.3 illustrates the case of an unpolarized light entering a surface at the Brewster angle. The reflected light is perfectly S-polarized and the transmitted light only slightly polarized.

Brewster angle can be easily found using Snell's law and is mathematically equivalent to the following equation

$$\theta_B = \arctan\left(\frac{n_2}{n_1}\right) \tag{2.1}$$

With θ_B the Brewster angle, n_2 the refractive index of the glass and n_1 the refractive index of air, i.e. 1.

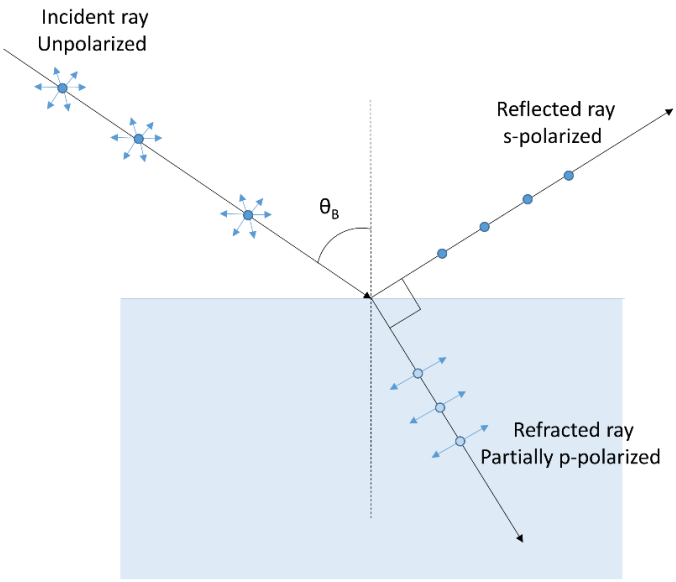

Figure 2.3. Polarization of light encountering an interface at Brewster's angle

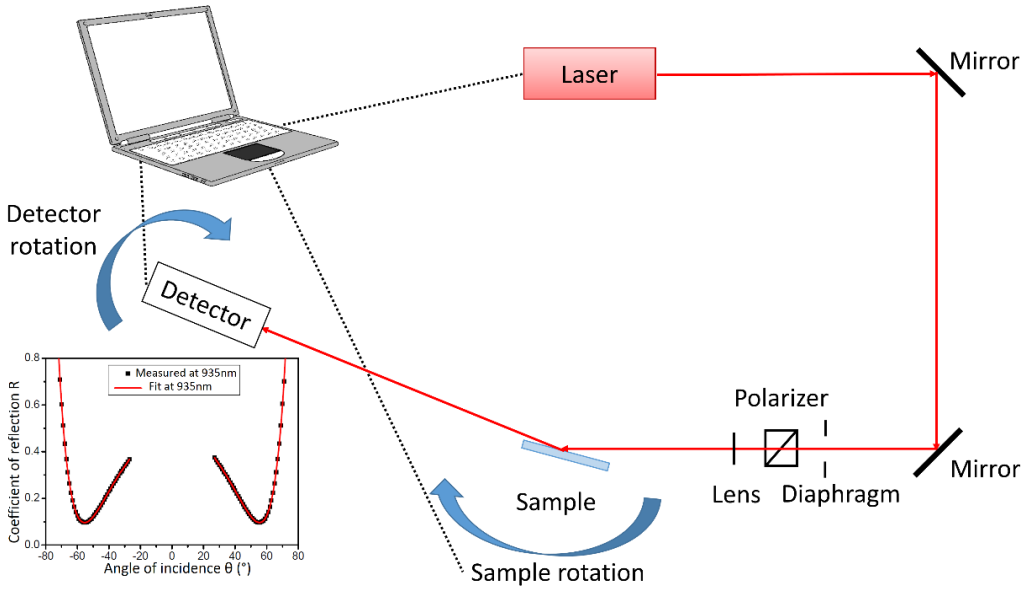

Figure 2.4. Refractive index measurement with the Brewster angle setup

Brewster angle measurements then consists at shining a P polarized light at the sample and varying the incident angle. The variation of the reflected light's intensity is measured every angle between -80° and 80°. A plot such as the one in the insight of Figure 2.4 is obtained. The obtained variation is then fitted [1] and the refractive index is then determined with a precision of ± 0.01.

The second set-up used to measure the refractive index at higher wavelength is a modified Metricon prism coupler (model 2010 M) by Dr. Gleason from the GPCL group, which can operate in the infrared. The indices were measured using a GaP prism and measurements were performed at 4.5 µm. It is necessary for the prism to have a higher index as the sample to be measured. Several prisms are available: Ge, Si, Rutile and GaP. The Metricon prism coupler is based on the m-lines spectroscopy which is usually used to measure thickness and refractive index of thin films but can also be used to measure refractive indices of bulk samples. The sample to be measured is pressed against a prism sitting on a rotating stage to variate the light incident angle, see Figure 2.5.

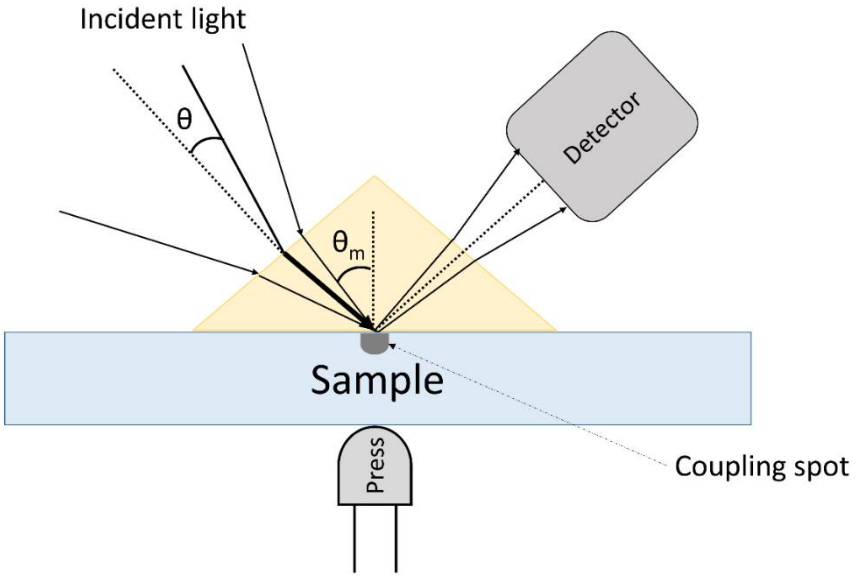

Figure 2.5. Prism coupling (M-lines) principle

The light is shined through the prism, refracted in it and then reached the interface between the prism and the sample. For a given range of angles, light is totally reflected when it encounters the interface since the prism has a higher refractive index. Light then exits the prism and is collected. However, for specific angles, part of the light couples with the sample leading to a drop in the detected light exiting the prism. The plot of the intensity as a function of position will thus possess a knee when light couples to the sample. From the position of this knee, it is possible to determine the refractive index of the sample.

2.5 Thermal poling of the glass sample: description of the poling cell

The poling cell used during the process was custom-built in Bordeaux university. A schematic representation of it is given in Figure 2.6.

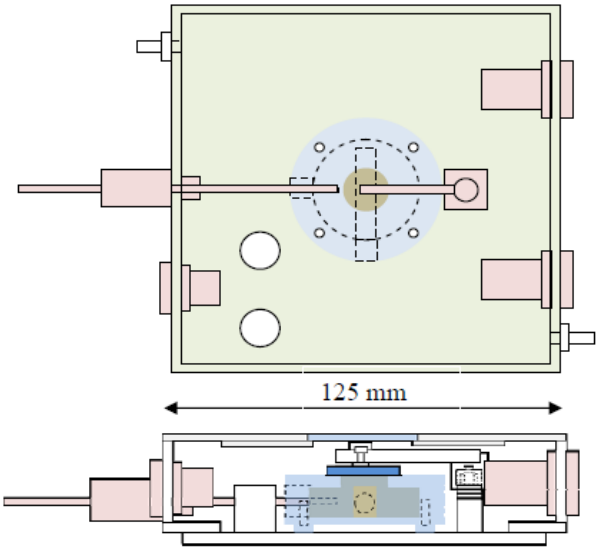

Figure 2.6. Schematic representation of the poling cell

The poling cell consists of a chamber which can be hermetically sealed to perform treatments under controlled atmosphere (argon or nitrogen) or under a primary vacuum. The top of the poling cell is fitted with an optical window made of fused quartz. The cell is small enough to fit under an optical microscope and allows to perform Raman and SHG measurements under controlled atmosphere.

The heating system consists of a heating element inserted in an aluminum piece which serves also as a cathode. The maximum working temperature is 350°C, which is high enough for most of the glasses, as the treatment is performed under T_g. A thermocouple is inserted inside the aluminum piece to control the temperature. The temperature of the sample was measured with a second thermocouple to measure the temperature gradient and to calibrate the set-up.

A high tension source is connected to the cell and can deliver high voltage up to 10kV with 5mA of current. A Labview program control the high tension source and permits to control the ramp rate, the maximum current and to record its variation over time.

2.6 Structuring electrodes for thermal poling

In some of the work that will be presented in this thesis, structured electrode will be used instead of plain electrodes. The structured electrodes are prepared by laser ablation of a 100 nm thick ITO coating (8-12 $\Omega.sq^{-1}$) deposited on a microscope slide. The ablation of the ITO layer is performed with a nanosecond yttrium aluminum garnet (YAG) laser source at 1064 nm. The electrode is placed on a microscope stage which is controlled by a software. Patterns to be inscribed can be loaded on the software which then inscribed them on the electrode. The laser power is chosen so that the entire ITO layer is ablated by the laser pulse. The ITO coated microscope slide is then formed of alternating conductive and non-conductive areas. Once structured, silver conductive paint is applied on the ITO free side of the electrode and on the sides to ensure conductivity. The prepared electrode will then be used as an anode during thermal poling, with the ITO coating facing the sample to be poled.

2.7 Measurements of the SHG response by mean of the Maker fringes

Various techniques are available to determine second order nonlinear optical coefficients. The one used in this work, the Maker fringes, [2] is based on the observation of second harmonic generation from the sample and is compared to a reference (α-quartz). This measurement is a second harmonic ellipsometry technique and consists in irradiating a sample with a frequency ω and to record the intensity generated by the sample at 2ω. The incident angle varies during the measurement. Hence,

when passing through the sample, variation of the optical path due to the change of incident angle allows the measurement of interference fringes.

Two setups are available in the laboratory with two different incidence wavelength, 1550 and 1064 nm. Both laser are nanoseconds and operate at 30 Hz and which deliver maximum impulsions of 100 μJ during a pulse of 20 ns of duration. The typical setup is presented on Figure 2.7.

The beam is first going through a power unit, consisting of a half-wave plate and a Glan polarizer, that controls the intensity of the laser. An optical fiber collects a fraction of the incident laser beam I_ω to measure its intensity. The beam then goes through the polarization unit which controls the incident polarization state. A filter associated with a lens focus the beam onto the sample surface. The output harmonic goes through a high optical density step filter, transparent in the visible but absorbent for the 1064 nm (or 1550 nm) wavelength. Then it goes through a band-pass filter (532 or 775 nm depending on the incident wavelength) which only allows the harmonic light to pass. The analyzed polarization is then selected between two states: S (vertical) or P (horizontal). The sample is mounted on a motorized stage allowing to perform measurements as a function of incident angle. Each measured intensity is an average of 64 to 250 pulses. This type of scan will be referred as a θ-scan. Four different scans can be recorded: p-p, s-p, p-s and s-s. The first letter corresponds to the polarization of the incident beam and the second one to the polarization of the harmonic.

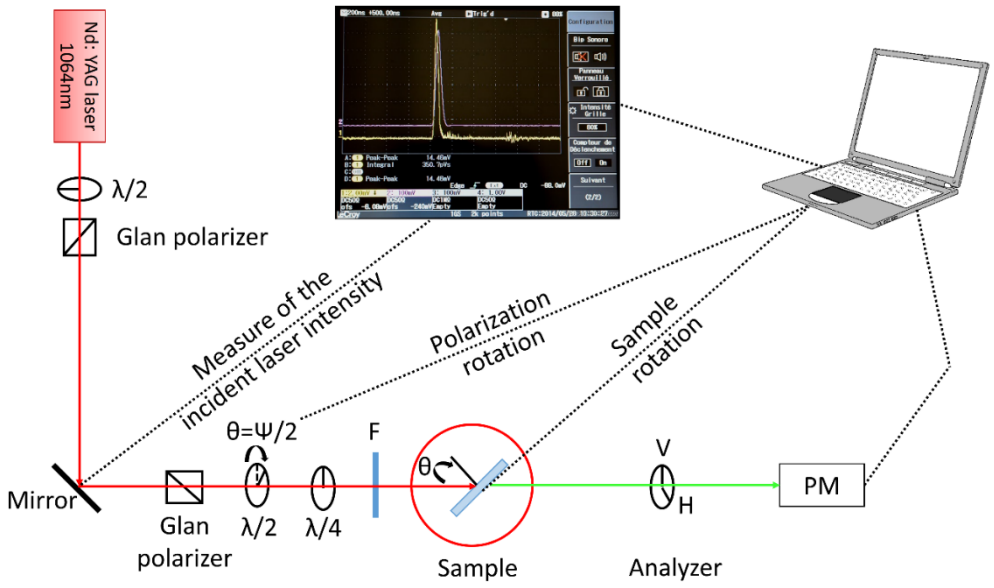

Figure 2.7. Representation of the Maker fringes setup

A second type of scan is usually performed: ψ-scan. It consists in recording the SHG intensity at a fixed angle of incidence as a function of the incident polarization state. This type of scan is especially useful to probe the various components of the tensor. The polarization unit allows to obtain all possible polarization state as illustrated on Figure 2.8. [3]

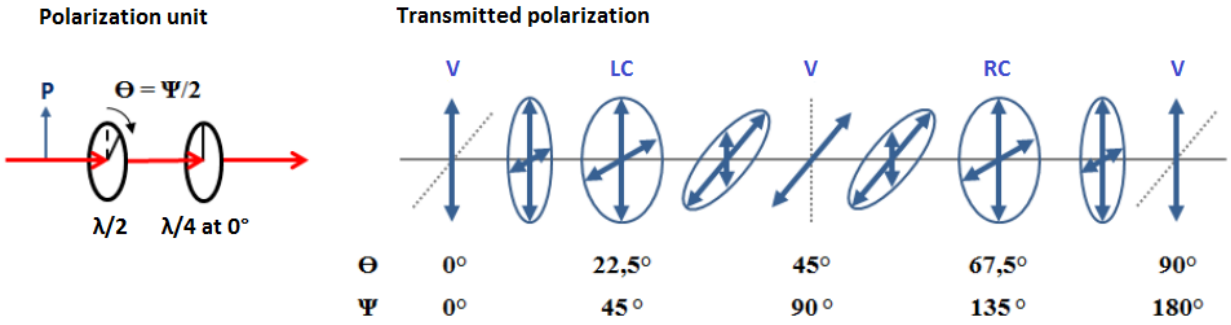

Figure 2.8. Various polarization obtained while varying the incident polarization

The Maker fringes technique allows to probe the second order susceptibility tensor defined in the previous chapter. To obtain a quantitative measurement of the second order nonlinear optical coefficients, it is necessary to calibrate the set-up using a reference material. A quartz sample with a d_{11} of 0.3 pm/V at 1064 nm is used as the reference. [1, 4] The crystallographic orientation used during calibration is on the crystallographic axis C along the z direction, the A axis is 75° from the X-axis (P) and the B axis is 15° (S) for θ equal to 90°. Maker fringes are then recorded on the sample and theta scans with the four various polarization (p-p, s-p, p-s and s-s) are measured. With the four different scans, it is now possible to start the calibration. We use a program developed by Vincent Rodriguez [1] which allows to fit a variety of parameters using a Monte Carlo algorithm for absorbing anisotropic multilayers systems. The main parameters are the thickness of the sample, the various elements of the $\chi^{(2)}$ tensor, a potential offset of the optical elements and motors in the set-up and two coefficients describing the law of the second order nonlinear response:

$$((A + I_{\omega})^2)\, B \tag{2.2}$$

The $\chi^{(2)}$ tensor is based on the point group to which belongs the crystal (32 for quartz) and the tensor shown in the opening chapter is chosen. Once all important parameters are found, it is possible to finalize the calibration by doing a study as a function of power. Several theta-pp scans are recorded with increasing laser power. As we face a second order nonlinear phenomenon, the response of the material should vary quadratically with incident laser power. In this step of the calibration, all parameters are fixed and only parameters A and B are fitted. Once A and B are found, they can be used to fit data of the poled glasses. An example of fit made for the quartz is presented in Figure 2.9.

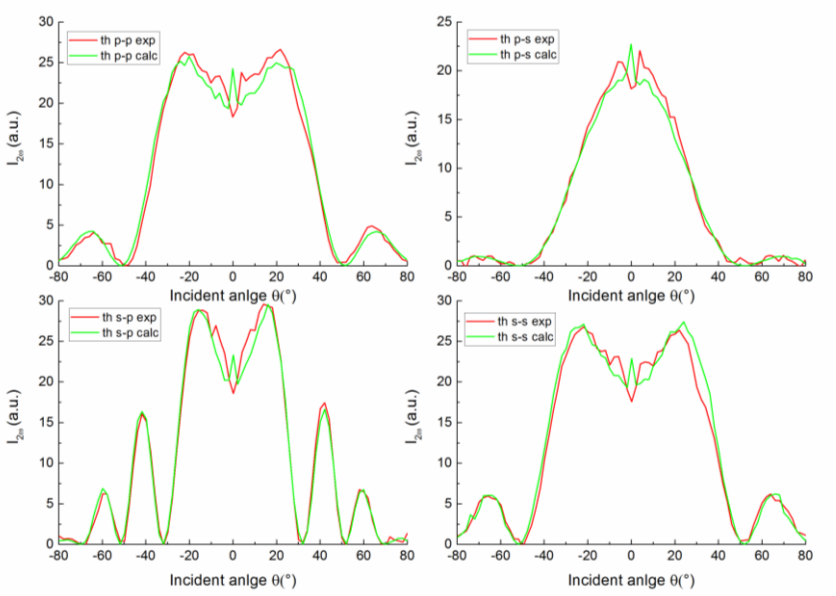

Figure 2.9. Maker fringes recorded on the quartz sample with various polarizations (red) plotted with the simulated fringes for the same conditions (green)

Finally, to understand the various fit that will be performed in chapter 5, Figure 2.10 defines the laboratory frame in which the measurements are performed, which is necessary to keep in mind for the fits that will be performed later on.

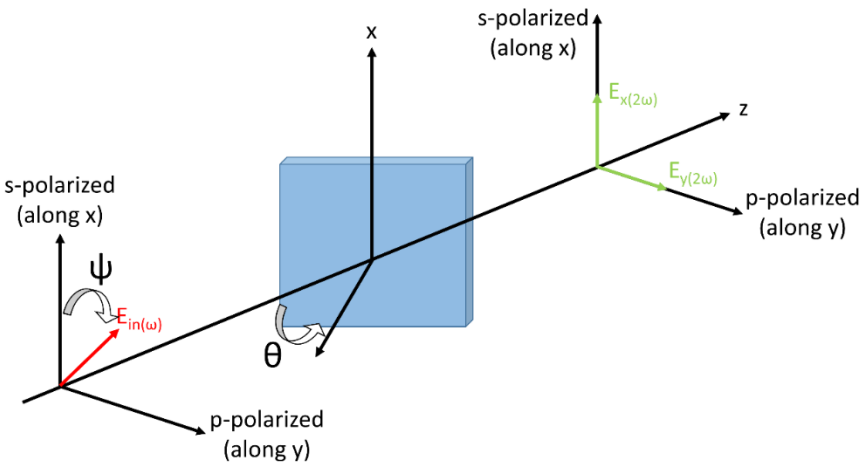

Figure 2.10. Scheme detailing the laboratory frame for all Maker fringes experiments

2.8 Optical spectroscopy

Optical spectroscopy refers to a set of technique which is based on the interaction between light and matter. Various techniques will be used to probe the structure of the glasses before and after poling but also to characterize the transmission region of the glasses before and after poling.

To better understand the overall concept of spectroscopy, it is important to consider an isolated molecule and the various level of energy required to describe it.

A typical molecule with N atoms can have its movement in space described by 3N degrees of freedom: 3 degrees of freedom for translations, 3 degrees of freedom for rotation and 3N-6 degrees of freedom for vibration. The total energy of the molecule is given by

$$E_{total} = E_T + E_R + E_V + E_E \quad (2.3)$$

The terms E_R (rotation), E_V (vibration) and E_E (electrons) are quantified, meaning that they can only take specific values. The last term E_E is related to the electrons and is based on the assumption that their movement can be isolated from the rest of the nucleus according to the Born-

Oppenheimer approximation. The E_T term (translation) can be classically described and the gas kinetic theory gives $E_T = 3/2k_BT$, with k_B being Boltzmann constant.

The population of every level is highly dependent on temperature. At room temperature, the rotational level is the more densely occupied, followed by the vibrational level while the electronic level is not occupied except at the fundamental level. The following plot shows the order of magnitude of the energy of each level as well as the thermal agitation level at 300 K as a reference.

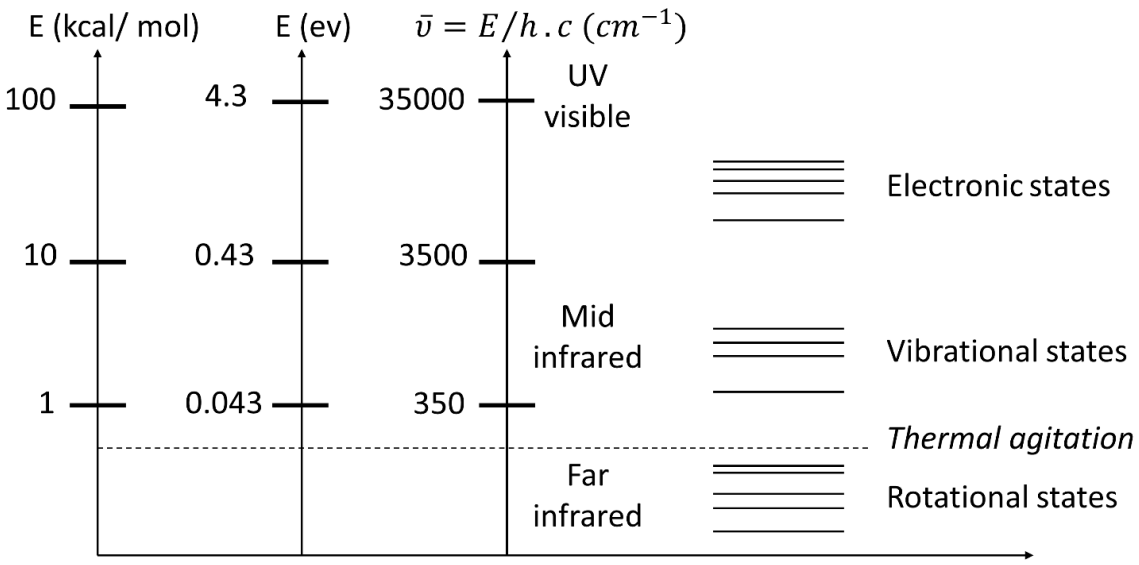

Figure 2.11. Order of magnitude of the various energy states, thermal agitation is plotted at 300K is plotted as a reference (600 cal)

2.8.1 Infrared spectroscopy

Infrared spectroscopy is based on the light and matter interaction in the infrared regime. The infrared region can be separated in three regions, the near-infrared (NIR), the mid-infrared (MIR) and the far-infrared (FIR). Depending on the community of user, these three regions can vary in term of wavelength. In this work the norm ISO 20473 is used to define the tree regions and

specifies that the NIR spans from 0.78 to 3 μm, the MIR spans from 3 to 50 μm and the FIR from 50 to 1000 μm.

Measurements were performed using three different techniques: IR in specular reflectance mode (macroscopically and microscopically), IR in transmission mode and Attenuated Total Reflectance (ATR). These various techniques are complementary as they do not penetrate the sample in the same depth. To better grasp the difference between the various IR technique, it is necessary to define the concept of complex refractive index which can be written as:

$$\hat{n} = n + ik \tag{2.4}$$

With n the linear refractive (real part) index and k the extinction coefficient (imaginary part). The main difference between the transmission and the reflection technique is that transmission spectra only probe the imaginary part k while reflection spectra probe the imaginary and the real part of the refractive index.

Spectra were recorded in reflection mode to obtain information on the structural changes associated with the poling treatment. When light encounters a surface, part of it is transmitted or absorbed and another part is reflected. In the ideal case of a perfectly plane surface, this phenomenon is described as specular reflectance and the incident angle is equal to the reflected angle. There is no such thing as an ideal surface so depending on the sample roughness, part of the light is scattered. This phenomenon is called diffused reflection and is another spectroscopic technique which will not be described here.

The amount of reflected light is highly dependent on the nature of the sample but most importantly, the amount of reflected light is a function of the incident light frequency and is maximum for

frequencies where the absorption is maximum. The fact that the amount of reflected light depends on the incident frequency also means that the depth over which the incident light penetrate the sample varies with frequency. This is especially important when measuring IR spectra on poled sample as the thickness of the modified layer can be of the order of few microns. Typically, specular reflectance probes the first micron underneath the surface. [5]

A reference spectrum is made with a gold mirror which theoretically reflects 100% of the incident light I_{ref}. Macro-IR spectra were recorded on a Vertex 70V (Bruker) vacuum spectrometer equipped with a DTGS detector and a MID/FIR range beam splitter. Spectra were recorded under a primary vacuum to remove the contribution of water from the atmosphere. For measurements performed on reactive glasses, a glove bag was positioned above the sample chamber. The poling cell (under vacuum) was introduced in the glove bag. The glove bag and the spectrometer were put under vacuumed then filled with nitrogen, allowing for measurements without any contact with air. Infrared spectra in reflection mode were recorded using an external reflection attachment (Graesby, Specac) with a 12° incidence angle.

Micro-infrared mapping of the surface was performed using a Perkin-Elmer Spotlight 400 spectrometer. Spectra were recorded under air with a resolution of 4 cm^{-1} between 4000 and 750 cm^{-1}. It is important to recall the resolution in the x-y plane of a sample when using micro-IR spectroscopy. The resolution is dependent on the wavelength of the light and will be coarser when working in the infrared spectrum compared to the visible. When working with oxide glasses, the main region of interest is around 1000 cm^{-1} where the resolution is at best around 12 μm. The resolution is going to improve as we go to higher wavenumber and can be as good as 2 μm around

4000 cm^{-1}. Masks are used to spatially control the illuminated area, to obtain a better signal to noise ratio, 15x15 μm masks were used and spectra were accumulated 100 times on each points.

Transmission spectra were recorded in air to determine the transmission window of the glass on a Perkin Elmer FT-NIR spectrometer Frontier. Maximum of transmitted intensity varies as a function of refractive index of the glass. For instance, the transmission maximum in Ge-Sb-S glasses is around 75 %. The transmission window can be determined from the transmission spectra. The optical band gap corresponds to the region above which photons are absorbed by the medium. The band gap is defined in term of energy, when we refer to above band gap, it means higher energy (in eV). It is difficult to determine precisely the optical band gap of a bulk sample. The optical band gap will thus be defined as 70 % of the maximum transmitted intensity. Similarly, at higher frequency it is possible to determine the multiphonon edge which corresponds to the threshold under which (in term of energy) light is no more transmitted. In addition to determine the transmission window, an IR transmission spectrum can also inform on some impurities present in the glass.

Attenuated Total Reflectance infrared spectroscopy was used to record spectra of powders. Powders were deposited on the ATR crystal and pressed. Spectra were recorded under air on a Nicolet iS50 FT-IR spectrometer between 400 and 4000 cm^{-1} with a 1 cm^{-1} resolution.

2.8.2 Ultraviolet-visible spectroscopy

UV-vis spectra in transmission mode were also recorded and are really similar in principle to the IR transmission spectra. The main difference is that it measures the transmission in the visible and ultraviolet region of the light spectrum. In term of apparatus, a UV-vis spectrometer

measures the transmission over small spectral window and then constructs the transmission spectra. As opposed to an IR spectrometer which measures a broad spectral window.

2.8.3 Raman spectroscopy and correlative µ-SHG mapping

Micro-Raman and micro-SHG measurements were recorded in backscattering mode on a modified micro-Raman spectrometer HR800 (Horiba/Jobin Yvon). A representation of the assembly is presented on Figure 2.12.

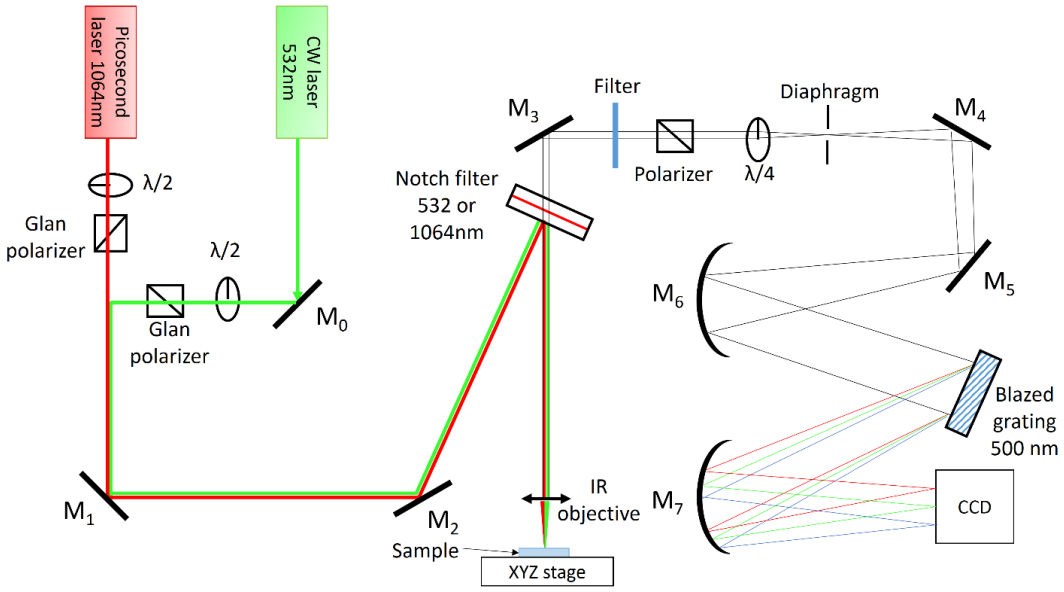

Figure 2.12. Principle of the combined Raman / SHG microscope setup

A continuous laser operating at 532 nm is used for Raman and a picosecond laser at 1064 nm is used for micro-SHG measurements. The use of a confocal microscope and a motorized stage (X,Y,Z) enables 3D mapping with good spatial resolution (0.5µm). Typical resolution used for Raman is 2.5 cm-1. Measurements of the SHG response was performed using a doughnut radial polarization to probe the electric field in the z-direction. This particular polarization was obtained

by a polarization convertor from Arcoptix. The peak centered at 2ω is integrated and gives the second harmonic response of the sample.

Raman spectroscopy is complementary to infrared spectroscopy presented before. The main difference is that it uses light in the visible which does not correspond to the energy level presented in the energy diagram Figure 2.11.

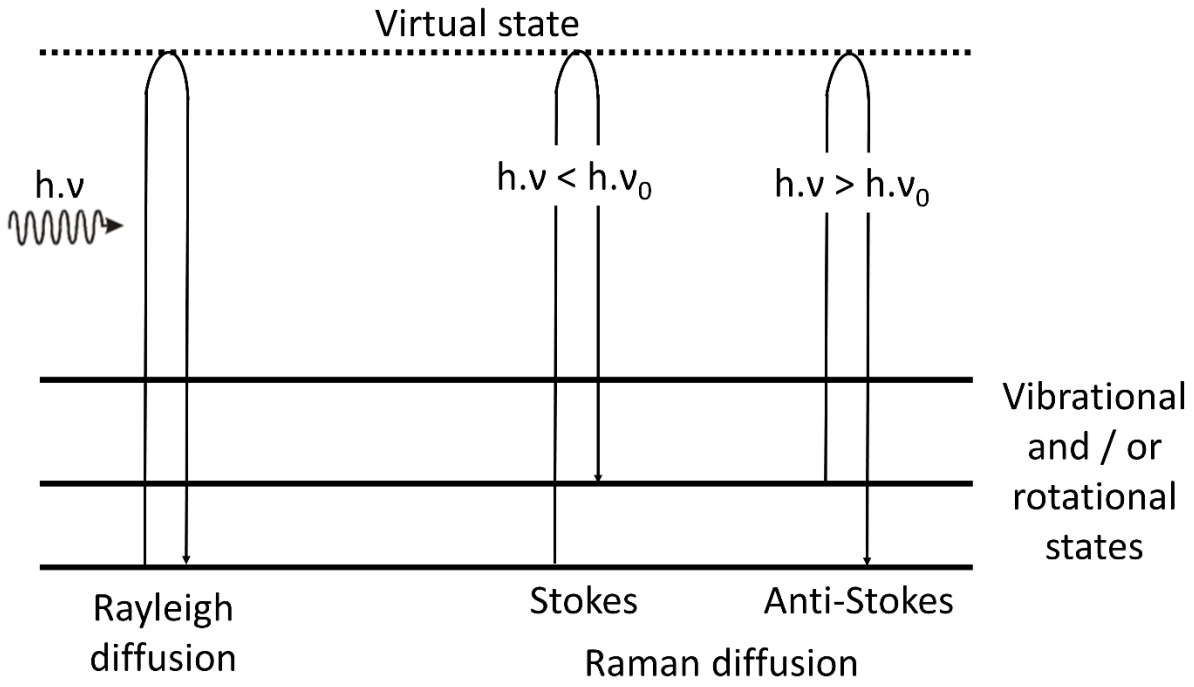

Figure 2.13. General principle of Raman scattering

The energy of the light is usually in between the electronic level and the vibrational level. The incident light thus does not correspond to any transition, i.e. hν ≠ Ef - Ei, light is hence scattered and accompanied by a change in propagation direction and sometimes energy. Molecules are briefly excited to a metastable virtual level and goes directly back to an allowed energy level.

When the scattered light has an energy different from the original incident light, we then have *Raman scattering*. The various possibilities of light scattering are summarized in Figure 2.13.

Raman spectroscopy informs on the glass structure in the low frequency region (below 1600 cm^{-1}) while at higher frequency, the main region of interest will be between 3000 and 4000 cm^{-1} to gain information on water and OH groups in general. In the chalcogenide part of this work, the reduced Raman spectra are usually presented as it allows to greatly minimize the effect of the boson peak at low wavenumbers. The reduced Raman spectra were calculated following the procedure described by Koudelka [6] using equation (2.5):

$$\rho(\nu) = \nu(\nu_i - \nu)^{-4}(1 - \exp(-h\nu/kT))I(\nu, T) \qquad (2.5)$$

Where ν_i is the frequency of the incident laser beam, ν is phonon frequency defined as $\nu = \nu_i - \nu_s$, with $\nu_s$being the frequency of the scattered light, the Bose Einstein factor is under bracket and $I(\nu, T)$ is the experimental Raman intensity. In some cases, the resulting reduced Raman spectra is normalized to the peak of higher intensity to allow for easier comparisons.

In addition to Raman spectroscopy, the set-up presented above allows to measure the SHG response of the medium. To perform the μ-SHG measurements on the sample, the laser bean at 1064 nm is polarized using an Arcoptix polarization converter. Two polarizations states can be obtained, (i) radial polarization and (ii) azimuthal polarization which are represented on Figure 2.14.

A radially polarized beam exhibits a high longitudinal component when focused on a surface using a high numerical aperture objective. [7] It was therefore used to probe the SHG in this direction.

This setup therefore allows to perform a correlative study of the material structure and SHG capability. This set-up is quite unique and is especially useful to fully characterize the process taking place during poling.

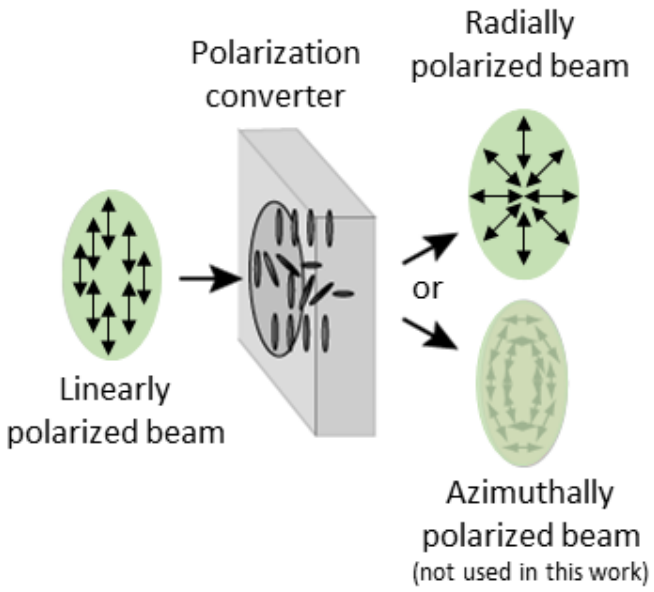

Figure 2.14. Principle of the polarization converter

2.9 Atomic Force Microscopy

Atomic Force Microscopy (AFM) is a technique which consists in scanning the surface of a sample with a probe not only to visualize its topography but also to measure surface properties of a sample.

An AFM is comprised of a nanometer size sharp tip which is placed at the edge of a cantilever. As the tip is brought closer to the surface, attraction forces interact with it causing the cantilever to flex towards the surface. When the tip touches the surface, repulsion forces take over the attraction forces which cause the cantilever to flex in the opposite direction, away from the surface. During an AFM measure, the deflection of the cantilever is monitored by mean of a laser beam focused

on top of the cantilever. Any deflections of the cantilever will cause the reflected beam to deviate. Four photodiodes allow to record these changes.

As the probe scans the surface, any changes of topography cause deflection of the cantilever. A feedback loop is used to control the height of the tip above the surface and to keep it constant. The deflection is hence constant over time and a precise map of the surface topography can be obtained. The principle of the AFM measurement is summarized on Figure 2.15.

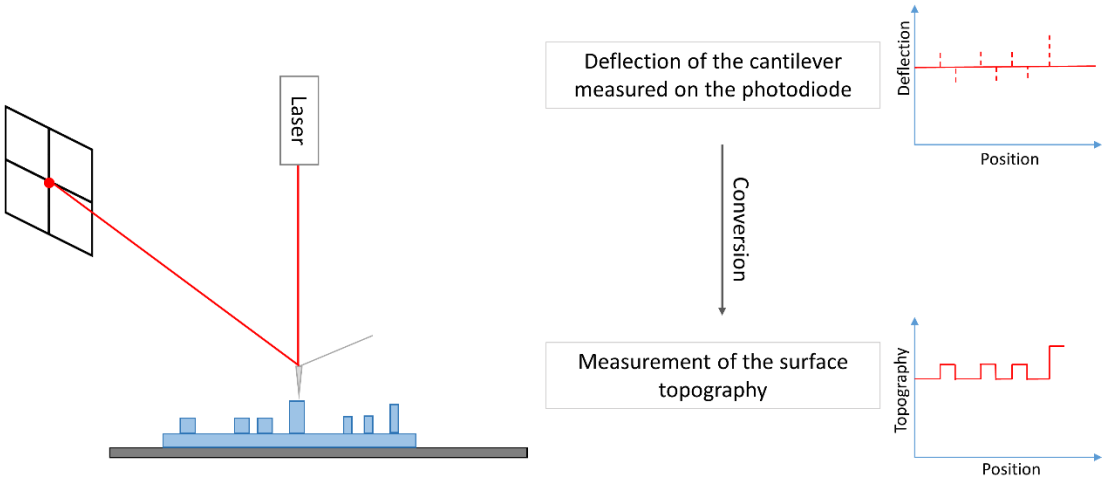

Figure 2.15. Principle of the AFM measurement for topography measurements

Three main modes of AFM imaging can be listed: the contact mode, the non-contact mode and the tapping mode.

The contact mode scans the surface with the tip in contact with the surface. As it is in contact with the surface, only strong repulsive forces act on the cantilever and deflect it as it encounters changes of topography.

The non-contact mode scans the surface without touching it. The cantilever oscillates above the surface and the oscillation amplitude decreases as the tip approaches the surface. A feedback loop

is used to correct for these amplitude changes and a map of the topography can be obtained. The advantage of that method is that the tip cannot touch the surface which improves its lifetime.

The tapping mode is a combination of the two previous modes. In the same manner as the non-contact mode, the cantilever oscillates above the surface but this time with higher amplitude oscillations. As the tip touches the surface, it will wear out more rapidly.

The three different modes can be summarized as a function of the tip to surface interaction represented on Figure 2.16.

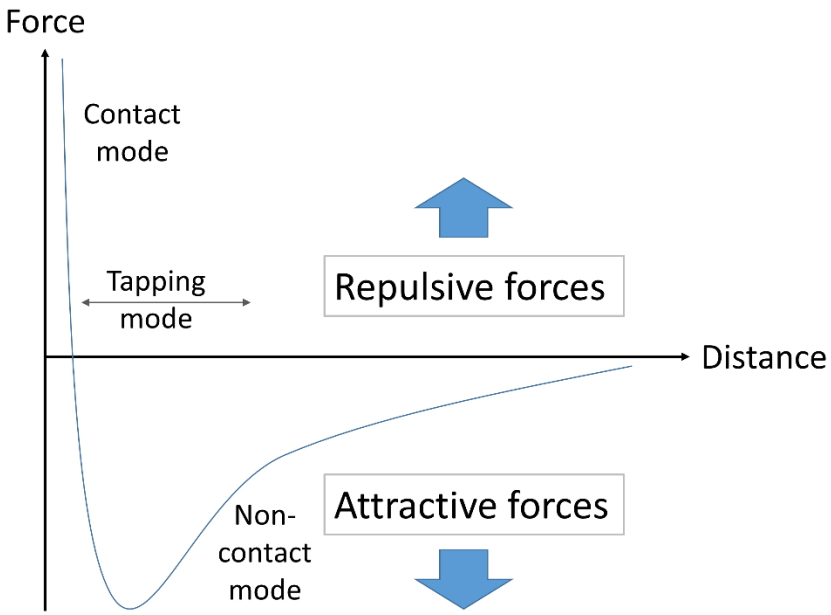

Figure 2.16. The three principal modes of AFM relative to their tip to sample interactions

In addition to surface topology measurements, AFM can be used to measure surface properties of a material such as mechanical properties (Young modulus, adhesion, dissipation, deformation) by mean of the PeakForce mode which record force curves on the surface. In addition, electric

properties such as surface potential can be measured by mean of the Kelvin Probe Force Microscopy (KPFM). During this PhD, a mixed of these two modes was used: PeakForce KPFM.

PeakForce KPFM uses a conductive cantilever. When placed in an electric field, its effective spring constant is the sum of the electric force gradient and its natural spring constant. An AC voltage is applied on the piezoelectric so that the cantilever oscillates at its resonant frequency ω. An AC bias is then applied between the sample and the tip at frequency ω_m which modulates the resonant frequency. The modulation of the resonant frequency leads to the apparition of two side-bands $\omega \pm \omega_m$ and $\omega \pm 2\omega_m$. As with the cantilever deformation, the bias (DC or AC) is adjusted so that the side bands disappear, the surface potential can hence be measured.

When using this mode, the measurements typically involves two steps. The topography and mechanical properties are first mapped using the PeakForce mode. In a second step, the surface potential is measured in KPFM mode by scanning the surface with the cantilever at a fixed height. This technique allows to access surface properties and to correlate them with the surface topology.

2.10 Electron Microprobe Analysis

Elemental compositions of glasses can be measured using electron microprobe analysis to check the final composition of the glass and eventual compositional changes following poling. These measurements are made in a Scanning Electron Microscope (SEM) to which an Energy-dispersive X-ray spectrometry (EDS or EDX) system and a Wavelength dispersive spectrometry (WDS) system are attached. Both techniques allow to qualitatively or quantitatively (using the correct standards) measure the composition of a material.

A beam of accelerated electrons is focused on the surface which interacts with the material by producing X-rays. The X-rays are then collected and counted by a detector which are then converted into a spectrum giving specific peaks for specific energies which correspond to specific elements. This type of measurement corresponds to EDX and possess drawbacks that are a limited spectral resolution and low sensitivity to light elements and low quantity.

For more accurate measurements, WDS is preferential as it has a spectral resolution and detection limit an order of magnitude better than EDX. The main difference is that the spectrometer is tuned to the X-ray of interest in the analysis (associated with a particular element).

2.11 Secondary Ion Mass Spectrometry

As described in the first chapter, upon poling cations migrate towards the cathode leaving a cation depleted layer underneath the anodic surface. The thickness and position of this layer is dependent on the glass network and the poling conditions. To probe the thickness and position of the depleted layer, Secondary Ion Mass Spectrometry, i.e. SIMS, is an adequate technique.

SIMS consists in sputtering a surface with a focused ion beam while collecting all secondary ions ejected from the sample. A mass spectrometer allows to determine the elemental composition from the mass to charge ratio of the ejected secondary ions. SIMS is mainly a qualitative technique which requires good standards to obtain quantitative measurements. The first 1 or 2 nanometers are probed using that technique and it is possible to do depth measurements by recording series of spectra on the same point. As the surface is gradually removed under the focus ion beam, an evolution of the intensity of a mass signal can be recorded as a function of time. This can then be converted to a depth profile. SIMS main advantage over other quantitative / qualitative techniques

is its good sensitivity to low concentration and light element. SIMS is a destructive technique and is the final measurement performed on the glass samples.

All SIMS measurements done during this PhD work were performed by Mikhail Klimov from the Materials Characterization Facility in UCF.

2.12 References

(1) Rodriguez, V.; Sourisseau, C. General Maker-Fringe Ellipsometric Analyses in Multilayer Nonlinear and Linear Anisotropic Optical Media. *J Opt Soc Am B* **2002**, *19*, 2650-2664.

(2) Maker, P. D.; Terhune, R. W.; Nisenoff, M.; Savage, C. M. Effects of Dispersion and Focusing on the Production of Optical Harmonics. *Phys. Rev. Lett.* **1962**, *8*, 21-22.

(3) Verbiest, T.; Clays, K.; Rodriguez, V. In *Second-Order Nonlinear Optical Characterization Techniques: An Introduction;* Taylor & Francis Group, Ed.; Boca Raton, 2009; .

(4) Bosshard, C.; Gubler, U.; Kaatz, P.; Mazerant, W.; Meier, U. Non-Phase-Matched Optical Third-Harmonic Generation in Noncentrosymmetric Media: Cascaded Second-Order Contributions for the Calibration of Third-Order Nonlinearities. *Physical Review B - Condensed Matter and Materials Physics* **2000**, *61*, 10688-10701.

(5) Dussauze, M.; Rodriguez, V.; Lipovskii, A.; Petrov, M.; Smith, C.; Richardson, K.; Cardinal, T.; Fargin, E.; Kamitsos, E. I. How does Thermal Poling Affect the Structure of Soda-Lime Glass? *Journal of Physical Chemistry C* **2010**, *114*, 12754-12759.

(6) Koudelka, L.; Horák, J.; Pisárcik, M.; Sakál, L. Structural Interpretation of Raman Spectra of (As2S3)1-X(AsBr3)X System Glasses. *J. Non Cryst. Solids* **1979**, *31*, 339-345.

(7) Wilson, T.; Massournian, F.; Juskaitis, R. Generation and Focusing of Radially Polarized Electric Fields. *OPTICAL ENGINEERING* **2003**, *42*, 3088-3089.

CHAPTER 3: MICRO-POLING OF A NIOBIUM BOROPHOSPHATE GLASS: A WAY TO CONTROL THE 2ND ORDER NONLINEAR OPTICAL PROPERTIES AT THE MICROMETRIC SCALE

In the literature chapter, it has been shown that the niobium borophosphate (BPN) system was well suited for thermal poling applications. One of the highest induced $\chi^{(2)}$ ever induced via thermal poling on an oxide glasses was obtained for a niobium borophosphate glass. [1] The reason for this high induced 2nd order nonlinearity is now better understood and was linked to the particular structural properties of this glassy system. [2] Now that the mechanisms are better described, it is possible to try to find concrete applications for a thermally poled BPN glass. In the domain of microphotonic, and especially in photonic integrated circuit (PIC), there is a strong need for nonlinear active materials. These materials should have sufficiently high nonlinearity, low losses, a large domain of optical transparency and ideally optical properties should be controlled at the micrometer scale.

In the present chapter, thermal poling is presented has a simple way to imprint second order optical properties on an amorphous substrate. The chapter is divided in three main sections. First it describes the glass and studies the patterned electrodes prior poling. After poling is undergone, the poled glass is carefully studied, especially the transfer fidelity of the patterns, as well as structural changes and μ-second harmonic generation around the patterns. The last section of this chapter is a discussion on the localization of the SHG signal around the patterns and on the influence that the electrode material has on it.

3.1 Study prior thermal poling

3.1.1 Description of the glass network structure using vibrational spectroscopy

The glass used in this study is a niobium borophosphate glass of nominal composition 0.58 (0.95 $NaPO_3$ + 0.05 $Na_2B_4O_7$) + 0.42 Nb_2O_5 (in mol %) that will be subsequently referred to BPN 42. This composition was deeply investigated in Bordeaux over the last 10 years and showed particularly good results and was thus chosen for this study. [2-5]

Prior thermal poling, it is necessary to study the glass's network structure to then evaluate any changes during the process. BPN glasses are made of two main structural entities, the phosphate network and the niobate network. The elementary structural unit of the phosphate network is a $(PO_4)^{3-}$ tetrahedron and the one of the niobate network is a NbO_6 octahedron. As sodium is added to the glass matrix, the various structural elements are connected through very short chains of mainly dimer. Regarding the phosphate network, the various elongation modes of the P-O bonds can be studied with IR spectroscopy. However, in the study presented herein, we aim at imprinting patterns few microns wide on a glass surface, which size is not suitable for IR spectroscopy.

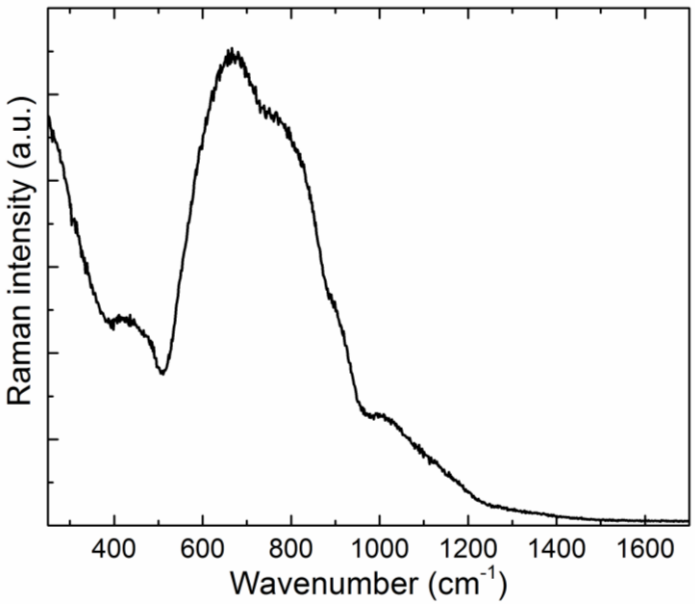

Figure 3.1. Raman spectrum of BPN 42 before poling

The structural study is thus focused on Raman spectroscopy which gives valuable information mainly on the niobate network. The Raman spectrum of BPN 42 is shown in the Figure 3. and its interpretation will focus on the spectral domain between 500 and 1000 cm^{-1} that is characteristic of the elongation modes of the Nb-O bonds.

The spectrum can be divided in three main domains involving the NbO_6 octahedra. The first one, between 500 and 750 cm^{-1}, is related to the 3D niobium network. These entities tend to form NbO_6 octahedra similarly to $LiNbO_3$ and $NaNbO_3$ crystals where the octahedra are corner shared. The second one, between 750 and 860 cm^{-1}, is attributed to symmetric stretching modes of Nb-O-P bridging bonds. Finally, between 860 and 1000 cm^{-1}, the symmetric stretching mode of the ionic bond between a sodium and a non-bridging oxygen, $Nb\text{-}O^{-}\ldots Na^{+}$ can be observed. [4, 6-8]

3.1.2 Preparation and characterization of the structured electrodes

The electrode used at the anodic side of the glass was structured by laser ablation of a 100 nm thick indium tin oxide (ITO) (8-12 Ω. sq^{-1}) layer deposited on a microscope slide. ITO strips were ablated using a nanosecond yttrium aluminum garnet (YAG) laser as described in the experimental techniques chapter. For this specific study, lines of various sizes and several millimeters long were written on the electrode with a pitch of 50 µm.

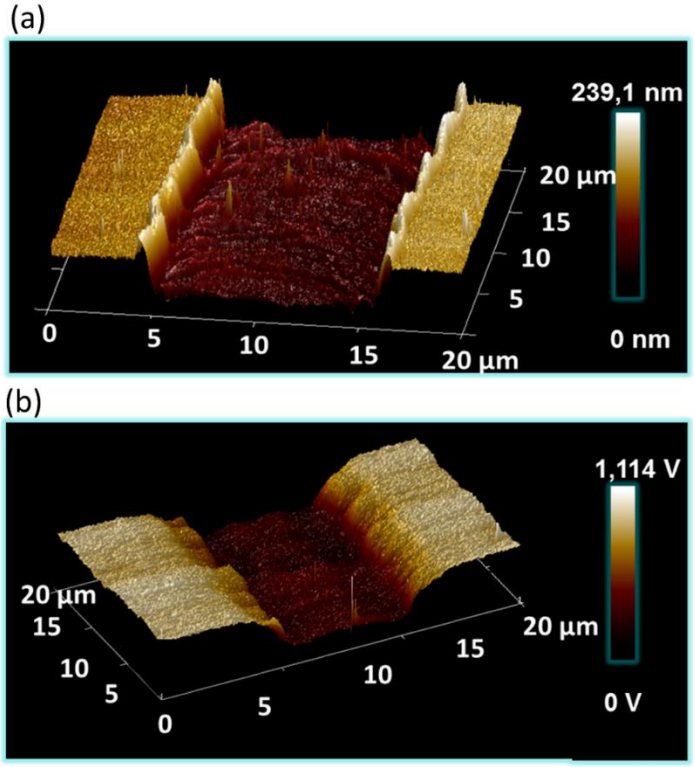

Figure 3.2. AFM measurements performed in KPFM mode across a line, showing the surface topology (a) and the surface potential (b)

The prepared electrode was then studied using atomic force (AFM) microscopy in Kelvin probe force mode (KPFM) to access both surface topology and surface potential. Figure 3.2 compares the surface topology and surface potential of a same line written on the ITO. It is observed that

clean lines are formed by total ablation of the 100 nm thick ITO layer. Lines are formed of a 100 nm gap and of a thin ridge on each outer sides of the lines. On part (b) the surface potential image shows the absence of measured potential in the line where ITO was removed, while outside the lines a homogeneous potential is recorded. The structured electrode can be seen as alternating conducting and non-conducting areas on top of the microscope slide.

3.2 Thermal poling and subsequent study of the poled glass

Once the structured electrode prepared and the base glass characterized, thermal poling can be undertaken. The structured electrode is placed at the anode and is used as a stamp during the poling process. A 100 µm thick borosilicate glass slide is placed at the cathode to prevent reduction of niobium cations in the glass from the +V oxidation state to +IV which would give a blue coloration to BPN glasses. This glass slide also serves a second purpose, that is to increase the resistivity of the overall assembly. The cathode is considered non-blocking as species can easily escape the glass and be transferred to the microscope slide at the cathode. A silicon wafer is then placed underneath the thin glass slide. The electrodes are mechanically pressed on the BPN glass and the assembly is heated up to 230°C (T_g = 625°C) and a DC bias of 1600 V is applied across the sample. A diagram of the thermal poling assembly is shown in Figure 3.3.

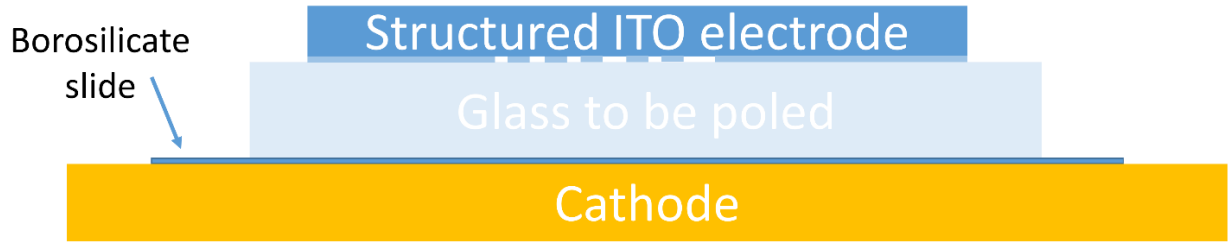

Figure 3.3. Thermal poling assembly for the BPN 42 glass using a structured electrode at the anode

The atmosphere of the poling cell is placed under nitrogen to obtain blocking anode conditions. Injection of species such as protons or hydroxyl from the atmosphere inside the glass are thus prevented. The thermal poling treatment lasts for 30 minutes, after which the sample is brought back to room temperature and the applied electric field subsequently removed.

3.2.1 Study of the topological changes by Atomic-force microscopy

The optical micrograph presented in Figure 3.4 shows that patterns from the electrodes are transferred to the glass substrate. Part (b) of this same figure shows an AFM map of one of these lines. A change of topology takes place upon poling with the imprinting of lines 7 µm wide and with a surface relief of 100 nm high. These features appear on areas that were in contact with lines written on the electrode. Lines on the electrode were 10 µm wide and 100 nm deep. It can also be observed that ridges on the outer part of the line on the electrode result in the appearance of tranches on the glass surface. The structured electrode can thus be seen as a stamp to change the surface topology of a glass. Such a process was previously reported in the literature and is known as electrostatic imprinting process of topology. [9-11]

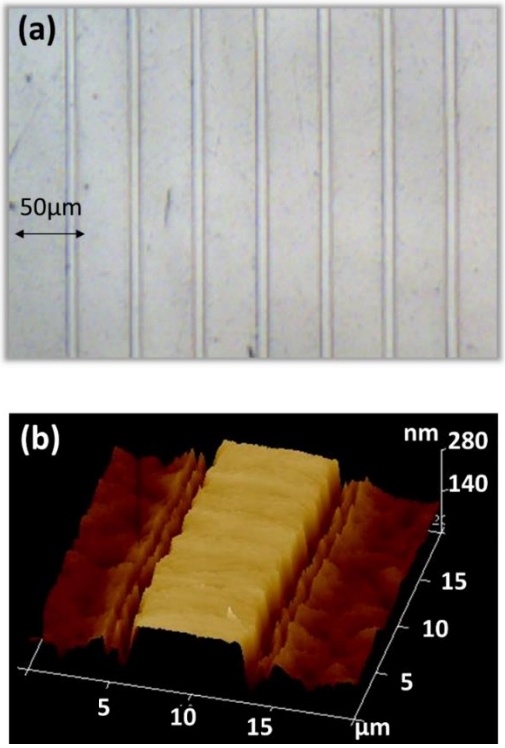

Figure 3.4. Optical micrograph (a) and topology image of the glass surface after thermal poling (b)

3.2.2 Study of the compositional changes by electron microprobe analysis (EDX/WDS)

Eventual chemical composition changes were studied using EDX spectroscopy. In a classical thermal poling experiment, once the electric field is applied across the sample, mobile cations start moving towards the cathode. In most glass compositions, highly mobile sodium cations are responsible for the recorded cationic conduction. Upon poling a Na-free layer builds up at the anodic surface which location corresponds to the SHG active layer. In a classical thermal poling made without structured electrodes, the sodium departure is observed on the entire glass surface in contact with the anodic electrode. EDX maps of sodium and niobium distribution were made across one line (5 µm wide) imprinted on the glass, which image can be seen in backscattering electrons Figure 3.5 (a).

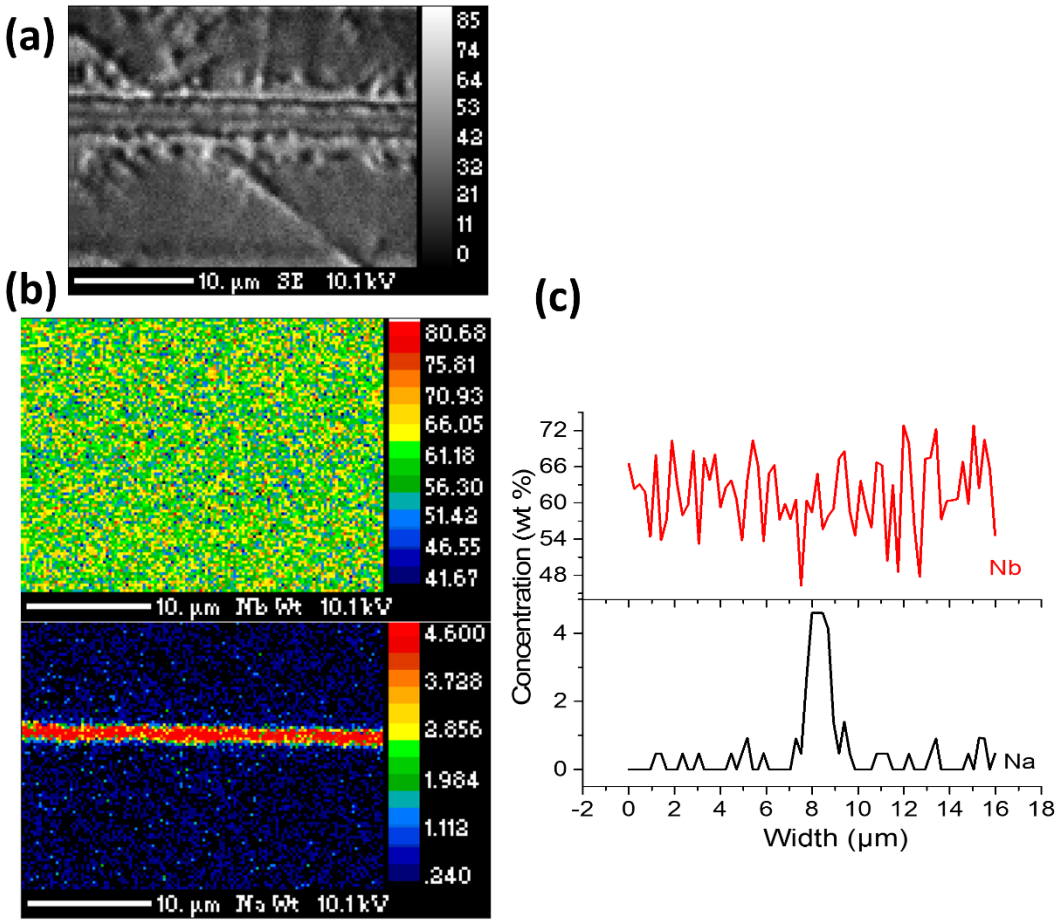

Figure 3.5. BSE image of a 5 µm wide line imprinted on the glass (a), map of the Nb and Na distribution (from top to bottom) (b), concentration profile of Nb and Na across the line extracted from the map (c)

Regarding any changes in the niobium distribution, Figure 3.5 (b), no real trend is observed. The elemental density profile shown in Figure 3.5 (c) also confirms these trends. This is expected for niobium, as a network former it is not mobile and should not drift under the electric field. However, regarding the sodium level across the map, a close to total depletion is observed outside the line, whereas inside the line, only a small decrease from the nominal composition is observed. The corresponding profile, Figure 3.5 (c), shows a sharp contrast in the sodium concentration, which

goes from 0 to 4.6 wt % in less than 2 μm. The distribution of sodium across the surface can be linked to the electric potential at the surface of the glass during poling. As it was observed in KPFM measurement on the anode, the surface potential inside an ablated ITO line is null. The distribution of sodium thus strictly follows the potential effectively applied on the glass surface and sodium migration only occurs in areas where the potential is non-zero, i.e. in areas where ITO remains.

3.2.3 Study of the structural modifications by Raman spectroscopy

Sodium departure should also lead to structural changes in the glass after poling. Potential spectral changes were investigated using Raman spectroscopy and are presented in Figure 3.6.

Spectral changes are only observed outside the line while in the line the obtained spectrum corresponds to the base glass. Figure 3.6 presents a spectrum taken inside the line (black) and a spectrum taken outside the line (red). The first changes are impacting the niobate network between 500 and 900 cm^{-1}. They are especially visible on two vibrational modes at 820 and 900 cm^{-1} that we earlier attributed to symmetric stretching bonds of Nb-O-P and Nb-O^-…Na^+. Regarding the main vibrational band between 600 and 750 cm^{-1}, its contribution seems to be increasing. It is however important to note that this large band actually arises from two contributions both related to NbO_6 octahedra. The first one, centered around 620 cm^{-1} is attributed to regular corner shared tetrahedra. The second one, centered around 670 cm^{-1}, is however attributed to irregular edge sharing octahedra. After poling, the first contribution decreases while the second once increases.

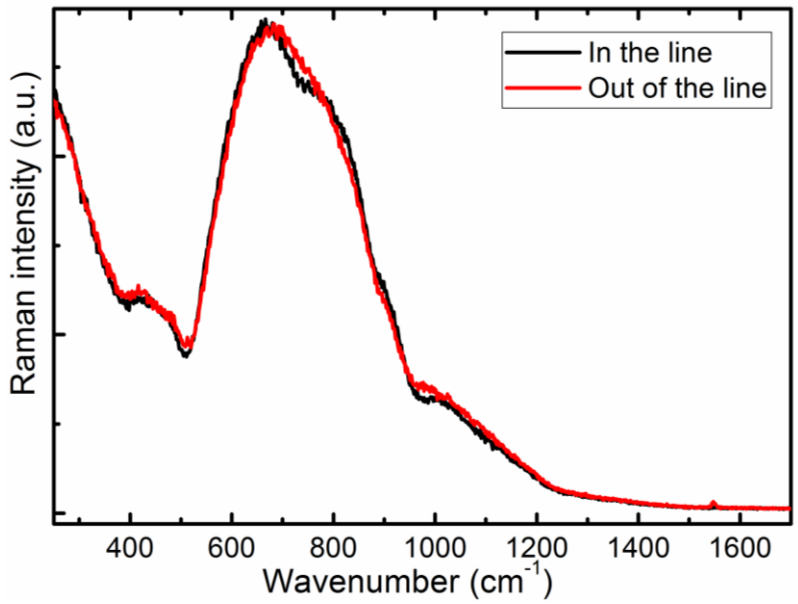

Figure 3.6. Raman spectra measured in (black) and out (red) of the line imprinted on the glass surface

Similar structural changes upon thermal poling of BPN glasses were already reported in the literature. [2, 5]

Finally, a new contribution at 1550 cm^{-1} appears on spectra taken outside the line. This last contribution was already observed and attributed to the symmetric stretching vibrational mode of molecular oxygen. The area around a line inscribed on the glass surface was then mapped in Raman spectroscopy. The Raman spectra were then normalized to the maximum intensity of the main vibrational band around 720 cm^{-1}. To highlight the observed changes, the difference between normalized spectra recorded on this map and the spectrum of the base glass was calculated and is shown on part (a) of Figure 3.7. This allows to highlight the various dissimilarities that we discussed in the preceding paragraph. From this difference spectra, several maps were plotted and are shown on part (b), (c) and (d) of the same figure.

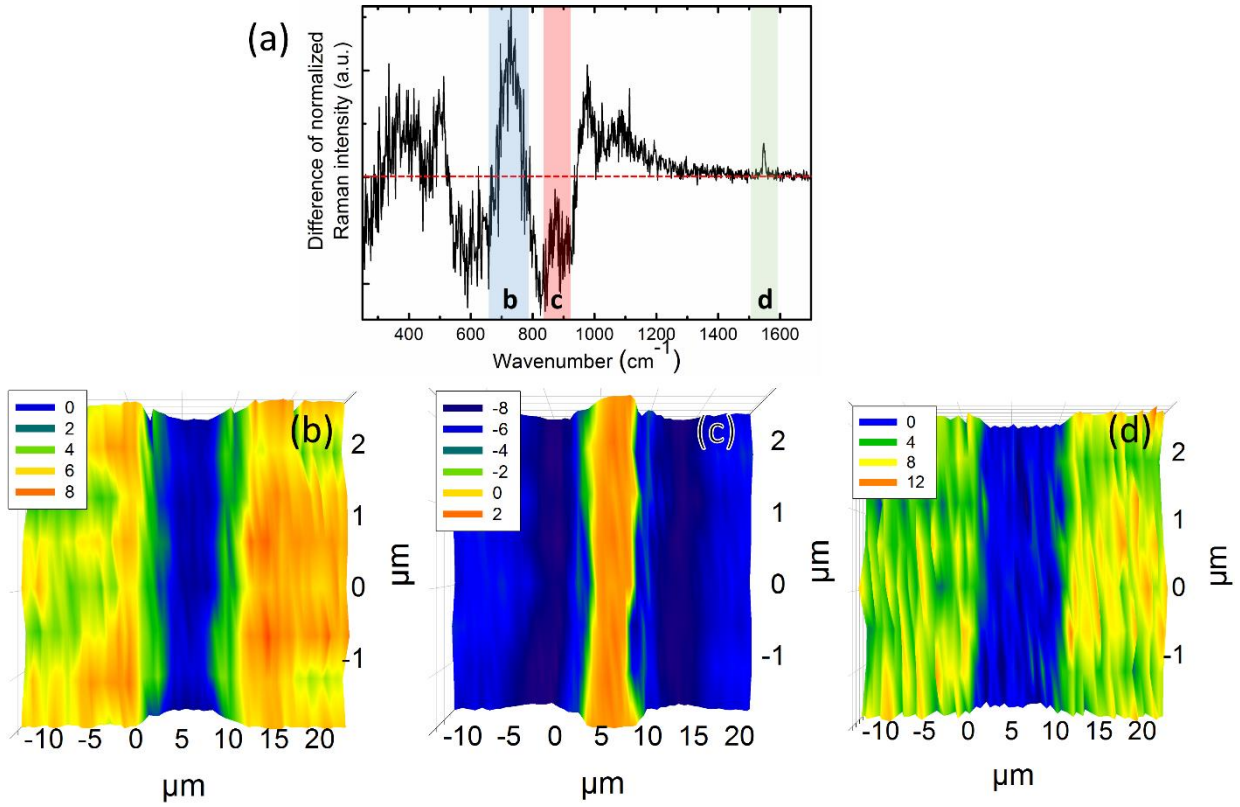

Figure 3.7. Difference of normalized Raman intensity (a), corresponding maps of spectral domains b (b), c (c) and d (d)

These three maps allow to visualize the spatial correspondence between structural changes observed in Raman spectroscopy and the sodium depletion measured in EDX. The structural changes taking place can be linked to the potential effectively on the glass surface. On areas where ITO is left on the electrode, the electric potential is effectively applied on the glass surface during poling. Sodium cations thus start to move away from the vicinity of the anodic surface while they remain motionless under the ITO ablated areas. This is in agreement with the EDX measurements previously shown. Following sodium departure, the glass network needs to rearrange which is directly observed by modifications involving the Nb-O-P and $Nb\text{-}O^{-}\ldots Na^{+}$ bonds vibration modes. They present a decrease in intensity, as they are directly linked to sodium presence. In the absence

of sodium cations, the local composition goes towards a pure niobate network without sodium modifiers to create non–bridging oxygens. The main vibrational band between 500 and 750 cm^{-1} is consequently impacted with an opposite change involving its two components. The contribution from the regular tetrahedra decreases and the one of edge-sharing octahedra increases. The niobate network is therefore distorded. Finally, the last map shows that molecular oxygen is forming in areas in contact with ITO. The formation of molecular oxygen in a near anodic region can be related to compensation mechanisms taking place upon poling. [12-14]As sodium cations migrate towards the cathode, it is necessary to account for compensation processes which absence would lead to exceed the dielectric breakdown. It was shown that the NbO_6 tetrahedra were converted from corner sharing to edge sharing octahedra. This conversion is necessarily followed by the release of an oxygen anion. The reactional path to form molecular oxygen is not yet perfectly understood but two hypotheses can be considered. The first one implies formation of oxygen anions which migrate towards the anode and oxidized to form molecular oxygens. [13-15] The second one is based on a purely electronic process, with an electron departure and the formation of highly reactive peroxide species with an unpaired electron on a non-bridging oxygen. [12] These reactive species would recombine under the strong mechanical constraints arising during thermal poling. None of these two hypotheses can be rejected as we lack of a good experimental technique that could directly indicate the formation of one of these intermediates over the other.

3.2.4 Characterization of the Second Order optical properties via µ-SHG microscopy

The formation of a sodium depletion indirectly indicates that charges are frozen inside the glass matrix. Such an internal electric field is known to break the glass's inversion symmetry thus giving Electric Field Induced Second Harmonic. The impact of the electrode structuring on induced

SONL properties was investigated using our confocal µ-SHG setup presented in the experimental techniques chapter. To fully characterize the material response, a study with various polarization was performed. Such a study allows to probe the SHG response along numerous directions. Part (a) of Figure 3.8 shows an optical micrograph of the studied area. The SHG map was recorded on a single line shown in the black rectangle. Part (b) and (c) show the SHG maps recorded on this line with two different polarization state of the incident laser beam. The map presented on part (b) was recorded using a radial polarization which probes the longitudinal SHG response (denoted $I_{2\omega\perp}$) while map on part (c) was linearly polarized to record the in plane contribution (denoted $I_{2\omega\parallel x}$and $I_{2\omega\parallel y}$).

Regardless of polarizations, these two maps show that the SHG signal is intensely present near the edges of the line. The signal recorded on the line's edges is greater by two order of magnitude compared to the signal recorded in and out of the line. Structuring of the electrode seems to enhance the SHG response of the glass around the patterns. However, there is more to be said regarding the effect of the structured electrodes on induced SONL properties, especially on the spatial location of the various SHG responses. When measuring the in-plane response of the SHG signal with an excitation polarization parallel to the line ($I_{2\omega\parallel x}$), no SHG response is recorded. Changing this excitation polarization so that it is now perpendicular to the line ($I_{2\omega\parallel y}$) leads to the measurement intensity maximum for the in-plane component of the SHG on each outer edges of the line. Finally, when measuring the longitudinal response of the SHG signal ($I_{2\omega\perp}$), two maxima of intensity are measured on each outer edges of the line.

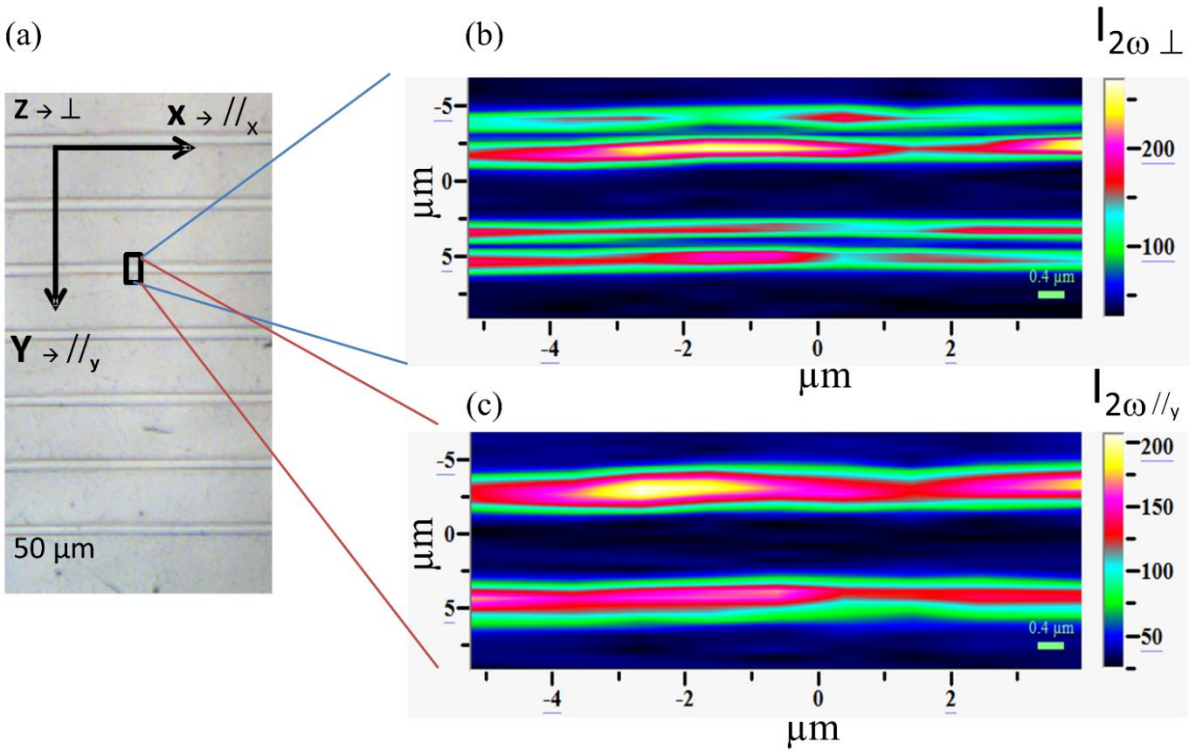

Figure 3.8. Optical micrograph of lines obtained during the imprinting process (a), map showing the SHG intensity distribution of the longitudinal component (b) and in plane component (c)

An intensity profile of the SHG response in the plane and out of the plane is plotted on Figure 3.9. From this plot, it is observed that the SHG signal is confined over 5 µm for both contributions on the two edges. The two contribution ($I_{2\omega\perp}$ and $I_{2\omega\parallel y}$) are also spatially complementary as the maximum of the in-plane contribution is located in the center of the out-of-the-plane dual contribution.

The fact that there is an in-plane contribution while recording SHG in the poled glass is rather unexpected. As stated in the introductory chapter, upon thermal poling a static electric field is induced in the glass matrix along the z-direction. This electric field breaks the glass's centrosymmetry and gives access to SONL properties by interacting with the intrinsic $\chi^{(3)}$ of the

glass. The recorded SHG response is then typical of a $C_{\infty v}$ point group and should only present contribution out-of-the-plane of the glass. In the case presented herein, additional contributions in the plane of the glass are recorded. The structuring of the electrode and the nature of the electrode itself seem to induce side effects leading to local field enhancement across the surface, potentially linked to a non-homogeneous charge density. To validate this hypothesis, it is necessary to test it using simulation tools.

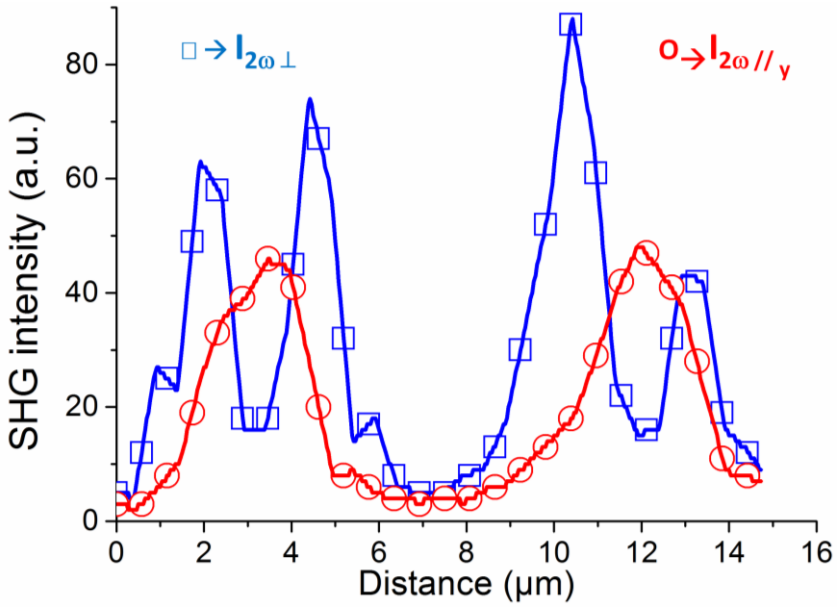

Figure 3.9. SHG profiles measured with two different polarizations across a line

3.3 Development of an electrostatic model to describe the SHG measurements

In a classical thermal poling, the charge repartition inside the glass can be fairly well described. Under blocking anode conditions, it has been estimated that 5 x 10^4 $C.m^{-3}$ were trapped within the first few micrometers underneath the surface. [2] The charge estimate was made considering the value of the induced electric field and the thickness of the sodium depleted layer. The poled sample is only locally charged and positive charges are distributed in the remaining bulk glass, ensuring

global neutrality and satisfying the Gauss law. This positively charged layer is several hundreds of micrometer thick and its charge concentration is at least two order of magnitude lower than that near the electrode. The poled sample can thus be seen as a thin negatively charged layer on top of a weakly positively charged bulk. This representation of a poled sample is shown on Figure 3.10.

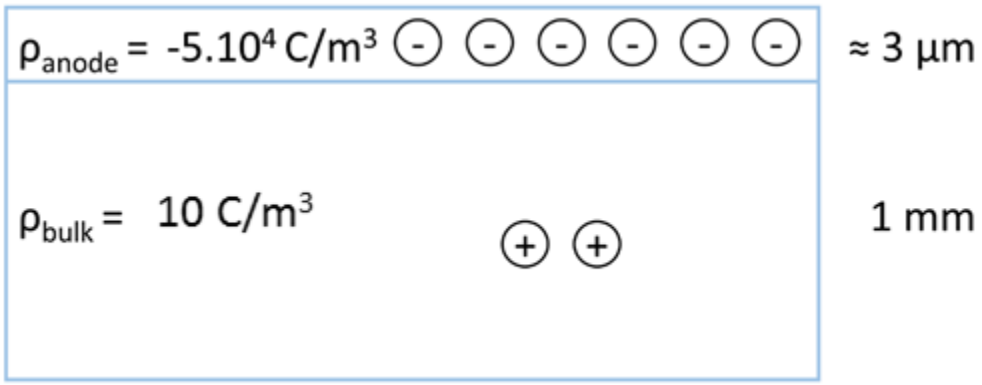

Figure 3.10. Representation of the classical charged sample after poling

We now know that the use of structured electrodes induces a deviation from this model with the apparition of in-plane contributions. In the SHG study shown earlier, it was observed that the SHG intensities along the lines written on the glass were two order of magnitude higher than across the rest of the poled surface. The SHG measures are directly related to the static electric field and thus to the frozen in charges. These measurements can thus serve to estimate the concentration of trapped charges which should therefore be one order of magnitude higher on the lines compared to outside of them. The thickness of the sodium depleted layer, where charges are frozen in, was taken equal to 3 µm. This depth was obtained from previous measurements performed on the same glasses, poled in the same conditions. [2] The charge concentration in this layer was taken to be equal to ρ_{anode} = -2 x 10^3 C.m^{-3}. As stated earlier, it is suspected that structuring the electrode leads to a field enhancement and a change of the charge distribution. To evaluate this effect, trapped

charges on the edges of the lines were considered to be coming from two regions similar in size with a charge concentration one order of magnitude higher than that of the rest of the anode. These two regions were defined with opposite signs, so that $\rho_{side1} = -\rho_{side2} = -2 \times 10^4$ C.m^{-3}. ρ_{side1} corresponds to a structured region, underneath the electrode while ρ_{side2} corresponds to the volume next to ρ_{side1} which is outside the electrode. A simple schematic representation of the model is presented on Figure 3.11.

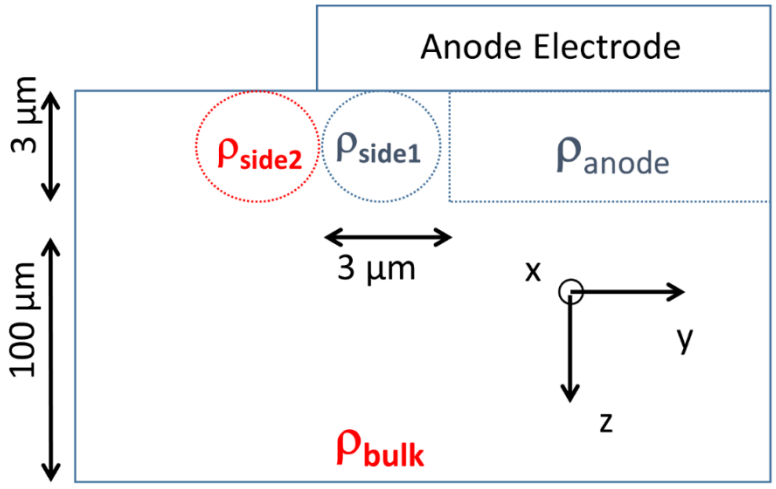

Figure 3.11. Diagram presenting the parameters used in the electrostatic model of a structured electrode

The model was computed using COMSOL Multiphysics and the electric potential as well as both in-plane and out-of-the-plane components of the electric field were extracted from the simulation. The results are presented in Figure 3.12.

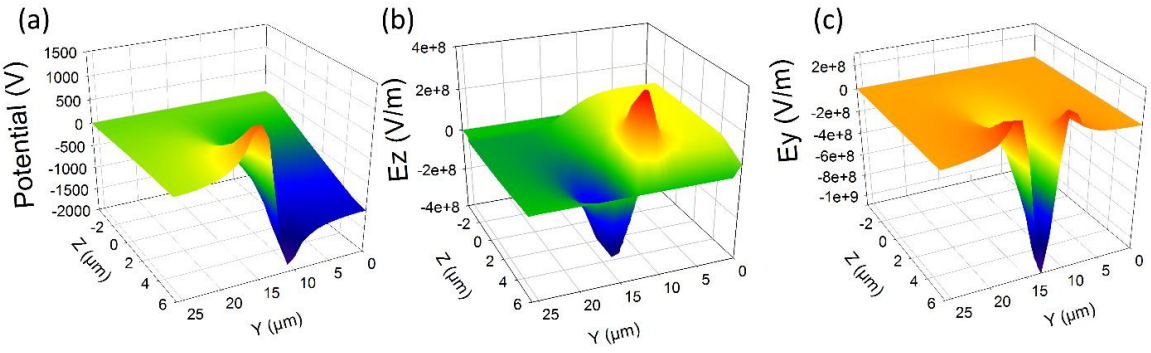

Figure 3.12. Simulated maps of the potential (a), the electric field component along z (b) and the electric field component along y (c)

The potential map obtained from the simulation (Figure 3.12 (a)) shows that there is a sharp change of potential within 10 µm with a positive potential outside the poled area and a negative potential underneath the poled area. Outside the poled area, the potential quickly goes back to zero, while under the poled area, it quickly goes back to lower non-zero negative values (≈ 1000 V). Now looking at the electric field distribution (map (b) and (c)) a similar phenomenon is observed. The longitudinal component of the electric field has two components with opposite directions. Underneath the poled area, the direction goes outside the sample as expected in thermal poling as the static electric field is here to compensate the applied electric field. The in-plane components of the electric field also have two contributions. The main contribution is maximum right at the border of the lines and two small contributions of opposite signs are found outside the border lines. The simulated electric field contributions can be compared to the measured SHG along the line. Both profiles are plotted in the following figure.

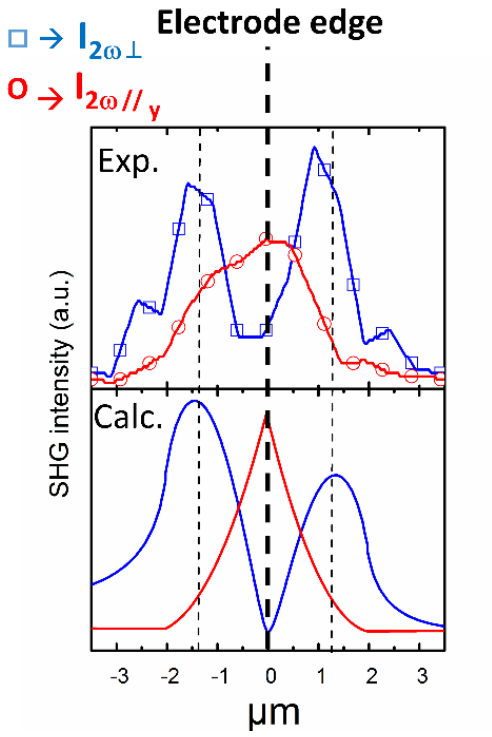

Figure 3.13. Experimental SHG profile (top) and calculated from the electrostatic model

A really good correlation is obtained which tends to prove the veracity of this model. Using structured electrode, the repartition of charges frozen inside the glass varies and more charges accumulate near the edges of the patterns following a side effect promoting a field enhancement. The in-plane contributions are no-longer negligible and play an important role in the structuring of the SHG response.

The simulation done so far focused on the charge repartition after thermal poling to explain the results obtained in µ-SHG measurements. However, it does not study the influence of the electrode structuring and of the electrode nature on the applied electric field during thermal poling. To study these two parameters, additional simulations were performed to visualize the electric field lines during poling using (i) a structured ITO thin film electrode or (ii) a structured metal electrode. The

first case then corresponds to an alternation of conductive and non-conductive areas while the second corresponds to topology variation of a conductive material.

Both electrodes were structured with similar patterns and the glass poled with the same conditions. The only difference resides in the nature of the electrode. The metal electrode was chosen to be made of copper (other metals lead to the same results) while the ITO electrode was defined as a glass slide with a conductive coating on its outer sides which was locally ablated. The results presented after correspond to what would be observed at t=0s during thermal poling. The electric potential at the surface of the glass was first studied and is shown for both configurations on Figure 3.14.

In the case of a metallic electrode (Figure 3.14 (a)), the structuring induces variation in intensity of the potential applied at the surface of the glass. However, when using a structured ITO electrode with the same designs, (Figure 3.14 (b)), the intensity variation of the potential at the surface is higher than with the metallic electrode. In the introductory chapter, it was shown that work by Quiquempois et al. [16] demonstrated the existence of a potential threshold for thermal poling to take place. It can thus directly be understood that a higher potential gradient at the surface of the glass induces large difference in cationic migration inside the glass. Thermal poling will be structured in both cases, but it is expected that differences on the surface with the ITO electrode will be more drastic.

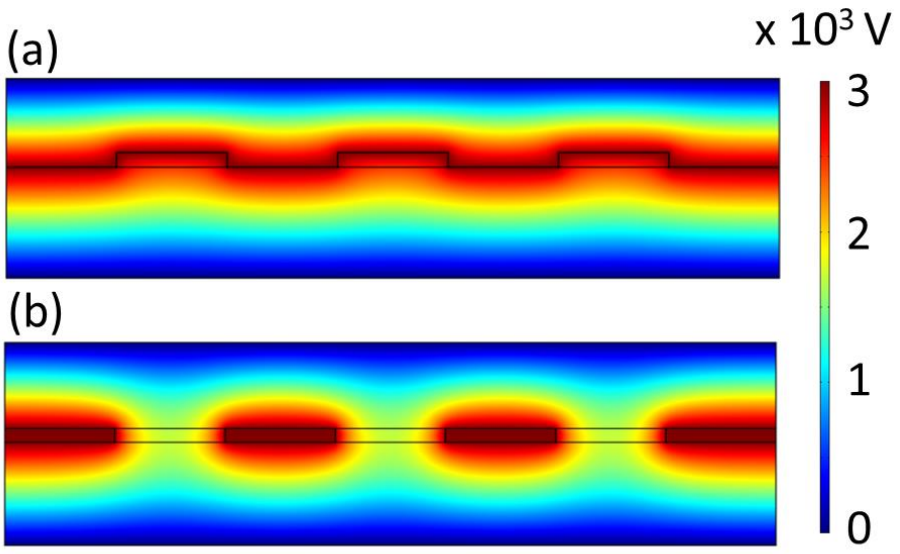

Figure 3.14. Electrostatic simulation of the potential distribution at t=0s when using a structured metallic electrode (a) and a structured ITO electrode (b)

If the electric field lines are plotted with both configurations, additional information can be obtained from the simulation. Figure 3.15 shows the distribution of the electric field lines in both configurations.

In the case of the structured metallic electrode (Figure 3.15 (a)), the electric field lines are directed towards the cathode only a longitudinal direction. There is no component of the electric field in the plane of the glass surface. However, in the case of the structured ITO electrode (Figure 3.15 (b)), the distribution of the electric field lines is different. In addition to the longitudinal components, a strong component in the plane of the glass appears. Not only the glass is poled along the z-direction but also along the x-y plane.

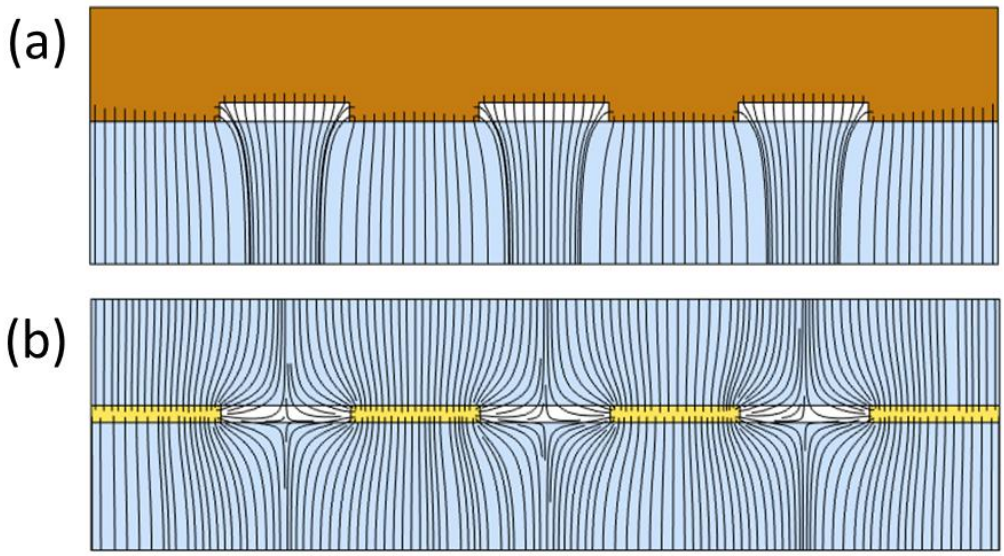

Figure 3.15. Electrostatic modeling presenting the electric field lines for a structured metallic electrode (a) and a structured ITO electrode (b)

The use of the ITO electrode is at the origin of the local field enhancement and side effects observed in the experimental measurements of the SHG by promoting both migration in and out of the plane of the glass's surface. The side effects are not taken into account in this last simulation. The extra-migration along the x-y plane can explain the new distribution of charges which will also accumulate along the structured patterns thus giving the extra contribution which is observed on the μ-SHG patterns. With this the two simulations presented here, we have the distribution of the electric field and surface potential at the beginning of the process (second model, t=0) and the end of the process (first model, t=∞).

These two models give satisfying explanation for the results obtained experimentally. To further confirmed the veracity of the first model presented before and to demonstrate the potential of this imprinting technique, a large periodical array of lines was imprinted on a glass surface to design

its SONL properties. A 4 mm^2 array of 2 mm lines was written on an electrode with a pitch of 3 µm in-between 3 µm thick lines. Figure 3.16 (a) shows part of the array imprinted on the glass surface with a high fidelity transfer. The corresponding µ-SHG map is presented on part (b) of the same figure.

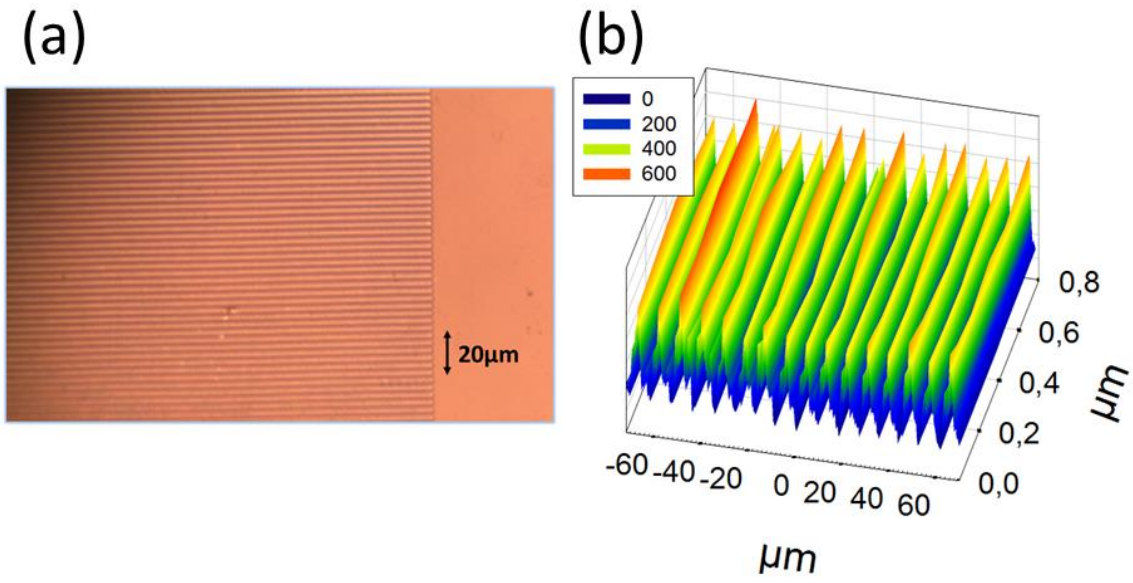

Figure 3.16. Optical micrograph of part of the gratings imprinted on the glass (a), corresponding µ-SHG map recorded on the grating (b)

The optical micrograph shows a good transfer on the glass surface with a good periodicity and homogeneity of the lines. On the µ-SHG map, it is observed that the intensity contrast between the lines and the rest of the glass is greater by two order of magnitude, similarly to what was obtained previously. The array of SHG active lines also present a high periodicity and good homogeneity. To evaluate the effectiveness of this poled glass as potential diffraction gratings, SHG diffraction measurements were performed. The Maker fringes presented in the experimental techniques chapter was used for this purpose. The incident polarization was linearly polarized perpendicularly

to the imprinted lines. The sample was fixed and the diffraction pattern was measured by scanning the 2ω response at across a range of detection angles. The diffraction pattern presented in part (a) of Figure 3.17 was obtained. It presents four distinct diffraction peaks and an extinction at the 0-order line. The quality of the recorded diffraction pattern proves the good long range homogeneity of the imprinted structure.

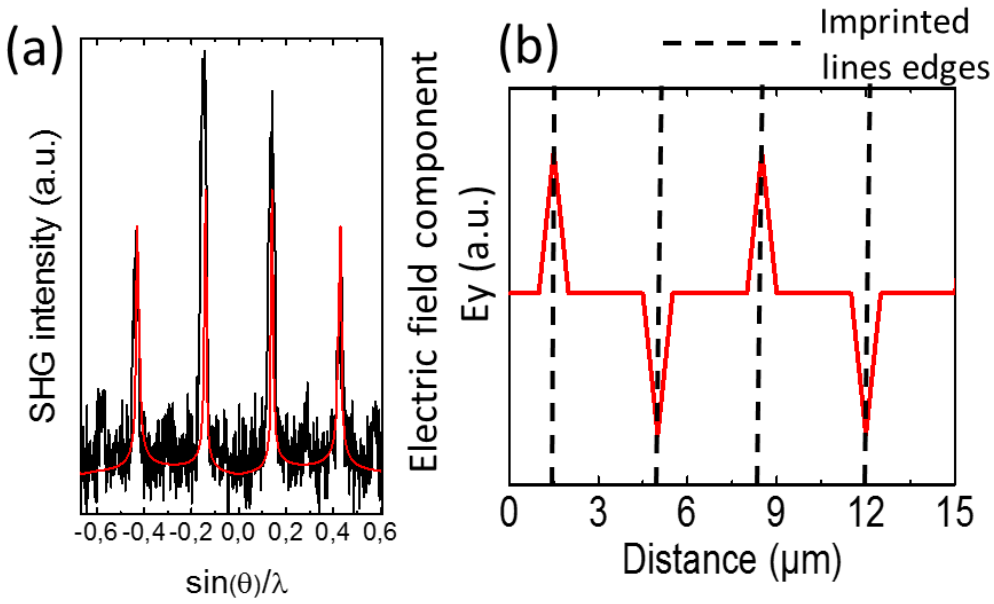

Figure 3.17. SHG diffraction pattern recorded in transmission with an incident linear polarization along the y axis and a rotation around the y-axis in the x-axis (black) and corresponding calculated diffraction pattern (red) (a) using the periodic model of the in-plane component of the induced electric field (b)

In addition, it is possible to use the first electrostatic model presented before, with a local increase of the charges near the lines, to fit the obtained SHG diffraction pattern. As stated earlier, when linearly polarized perpendicular to the lines, the in-plane components of the poled sample are probed and can be found on each edges of the lines. According to our model, for each line, both edges have opposite directions for the electric field in-plane components. The electric field components distribution expected across the structure is represented on part (b) of Figure 3.17 .

After Fourier transform of this structure, a diffraction pattern is then obtained which is then compared to our experimental data (red pattern on Figure 3.17 (a)). The good correlation between the recorded diffraction pattern and the one obtained from our model tends to confirm the truthfulness of our simple model and the high potential of this imprinting process.

3.4 Conclusion and future work

In this chapter, we were able to show that once the mechanisms of thermal poling for a classical thermal poling are understood, it is possible to move on to more applications-oriented studies. This chapter presented a novel approach to thermal poling with the use of structured electrodes. Structured electrodes were previously used to structure a glass response to thermal poling but in the case presented here, it was shown that a good selection of the electrode material could change the response of the glass. We discussed a new configuration to thermal poling which consists in using an electrode made of a dielectric, coated with a conductive layer (ITO). After local laser ablation of the conductive coating, in plane components of the applied electric field are appearing which promote sodium motion both in and out of the plane of the glass's surface. The use of this electrode leads to sides effects, with more charges being trapped in the vicinity of the imprinted patterns, thus giving a local field enhancement. This result is of the utmost importance, not only is it possible to pattern large areas using this technique but above all, it allows to induce sodium cations displacement in two directions. So far, we have seen that thermal poling could induce changes of structure, refractive index, surface reactivity, surface mechanical properties and other properties. All of these properties change can be linked to the sodium departure and the trapping of charges inside the glass matrix. If one is able to control where and over which distance the

sodium departure and charge trapping occur, then it should be possible to precisely control of the properties listed before.

In the following chapters, all of our studies will be done with one common goal, to try to control one of these properties at a small scale. To show that it is possible, we have selected two glass families of interest: a borosilicate glass and chalcogenide glasses. Borosilicate glasses were chosen for their relative low cost and abundance in the glass industry. A specific composition was picked with the goal in mind to spatially control its surface reactivity towards atmospheric water. Chalcogenide glasses on the other hand are glasses which belong to a smaller market but with a higher retail price. They are used for their good optical properties in the mid-IR and it was therefore decided to try to tailor their optical properties (both linear and non-linear).

3.5 References

(1) Dussauze, M.; Fargin, E.; Lahaye, M.; Rodriguez, V.; Adamietz, F. Large Second-Harmonic Generation of Thermally Poled Sodium Borophosphate Glasses. *Optics Express* **2005**, *13*, 4064-4069.

(2) Dussauze, M.; Kamitsos, E. I.; Fargin, E.; Rodriguez, V. Structural Rearrangements and Second-Order Optical Response in the Space Charge Layer of Thermally Poled Sodium-Niobium Borophosphate Glasses. *Journal of Physical Chemistry C* **2007**, *111*, 14560-14566.

(3) Dussauze, M.; Bidault, O.; Fargin, E.; Maglione, M.; Rodriguez, V. Dielectric Relaxation Induced by a Space Charge in Poled Glasses for Nonlinear Optics. *Journal of Applied Physics* **2006**, *100*.

(4) Dussauze, M.; Fargin, E.; Malakho, A.; Rodriguez, V.; Buffeteau, T.; Adamietz, F. Correlation of Large SHG Responses with Structural Characterization in Borophosphate Niobium Glasses. *Optical Materials* **2006**, *28*, 1417-1422.

(5) Dussauze, M.; Fargin, E.; Rodriguez, V.; Malakho, A.; Kamitsos, E. Enhanced Raman Scattering in Thermally Poled Sodium-Niobium Borophosphate Glasses. *J. Appl. Phys.* **2007**, *101*.

(6) Lipovskii, A. A.; Tagantsev, D. K.; Vetrov, A. A.; Yanush, O. V. Raman Spectroscopy and the Origin of Electrooptical Kerr Phenomenon in Niobium Alkali-Silicate Glasses. *Optical Materials* **2003**, *21*, 749-757.

(7) Efimov, A. M. IR Fundamental Spectra and Structure of Pyrophosphate Glasses Along the 2ZnO · P2O5-2Me2O · P2O5 Join (Me being Na and Li). *J. Non Cryst. Solids* **1997**, *209*, 209-226.

(8) Ducel, J. F.; Videau, J. J.; Couzi, M. Structural Study of Borophosphate Glasses by Raman and Infrared Spectroscopy. *Physics and Chemistry of Glasses* **1993**, *34*, 212-218.

(9) Brunkov, P. N.; Melekhin, V. G.; Goncharov, V. V.; Lipovskii, A. A.; Petrov, M. I. Submicron-Resolved Relief Formation in Poled Glasses and Glass-Metal Nanocomposites. *Technical Physics Letters* **2008**, *34*, 1030-1033.

(10) Takagi, H.; Miyazawa, S. -.; Takahashi, M.; Maeda, R. Electrostatic Imprint Process for Glass. *Applied Physics Express* **2008**, *1*.

(11) Yang, G.; Dussauze, M.; Rodriguez, V.; Adamietz, F.; Marquestaut, N.; Deepak, K. L. N.; Grojo, D.; Uteza, O.; Delaporte, P.; Cardinal, T.; Fargin, E. Large Scale Micro-Structured Optical Second Harmonic Generation Response Imprinted on Glass Surface by Thermal Poling. *J. Appl. Phys.* **2015**, *118*.

(12) Redkov, A. V.; Melehin, V. G.; Lipovskii, A. A. How does Thermal Poling Produce Interstitial Molecular Oxygen in Silicate Glasses? *J. Phys. Chem. C* **2015**, *119*, 17298-17307.

(13) Cremoux, T.; Dussauze, M.; Fargin, E.; Cardinal, T.; Talaga, D.; Adamietz, F.; Rodriguez, V. Trapped Molecular and Ionic Species in Poled Borosilicate Glasses: Toward a Rationalized Description of Thermal Poling in Glasses. *Journal of Physical Chemistry C* **2014**, *118*, 3716-3723.

(14) Guimbretìre, G.; Dussauze, M.; Rodriguez, V.; Kamitsos, E. I. Correlation between Second-Order Optical Response and Structure in Thermally Poled Sodium Niobium-Germanate Glass. *Appl. Phys. Lett.* **2010**, *97*.

(15) Carlson, D. E.; Hang, K. W.; Stockdale, G. F. Electrode "Polarization" in Alkali-Containing Glasses. *Journal of the American Ceramic Society* **1972**, *55*, 337-341.

(16) Quiquempois, Y.; Godbout, N.; Lacroix, S. Model of Charge Migration during Thermal Poling in Silica Glasses: Evidence of a Voltage Threshold for the Onset of a Second-Order Nonlinearity. *Physical Review A. Atomic, Molecular, and Optical Physics* **2002**, *65*, 438161-4381614.

CHAPTER 4: TUNING THE SURFACE REACTIVITY OF A BOROSILICATE GLASS VIA THERMAL POLING

The control of surface properties is a key element to create “smart substrate” used in domains such as biotechnology or lab-on-a-chip. The surface properties define the ultimate function of a surface. Ideally a substrate with tunable surface reactivity at a micrometer scale should be developed to meet the users need. Tunable chemical reactivity associated with detection techniques accessing surface information would be especially useful for a wide range of applications. Optical glasses are ideal candidates for these type of applications as they are easy to manufacture and the surface information is easy to probe via optical methods. One can then imagine to create a substrate with confined enhanced surface reactivity associated with an optical circuit to create an analyzing tool. To achieve this, new tools need to be elaborated to tailor surface reactivity of glasses.

In this chapter, thermal poling and its possible use as a surface reactivity tailoring tool will be presented. As stated earlier thermal poling has already been proved useful to enhance surface reactivity in bioactive glasses. In the present study we focus on trying to locally enhance the glass’ reactivity towards atmospheric water by carefully choosing the glass composition and poling conditions.

The chapter is separated in four sections. The first explains the choice of the glass composition, poling conditions and characterization of the glass prior poling. The second section presents the thermal poling of the borosilicate glass as well as the post-poling characterization performed in controlled atmosphere. The third shows the change of surface reactivity of the glass placed in the laboratory atmosphere. Lastly, two possibilities of micro-poling technique are described which have been developed to control all processes at the micrometric scale.

4.1 Study of the glass before poling

4.1.1 Choice of the glass composition

Oxide glasses have been the main materials used in thermal poling. The mechanisms and property changes occurring are now better described. In addition to the nonlinear optical properties induced in the post-poled glasses, studies in the bioglasses community have shown that these glasses are good candidates for thermal poling, thanks to their high alkali content. [1] Bioactive glasses are typically glasses containing SiO_2, CaO, Na_2O and P_2O_5 and were first developed in the late 1960s by Hench. [2] After thermal poling, the presence of a strong induced electric field inside the glass has been suggested to enhance the reactivity of the glass, making it more prone to hydroxyapatite formation. [3-7] However, surface reactivity control has not yet been widely studied and efforts are still necessary to find a good composition giving a glass with suitable properties for concrete applications. In this work, the chosen glass composition is a borosilicate glass which composition, B_2O_3 (51 mol%), SiO_2 (39 mol%), Na_2O (10 mol%), lies in the region of the boron oxide anomaly, defined for a ratio $R=Na_2O/B_2O_3 < 0.2$. [8] This point is termed as an anomaly as the glass properties exhibit a local extremum and property trends revert directions, for instance a maximum in T_g. This particular behavior was linked to structural changes involving the borate network. To better grasp the impact of sodium on the boron network, it is easier to start with a pure borate glass (B_2O_3). In this glass, the network is formed of $B\emptyset_3$ triangular units connected to each other, forming boroxol rings ($\emptyset$ denotes a bridging oxygen). Now, if sodium is added to the glass, the coordination number of boron changes from 3 to 4 following the formation of $B\emptyset_4^-$ tetrahedra with a neighboring compensating sodium cation. The structure is strengthened as the interconnectivity of the network

is higher. If the sodium content increases and the ratio of sodium to boron is higher than 0.2, the network weaken through the formation of borate triangle with non-bridging oxygens. The evolution of the glass network with alkali content is summarized in Figure 4..

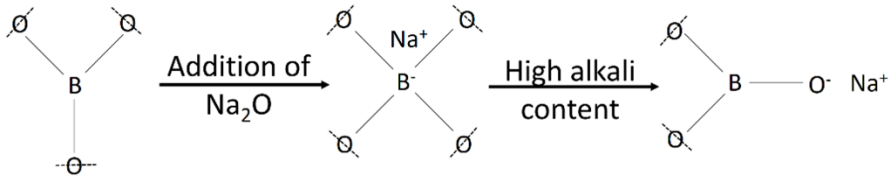

Figure 4.1. Evolution of the structure of the borate network with alkali content (here the example of sodium)

In a borosilicate glass, the same ratio is defined and below the 0.2 value, all sodium added to the glass goes with the boron network to convert $B\emptyset_3$ triangular units to $B\emptyset_4^-$ tetrahedra without formation of non-bridging oxygens and leaving the silica network fully reticulated.

This composition is especially interesting for thermal poling as this process implies migration of cations under the electric field. Sodium is the cation more prone to migrate under the electric field, due to its high mobility. It is thus expected that under the effect of the electric field, sodium cations neighboring boron tetrahedra migrate towards the cathode. The unbalanced structured would then be forced to rearrange to compensate the departure of sodium cations. The formation of $B\emptyset_3$ triangular units would be a way for the glass to accommodate sodium departure. Thus it should be possible to control the structure of the glass by using thermal poling. In addition, $B\emptyset_3$units and boroxol rings have the particularity to be extremely reactive in air. A glass made of areas of boroxol rings should see its affinity towards atmospheric water enhanced.

4.1.2 Characterization of the glass prior poling

Before poling the sample, it is essential to have a good description of the glass' structure to understand the changes taking place upon poling.

The glass' structure was investigated using vibrational spectroscopy: infrared and Raman. The infrared spectrum of the base glass was recorded under vacuum in reflectance mode. The spectrum is plotted in Figure 4.2.

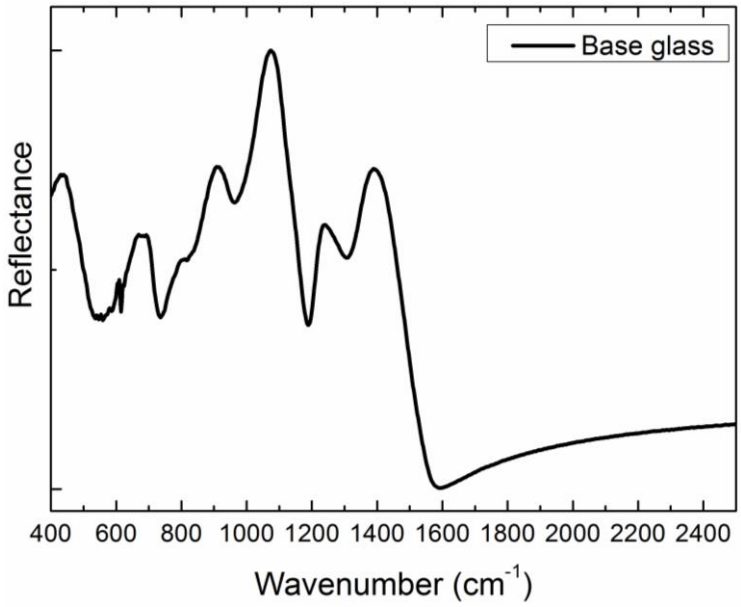

Figure 4.2. IR reflectance spectrum of the base glass recorded under vacuum

The glass network being composed of silica and borate and the glass being on the boron oxide anomaly, it should be mainly made of $Si\emptyset_4$ tetrahedra, $B\emptyset_4^-$ tetrahedra with a neighboring sodium cation and some $B\emptyset_3$ triangular units. The band peaking at 1075 cm^{-1} is associated to the asymmetric stretching vibrations of fully linked silicon-oxygen tetrahedra, Q_4. [9-11] A contribution at 1050 cm^{-1} is attributed to the asymmetric stretching vibrational modes of B_4-O-Si, where B_4 denotes a boron tetrahedra without non-bridging oxygen. Between 1250 and 1500 cm^{-1} two bands

are observed and associated with the $B\emptyset_3$ structural units present in various rings and non-rings configurations. [12] At 910 cm^{-1}, a band associated to the asymmetric stretching vibration mode of $B\emptyset_4^-$ tetrahedra can be observed. [12-14] Finally, below 900 cm^{-1}, numerous contributions are observed and are associated with highly coupled deformation modes, originating from the various constituent of the glass matrix such as B-O-B, Si-O-Si or mixed B-O-Si.

The Raman spectrum of the base glass is shown in the Figure 4.3.

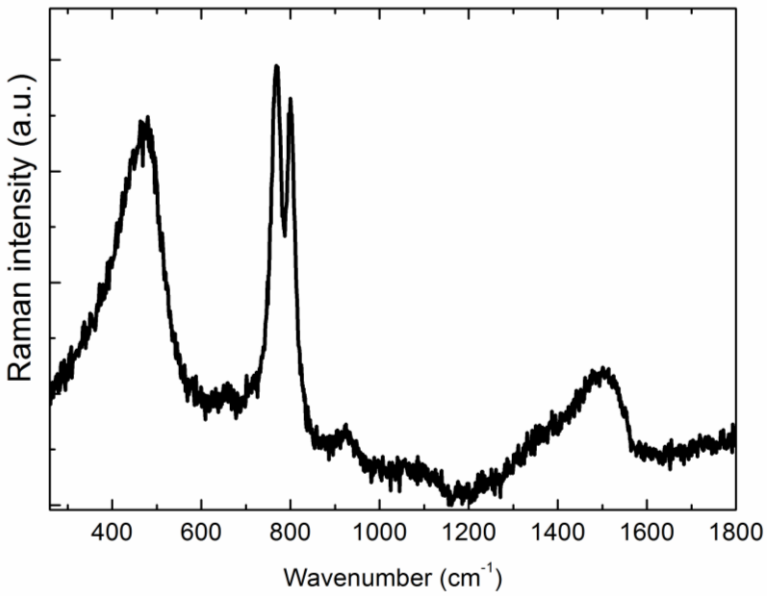

Figure 4.3. Raman spectrum of the base glass

Two main bands at 770 and 805 cm^{-1} can be respectively attributed to a triborate group with one $B\emptyset_4^-$ and to $B\emptyset_3$ boroxol rings. [15-17] The large contribution around 450 cm^{-1} is attributed to mixed stretching and bending vibrations from the silicate network [18] while the band around 1500 cm^{-1} originates from asymmetric stretching vibration of $B\emptyset_3$units.

With insight on the structure from Raman and IR spectroscopy, the general structure of the glass can be described. Sodium borosilicate glass in the boric oxide anomaly tends to phase separate and to be formed of a silica-rich phase and a borate-rich phase. [8] The second phase can hence be seen as close to a pure binary sodium-borate glass. The infrared spectrum showed previously tells us that the silicate network is fully reticulated as only the contribution from the Q_4 groups is seen. Additionally, no contribution from Q_3 species are observed in the Raman spectrum, in which case the stretching vibration of $Si\text{-}O^-$ bonds would peak at 1100 cm^{-1}. All the sodium added to the glass is hence going with the borate network to form 4-coordinated tetrahedra. From the composition of the glass itself, it can be deduced that one sodium is available for five boron, potentially forming one 4-coordinated boron and four additional 3-coordinated boron. Such a ratio corresponds to the pentaborate structure which is formed of two boroxol rings interconnected by a boron tetrahedron. A pentaborate structure is composed of two boroxol rings linked together by a 4-coordinated boron tetrahedra, as presented in Figure 4.4. By comparing the IR spectrum of the base glass with IR spectra of binary lithium-borate glasses close to the pentaborate composition, similarities can be highlighted. In the study from Kamitsos et al. [14] and in this one, the large band of the $B\emptyset_3$ has two contributions around 1250 and 1390 cm^{-1}, similarly the $B\emptyset_4^-$ has two contributions in IR, one around 940 cm^{-1} and one around 1080 cm^{-1}. The vibrational spectroscopy study of this borosilicate glass shows similar band ratio and positions as a binary alkali-borate glass close to a pentaborate structure. The boron network in this glass can hence be described as a pentaborate-like structure.

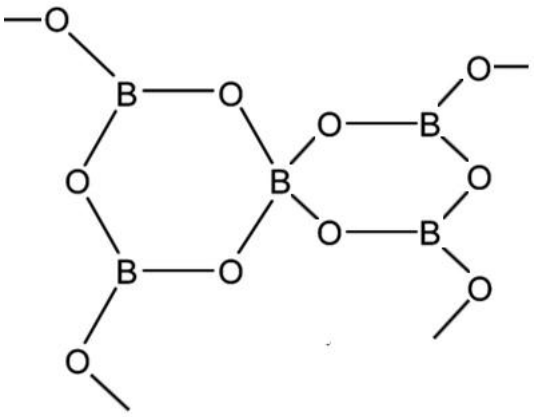

Figure 4.4. Schematic representation of a pentaborate group

The Raman spectrum confirm that sodium added to the glass matrix is neighboring boron atoms to form four-coordinated $B\emptyset_4^-$ tetrahedra giving the band at 770 cm^{-1}. The presence of both $B\emptyset_4^-$and $B\emptyset_3$ groups is observed by the two band at 770 and 806 cm^{-1}. [17] In addition, the ratio of these two bands is directly correlated to the amount of alkali acting as charge compensators in the vicinity of $B\emptyset_4^-$ tetrahedra. Raman spectra of sodium borosilicate found in the literature present similar band intensities. [12, 13, 16]

4.1.3 Surface reactivity and structure variation of the glass prior poling

As surface reactivity is a property we wish to control using thermal poling, the original surface reactivity of the glass prior poling needs to be evaluated. A blank sample was prepared and sit in air for more than a year. No significant attraction from the atmospheric water was observed. However, IR spectrum showed an evolution of the boron network organization over time.

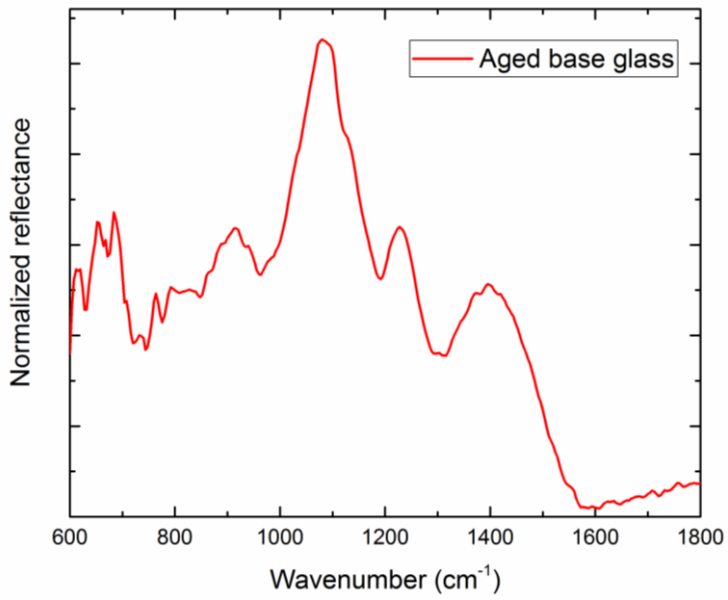

Figure 4.5. IR reflectance spectrum of an aged sample (1 year in air)

The two contributions from the $B\emptyset_3$ triangular units in the IR spectrum change in intensity, indicating a change in the distribution of the $B\emptyset_3$ triangular units in rings and non-rings configuration in the near surface. The change is small considering the time scale over which it takes place. It was however decided to store the glass samples in a desiccator to prevent the glass reaction. It is important to note that the change that we wish to prompt through thermal poling should take place on a smaller time scale and be more drastic.

4.1.4 Second Harmonic Generation in the base glass

The poled glass is expected to exhibit SONL properties such as SHG following thermal poling. The SHG of the base glass was evaluated using the Maker fringes technique and no signal at 2ω was measured. This was expected as glasses do not exhibit 2nd order nonlinear optical properties due to their centrosymmetry.

4.1.5 Justification of the poling conditions

As described in the literature review, upon poling, many charges migrate inside the glass matrix. A good understanding of the poling conditions and their effect on the final glass is essential to achieve a control change of structure and properties. Two types of poling conditions can be used, blocking anode and non-blocking anode. When performing poling under non-blocking anode conditions, the electrodes are able to inject charges inside the glass. For instance, if performing the poling under air with silicon electrodes, hydroxyl species and proton can be injected inside the glass matrix from the anode side. The injection of these species can counterpart the re-arrangement that we look for. It is thus necessary to perform thermal poling in blocking electrode conditions. The procedure is thus done in a cell with controlled atmosphere filled with nitrogen. This minimizes the amount of hydroxyl species available and susceptible to be injected in the glass. Charge compensation and re-arrangement is still expected following sodium departure but should only take place through modifications originating from the glass network.

4.1.6 Conclusion of section 4.1

Once the structure of the glass and its initial surface properties are described, the glass can be thermally poled. As stated earlier, thermal poling should induce new nonlinear optical properties, potential structural changes, cations migration and reactivity changes. Following thermal poling, changes of these properties are the main interest of our study.

4.2 Thermal poling of a borosilicate glass

4.2.1 Thermal poling of the borosilicate glass

During thermal poling, the glass sample is placed in a cell filled with nitrogen. The sample is then heated at 300°C, well below the glass transition temperature. The sample sits in the chamber for 10 minutes so that a homogeneous temperature is reached across the sample.

A voltage of 3000 V is then applied across the sample. The poling is performed for 30 minutes after which the sample is brought back to room temperature and only then is the DC bias removed.

During the poling procedure, the current is constantly measured as a function of time. An example of a current curve vs time and the voltage ramp vs time are represented in Figure 4.6.

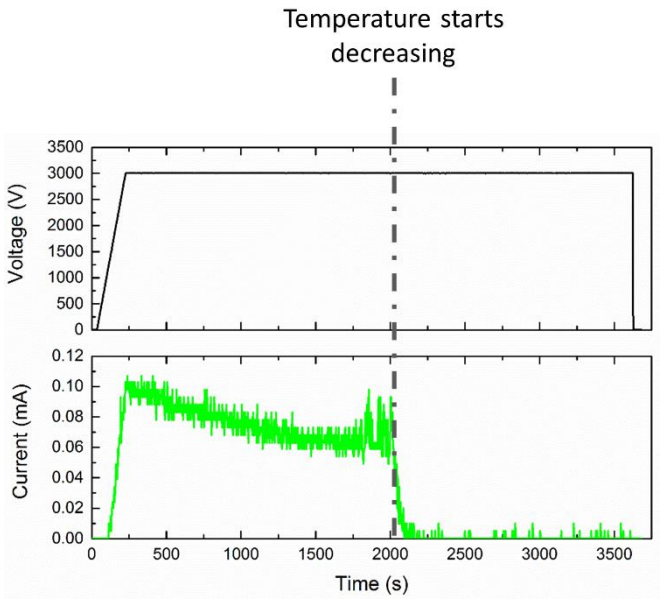

Figure 4.6. Example of recorded voltage and current curves during thermal poling

The voltage bias across the sample is applied gradually and the current flow only starts once a threshold is reached. Once the maximum voltage is reached the current starts decaying progressively until a sudden drop. This current drop is concomitant to the stop of the furnace. The current measured across the sample then quickly reaches 0. The DC bias is maintained across the sample and is only turned off once room temperature is reached to prevent charge mobility in the glass network. The charges that moved during poling are then frozen in the glass matrix and the sample is said to be polarized. The current curve presented above is typical of a successful thermal poling procedure.

4.2.2 Evaluation of the post-poling properties of the glass in controlled atmosphere

4.2.2.1 Structural changes in the poled area

To perform measurements on the post poled sample, the poling chamber was placed under vacuum once the poling procedure finished. The valves were then closed to ensure that the sample was kept under vacuum. The entire poling cell was placed in a glove bag. The glove bag was vacuumed and then filled with nitrogen. Once filled with nitrogen, the poling cell was opened to remove the electrodes pressed on the samples. The sample could then be studied without being in contact with air.

During thermal poling a space charge can be created following cation migrations. As stated earlier, depending on the poling conditions, open or blocking anode, the charge compensation is going to take place through different paths. Under open anode conditions, the cation departure is going to be compensated through the injection of protons and hydroxyl species from the atmosphere and by reticulation of the network. [19-21] Samples discussed here were poled under nitrogen to meet blocking anode conditions and to prevent any injection from the surrounding atmosphere in the

glass matrix. Vibrational spectroscopy allows to verify that blocking anode conditions were met by monitoring water injection. It also allows to study the potential structural changes taking place in the glass network to compensate for the sodium departure.

Infrared spectroscopy in reflection mode is especially suitable to probe the first microns underneath the surface of the sample. The sample was placed in the spectrometer which was linked to the glove bag and also filled with nitrogen. Once the sample inside the chamber, the spectrometer was placed under vacuum.

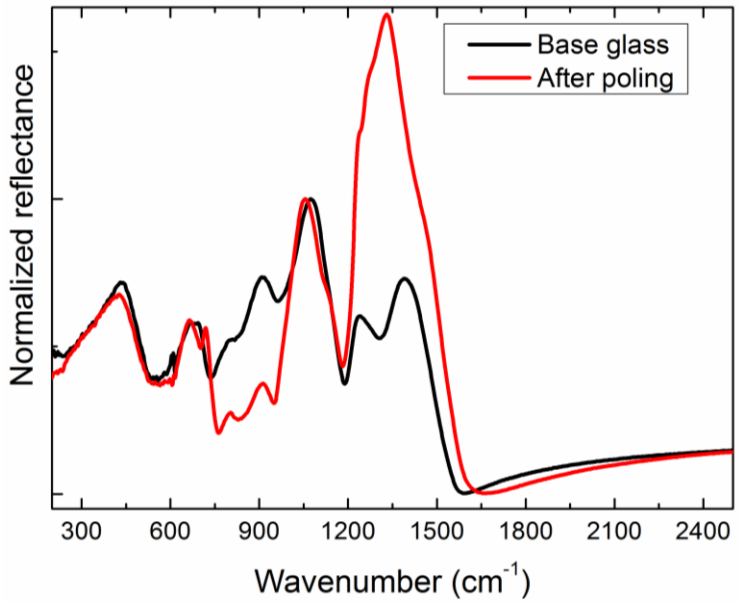

Figure 4.7. IR reflectance spectra of the glass sample before poling (black) and after poling (red) recorded under vacuum. Both spectra are normalized to the vibrational mode of the Q_4 groups of silica at 1075 cm^{-1}

Figure 4.7 shows both spectra of the base glass and of the polarized sample in the first minutes following poling. For comparison purpose, both spectra were normalized to the band peaking at 1075 cm^{-1} which remains unchanged. The silica network is not impacted by the treatment and still made of Q_4 tetrahedra. The absence of water band above 3000 cm^{-1} (not shown here) indicates that

no injection took place during the treatment and that the poling was performed in blocking anode conditions. Now looking at potential structural changes, several changes should be highlighted on the spectrum of the poled glass, especially in the region of the borate network. The contribution of the $B\emptyset_3$ triangular units between 1250 and 1500 cm^{-1} goes from a double band to a large single band of higher intensity. The contribution around 910 cm^{-1} arising from the $B\emptyset_4^-$ tetrahedra diminishes in intensity. The evolution of the two bands related to the boron network gives insight on the cationic migration occurring during thermal poling, in the present case, mainly related to sodium. The base glass being made of pentaborate units, following sodium departure, $B\emptyset_4^-$ tetrahedra bear a charge no longer compensated. The borate network hence needs to re-arrange to form neutral entities, i.e. $B\emptyset_3$triangular units. The changes in the borate network observed in infrared spectroscopy is consistent with that hypothesis. Following sodium migration, the $B\emptyset_4^-$ tetrahedra re-arrange to form $B\emptyset_3$ triangular units, therefore leading to an increase of the $B\emptyset_3$ band. It is worth pointing out that the $B\emptyset_3$ signature goes from a double-band to a single-band. The reflectance spectrum of the poled glass exhibit strong similarities with the one of pure B_2O_3 glass. Such a glass is entirely made of $B\emptyset_3$ groups in boroxol rings and independent triangles. The reflectance spectra of B_2O_3 therefore does not present contributions between 800 and 1200 cm^{-1} and present a large band between 1200 and 1600 cm^{-1}.[14] The polarized glass therefore deviates from pentaborate groups and form a B_2O_3-like structure. The mechanism taking place was already proposed by Möncke et al. [13] and can be written as:

$$NaB\emptyset_4 \rightarrow Na^+ + B\emptyset_3 + {}^1/_2\, O^{2-} \qquad (4.1)$$

Following sodium departure, and the conversion of $B\emptyset_4^-$ tetrahedra to $B\emptyset_3$triangular units, two extra-oxygen could recombine to form molecular O_2 inside the glass matrix. The evidence of molecular oxygen inside the glass matrix was not observed in Raman spectroscopy and it is difficult to conclude on the intermediate reaction and on the nature of the oxygen species during this process but two hypotheses can be expressed: (i) the creation of oxygen anions or (ii) the creation of peroxide radicals. The nature of the negative charges is still unclear. Oxygen seems to play an essential role and the structural changes observed in this infrared study proves the importance of negative charges but their nature, i.e. electronic and/or anionic, is yet to be determined. [1, 19-25] The formation of oxygen anions was already considered by Carlson in 1972. [19] He proposed that they could form and migrate towards the anode where they would be neutralized. More recent studies have mentioned the formation of molecular oxygen through oxidation of oxygen anions, but the conductivity was not taken place through anionic conduction but through the released electrons during the oxidation. [26-29] The last possibility is the breakage of a $B-O-Si$ or a B-O-B bond followed by the release of one electron and the formation of peroxide radicals. Two of these peroxide entities would then react to form molecular oxygen, the released oxygen atoms then recombine to form molecular oxygen O_2. This is the process developed by Redkov et al. in 2015. [25] In this last case the process is purely electronic and no oxygen anions are formed. In our case, we do not rule out any of these possibilities but conclusions cannot easily be drawn and the question remains open.

4.2.2.2 Induced 2nd order nonlinear properties

An effective thermal poling induces a strong static electric field inside the sample after the drift of the cations and the freezing of this state. This static electric field breaks the centrosymmetry of the

glass, giving rise to second order nonlinear properties such as second harmonic generation. Second Harmonic Generation (SHG) microscopy is used to probe the electric field induced in the glass.

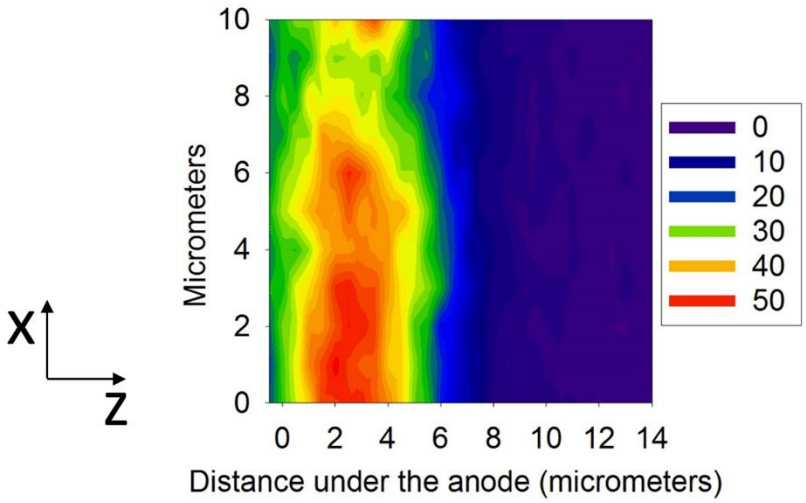

Figure 4.8. SHG map recorded on a poled sample, from the surface (x=0) going inside the sample

A map, showing the SHG profile from the top of the surface to the inside of the sample is shown on the Figure 4.8. The intensity of the SHG signal is expressed in arbitrary units but corresponds to the integrated area under the SHG peak at 532 nm. This map shows that the signal is buried under the anode within the first 4 micrometers. This result is in good agreement with results reported in the literature for poling performed in similar conditions. [30] It also indirectly confirms that blocking anode conditions were met as open anode conditions lead to a thicker SHG active layer. [30] The sample was kept under vacuum for two days to evaluate the stability of the newly induced 2nd order nonlinear property. Maps recorded over this period of time did not show significant variation, proving the stability of the new properties in these storage conditions.

4.2.3 Conclusions of section 4.2

The infrared and SHG studies shows the structural changes upon poling as well as the new nonlinear optical properties. More specifically, the infrared spectrum indirectly shows sodium departure from the near surface region. Following poling the glass structure went from a network close to a pentaborate structure interconnected with SiO_4 tetrahedra to a pure B_2O_3 network interconnected with SiO_4 tetrahedra. The resulting new borate structure is also associated with a strong static electric field, breaking the centrosymmetry of the glass. The poled area can be thus described as made of a new charged borate structure.

4.3 Evolution of the poled glass properties in the laboratory atmosphere

4.3.1 Evidence of enhance surface reactivity

Once the structural changes and the SHG efficiency of the glass is asserted, the glass' behavior inside the laboratory atmosphere can be studied.

The nitrogen filled cell was open and the glass piece was placed under an optical microscope to record a video of the surface evolution. In the first minutes after opening the cell, black spots appeared on the glass surface. The first picture taken in the first minute following the cell opening already shows signs of reaction. In less than an hour, the surface of the poled area was fully covered with these spots. Figure 4.9 presents the evolution of the surface of the glass over time.

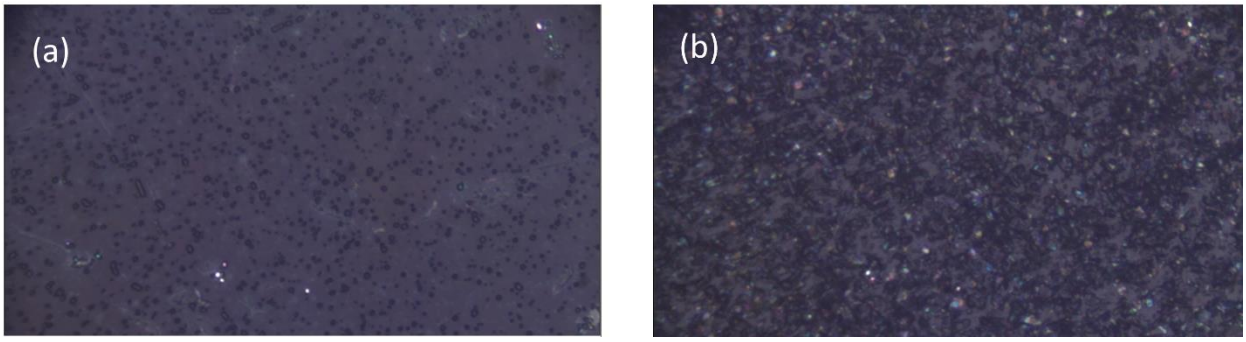

Figure 4.9. Picture taken after the glass was placed in the laboratory atmosphere, t=0s (a), t=1h (b)

The kinetic of this reaction is strongly humidity dependent, it was possible to accelerate the deposition rate by placing a source of water close to the poled sample. The impact of atmosphere humidity was however not studied during this PhD work.

The nature of the new layer was investigated using IR-spectroscopy. Figure 4.10 presents micro-IR spectra recorded inside and outside the poled zone, as well as an attenuated total reflectance spectrum of boric acid, an optical micrograph of the studied zone and an infrared map of the same zone.

Let us first discuss the infrared spectrum taken within and outside the poled area (the poled area corresponds to the area which was in contact with the electrode during poling). The spectrum taken outside the poled area presents strong similarities with the base glass. Modifications appear in the region in the region between 1250 and 1500 cm^{-1} and could be attributed to the various possible configurations of the BO_3 triangular units in rings and non-rings entities. Even if the area that is not in contact with the electrode is not expected to change, it is possible that changes in the poled area impact the network outside of this zone as both areas remain interconnected.

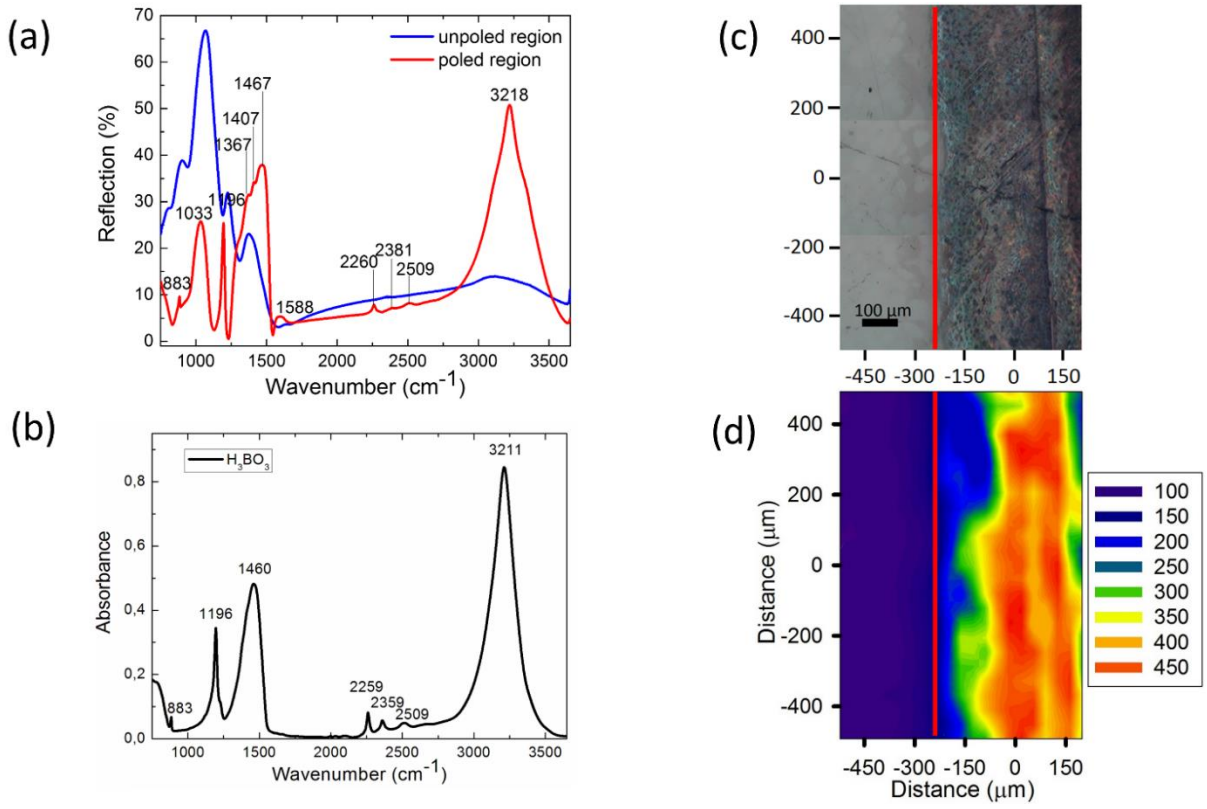

Figure 4.10. (a) Micro-infrared reflectance spectra taken outside and inside the poled region, (b) corrected ATR spectrum of boric acid powder (c) optical image of the mapped zone in infrared, (d) infrared map of the OH band (integrated intensity between 2800 and 3600 cm^{-1}) distribution along the frontier between the poled and unpoled region of the glass, red line showing the limit between unpoled region (left) and poled region (right)

If we now focus on the spectrum of the poled area, several changes from the post-poled structure can be highlighted. Once the sample is in contact with air, a large band around 3200 cm^{-1} appears due to the stretching mode of OH bonds which corresponding deformation mode can be found at 1588 cm^{-1}. This shows the presence of water molecules at the surface of the glass. In addition to water bands, new contributions appeared on the poled area that can be compared to the ATR spectrum of boric acid, shown in part b of Figure 4.10. This ATR spectrum was corrected for more accurate comparison with reflection spectra. The spectrum of boric acid can be decomposed in several bands with the following attributions: (i) at 1196 cm^{-1} a contribution from the B-OH

bending mode, (ii) at 883 cm^{-1} and 1460 cm^{-1}, two contributions from the B-O stretching mode respectively symmetrical and antisymmetrical and (iii) the O-H stretching mode vibrates at 3211 cm^{-1}. Smaller contributions are observed between 2200 and 2600 cm^{-1} and are assigned to combinations of the main bands. [31, 32] The spectrum recorded inside the poled area presents several comparable bands, especially the bands at 883, 1196, 1467, 2260, 2381, 2509 and 3218 cm^{-1}. The similarities between the boric acid spectral signature and the spectrum of the glass surface after it reacted shows that once in atmosphere and following water attraction, boric acid is formed on the surface of the glass.

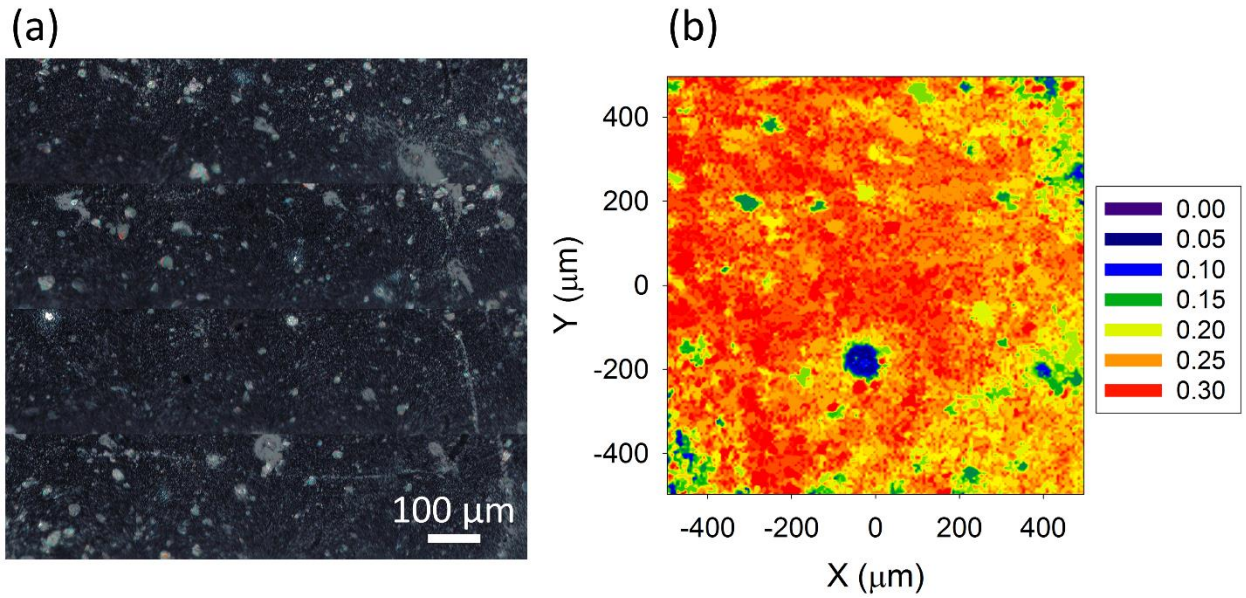

Figure 4.11. Optical micrograph taken inside the poled area after it reacted (a) IR map showing the distribution of the intensity of the water band around 3200 cm^{-1} (b)

An IR-map of a large area at the border of the poled and unpoled zone was made to localize the water layer on the glass surface. The area under the band between 2800 and 3600 cm^{-1} was integrated and the intensity of this band was plotted. The distribution of OH is restricted to the poled area and a sharp delimitation exists between this zone and the non-treated region. Moreover,

to evaluate the homogeneity of the OH layer, a map inside the poled region was made and is shown on Figure 4.11. The surface coverage with water is homogeneous as the intensity of the integrated band does not vary by more than 10 % across the studied area.

A Raman study was also conducted to confirm the presence of boric acid on the surface. Figure 4.12 presents the spectrum of the base glass, the spectra of boric acid, the surface of the glass after air contact, an optical micrograph of the limit between the poled area and unpoled area and a Raman map of this same area.

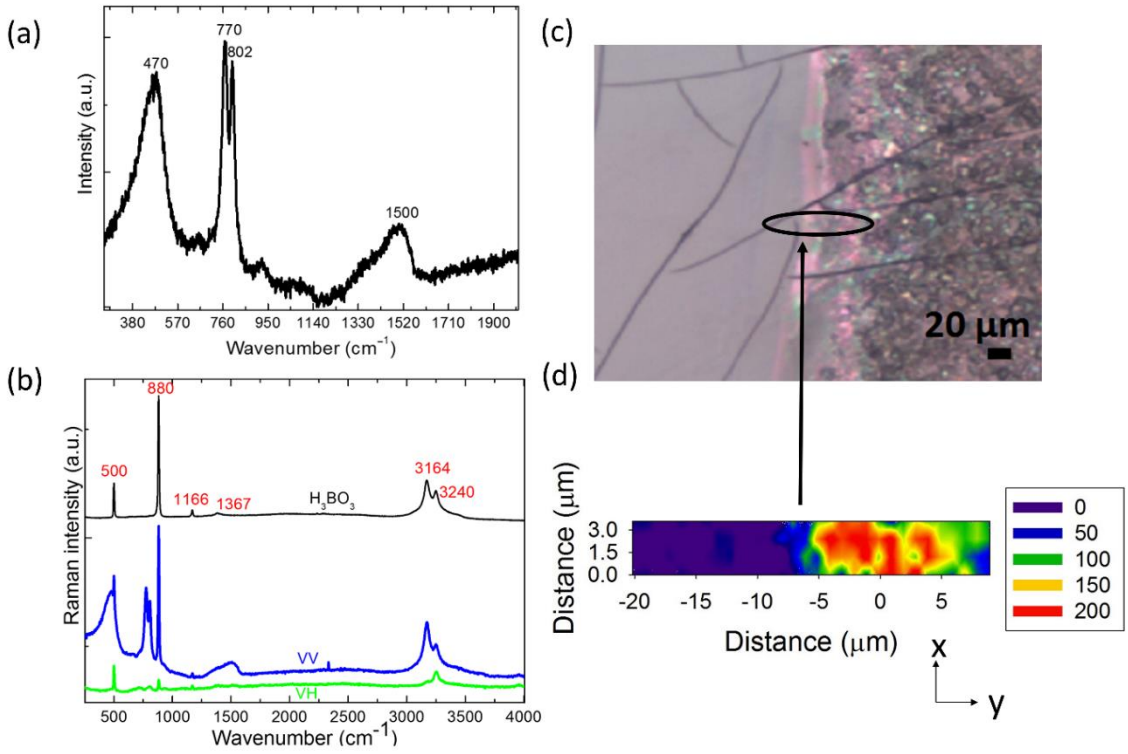

Figure 4.12. (a) Raman spectrum of the base glass (b) Raman spectra of boric acid (black) and the surface of the glass in VV (Vertical incident polarization– Vertical analyzed polarization) and VH (Vertical incident polarization– Horizontal analyzed polarization) polarization inside the poled region (c) optical image of the surface and (d) Raman map of the circled area presenting the intensity distribution of the band at 880cm $^{-1}$ of boric acid

The Raman spectra taken inside the reacted region use two polarization states: (i) VV polarization corresponding to vertical incident polarization and vertical analyzed polarization and (ii) VH polarization corresponding to vertical incident polarization and horizontal analyzed polarization. In addition to the contributions originating from the glass itself, new features are present on these spectra. The VH polarized spectrum is used to minimize the isotropic contribution from the glass network and highlights six additional contributions at 500, 880, 1172, 1384, 3165 and 3251 cm^{-1}, corresponding to the one found in the Raman spectrum of pure boric acid. [31, 32] The following attributions can be made: the mode at 500 cm^{-1} corresponds to the bending mode of the O-B-O bounds, the B-O stretching vibrational modes has two components at 880 and 1384 cm^{-1}, the mode at 1172 cm^{-1} is attributed to the B-OH bending modes while the two final contributions at 3165 and 3251 cm^{-1} both corresponds to O-H stretching vibrational modes. Raman spectroscopy confirms the presence of boric acid following the glass reaction.

A Raman map Figure 4.12 (d) of the limit between the poled and unpoled region was recorded. As it uses a shorter wavelength, Raman spectroscopy has a better resolution in the XY plane compared to micro-IR spectroscopy. The map was made by plotting the intensity of the area under the band at 880 cm^{-1} corresponding to the mode of boric acid with highest intensity. Outside the poled area, all spectra recorded are identical to the base glass while in the poled region, in addition to the base glass spectrum, boric acid peaks are found. It is important to discuss why Raman spectroscopy does not show large variation in the borate bands in- and outside the poled area. It was shown with the µ-SHG profile that the nonlinear active layer is underneath the surface in the first micrometers. The resolution along z in Raman spectroscopy is coarser (several µ-m) than that of IR-spectroscopy in reflection mode (< 1µm). In Raman spectroscopy, the spectra recorded in the poled

area are therefore averaged out by the contributions from the bulk glass, making it more difficult to observe changes. However, the good XY spatial resolution of Raman spectroscopy allows to characterize the length of the transition zone from base glass to poled glass, which is of the order of 2 microns.

4.3.2 How does boric acid form on the glass surface?

The formation mechanism of boric acid on the surface of the glass needs to be described to fully characterize the reaction taking place. As shown by the large OH band observed in infrared spectroscopy, the poled area presents a strong affinity towards atmospheric water. The surface coverage is almost total as shown by the optical images, the IR map and the Raman map. The new affinity of the glass towards water is partially attributed to the new boroxol-like structure which is known to be hygroscopic. The presence of the strong static electric field in the vicinity of the surface might further enhanced that reactivity through electrostatic interactions. [33, 34] Once present on the glass surface, water reacts with it through a standard leaching process. The boron-rich glass is now formed of boroxol rings and comprised of a large amount of B-O-B bonds. Water preferably reacts at these points and B-OH bonds are formed. [35]As the leaching continues, boron is released from the glass matrix and forms boric acid, H_3BO_3, in the water layer. This is confirmed through micro IR and Raman measurements. Slight variations between the ATR spectrum of boric acid and the IR spectrum of the reacted glass can be observed and related to the water-rich environment of the diluted boric acid on the glass surface. This is a different environment from the ATR spectrum which was recorded on boric acid powder. However, the presence of boric acid in the water layer is definitely confirmed by the Raman measurements and the presence of fine boric acid peaks in addition to the base glass features. It is reported in the literature that the Raman spectrum

of dissolved boric acid is comparable to the one of boric acid in powder form. [36] Further information can be obtained from the Raman measurements, especially an insight on the amount of boric acid diluted in the solution can be determined through the ratio of the 880 cm^{-1} and the 3400 cm^{-1} band. If we apply the methodology given by Thomas [36] on the Raman results showed here, a concentration of boric acid as high as 20 wt% can be estimated in the water rich layer.

4.3.3 Evolution of the glass' 2nd order nonlinear properties in atmosphere

It is now understood that once in air the poled area presents a strong affinity towards atmospheric water which then reacts with the glass itself through a leaching process to produce boric acid. It is primordial to evaluate the stability of the induced SHG during the leaching step. A poled glass sample was kept under vacuum several days and showed no sign of SHG decay. The cell was then opened and SHG maps were recorded on the sample using the μ-SHG setup. Figure 4.13 shows three maps recorded on the same day and shows the evolution of the SHG as the leaching process takes place.

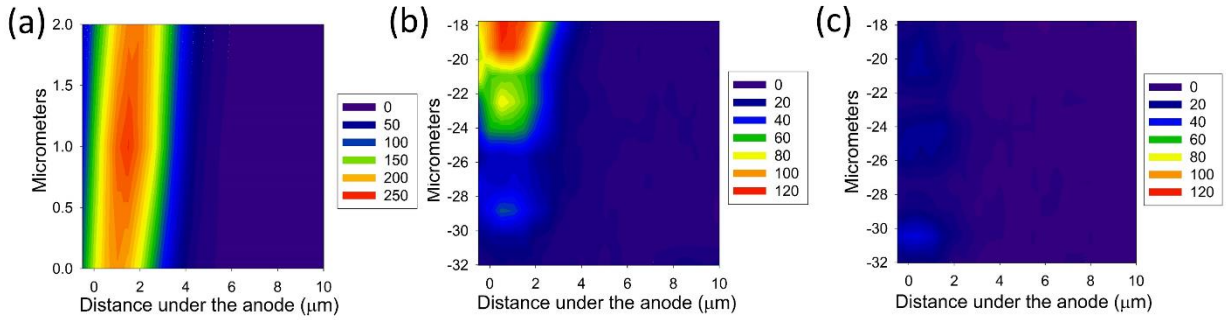

Figure 4.13. μ-SHG profiles recorded on the sample at different time after opening the poling cell (a) t_0, (b) t_{0+7h}, (c) t_{0+9h}

The first map recorded in the first minutes following atmosphere exposure shows a strong signal buried under the anode. The signal maximum is seen within a 2 μm wide band. Any changes in signal intensity between the results shown here and the map shown on Figure 4.8 can be explained by the set-up used during these two measurements. For the measurements made under vacuum, as the beam goes through the window of the poling cell, there is a decrease in the numerical aperture when focusing on the glass sample within the cell. The z resolution is thus decreased which can explain the difference in width and in relative intensity between the measurements under vacuum and in air.

As water is attracted to the glass surface and the leaching process is taking place, a decay in SHG intensity is observed. After 7 hours, the signal has lost half of its intensity while 9 hours after being in contact with the atmosphere, the SHG signal is 10 times smaller as after the cell was opened. The SHG decay is directly linked to the leaching of the glass network. As water is attracted on the poled area, it slowly reacts with the borate network and dissolves it. The modified layer which also contains the sodium depleted layer, responsible for the apparition of the static electric field is partially destroyed. This explains the decay of the SHG signal, as the modified layer is removed, the new nonlinear optical properties decay. A necessary precision needs to be added, water attraction takes place in approximately an hour and then plateaus. Whereas the SHG present a strong signal in the first minutes after opening the cell and only then slowly decays towards a minimum. This could be an indirect proof that water attraction is accelerated by the presence of the strong internal electric field and is not only due to the modified structure. As water is present at the surface, the induced electric field is slowly neutralized.

4.3.4 Study of the removal of the leached water layer under vacuum

So far, we showed that following thermal poling, structural changes locally takes place giving a structure closer to pure boroxol rings. This new structure is associated with a strong static electric field giving the glass new nonlinear optical properties such as second harmonic generation. Once exposed to laboratory atmosphere, the charged borate structure attracts atmospheric water on the surface of the glass. Water present at the surface reacts with the glass structure through a leaching process to form boric acid resulting in the decay of the SHG signal. It is now interesting to study the possibility to remove this water layer and to measure the structural changes as well as the surface properties modifications.

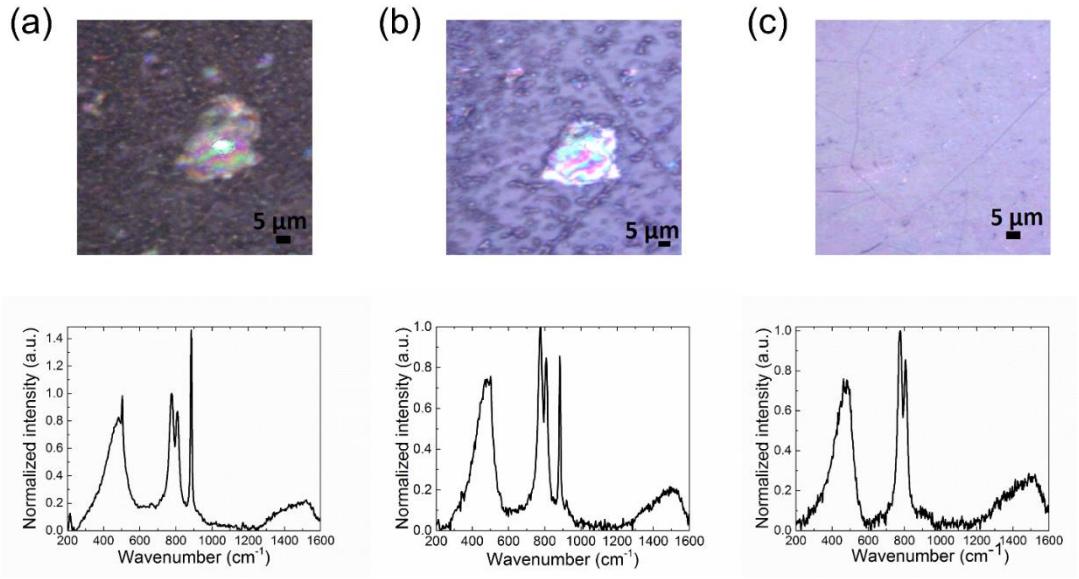

Figure 4.14. Optical micrograph images of glass surface (top) and Raman spectra (bottom) of glass surface recorded under vacuum, at times (a) t_0, (b) $t_{0+20\ min}$ and (c) t_{0+14h}

The layer on top of the surface was simply removed by placing the sample under vacuum. The removal of the OH-rich layer can be monitored using optical microscopy. The layer was easily removed and no heating was necessary to come back to a clean surface. While the sample is under

vacuum, Raman spectra were recorded in-situ and are presented in the Figure 4.14 with their corresponding optical micrographs.

The surface coverage of the water layer decreases rapidly when exposed to vacuum. In a similar trend, Raman spectra recorded during the process show a reduction of the intensity of the boric acid peaks. Once the surface is clean, no boric acid signature is found on the Raman spectra. Boric acid is known to be volatile in solution and can easily evaporate upon heating. As it is easily removed under vacuum, this indirectly proves that it was not bonded to the glass network. The glass surface presents scratches after water was removed. During the leaching process, as water reacted with the surface, it revealed scratches not observable before, similarly to etching of a glass with acid.

The glass structure needs to be studied once again to evaluate the impact of the leaching process. Raman spectra recorded on the surface do not show significant modifications with the one of the base glass. Once again, this is due to the z-resolution of Raman spectroscopy as compared to the thickness of the poled layer evaluated to be 2 μm in Figure 4.13. However, using IR spectroscopy in reflectance, the depth probed is dependent of the wavenumber but is below 1 micron in the region of the boron network. Figure 4.15 summarizes the various IR spectra recorded before, after reacting with the atmosphere and once the OH-rich layer has been removed. The spectrum in red presents a large OH band around 3250 cm^{-1} showing the glass reactivity. The band of the $B\emptyset_3$ triangular units has decreased in intensity and the boric acid characteristic peaks are present on the spectrum. This is an indication that the leaching process is taking place and is associated with the consumption of the newly formed boroxol rings leading to the formation of boric acid in water solution. Once place under vacuum and the OH-rich layer removed, the IR spectrum once again

presents variations. The broad peak at 500 cm^{-1} is not modified over time, as well as the silica network at 1075 cm^{-1}. The contribution from the $B\emptyset_3$ triangular units is greatly decreased. Regarding the $B\emptyset_4^-$ tetrahedra, their contribution band has also shrunk. Finally, the OH contribution at higher wavenumber is absent from the spectrum. The boron network appears to be less probed relatively to the silica network. All of these changes indicate that the boron network has been partially etched away from the surface forming boric acid, leaving mostly the silica network. The glass network is finally in an intermediate state between the base glass and the post-poled structure. It would be interesting to study the evolution of the structure if the leaching process was allowed to continue for longer time. Interestingly, once the water is removed from the surface, it does not come back. It shows that the new water affinity was mainly due to the new charged borate structure and once partially destroyed, the new properties vanish.

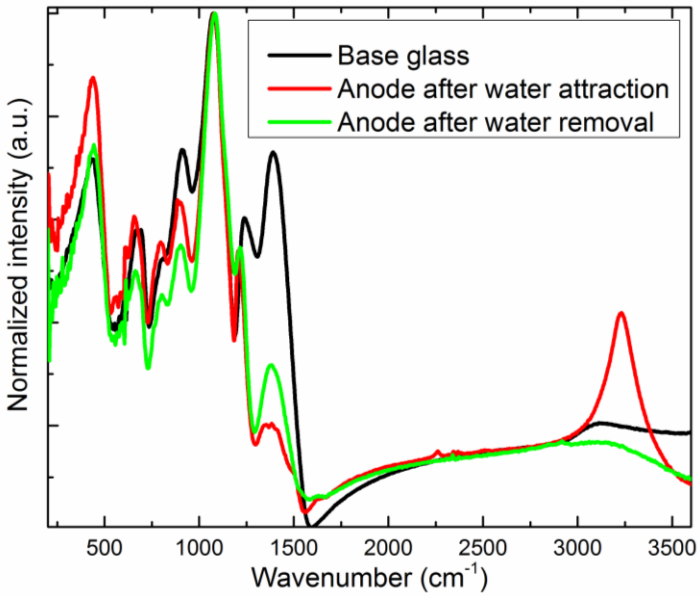

Figure 4.15. Infrared spectra of the glass: Evolution of the structure after poling

AFM measurements were performed on the glass sample after the leaching process and water removal under vacuum. Figure 4.16 shows a reference sample and one polarized sample after it reacted with the atmosphere and went through the leaching process.

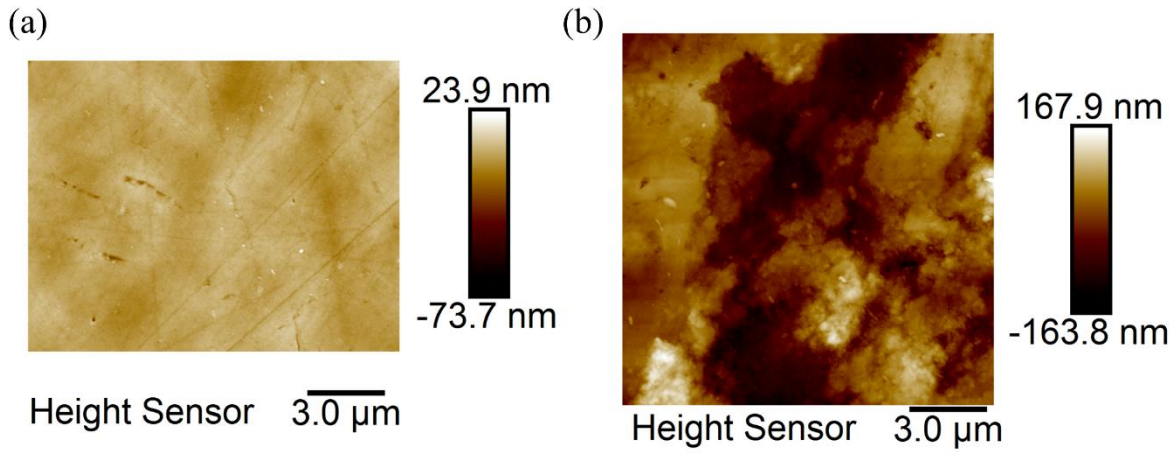

Figure 4.16. AFM measurements performed on: a reference sample (a) and a poled sample after it went through the leaching process and that the reacted layer was removed

The average roughness was measured across these two surfaces. The reference sample presents an average roughness of 3.09 nm while the reacted sample presents an average roughness of 54.7 nm. This large increase is due to the formation of trenches on the glass surface as deep as 150 nm. The leaching process seems to greatly affect the surface relief. This process resembles the one used in the production of porous glasses, such as Vycor ®. To make such a glass, phase separated glasses are used and react with water which etches away the boron rich phase. The glass is then made of a silica rich network which is not attacked during the process and present a large porosity. [8] The glass used in this study is known to be in a region which easily form phase-separated glasses. The quenching rate was adapted to prevent extended phase separation but phase separation at a small scale is still possible. The water present on the glass surface would then selectively attack the

borate network thus forming open porosity on the glass. IR spectroscopy tends to agree with that reasoning as the post-reacted sample shows a decrease of the band of the $B\emptyset_3$ triangular units following water removal.

The post-vacuum surface also presents a particular affinity towards water. Contact angle measurements were performed and a near to perfect wettability of the poled region was observed. The droplet of water was confined to the poled area. Figure 4.17 shows contact angle measurements done on the poled glass. A strong difference in wettability of the glass surface is observed with a total wettability of the poled area. Such an effect could be due to the new structure, surface topology and remaining static electric field. However, it is difficult to clearly evaluate the contribution of these various effects.

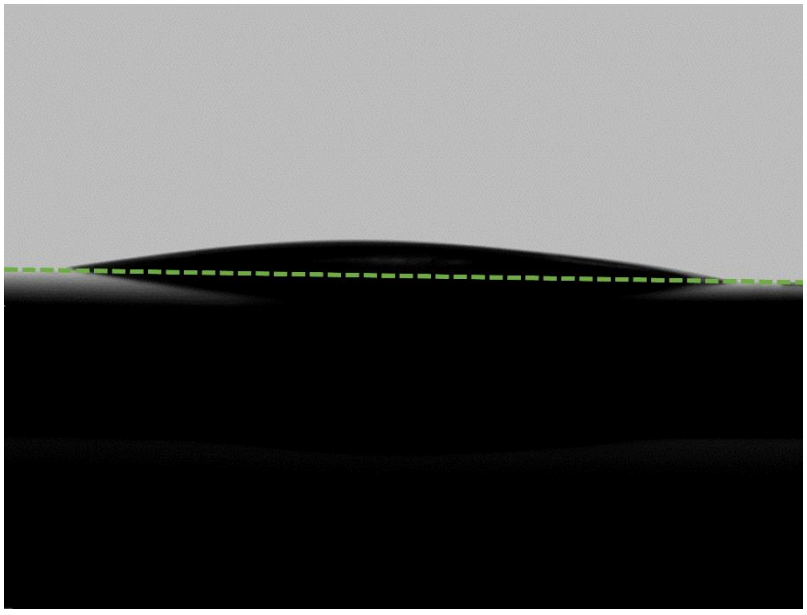

Figure 4.17. Contact angle measured on the poled sample, the green line delimits the surface

4.3.5 Conclusions of section 4.3

It has been demonstrated that by using a thermal poling technique, it is possible to tailor the glass structure, break its centrosymmetry ensuring SHG and to enhance its surface reactivity towards atmospheric water. Here we have fully described the mechanism of the process highlighting its behavior and reversibility. This process is only possible with a good understanding of the glass chemistry to find the appropriate composition for such an application. After thermal poling, a new charged borate structure is formed which reacts with atmospheric water. Once an OH-rich layer starts to form at the surface, a leaching process starts resulting in the formation of boric acid. This layer of boric acid dilute in water can be easily removed by placing the sample under vacuum. The surface is however damaged after the leaching process and presents large trenches in areas which were in contact with water.

However, this example is a good proof of concept showing that by careful selection of a glass composition and with the adequate treatment, thermal poling can not only induce Second Order Non-linear (SNOL) optical properties in the glass but also can change its structure and surface properties. This study is the first to definitively prove and explain the mechanism associated with the enhancement of surface reactivity towards water of a sample, after thermal poling.

4.4 Micro-structuring the surface reactivity of a borosilicate glass

Once the process of macro-poling and its impact on the post-poling properties is understood, the idea to control it at a smaller scale was developed. Being able to control the process on a micrometer scale presents the advantage to open up new applications in micro-sensors or lab-on-a-chip devices where reactions and process take place at small scale.

To design ways to control the poling process at smaller scale, it is important to first identify the key parameters for the process to take place. As described previously, upon heating the sample, charges gain mobility and once the DC bias applied across the sample, charge separation and cations migration occurs. The formation of the cation depleted layer is then responsible for the modification of the glass' structure, the appearance of the internal electric field and the new surface properties. Two approaches can thus be considered to control thermal poling at small scales, (i) a confinement of the heat in small region for the cations to only gain enough mobility there, (ii) find a way to apply the DC bias in certain areas of the sample to control positions where thermal poling takes place.

The two approaches investigated and will be discussed in this section. The first approach is based on laser-induced heating to locally heat the sample. The second approach relies on the use of a micro-patterned electrode as developed in the previous chapter.

4.4.1 Micro-poling of a borosilicate glass through laser induced samarium absorption

Borosilicate glasses were doped with 8 wt% of samarium oxide, an element of the lanthanide family, with oxidation state Sm^{3+}. An optical absorption spectrum of the Sm-doped borosilicate is shown in Figure 4.18.

Several absorption band can be observed in the infrared region at 1.47, 1.1, 1.92, 2.62 and 4.1 μm. The absorption band of interest for our study is the band around 1.1 μm, corresponding to the f-f transition of $^6H_{5/2} \rightarrow {}^6F_{9/2}$. [37, 38] Upon irradiation with a 1064 nm CW laser, both continuous f-f transitions and non-radiative electro-phonon is expected, resulting in a temperature change. The goal is to provide enough heat for the charge separation to take place in a confined zone under the

laser beam. Upon application of the DC bias, the charges should only move under the illuminated area. This process has been referred to Samarium Atom Heat Processing and has been successfully used to locally crystalize a glass under laser irradiation. [38, 39]

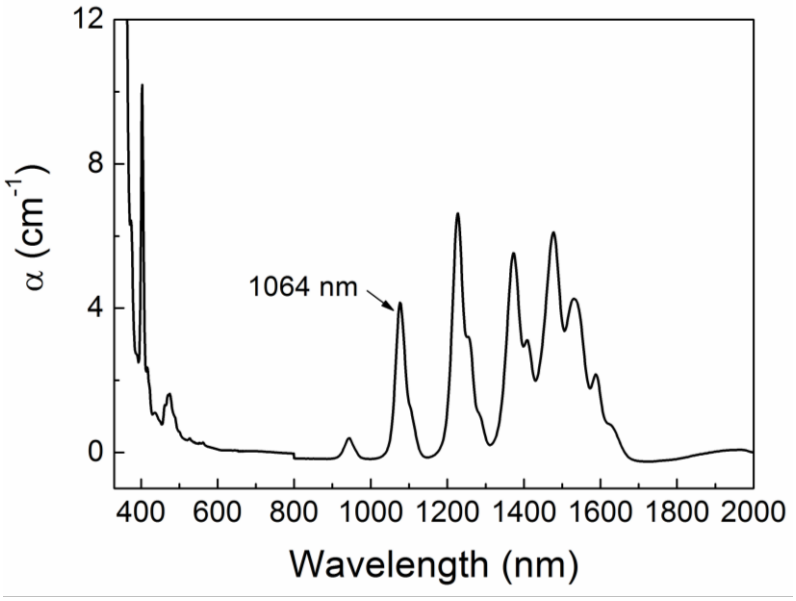

Figure 4.18. Absorption spectra of a glass doped with samarium

The absorption process needs to provide enough heat for the temperature to reach values close to 300°C that is the temperature used previously during poling of this glass. To prevent apparition of large temperature gradients, the sample is held at a constant temperature, below 300°C which is insufficient for thermal poling. Large temperature gradients could lead to crack formation upon rapid heating and cooling of the irradiated areas. Finally, the laser power should be kept rather low to prevent damages to the glass' surface and electrode.

Listed here are the parameters playing an important role during the poling process:

- The temperature of the hot plate

- The laser power
- The amount of samarium added to the glass
- The laser dose

4.4.1.1 Evaluation of the impact of the hot plate temperature on local temperature

The glass sample was placed on a hot plate fitted underneath an irradiation set-up using a 1064 nm CW laser with a 20x IR transparent objective. The hot plate was set up at a fixed temperature and the glass was irradiated with the laser at various incident powers. Upon irradiation of the sample, the temperature rise in the middle of the laser spot was measured by mean of an IR camera. The set-up used during this experiment is presented in Figure 4.19.

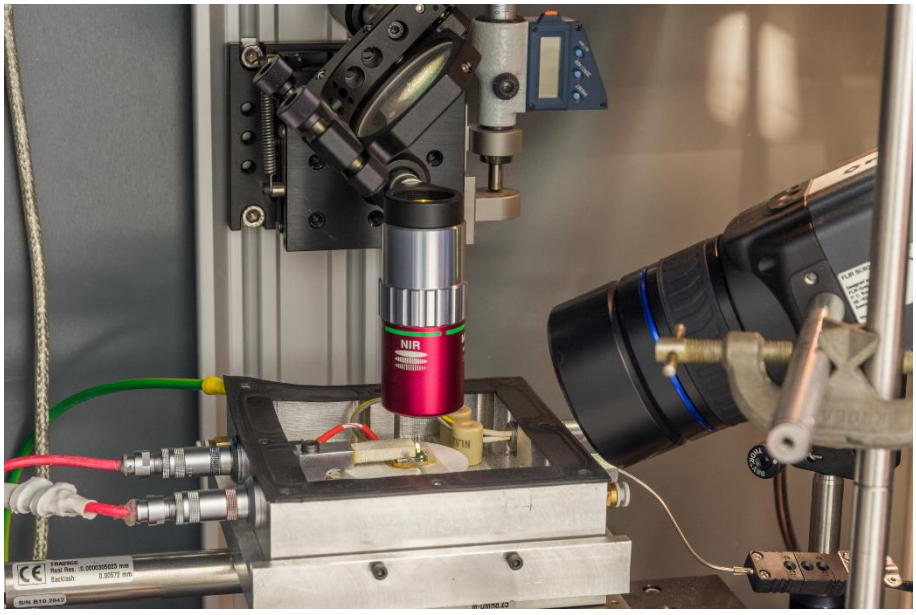

Figure 4.19. Irradiation set-up with the poling cell fitted underneath. An IR camera measures the temperature raise in the irradiated area

Several fixed temperature of the hot plate were tested as well as various incident laser power. Results of these experiments are reported in Figure 4.20.

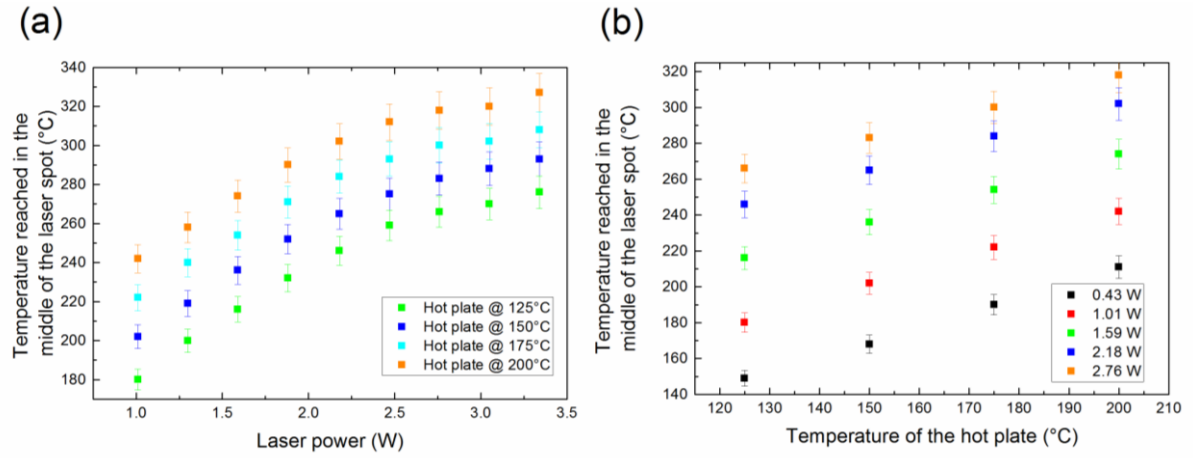

Figure 4.20. Maximum temperature measured in the center of the irradiated spot as a function of laser power (a) and of the hot plate temperature (b)

The plot on the left shows that an increase of the laser power results in a non-linear increase of the temperature in the middle of the laser spot. At maximum power, the temperature rise measured is up to 150 °C when the plate is set up at the lowest temperature.

The right plot however shows a linear increase of the temperature at the center following change of temperature of the hot plate.

An important parameter to evaluate is the distance over which the temperature rise takes place. It was observed that when increasing the laser power, the area over which the heating process takes place was also increasing and could reach distance as wide as tens of microns.

It is worth noting that the measurements were performed with the glass sample directly sitting on the hot plate. During thermal poling, the laser beam has to go through the window of the poling cell and through an ITO coated piece of glass used as an electrode. Every interfaces the laser beam

encounters lead to loss by reflection, which should be accounted for when choosing the right hot plate temperature and laser power. It is expected that 10% of the laser power is lost as the beam goes through the various layers above the glass. Another important information to take into account when measuring temperature with the IR camera is spatial resolution. The pixel size of the camera is larger than the spot size of the laser (25 µm). The temperature is thus averaged out on this pixel size. The maximum temperature in the middle of the Gaussian beam of the laser is therefore higher than the temperature read on the camera.

4.4.1.2 Micro-poling of Sm-doped borosilicate glasses

Glasses to be poled were placed in the poling cell and sandwiched between a silicon wafer to serve as cathode and an ITO coated microscope slide to be used as the anode. The poling cell was mechanically sealed and placed under nitrogen to ensure blocking anode conditions. The hot plate was set up at a fixed temperature (180°C) and a DC bias of 3000 V was applied between the anode and cathode. The sample was then irradiated with the laser to form patterns on the surface. The laser power was limited to 1.9 W as further increases lead to damage of the surface. Once all patterns inscribed on the glass, the sample was brought back to room temperature and the DC electric field was turned off. A typical example of patterns inscribed on the glass is reported on Figure 4.21.

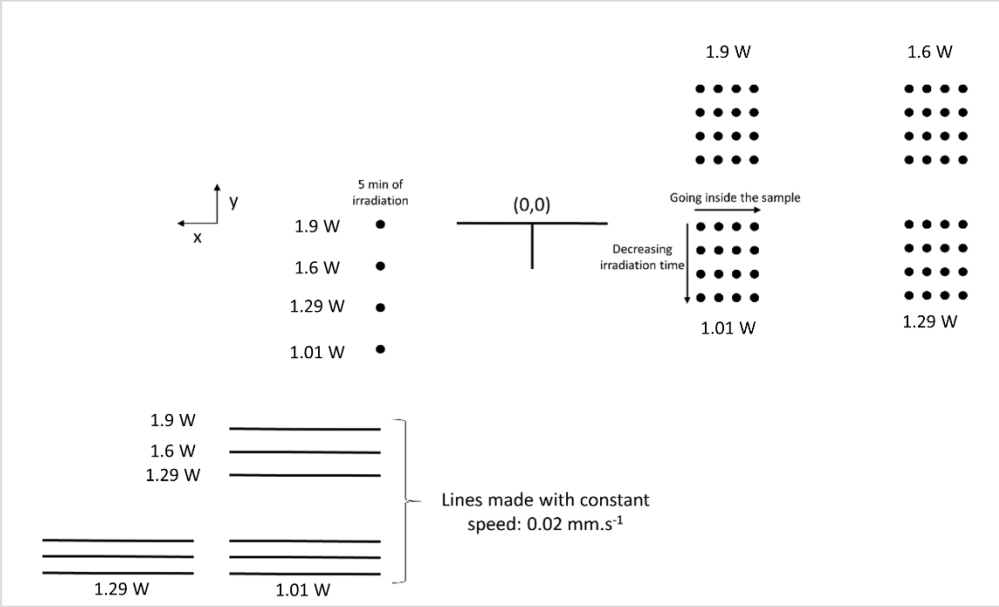

Figure 4.21. Typical patterns written on the glass during laser irradiation

Matrices were written at constant laser power but with varying irradiation time and focus plane to evaluate their respective impact. Each point on the left hand side of the matrix are focused on the surface and the laser is focused deeper in the sample (going right on the lane) by increment of 5 μm. Points on the first lines were irradiated for 5 minutes, the second line for one minute, the third line for 30 seconds and the last one for 10 seconds. Lines were also written on the glass to evaluate the possibility to imprint more complex patterns. Following the irradiation of the glass sample, the efficiency of the poling process was evaluated using μ-SHG measurements to probe for the presence of the internal electric field using a radially polarized incident laser beam.

4.4.1.2.1 Micro-SHG measurements

The μ-SHG measurements were performed using a doughnut beam in radial polarization to probe the longitudinal component of the electric field. Figure 4.22 shows the optical images as well as corresponding SHG maps recorded on two points with irradiation time of 5 minutes and with

respectively 1.6 (top) and 1.9 W (bottom). No SHG was measured on the other points irradiated with lower power. These other irradiation conditions correspond to temperature in the center of the spot inferior to 260°C. The temperature could be too low to provide enough mobility for the cations to migrate under the electric field.

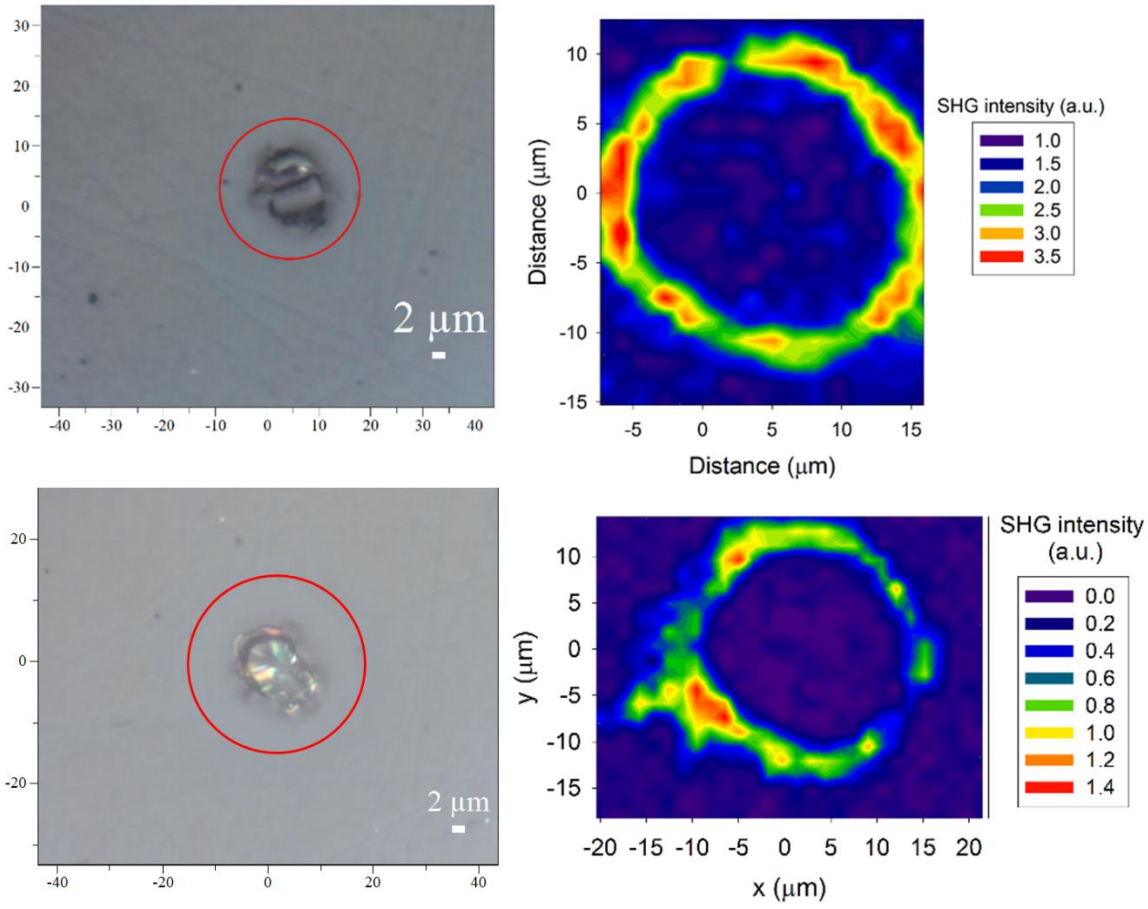

Figure 4.22. Optical micrographs of the points (left) and SHG map recorded on the same area in radial polarization(right). The red circle delimit the outer part of the SHG active ring

Both points made with 1.6 and 1.9 W show a strong SHG active ring around the point of impact without any signal outside and a small signal intensity inside the irradiated area. The SHG active area can be spatially correlated on the optical micrograph to a bright halo around the point which

is highlighted by the red circle. The point made with the highest incident power present a larger ring by 1 to 2 µm, associated with an overall decrease of the SHG intensity in it.

4.4.1.2.2 AFM measurements on the surface of the glass and on the ITO electrode

AFM measurements were performed in KPFM mode on the poled sample and in Peak Force Tapping mode on the electrode. The following figure shows a map done on a point made at 1.6 W with an irradiation time of 5 minutes.

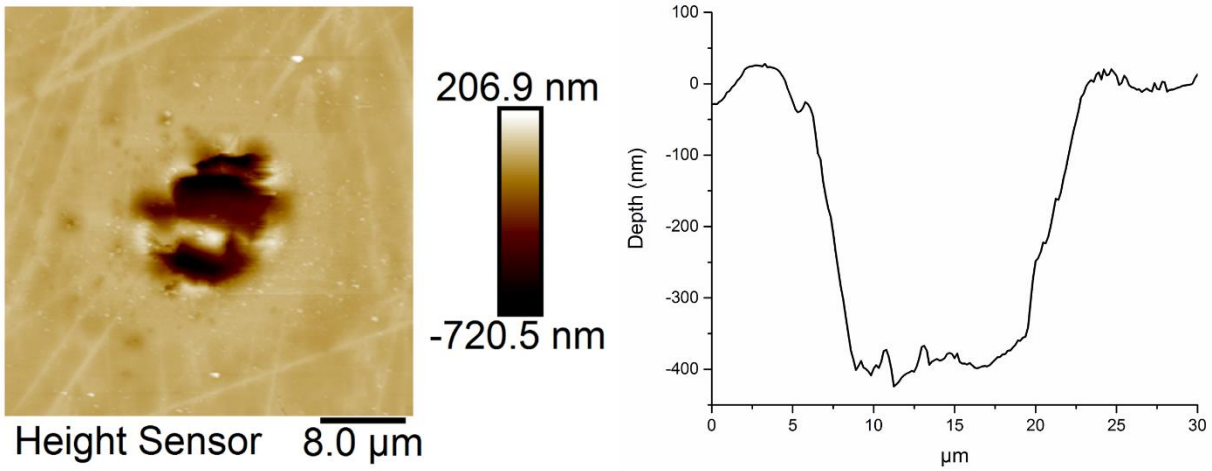

Figure 4.23. AFM measurements measured across an irradiated spot (left) and corresponding topology profile (right)

Under laser irradiation the glass surface is partially damages, resulting in a pit between 400 nm and 600 nm deep, with deepest area as deep as 720 nm. The incident laser power causes damages to the surface, however, a lower incident power was proven insufficient to induce charge migration as shown in the previous paragraph where no SHG was measured.

The rest of the surface is rather flat with an average roughness measured at 16 nm. Interestingly, a ring is observed around the point with a lower roughness, between 10 and 12 nm.

Similar measurements were done on the ITO electrode that showed large damages in the irradiated area, as seen in Figure 4.24.

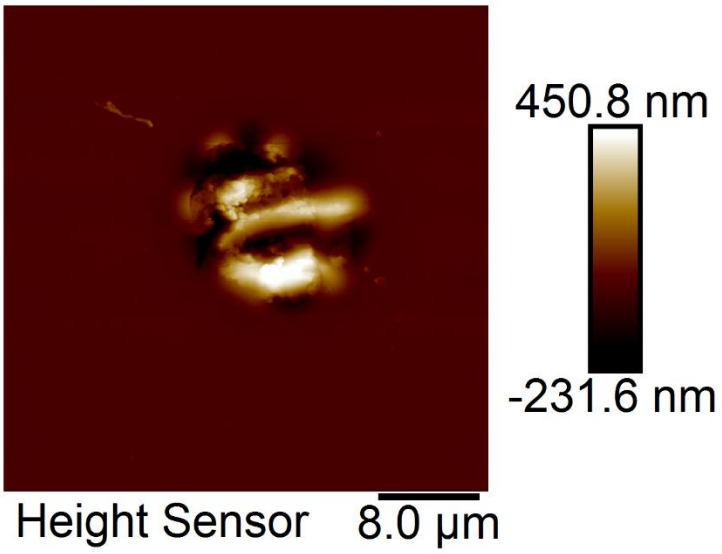

Figure 4.24. AFM map measured on the ITO electrode after poling

Finally, on the poled sample the map was recorded using the KPFM technique that gives additional information on the potential at the surface of the glass. The surface potential map is shown on Figure 4.25. This KPFM map can be divided in three zones. The first one is the inner part of the point which present a surface potential close to 0 or slightly negative. The second part corresponds to a negatively charged ring around the laser spot. Finally, a third zone corresponding to the rest of this map present a positive surface potential. This small map presents an abrupt change of the surface potential sign around the irradiated zone. The negatively charged region can be spatially correlated to the red circle in Figure 4.22.

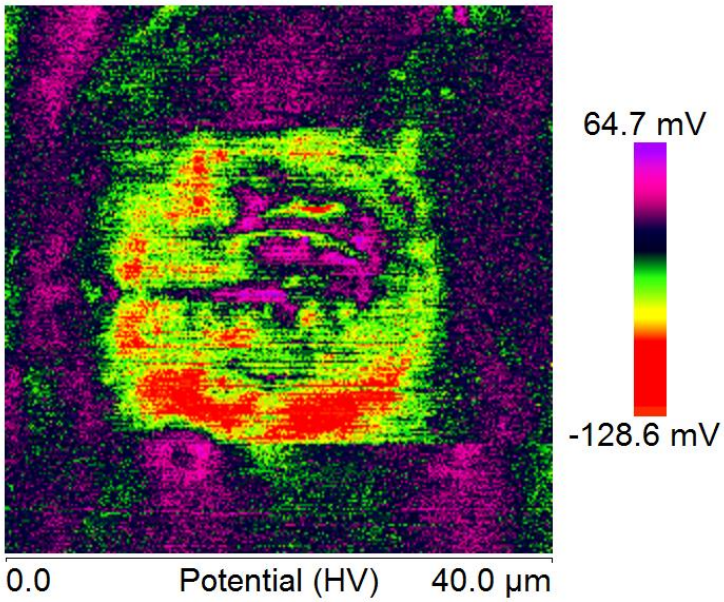

Figure 4.25. Potential map recorded in KPFM mode on the point irradiated with 1.9 W

The µ-SHG measurements and AFM/KPFM measurements presented so far need to be discussed together to understand the underlying mechanisms of these observed phenomena.

4.4.1.2.3 Spatial correlation between µ-SHG and AFM measurements

The µ-SHG measurements have shown that no signal was measured outside the irradiated area. We have observed that no signal was measured when using irradiation power below 1.6 W which correspond to a temperature close to 260°C. We suggest that below this temperature, the mobility of the charges is not high enough for thermal poling to take place. Therefore, when doing the thermal poling just above this limit, the temperature quickly drops below this limit as we exit the irradiated area. No cation migration can take place in these areas and at the end of the process, no electric field is induced in these area and no SHG signal can be recorded. This is confirmed with the AFM measurements which show no sign of topology change outside the point and which show a slightly positive surface potential in this same area.

On the other hand, a SHG active ring is observed around the irradiated spot with a strong intensity and a good spatial confinement. This SHG active zone can be correlated to a flat area in the AFM measurements that can be clearly seen in Figure 4.23. Once again, this ring is found in the KPFM measurement as a negatively charged zone around the point in Figure 4.25.

In the center of the point, no SHG signal is observed while AFM measurements show a damaged surface and a surface potential close to zero.

In addition, AFM measurements on the ITO electrode show a damaged surface which probably impacts the ITO conductivity. The process cannot be described solely as a local heating process but it is also necessary to take into account electrode structuring during the process. As shown in chapter 3, the electrode is therefore seen as a conductive area and a non-conductive area (in the middle of the laser spot). The KPFM measurements agree well with this view and should be compared to the electrostatic model used to simulate thermal poling with a structured electrode in chapter 3. We used the SHG measurement as a probe of the induced electric field on glass pattern with a structured electrode. To simulate the recorded SHG, two zone of opposite sign were defined. It was expected that negative charges would be induced in areas where poling was effective and associated with a positively charged area next to it, where the poling was not taking place (in the structured area). In the case presented here, a similar process is taking place. As sodium cations exit the vicinity of the surface, negative charges are left behind contributing to the apparition of the static electric field at room temperature. From all these measurements it can be concluded that the static electric field is only induced in a thin ring around the irradiated spot.

In the case discussed herein, the resulting induced electric field can be seen as the image of two processes, (i) the local increase of the charges mobility through local heating and (ii) the use of a structured electrode. When the laser irradiates the glass sample, it first goes through the window of the poling cell then go through the electrode and is focused on the glass' surface. As it encounters the glass sample, the samarium ions Sm^{3+} absorb and convert the absorbed energy to heat through continuous f-f transition and non-radiative transitions. The process locally provides enough heat to the cations to increase their mobility. Upon applications of the electric field, the positive charges migrate towards the cathode and charges are separated resulting in the apparition of the induced electric field. At the same time, structuring of the electrode and damages to the ITO coating occur. The electrostatic model in the preceding chapter has shown that a structured ITO electrode promote components of the electric field in the plane of the surface and enhancing charges at the border of the structure. If the progressive structuring of the electrode, associated with the local heating process are both taken into account, it can be concluded that the cations migration should be maximum just at the outer limit of the laser spot, small inside the laser spot and close to 0 outside of it. Indeed, this ring would correspond to an area where the temperature is high enough to provide mobility to the charges and where the outside electric field is effectively applied to separate the charges. At the end only this ring with a high density of charges should be obtained. The induced electric field is therefore maximum in a ring around the irradiated spot and null inside of it.

The use of a Samarium Atom Heat Processing allows to control both the temperature and the applied electric field in a small area. The treated sample then presents a structuring of the induced electric field leading to a structuring of its 2^{nd} order nonlinear properties.

4.4.1.2.4 Reaction upon atmosphere exposure

As discussed in the first section, once exposed to the laboratory atmosphere, poled areas of the borosilicate glass exhibit a strong affinity towards atmospheric water. It was proved that water then reacts with the glass network though a leaching process, leading to the formation of boric acid dilute into water. The micro-poled sample was left in the laboratory atmosphere for several hours, which is usually more than enough for water attraction to take place. We have previously demonstrated the usefulness of Raman or IR vibrational spectroscopy to identify boric acid formed at the surface of the glass. However, the presence of a rare-earth inside the glass matrix prevent the use of Raman spectroscopy due to the high luminescence masking the entire Raman spectrum of the sample. Several incident wavelengths were tried but even the use of a higher incident wavelength such as 785 nm does not prevent luminescence.

Micro-IR spectroscopy does not suffer from the samarium presence but here the limitation in the x-y resolution prevents making measurements in the irradiated areas which are approximately 10 μm in diameter. The smallest spatial resolution that can be obtained using micro-IR, while maintaining good spectral resolution, (~ 15 μm); while adequate to confirm the effect, this is too large to probe the inner part of the point. Finally, damage to the surface was observed in AFM and this is an issue for obtaining good specular reflection measurements.

We therefore have no experimental proof of enhanced surface reactivity using the Samarium Atom Heat Processing. This process can still however be used to structure the 2^{nd} order nonlinear optical properties of a glass at a scale of few microns.

Thus, a second technique was developed to allow us to measure the effect of our process. Here, another technique was developed to assess both the 2nd order nonlinear properties and the surface reactivity at a micrometric scale. This technique is further discussed in chapter 3: the use of micro-patterned electrodes.

4.4.2 Micro-poling of a borosilicate glass using patterned electrode

The use of micro-patterned electrodes during thermal poling as used with the BPN 42 glass was then tested on the borosilicate glass (without samarium oxide addition). Here, the electrode which is made of an ITO layer deposited on a microscope slide is patterned by laser ablation selectively removing regions of the ITO conductive layer. This results in a patterned electrode made of alternating conductive and non-conductive areas. As shown previously, the ITO-free areas should not participate in the poling process. So far this technique was only used to pattern the Second Harmonic Generation (SHG) signal, but in the case presented here, it aims not only to tailor the glass' surface SONL properties at the micrometric scale but also to tailor its reactivity and network structure at the micrometer scale.

4.4.2.1 Structuring of the ITO electrode

The ITO layer was structured by laser ablation using a 1064 nm nanosecond yttrium aluminum garnet (YAG) laser as described before. Various patterns were written on the surface by moving the sample with a motorized stage (X, Y) under the laser beam. Rectangles 40x60 μm^2 were written on the ITO electrode as this dimension allows spatial mapping over this area using μ-SHG, μ-Raman and μ-IR spectroscopy. AFM measurements, shown on Figure 4.26 , demonstrate the total ablation of the ITO coating.

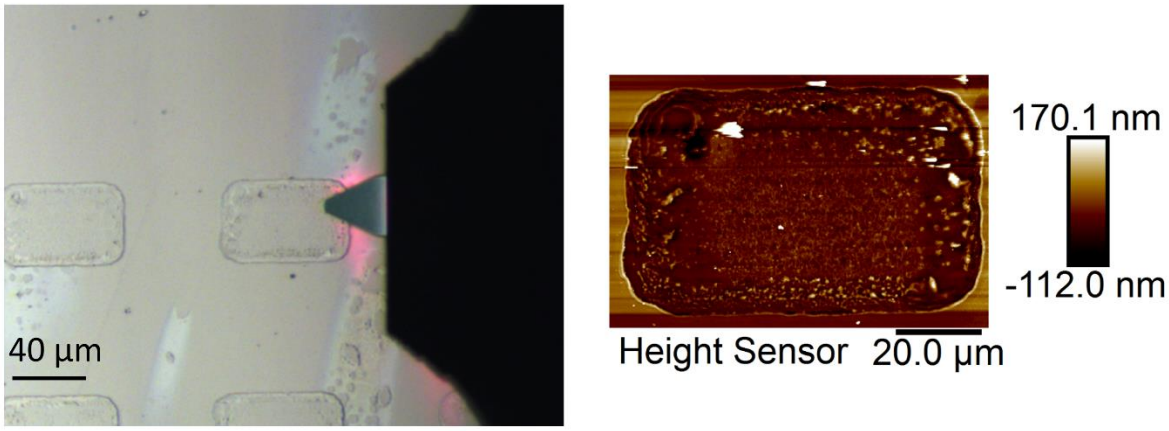

Figure 4.26. Optical micrograph (left) and corresponding AFM topology measurement on the electrode (right)

The glass sample was put between the patterned electrode at the anode and a silicon wafer at the cathode and placed in the poling cell. The treatment took place in a nitrogen atmosphere and the sample was heated at 300°C. After 10 minutes, when a constant temperature was reached, a DC bias of 3000 V was applied across the sample for 30 minutes. The sample was then brought back to room temperature and only then the DC bias was removed.

As the polarized sample is expected to present enhance reactivity towards atmospheric water, the cell was placed in a glove bag, filled with nitrogen, once the poling performed. The sample was taken out of the poling cell and placed in inert atmosphere to perform the same set of characterization as in the macro-poling experiment described in section II and III. To evaluate the efficiency of the thermal poling, the sample was first studied under an optical microscope to examine the patterned electrode's transfer fidelity to the glass' poled surface. The pattern is precisely transferred to the glass surface through the electrostatic imprint process taking place during poling, as observed on Figure 4.27. [40]

4.4.2.2 Micro-SHG measurements

As reported before, an efficient thermal poling breaks the centrosymmetry of the glass by inducing a strong static electric field in the near anode surface. [41] This electric field contributes to SHG in the glass through the electro-optical effect EFISH mentioned earlier. To probe the induced electric field, we used the modified micro-Raman spectrometer HR800 equipped with a 1064 nm picosecond laser, described previously. [42] A SHG map of one of the rectangle imprinted on the glass surface was obtained with a 50x objective, using a radial polarized doughnut shaped beam profile that probes the longitudinal SHG contribution, Figure 4.27-b.

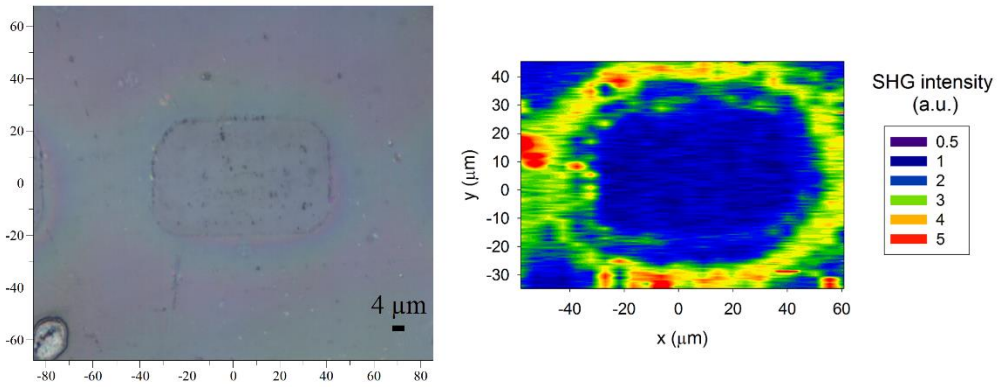

Figure 4.27. (a) Optical micrograph of a rectangle inscribed on the surface after poling, (b) corresponding µ-SHG map across the rectangle imprinted on the sample, (c) SHG profile across the same rectangle.

The SHG active zone is spatially located around the rectangle. The maximum of intensity in the active zone is 10 times higher than the background signal measured inside the rectangle pattern. The intensity variation between the ITO-free area and the poled area and the location of the SHG active zone are in agreement with the literature. [43] These measurements however differ with our results discussed in the niobium borophosphate chapter. In this other study, we could observe two

contributions to the SHG signal with the longitudinal polarization that were located on each side of the edges of the patterns. In the case of the borosilicate glass presented here, the second contribution is not clearly observed. The second major difference with previous literature results is that the SHG active zone is present over distances as wide as 10 μm, while in the BPN 42 of the previous chapter, the signal was confined to spatial regions of less than 5 μm. The third major difference in our study is that the in-plane components to the SHG signal are not contributing as much to the SHG signal and have considerably lower intensities.

The SHG response as depicted on Figure 4.27 is however clearly structured and is linked to an edge effects and a higher density of charges induced in the border of the patterns. In a classical thermal poling treatment, carried out *without* structured electrodes, the electric field is perfectly perpendicular to the surface thus only giving a longitudinal and uniform intensity of the SHG across the poled surface. By removing strips of ITO on the electrode, we have shown in the previous chapter that a field enhancement phenomenon is taking place by changing the charge density along the glass surface as well as promoting charge displacement not only along the z-axis but also in the x-y plane of the glass. Along the patterned area, an increase of two order of magnitude in the charge concentration is observed, thus giving more trapped charges after poling and enhancing the SHG in these areas. The in-plane poling contribution which should give the other contribution to the electric field is greatly related to the ITO-ablated area and to surface current formation. The overall SHG intensity is smaller in thermal poling of borosilicate glasses compared to borophosphate niobium glasses. The geometry of the electro-optical anisotropy induced in both glasses is different and it is possible that depending on the glass composition, surface currents responsible for this effect are accessible at different ranges in the structured areas.

The area over which the electric field is going to be induced and structure would therefore be different, therefore leading to various thickness and intensity of the SONL active area.

4.4.2.3 Evidence of structural changes

To evaluate the departure of sodium on the poled region, vibrational spectroscopy is suitable in this glass as sodium migration leads to a necessary re-arrangement of the glass matrix which greatly impacts the borate network. [13] We remind that the borosilicate used here lies on the boric oxide anomaly. Its structure was described in the previous section as made of fully reticulated silica tetrahedra and borate entities close to pentaborate groups. Every sodium added to the glass is present in the vicinity of a boron tetrahedron and act as a charge compensator. The remaining boron entities form 3-coordinated $B\emptyset_3$ triangular units in rings and non-rings units.

Following thermal poling, μ-IR reflectance spectroscopy was used to probe the structural changes close to the glass' surface inside and outside the patterns. An optical micrograph of several patterns were imprinted on the glass is shown on part (a) of the figure, as well as three individual spectra recorded on positions A, B & C, shown on the optical micrograph, and the corresponding IR-map showing the distribution of the intensity of the total integrated area under the curve for the band of the $B\emptyset_3$ triangular units between 1200 and 1550 cm^{-1}.

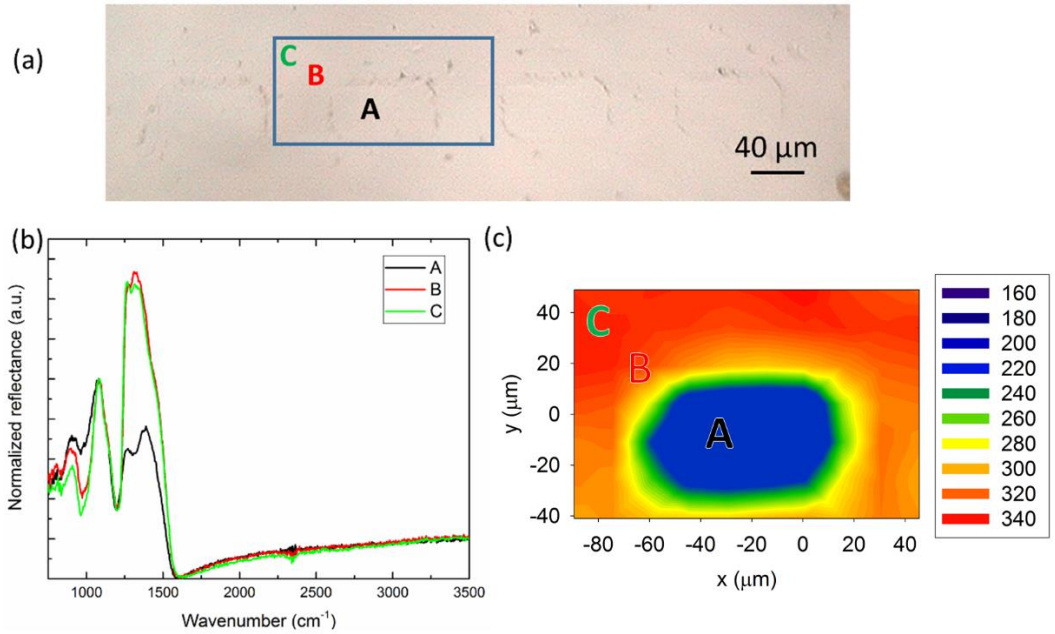

Figure 4.28. Optical micrographs of the surface (a), IR reflectance spectra taken on positions A, B & C shown in part (a) (b) and corresponding micro-IR map taken on the blue rectangle presenting the intensity distribution of the $B\emptyset_3$ band between 1200 and 1500 cm^{-1}(c)

All spectra presented in this figure were normalized to the intensity of the band peaking at 1075 cm^{-1}, attributed to the asymmetric stretching vibrations of Q_4 silicon – oxygen tetrahedra, i.e. fully linked SiO_4 tetrahedra. [9-11] The band peaking at 910 cm^{-1} is attributed to the asymmetric stretching vibrational mode of $B\emptyset_4^-$ tetrahedra, i.e. a boron tetrahedron with a neighboring sodium cation to balanced its charge. [13, 14] The boron network presents another contribution between 1250 and 1500 cm^{-1} that corresponds to an asymmetric stretching vibrational mode of $B\emptyset_3$triangular units in ring and non-ring configurations. [12] The IR spectrum taken inside of the pattern inscribed on the glass, position A present the same signature as the spectrum of the base glass, showing that poling was not effective in these areas. Now looking at the IR spectra taken outside the patterns, positions B and C, on figure Figure 4.28 (b) several changes should be highlighted. The most drastic change concerns the signature of the $B\emptyset_3$triangular units which, in addition to its large increase, goes from

a double band to a single band. Simultaneously, the band of the $B\emptyset_4^-$ tetrahedra decreases in intensity. The IR map (Figure 4.28-c) taken on the highlighted blue rectangle of the optical micrograph (Figure 4.28-a) shows the intensity distribution of the $B\emptyset_3$band around a pattern. It is observed that inside the pattern the contribution of this group is highly lowered compared to its surroundings.

Changes taking place during this micro-poling experiment are the same that were depicted in the previous section. As a reminder, they were linked to the sodium cations departure from a thin layer underneath the anode, moving towards the cathode. Absence of a charge compensator in the vicinity of the $B\emptyset_4^-$ tetrahedra was associated with a re-arrangement of the structure into $B\emptyset_3$triangular units, thus forming a network closer to pure B_2O_3 rings. [13] The silica network once again is not impacted by the treatment. As in the macro-poling of this glass, the IR spectroscopy indirectly indicates the departure of sodium and the formation of molecular oxygen. Once again, the identity of the negative charge carriers is still to be determined.

4.4.2.4 Evidence of spatially controlled reactivity

As shown in the macro-poling of the borosilicate glass, the polarized glass presents a new structure, associated with a strong internal electric field which enhances the glass' reactivity towards atmospheric water. All measurements shown so far were carried out before the glass reacted with the laboratory atmosphere, either under controlled atmosphere or in air before any reaction. To evaluate the glass surface's reactivity, the sample was let free to react with its surrounding environment until it started to show signs of reaction as observed previously. We want to remind the reader that the kinetic of this process is highly dependent on the humidity content of the laboratory and that this parameter is not controlled in this study.

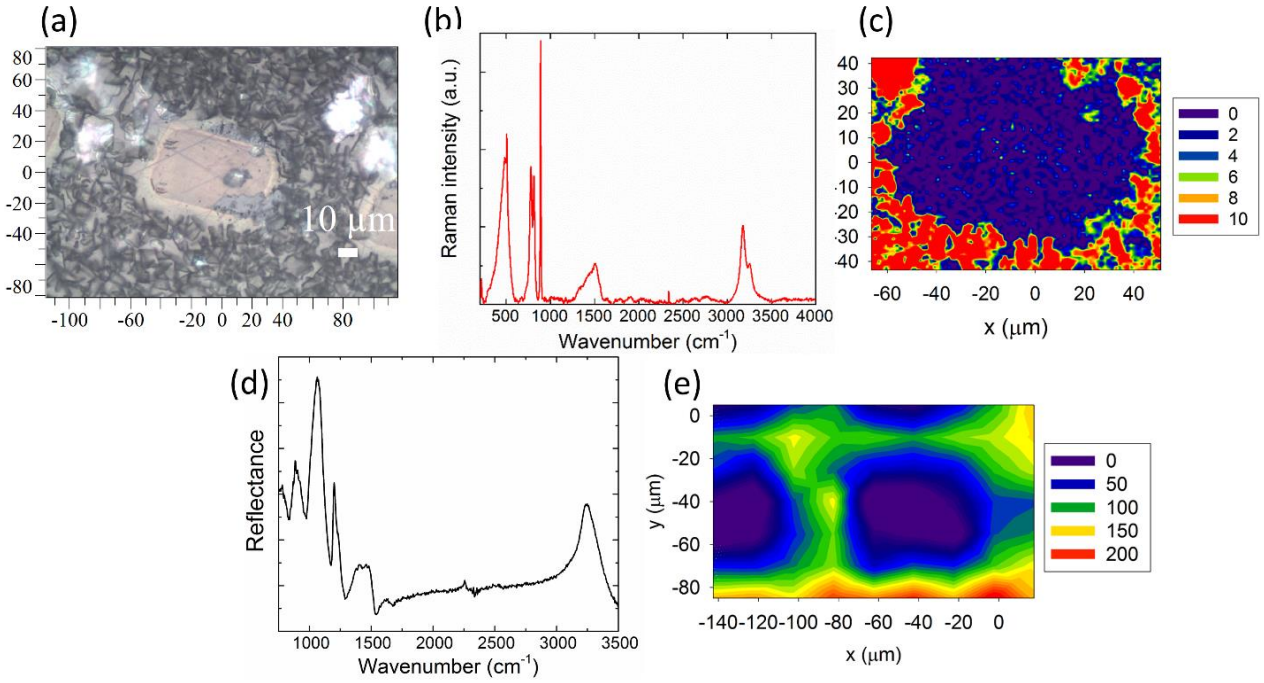

Figure 4.29. Optical micrograph of the glass surface after exposure to atmosphere (a), Raman spectrum taken outside of a pattern after exposure to atmosphere (b), Raman map recorded around the pattern presented on the optical micrograph, the intensity of the band of boric acid peaking at 880 cm^{-1} was imaged (c), IR reflectance spectrum taken outside a pattern after exposure to atmosphere (d) and IR map recorded around four squares showing the distribution of the intensity of the integrated band of asymmetric stretching vibration of OH groups between 3000 and 3500 cm^{-1} (e)

Figure 4.29 focuses on the vibrational study of the surface after it reacted with the atmosphere. The top row shows the Raman vibrational study and the bottom row, the infrared study. Both optical micrographs show signs of reactivity by the presence of dark spots on the surface of the glass. Part B of the figure presents a Raman spectrum recorded at the surface. First, the contributions from the glass network that were previously identified are present, i.e. two principle modes at 770 and 805 cm^{-1}, respectively corresponding to a triborate group bounded to one $B\emptyset_4^-$ and to $B\emptyset_3$ triangular units in rings. [15, 16] At lower wavenumbers, a large envelop is attributed to mixed stretching and bending vibrations from the silicate network. [18] In addition to the mode of

the glass, several contributions from boric acid, H_3BO_3, can be observed as detailed in the previous section. These modes identified earlier are not changed and the bending mode of the O-B-O bound at 500 cm^{-1}, the B-O symmetrical and antisymmetrical stretching vibrational mode at 880 cm^{-1} and 1384 cm^{-1} and the bending mode of B-OH bonds at 1172 cm^{-1} are all present. [31, 32] The two last contributions at 3165 and 3251 cm^{-1} are attributed to O-H stretching vibrational modes. [32] Presence of boric acid is easily explained, as it is now known that following the creation of the charged borate structure, atmospheric water is attracted to the surface of the glass, and then reacts with it through a leaching process to form boric acid. [35] Map (c) depicts the distribution of the integrated area under the main peak of boric acid at 880 cm^{-1}. From this map, it can be observed that boric acid is only present *outside* the pattern. The intensity of the integrated band is null across the pattern while outside of it, it is more than an order of magnitude stronger. Boric acid is thought to be dissolved in water at the surface of the glass as it is known to be soluble in water even at room temperature. [36]

Infrared reflectance spectroscopy (bottom row) allows further confirmation of the information observed with Raman spectroscopy. Spectra recorded in areas that have reacted with the atmosphere present a distinctly different signature from either the base glass or post-poled glass, illustrated in Figure 4.29 - d. A large contribution from asymmetric stretching vibration of OH groups is observed between 3000 and 3500 cm^{-1}. The vibrations originating from the glass network are also changed with a large decrease of the $B\emptyset_3$ triangular units. However, as a large water band is present in the spectrum, it is hard to draw conclusions on the glass network. Infrared reflectance measurements only probe the first few microns of a surface and the water layer thus masks the contribution of the sub-surface glass network. Such a spectrum can only give valid information on

the presence of water at the surface. A map of the distribution of this water band is shown on part (e) of Figure 4.29. The infrared map was recorded on a larger zone to image four squares (one fully and the three others partially). Water presence is correlated to the areas where changes occur upon poling while inside the patterns, no water signature is observed. The important information to remember from this IR-map is that inside the pattern, the OH band is null whereas outside of it, it strongly increases, thus showing the unique spatial selectivity of the surface reactivity enhancement imparted by the μ-poling process.

4.4.2.5 Conclusion of section 4.4.2

Two different approaches for micro-poling were presented in this section. The use of a laser induced heating process through laser absorption has shown limitations. The 2nd order nonlinear optical properties could be effectively structured but no sign of enhance reactivity could be observed. However, the use of a patterned electrode during thermal poling was proven reliable to imprint spatially specific designs, control the location of the induced electric field, control the scale over which structural modifications take place and finally control the reactivity on a glass' surface. The results obtained here also agree with the model and results already presented on BPN 42 glass. The use of structured electrodes leads to an enhancement of the SHG signal at the border of the patterns probably linked to side effects and a higher charge density in these areas. Moreover, on this specific glass composition, not only are the 2nd order nonlinear properties structured but the glass structure is also efficiently modified at a micrometer scale across the pattern. A poling-induced charged surface structure was formed and tailored on a micrometric scale. The poled area also exhibited enhanced surface reactivity towards atmospheric water. This reactivity was only enhanced on the effectively poled area, corresponding to areas in close contact with ITO upon

poling. These new results allow to foresee the use of a micro-poling technique to tailor physical and chemical properties of glasses and to use it for a variety of applications, ranging from photonics to lab-on-a-chip devices.

4.5 Conclusion of chapter 4

This chapter was designed to show that thermal poling can found applications in other domains than nonlinear optics. It can be an effective technique to tailor a glass structure and surface properties. These extended application possibilities were demonstrated on a specific glass composition, carefully chosen for its peculiar structure and properties. It is of the utmost importance to bear in mind that such a tailor of a glass surface properties can only be performed when one has a good understanding of its glass. However, the example presented herein broaden the range of applications of thermal poling and additional surface properties could be modified by thermal poling, such as mechanical properties or optical properties.

The polarized glass presented here presents interesting properties as a host for molecules that could be selectively presents at its surface. Especially, the micro-poling presented in section IV could be interesting to further develop substrates with areas of controlled hydrophilicity. The glass composition presented here might not be the adequate one and additional research on compositions in the same ternary or in more complicated systems are necessary to develop a useful substrate.

Finally, if one thing needs to be remembered from this chapter, it should be that with thermal poling, and especially with the use of patterned electrodes, we now possess a formidable tool to tailor glass substrate on a variety of properties.

4.6 References

(1) Mariappan, C. R.; Roling, B. Mechanism and Kinetics of Na+ Ion Depletion Under the Anode during Electro-Thermal Poling of a Bioactive Glass. *J. Non Cryst. Solids* **2010**, *356*, 720-724.

(2) Hench, L.; Splinter, R.; Allen, W.; Greenlee, T. Bonding Mechanisms at the Interface of Ceramic Prosthetic Materials. *J. Biomed. Mater. Res.* **1972**, *5*, 117-141.

(3) Yamashita, K.; Oikawa, N.; Umegaki, T. Acceleration and Deceleration of Bone-Like Crystal Growth on Ceramic Hydroxyapatite by Electric Poling. *Chemistry of Materials* **1996**, *8*, 2697-2700.

(4) Obata, A.; Nakamura, S.; Moriyoshi, Y.; Yamashita, K. Electrical Polarization of Bioactive Glass and Assessment of their in Vitro Apatite Deposition. *Journal of Biomedical Materials Research - Part A* **2003**, *67*, 413-420.

(5) Nakamura, S.; Kobayashi, T.; Nakamura, M.; Itoh, S.; Yamashita, K. Electrostatic Surface Charge Acceleration of Bone Ingrowth of Porous Hydroxyapatite/ß-Tricalcium Phosphate Ceramics. *Journal of Biomedical Materials Research - Part A* **2010**, *92*, 267-275.

(6) Mariappan, C. R.; Roling, B. Investigation of Bioglass-Electrode Interfaces After Thermal Poling. *Solid State Ionics* **2008**, *179*, 671-677.

(7) Mariappan, C. R.; Yunos, D. M.; Boccaccini, A. R.; Roling, B. Bioactivity of Electro-Thermally Poled Bioactive Silicate Glass. *Acta Biomaterialia* **2009**, *5*, 1274-1283.

(8) Shelby, J. E.; Lopes, M. In *Introduction to Glass Science and Technology;* The Royal Society of Chemistry: 2005; , pp X001-X004.

(9) Tenney, A. S.; Wong, J. Vibrational Spectra of Vapor-Deposited Binary Borosilicate Glasses. *J. Chem. Phys.* **1972**, *56*, 5516-5523.

(10) Bell, R. J.; Carnevale, A.; Kurkjian, C. R.; Peterson, G. E. Structure and Phonon Spectra of SiO2, B2O3 and Mixed SiO2B2O3 Glasses. *J. Non Cryst. Solids* **1980**, *35-36*, 1185-1190.

(11) Kamitsos, E. I.; Patsis, A. P.; Kordas, G. Infrared-Reflectance Spectra of Heat-Treated Sol-Gel-Derived Silica. *Physical Review B* **1993**, *48*, 12499-12505.

(12) Möncke, D.; Ehrt, D.; Varsamis, C. -. E.; Kamitsos, E. I.; Kalampounias, A. G. Thermal History of a Low Alkali Borosilicate Glass Probed by Infrared and Raman Spectroscopy. *Glass Technology: European Journal of Glass Science and Technology Part A* **2006**, *47*, 133-137.

(13) Möncke, D.; Dussauze, M.; Kamitsos, E. I.; Varsamis, C. P. E.; Ehrt, D. Thermal Poling Induced Structural Changes in Sodium Borosilicate Glasses. *Physics and Chemistry of Glasses: European Journal of Glass Science and Technology Part B* **2009**, *50*, 229-235.

(14) Kamitsos, E. I.; Patsis, A. P.; Karakassides, M. A.; Chryssikos, G. D. Infrared Reflectance Spectra of Lithium Borate Glasses. *J. Non Cryst. Solids* **1990**, *126*, 52-67.

(15) Konijnendijk, W. L. The Structure of Borosilicate Glasses, Eindhoven: Technische Hogeschool, 1975.

(16) Furukawa, T.; Fox, K. E.; White, W. B. Raman Spectroscopic Investigation of the Structure of Silicate Glasses. III. Raman Intensities and Structural Units in Sodium Silicate Glasses. *J. Chem. Phys.* **1981**, *75*, 3226-3237.

(17) Kamitsos, E. I.; Chryssikos, G. D.; Karakassides, M. A. New Insights into the Structure of Alkali Borate Glasses. *J. Non Cryst. Solids* **1990**, *123*, 283-285.

(18) Brethous, J.; Levasseur, A.; Villeneuve, G.; Echegut, P.; Hagenmuller, P.; Couzi, M. Etudes Par Spectroscopie Raman Et Par RMN Des Verres Du Système B2O3-SiO2-Li2O. *Journal of Solid State Chemistry* **1981**, *39*, 199-208.

(19) Carlson, D. E.; Hang, K. W.; Stockdale, G. F. Electrode "Polarization" in Alkali-Containing Glasses. *Journal of the American Ceramic Society* **1972**, *55*, 337-341.

(20) Carlson, D. E.; Hang, K. W.; Stockdale, G. F. Ion Depletion of Glass at a Blocking Anode - 1, 2. *J Am Ceram Soc* **1974**, *57*, 291-300.

(21) Carlson, D. E. Anodic Proton Injection in Glasses. *Journal of the American Ceramic Society* **1974**, *57*, 461-466.

(22) Krieger, U. K.; Lanford, W. A. Field Assisted Transport of Na+ Ions, Ca2+ Ions and Electrons in Commercial Soda-Lime Glass I: Experimental. *J. Non Cryst. Solids* **1988**, *102*, 50-61.

(23) Lipovskii, A. A.; Melehin, V. G.; Petrov, M. I.; Svirko, Y. P.; Zhurikhina, V. V. Bleaching Versus Poling: Comparison of Electric Field Induced Phenomena in Glasses and Glass-Metal Nanocomposites. *J. Appl. Phys.* **2011**, *109*.

(24) Cremoux, T.; Dussauze, M.; Fargin, E.; Cardinal, T.; Talaga, D.; Adamietz, F.; Rodriguez, V. Trapped Molecular and Ionic Species in Poled Borosilicate Glasses: Toward a Rationalized Description of Thermal Poling in Glasses. *Journal of Physical Chemistry C* **2014**, *118*, 3716-3723.

(25) Redkov, A. V.; Melehin, V. G.; Lipovskii, A. A. How does Thermal Poling Produce Interstitial Molecular Oxygen in Silicate Glasses? *J. Phys. Chem. C* **2015**, *119*, 17298-17307.

(26) Guimbretìre, G.; Dussauze, M.; Rodriguez, V.; Kamitsos, E. I. Correlation between Second-Order Optical Response and Structure in Thermally Poled Sodium Niobium-Germanate Glass. *Appl. Phys. Lett.* **2010**, *97*.

(27) Dussauze, M.; Kamitsos, E. I.; Fargin, E.; Rodriguez, V. Structural Rearrangements and Second-Order Optical Response in the Space Charge Layer of Thermally Poled Sodium-Niobium Borophosphate Glasses. *Journal of Physical Chemistry C* **2007**, *111*, 14560-14566.

(28) Dussauze, M.; Rodriguez, V.; Velli, L.; Varsamis, C. P. E.; Kamitsos, E. I. Polarization Mechanisms and Structural Rearrangements in Thermally Poled Sodium-Alumino Phosphate Glasses. *Journal of Applied Physics* **2010**, *107*.

(29) Dussauze, M.; Cremoux, T.; Adamietz, F.; Rodriguez, V.; Fargin, E.; Yang, G.; Cardinal, T. Thermal Poling of Optical Glasses: Mechanisms and Second-Order Optical Properties. *International Journal of Applied Glass Science* **2012**, *3*, 309-320.

(30) Dussauze, M.; Rodriguez, V.; Lipovskii, A.; Petrov, M.; Smith, C.; Richardson, K.; Cardinal, T.; Fargin, E.; Kamitsos, E. I. How does Thermal Poling Affect the Structure of Soda-Lime Glass? *Journal of Physical Chemistry C* **2010**, *114*, 12754-12759.

(31) Bethell, D. E.; Sheppard, N. The Infra-Red Spectrum and Structure of Boric Acid. - *Trans. Faraday Soc.* **1955**, *51*, 9-15-15.

(32) Krishnan, K. The Raman Spectrum of Boric Acid. *Proceedings of the Indian Academy of Sciences - Section A* **1963**, *57*, 103-108.

(33) Decher, G. Fuzzy Nanoassemblies: Toward Layered Polymeric Multicomposites. *Science* **1997**, *277*, 1232-1237.

(34) Palleau, E.; Sangeetha, N. M.; Viau, G.; Marty, J. -.; Ressier, L. Coulomb Force Directed Single and Binary Assembly of Nanoparticles from Aqueous Dispersions by AFM Nanoxerography. *ACS Nano* **2011**, *5*, 4228-4235.

(35) Zapol, P.; He, H.; Kwon, K. D.; Criscenti, L. J. First-Principles Study of Hydrolysis Reaction Barriers in a Sodium Borosilicate Glass. *International Journal of Applied Glass Science* **2013**, *4*, 395-407.

(36) Thomas, R. Determination of the H3BO3 Concentration in Fluid and Melt Inclusions in Granite Pegmatites by Laser Raman Microprobe Spectroscopy. *American Mineralogist* **2002**, *87*, 56-68.

(37) Zhenan, G. D-F and F-F Transition Bands of Praseodymium and Samarium Ions in Silica Glasses. *J. Non Cryst. Solids* **1986**, *80*, 429-434.

(38) Sato, R.; Benino, Y.; Fujiwara, T.; Komatsu, T. YAG Laser-Induced Crystalline Dot Patterning in Samarium Tellurite Glasses. *J. Non Cryst. Solids* **2001**, *289*, 228-232.

(39) Chayapiwut, N.; Honma, T.; Benino, Y.; Fujiwara, T.; Komatsu, T. Synthesis of Sm3+-Doped Strontium Barium Niobate Crystals in Glass by Samarium Atom Heat Processing. *Journal of Solid State Chemistry* **2005**, *178*, 3507-3513.

(40) Takagi, H.; Miyazawa, S. -.; Takahashi, M.; Maeda, R. Electrostatic Imprint Process for Glass. *Applied Physics Express* **2008**, *1*.

(41) Myers, R.; Mukherjee, N.; Brueck, S. R. Large Second-Order Nonlinearity in Poled Fused Silica. *Opt. Lett.* **1991**, *16*, 1732-1734.

(42) Rodriguez, V.; Talaga, D.; Adamietz, F.; Bruneel, J. L.; Couzi, M. Hyper-Raman Macro- and Micro-Spectroscopy in Materials: Towards High Quality Signals and Good Spatial Resolution. *Chemical Physics Letters* **2006**, *431*, 190-194.

(43) Yang, G.; Dussauze, M.; Rodriguez, V.; Adamietz, F.; Marquestaut, N.; Deepak, K. L. N.; Grojo, D.; Uteza, O.; Delaporte, P.; Cardinal, T.; Fargin, E. Large Scale Micro-Structured Optical Second Harmonic Generation Response Imprinted on Glass Surface by Thermal Poling. *J. Appl. Phys.* **2015**, *118*.

CHAPTER 5:THERMAL POLING OF CHALCOGENIDE GLASSES IN THE Ge-Sb-S SYSTEM: TUNING THE LINEAR AND NONLINEAR OPTICAL PROPERTIES

Chalcogenide glasses have been seen as potential candidates for thermal poling thanks to their high third order nonlinear susceptibility and their transparency in the mid-infrared (MIR) spectral region. As shown previously in this dissertation, thermal poling results in an induced second (2^{nd}) order nonlinearity ($\chi^{(2)}$) obtained through an electro-optical effect and the interaction of the third order nonlinearity of the glass and the induced electric field. As chalcogenide glasses have the highest third (3^{rd}) order nonlinearity ($\chi^{(3)}$) among glasses, it is thereby expected that they should also result in a high induced 2^{nd} order nonlinearity.[1] Moreover, their transparency in the MIR makes them extremely useful for a variety of applications, especially in sensors that can probe organic molecules which possess fingerprints in this region.

In the literature, chalcogenide glasses (ChGs) have been successfully poled but usually exhibit a major drawback in a lack of stability of the post-poling properties. The relaxation process typically observed in compositions studied to-date has been fast (time, t ~ hours to days) making the poled glasses unsuitable for most applications.

The portion of this PhD examining poling of chalcogenide glasses has focused on finding ways to stabilize the post poling properties through a selective choice of the composition to be poled and extending our understanding of the role of various poling parameters and glass structural changes on post-poling properties. Once a suitable composition and parameters was identified, another aim of this work has been to adapt the μ-imprinting on chalcogenide glasses to tailor and control the

optical properties via thermal poling. As will be shown, this work has resulted in an extension to the understanding of the mechanism of poling, and its stability, in ChGs.

This chapter will be separated in several sections. The first describes the choice of glass composition and the glass' properties and structure before poling.

The second part of the chapter is focused on thermal poling of these glass compositions with an emphasis on the effect of glass network, charge carrier nature and poling parameters on post poling properties and structure. The aim of this part is to identify potential differences in the poling mechanisms as the cationic content increases. Emphasis is put on the origin of the post-poling properties and on stability.

Finally, the last section will show ongoing work on the μ-poling adapted to chalcogenide glasses. Specifically, the work presented shows how thermal poling can be used to modify a glass' optical properties both linearly and non-linearly. Highlighting our understanding of the mechanism in these glasses is a specific example of tailoring surface properties and optical properties through the fabrications of μ-lenses and diffractive gratings in the poled glass surface.

5.1 Study of the chalcogenide glasses prior poling

5.1.1 Choice of the glass compositions

Chalcogenide glasses (ChGs) are interesting for thermal poling due to their high third order nonlinear susceptibilities which is directly proportional to the induced 2^{nd} order nonlinearity. Among them, selenium based and tellurium based glasses have the highest $\chi^{(3)}$ while sulfur glasses have the lowest.[1] However, selenium and tellurium-based glass systems also present drawbacks for thermal poling applications which are discussed here.

The main drawback of ChGs is their high electronic conductivity which makes them semi-conductor-like.[2, 3] As discussed in earlier chapters, thermal poling is performed on dielectric media and a high electronic conductivity could lead to difficulty to pole them as the high electric field is applied across the sample. [4] Chalcogenides also exhibit low glass transition temperatures and large glass-forming regions, which makes them attractive for their tailorable optical and physical properties. As stated earlier, post-poling stability is the main issues with poled chalcogenides, as sub-T_g relaxation and long term aging could further degrade desired post-poled property stability. [5, 6] A low T_g is thus not suitable as it would be easier for the glass network to re-arrange and for the charges to be neutralize in the glass matrix even at room temperature.

Finally, even if selenium and tellurium-based systems benefit from excellent transparency in the infrared window which is important for this effort, these attributes can be an issue in our study as the Se and Te ion's size and electronic properties, affects both structure and free volume. IR transparency in these glasses is determined by composition and is accompanied by a low bandgap and thus ChGs are not transparent in the visible spectrum, but become transparent in the 1 μm range. However, this is a necessary criterion for our study as our 1550 nm Maker fringes experimental setup requires glasses to be transparent at the 2ω wavelength (775 nm). Sulfur-based glasses on the other hand present a partial transparency at this wavelength that is sufficient for our study.

Since Se and Te-based materials often are not transmissive to near-infrared radiation, sulfur glasses are more attractive as they have a short wavelength cutoff wavelength in the visible region as low as 500 nm. They also have a more rigid glass network and higher glass transition temperature, as high as 360°C, due to a slightly higher bond strength as compared to the heavier metal-chalcogen

bonds with Se and Te. Additionally, sulfide glasses have electronic conductivity which is also lower than in selenium or tellurium based glasses. It is then necessary to choose the other elements which will enter the composition which do not adversely affect transmission, conductivity while providing a strong network backbone.

Among the sulfur glasses, the ternary Ge-Sb-S is a good candidate as its vitreous domain has been well described in the literature. Additionally, this material system has been well studied in our group and among others. Specifically, these glasses exhibit a reasonably high T_g, they are modestly transparent in the visible and have been previously shown to be compatible with the poling process as documented by Guignard et al. [7-10]

The presence of antimony in the composition is suitable to this desired application as it improves the glass' stability (aka, resistance to crystallization). Moreover, during melting of the glass, antimony and sulfur react together to form an intermediate compound which makes the melting process easier. Finally, none of the elements in the chosen ternary are present in the list of restricted substance in the REACH regulation of the European Union. [11] This regulation has been adopted to protect the environment and human health and has listed a series of substance with industrial use restriction (such as arsenic, lead, etc…). In the prospect of future industrial applications, potentially within the European market, restricted elements were not considered in this study.

The first glass in this ternary is the stoichiometric composition $Ge_{25}Sb_{10}S_{65}$. For this effort, it was decided to change the ratio of germanium to sulfur, going towards a composition with excess sulfur. A glass possessing excess sulfur will possess S-S homopolar bonds which should be especially interesting in our study as they add lone pairs which tend to increase the third order

nonlinear susceptibility of glasses. It has been shown that a high third order nonlinear susceptibility also yields the potential of a higher second order nonlinear response after poling. Too large of an excess however, will make the glass network less rigid by adding flexibility through creation of these sulfur-sulfur bonds resulting in the decrease of the glass transition temperature, potentially reducing the glass' post-poled stability. Hence, here a tradeoff is necessary. Glasses with an excess of germanium would have been more rigid but were not chosen as they do not present a suitable transparency in the visible region, necessary for some of our measurements. Hence, four glasses with increasing sulfur content were chosen to study the effect of sulfur excess as are discussed below.

The mechanism of formation of the trapped charges in chalcogenide is at the center of the stability process as it applies to poled glasses. Even if these glasses theoretically do not contain alkali, it has been shown that they are present in ppm concentration and that they play an important role in the process. In thermal poling of oxide glasses, cation migration is at the origin of the creation of a stable space charge responsible for the induced electric field. In addition to the base glasses, it was decided to dope these glasses with sodium through the incorporation of sodium sulfide Na_2S in the glasses with doping level of 1 mol% and 3 mol%. Sodium was chosen as it has a good mobility and that in previous study of thermal poling in chalcogenide, it played an important role in the process even at ppm level. [4] Other mobile cations could have been picked such as other alkali or alkaline-earth elements, as well as metals (silver, lead…). As discussed previously, some of these elements were not chosen as they fall under the REACH legislation (lead for instance) but others could be considered for future studies (silver for instance). Sodium's main advantage is that

it moves easily under an electric field and it is expected to change the glass's network and optical properties. It should give an additional lever to tailor post-poling properties.

The purpose of changing the glass composition (sulfur excess variation) is to evaluate the link between structure of the glass and final properties and stability of the post-poled glasses. When discussing the role of the structure regarding properties in chalcogenide, it is necessary to introduce the notion of mean (or average) coordination number (MCN). Chalcogenide glasses are known to be covalent semiconductors which is going to affect their physical and chemical properties. To better describe the glass network and its effect on properties, several propositions have been made in the literature. Especially, the average coordination number has been the center of multiple articles in the chalcogenide literature. The mean coordination number represents the average number of bonds in the glass network and is calculated as follow:

$$< MCN >= \frac{4x + 3y + 2z}{100} \qquad (5.1)$$

with x, y and z respectively the atomic percentage of germanium, antimony and sulfur (in our case). The weighing factors of each constituent are the coordination number of each element, on the assumption that germanium is 4-fold coordinated (CN=4), antimony 3-fold coordinated and sulfur 2-fold coordinated (CN=3 and 2, respectively).

The average coordination number is especially important as it has been shown to be correlated to peculiar changes of properties and structure of the glass. A threshold was found in the literature when <MCN> is equal to 2.4. [12-15] At this point, the system is said to be stable, below this point, the system is under-constrained or floppy while above this threshold, the network is over-constrained, thus rigid. This threshold point (T) has been referred to as PTT, after Phillips and

Thorpe, the authors who first discussed it. Later, Tanaka proposed another vision of a chalcogenide glass, by suggesting that some chalcogenide networks were formed of two-dimensional entities and that these layers of entities are forming a 3-D network. The threshold was also modified and a new point at 2.67 was proposed as a criterion for a stable glass. This threshold is referred to as the Tanaka threshold, i.e. the TT. [16]

Several studies have followed, studying the evolution of various properties as a function of the average coordination number and of these two thresholds. Glasses prepared in our study lie above the PTT criteria and below the TT criteria for stable glasses, with the stoichiometric composition being close to 2.67. It was not possible to study glasses above the TT criteria of stability as their transparency in the visible was not adequate for the Maker fringes measurements.

The four glass compositions chosen in our study and their average coordination number are reported in the following table. In the rest of this chapter, we will identify the glasses with letter (from A to D). A, in the study represents the stoichiometric composition and D the composition with the highest sulfur content, with its excess S being furthest from the stoichiometric compositions level of S-S bonds. In the series, S additions are made at the expense (reduction) of Ge content and the Sb level remains constant. All glass compositions in Table 5.1 are reported in molar percent.

Table 5.1. Mean coordination number calculated for the base glasses

Glass composition	**$Ge_{25}Sb_{10}S_{65}$ (A)**	**$Ge_{22.5}Sb_{10}S_{67.5}$ (B)**	**$Ge_{20}Sb_{10}S_{70}$ (C)**	**$Ge_{17.5}Sb_{10}S_{72.5}$ (D)**
<MCN>	2.6	2.55	2.5	2.45

5.1.2 Characterization of the glass properties prior poling

5.1.2.1 Thermal analysis

The glass transition temperature of all the prepared glasses was measured using standard thermal analysis techniques, as discussed in chapter 2. Figure 5.1 shows the evolution of the glass transition temperature of the base glasses measured after melting and annealing processes.

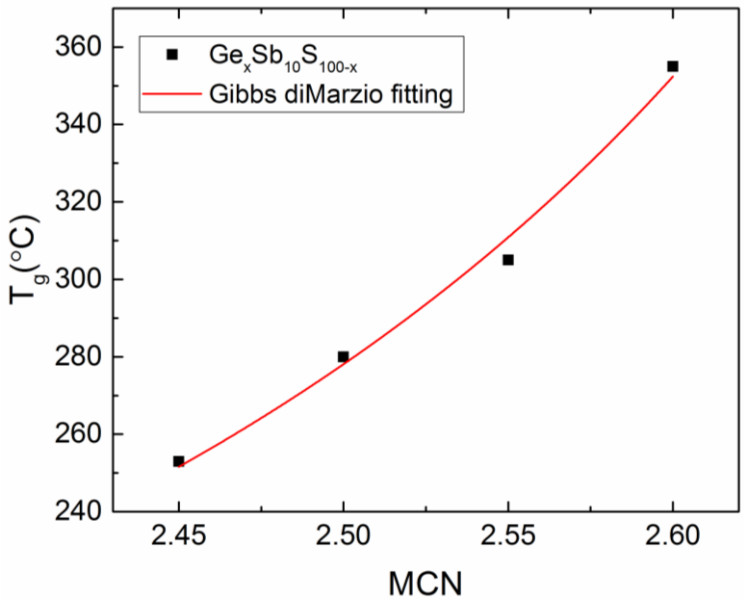

Figure 5.1. Evolution of the glass transition temperature of the base glasses as a function of MCN (black), Gibbs DiMarzio fitting (red). Compositions vary from D to A (from low to high CN)

The data were fitted using the Gibbs-DiMarzio equation which successfully describes the evolution of the glass transition temperature as the sulfur chains length increases. The Gibbs-DiMarzio equation is defined as [17]

$$T_g = \frac{T_0}{[1 - \beta(MCN - 2)]} \tag{5.2}$$

where T_0 is the glass transition temperature of pure sulfur (a fitting parameter here), β is a fitting parameter too while the MCN was previously calculated.

The fitting parameters in the Gibbs DiMarzio equation were found to be equal to T_0=135.39, β=1.02 giving a r^2 of 0.9917. The glass transition temperature of the base glasses increases with an increase of the MCN of the glass's network as the length of the sulfur chains decreases and the network gets more rigid with addition of CN=4 Ge, as one approaches stoichiometry.

The measured glass transition temperatures (inflection point) in the base glasses and glasses with addition of sodium are reported in Table 5.2.

Table 5.2. Glass transition temperature (T_g) of glasses A, B, C and D with and without sodium addition

	T_g (°C) **0 mol% Na_2S**	**T_g (°C)** **1 mol% Na_2S**	**T_g (°C)** **3 mol% Na_2S**
A	355	314	N/A
B	305	267	260
C	280	257	N/A
D	253	246	N/A

As expected, an increase of the sodium content leads to a decrease of the glass transition temperature, associated with the formation of non-bridging units in the structure. Further increase of the sodium content in the glass continues to decrease the glass transition temperature but to a lesser extent. The addition of one percent of sodium sulfide resulted in the appearance of a crystallization exotherm for composition A with at 482°C. The other compositions do not show any crystallization peak in the range of measurements, indicating a better stability of the glass

compositions against crystallization. A difference of 170°C between the T_g and T_x of the glass ($\Delta T = T_x - T_g$) is however considered large enough to form a stable glass.

5.1.2.2 Density

The densities of all base glasses were measured following the protocol described in chapter 2 and are plotted in Figure 5.2 as a function of mean coordination number, which evolves with varying sulfur content.

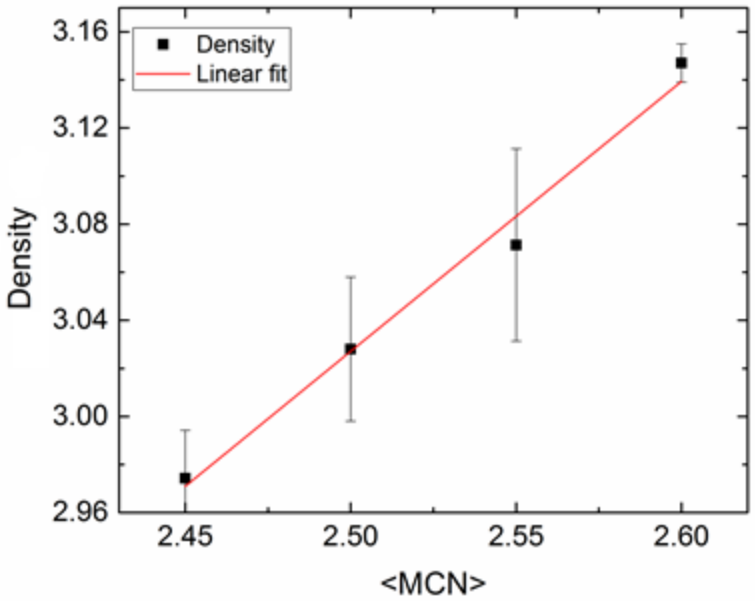

Figure 5.2. Evolution of the density as a function of mean coordination number (MCN)

As the sulfur content increases and the germanium content decreases, the density of the glasses decreases almost linearly. Glasses of the Ge-Sb-S compositions were previously studied in the literature and the density measured previously are given here as a comparison. Especially, Vahalová studied the properties and structure of glasses of same composition as sample A, C and D. [18] He measured density of respectively, 3.16, 3.03 and 2.98. Linke et al. [19] and El-Hamalawy [20] also studied similar glasses and respectively found densities of 3.13 and 3.35 for glass A. El-

Hamalawy also measured density on glass C and found a value of 3.19. Our results agree well with the work of Vahalová and Linke but there is a large difference with the work of Hamalawy. Overall, the same trend was observed in every work, as the network becomes "floppier" with increasing sulfur content, the density decreases almost linearly which agrees with a less dense and more flexible glass network.

In addition, the density of the glasses with addition of sodium (1 mol%) were measured. All measured densities are reported in Table 5.3.

Table 5.3. Measured density of the glasses A, B, C and D with and without addition of Na_2S

	Density (0 mol% Na_2S)	**Density (1 mol% Na_2S)**
A	3.15	3.21
B	3.07	2.99
C	3.03	3.03
D	2.97	2.99

The densities measured for the base glasses are indeed close to the measurements of Vahalová and Linke. For composition B, C and D, addition of sodium to the glasses do not lead to large variation but the glass' density tends to decrease. The density of glass A is however greatly increased with the addition of sodium sulfide. Even if the density of glass D also increased with addition of sodium sulfide, it varies to a lesser extent and actually stays rather stable. It is suspected that the sodium containing glass A, which presents the lower crystallization temperature, partially crystallizes during quenching and annealing. The formation of a partially crystallized glass could explain the

higher density of the glass. Further structural investigations are necessary to confirm this hypothesis.

5.1.2.3 Linear optical properties

5.1.2.3.1 UV-Vis transmission

The UV-Vis absorption spectra of all glasses were measured (as described in chapter 2) and the spectrum of glass B is given as an example in Figure 5.3. The other spectra of the glasses are shown in appendix B. The spectra give information on the absorption edge which is associated with the energy of their forbidden band between the valence band and the conduction band. It also gives information on their maximum of transmission which is related to the Fresnel losses (and so to the refractive index of the glass).

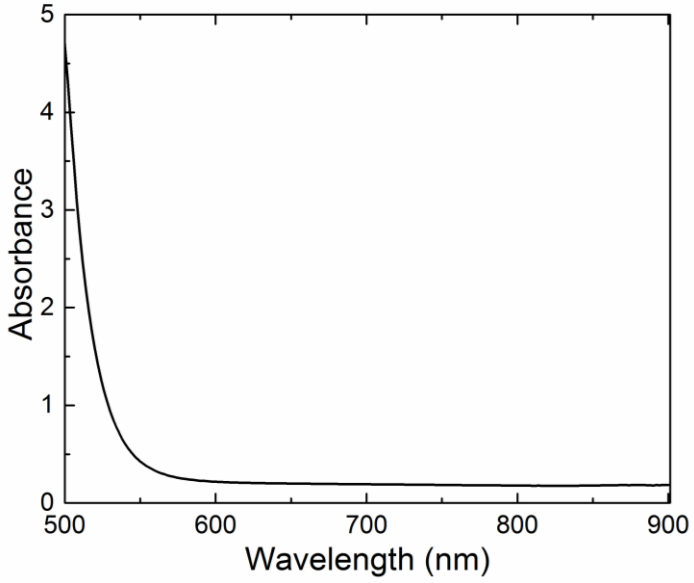

Figure 5.3. UV-Vis spectrum of glass B ($Ge_{22.5}Sb_{10}S_{67.5}$)

It is difficult to measure the optical band gap on bulk samples, thin films are more appropriate for this measurements and a Tauc power low would only give approximations. [21, 22] The band gap is

therefore not measured here and the absorption spectra are used only to approximate the absorption edge. The cut-off wavelength will be defined as the wavelength at which the absorption is equal to 10 cm^{-1}. The cut-off wavelength of the base glasses and doped glasses are given in Table 5.4.

Table 5.4. Cut-off wavelength in the visible for glasses with and without Na_2S

	Cut-off wavelength (nm)	**Cut-off wavelength (nm)**	**Cut-off wavelength (nm)**
	0 mol% Na_2S	**1 mol% Na_2S**	**3 mol% Na_2S**
A	557	551	N/A
B	537	557	563
C	535	553	N/A
D	538	560	N/A

The cut-off wavelength reported here are just indicative and were measured to determine the transparency of the glasses for the measurements that will be performed later on. The Maker fringes set-up that we use is adapted to these compositions as the 2ω frequency is at 775 nm so no absorption should take place. From these measurements, it appears that sulfur excess shifts the cut-off wavelength to lower values. Regarding the role of sodium, as it is added to the composition, the cut-off wavelength shifts to higher wavelength except for glass A for which it decreases. The sodium containing glass A once again presents an opposite behavior to the other glasses.

5.1.2.3.2 IR transmission

IR transmission spectra were recorded on the glasses to determine their multi-phonon absorptions. Figure 5.4 shows the transmission spectra of the B series which is representative of all compositions. The other IR transmissions spectra are given in appendix C.

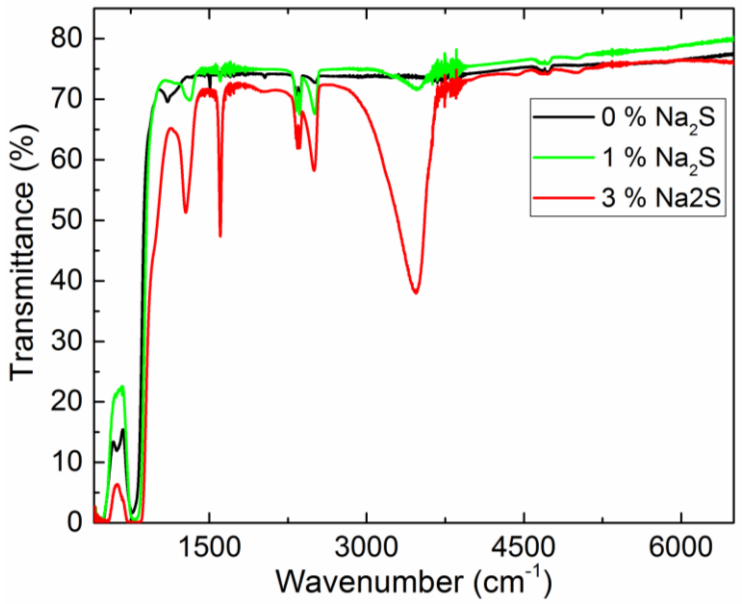

Figure 5.4. Transmittance spectra in the infrared of the B series with 0, 1 and 3% of Na_2S.

From all compositions, the end of the transparency window in the mid-IR region is at 10.5 µm. The samples are thus transparent from approximately 550 nm to 10.5 µm but several absorptions due to impurities exist in the mid-IR.

The absorption bands in the mid-IR can be linked to several impurities that are common in chalcogenide glasses prepared without additional purification steps. Absorption linked to presence of water, either as H_2O or as OH impurities, is responsible for the broad band near 3500 cm^{-1} and 1600 cm^{-1}. The band around 2500 cm^{-1} can be attributed to S-H stretching vibrational modes. A smaller band is observed around 2359 cm^{-1} and could be linked to molecular H_2S. Finally, a band between 1270 and 1315 cm^{-1} is attributed to S-O complexes. [23] As the sodium content increases so does the water contributions in the IR spectrum and the oxygen contamination bands. Na_2S is known to be hygroscopic and is directly linked to the presence of water in the composition. It was

suspected that addition of sodium to the composition could lead to the formation of a hygroscopic glass. Samples were left in the atmosphere and transmission spectra were recorded over time to check for a potential increase of this water band. No sign of change of the water band intensity was observed; hence it was concluded that most of this band originates from OH groups inside the glass network and not on the surface. The presence of these impurities in the glasses impact the optical properties of the materials. In the future, purification of the raw materials will be necessary and should lead to the disappearing of these bands and to a change in optical properties (transmission window, refractive index, …).

5.1.2.3.3 Linear refractive index and coherence length

The refractive indices of the glasses were measured using the two techniques presented in the experimental chapter. An example of plot with the Cauchy fit obtained for the composition A is shown in Figure 5.5. The Cauchy law describes the evolution of the refractive index as a function of wavelength and is written as:

$$n = n_0 + \frac{A}{\lambda^2} \tag{5.3}$$

The parameter of the Cauchy fit for all compositions are then reported in the with λ_ω is the wavelength of the incident laser light, n_ω and $n_{2\omega}$ are respectively the refractive index at the ω and 2ω frequency. The coherence lengths (Lc) of the various glasses are given in the same table as the Cauchy parameters.

Table 5.5. A Cauchy law was preferred over a Sellmeier equation, as we did not have enough experimental data to perform a good fit with the Sellmeier law. A Sellmeier equation usually necessitates at least seven (7) points of measurements at different wavelengths and we were not

able to carry out such analysis. However, while the Cauchy law does not perfectly describe the evolution of the refractive index in the infrared region, it is more suitable to use in the visible region. Therefore, the point at 4.5 µm was removed from the data set as it is too far in the infrared. In addition, the presence of absorption bands due to impurities in the infrared can also lead to large changes in the imaginary part of the refractive index (absorption) leading to changes in the linear part of the complex refractive index (linear part of the refractive index). The Cauchy fit was thus only performed between 639 and 1550 nm.

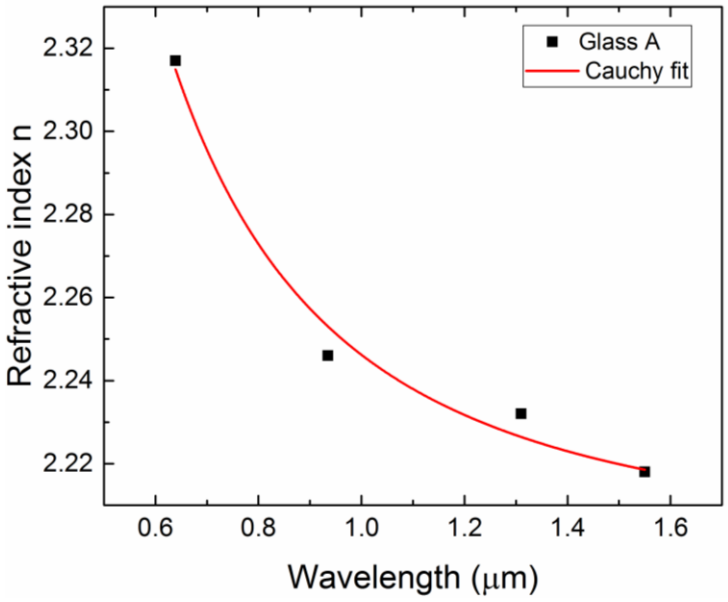

Figure 5.5. Refractive index measured on sample A along with its Cauchy fit

In Figure 5.6, the evolution of the refractive index at 4.5 µm was plotted as a function of mean coordination number for the base glasses and for the Na-rich glasses. In these measurements, the error is typically within the data point. It is observed that as the glass network gets more rigid, the refractive index of the glass increases. A glass can be seen as a solid solution and therefore its refractive index can be estimate using mixture rules such as the one developed by Gladstone and

Dale for minerals. [24] Pure germanium has a high refractive index of 4.01 at 4.5 µm, as the network goes towards higher germanium content, the refractive index therefore increases. Addition of sodium sulfide to the glasses leads to a slight increase of refractive index. This also can be linked to the glass composition. As sodium is added, the glass composition slightly deviates from its nominal composition, going towards the germanium rich region therefore increasing the refractive index. In addition, it was observed that sodium addition was associated with higher absorption band in the infrared, this can also lead to an increase of the refractive index in the infrared.

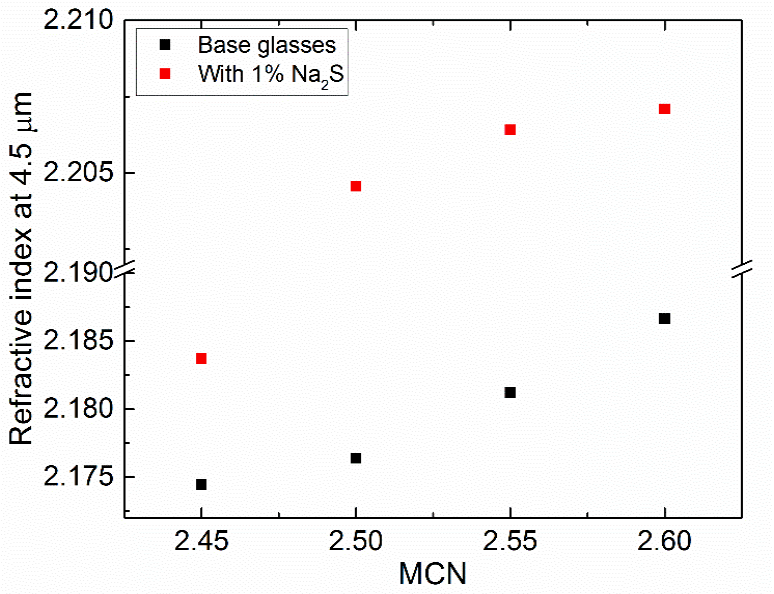

Figure 5.6. Evolution of the refractive index at a function of mean coordination number at 4.5 µm for Na-free and Na-rich glasses

From the refractive index, it is also possible to calculate the coherence length which is an essential parameter during the Maker fringes measurements. The following equation allows to calculate the coherence length (L_c)

$$L_c = \frac{\lambda_\omega}{4.(n_{2\omega} - n_\omega)} \quad (5.4)$$

with λ_ω is the wavelength of the incident laser light, n_ω and $n_{2\omega}$ are respectively the refractive index at the ω and 2ω frequency. The coherence lengths (L_c) of the various glasses are given in the same table as the Cauchy parameters.

Table 5.5. Cauchy parameters and coherence length for all prepared glasses

	n_0	**A**	**L_c (µm) for λ_ω = 1550 nm**
A - 0% Na_2S	2.191	0.052	6.0
A - 1% Na_2S	2.206	0.0599	7.4
B - 0% Na_2S	2.183	0.051	8.8
B - 1% Na_2S	2.194	0.0593	7.4
B - 3% Na_2S	2.199	0.0595	7.5
C - 0% Na_2S	2.17	0.0669	6.7
C - 1% Na_2S	2.201	0.0465	9.5
D - 0% Na_2S	2.167	0.0542	8.2
D - 1% Na_2S	2.175	0.0586	7.5

5.1.2.4 Structural study of the glasses

X-ray diffraction was used to confirm the glassy nature of the prepared materials. Raman and infrared spectroscopy were used to study the network structure (see experimental techniques chapter). Both techniques give similar information on the glass' structure and spectra of the base glasses will be described here.

5.1.2.4.1 X-ray diffraction

The amorphous nature of the prepared glasses was first checked using X-ray diffraction. All glasses presented amorphous features with broad bands such as the one presented here for the glass composition B 1% Na_2S.

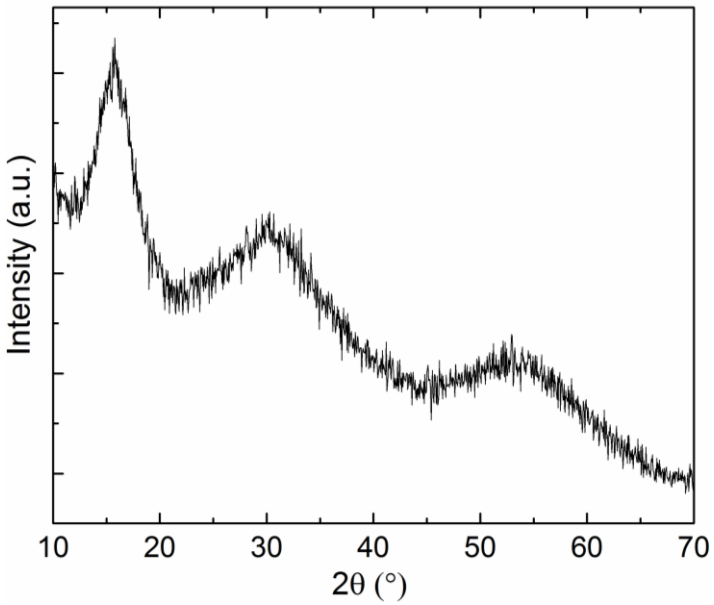

Figure 5.7. XRD spectrum of the glass composition B - 1% Na_2S

5.1.2.4.2 Raman study

The reduced Raman intensity was calculated and the spectra were normalized to the most intense band. The reduced Raman spectra of the base glasses, $Ge_{25}Sb_{10}S_{65}$ (A), $Ge_{22.5}Sb_{10}S_{67.5}$ (B), $Ge_{20}Sb_{10}S_{70}$ (C) and $Ge_{17.5}Sb_{10}S_{72.5}$ (D) are presented in the Figure 5.8.

Similar glasses have been investigated in the literature and present features found in the spectra presented here. Especially, the work of Koudelka et al. [25] on the study of the Ge-Sb-S system in the sulfur rich region showed spectra of glasses with similar compositions. The main vibrational band around 340 cm^{-1} is associated with the symmetric elongation of GeS_4 tetrahedra. [26] This band

overlaps with the band around 302 cm^{-1} associated with the vibrational mode of SbS_3 pyramids which is thus hard to resolve. Two other modes at 375 and 415 cm^{-1} can be identified and respectively attributed to two edge sharing GeS_4 tetrahedra ($Ge_2S_4S_{2/2}$) and two corner sharing GeS_4 tetrahedra (two tetrahedra connected through a bridging sulfur $S_3Ge\text{-}S\text{-}GeS_3$). As the sulfur content increases, a decrease of the two modes at 375 and 415 cm^{-1} is observed which shows that the association of GeS_4 tetrahedra by edge or corner sharing is reduced. Addition of sulfur is accompanied by the apparition of new modes at 151, 218 and 475 cm^{-1}. [27] It is worth noting that the two bands at 150 and 210 cm^{-1} only appear when the sulfur content is higher than 70 %. The band around 475 cm^{-1} is related to S-S bonds and shows that theses homopolar bonds are especially present at high sulfur content. As the sulfur content continues to increase, the two additional modes at 151 and 218 cm^{-1} appear and are characteristic of S_8 ring molecules. This is in agreement with the literature where the 3 modes of the S_8 rings were only observed for sulfur content above 70%. [25] The presence of S_8 rings in the glasses was discussed by Koudelka who ruled out the possibility of phase separation in the glass. There is no sign of extensive phase separation as the sulfur content increases and it is possible that the main glass network and the S_8 form a homogeneous solid solution. However, the presence of phase separation at a smaller scale (nanometric scale) is not impossible and would necessitate TEM analysis.

Raman spectra provide an indication of the glass composition's bonding configuration as they present the same features as same glass compositions discussed in the literature.

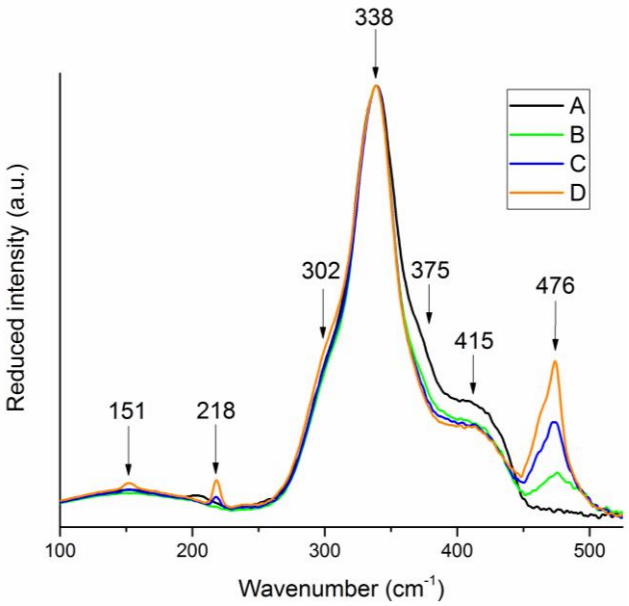

Figure 5.8. Raman spectra of the Na-free base glasses

Following addition of sodium sulfide to the compositions, reduced Raman spectra presented in Figure 5.9 were obtained and present several differences from the base glasses.

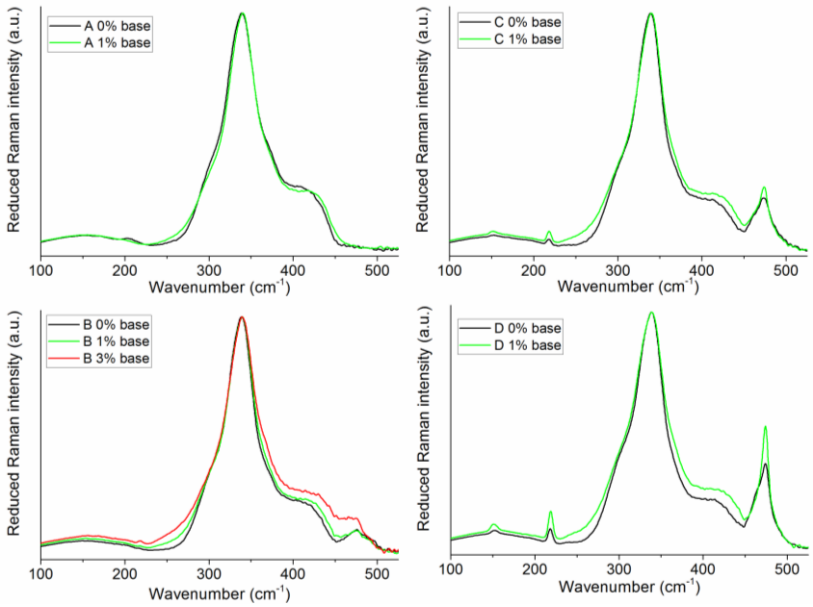

Figure 5.9. Reduced Raman spectra of the base glasses (black) compared to the glasses with addition of 1% sodium sulfide (green) and 3% sodium sulfide (red)

The main difference in the Raman spectra involves modes of to the sulfur-related bands (in the long wavenumber region) which are more present compared to the base glass, especially modes at 415 and 475 cm^{-1}. In addition, the main band at 340 cm^{-1} shifts to higher wavenumber with sodium addition by approximately 2 cm^{-1}. Moreover, the fine contributions attributed to S_8 in the sulfur excess region gets sharper with sodium addition, which effect is especially noticeable for composition D. These modifications are especially observed as we deviate from the stoichiometric composition. Overall, the deviation from the spectra of the base glass is more pronounced on the composition B doped with 3% of Na_2S. It is important to understand the role of the addition of sodium sulfide on the glass structure. By adding an alkali to the glass matrix, we add a potential modifier to the network. It is therefore plausible that non-bridging sulfur are created across the network. As the sodium addition seems to impact the sulfur-sulfur bonds, it is suspected that sodium preferentially breaks S-S bonds. One sulfur is then balanced by the neighboring sodium, but the other S needs to re-arrange. In this study, the hypothesis was made that when two S-S homopolar bonds are broken, the two sodium added will compensate for the dangling electrons associated with the split bond, while the two remaining sulfur will be bonded through the extra sulfur added to the composition, therefore creating longer chains of sulfur. This could explain changes observed in the Raman spectra with increasing sodium sulfide addition.

As alluded to previously, we had reason to suspect a low level of partial crystallization in composition A with 1% of sodium sulfide. Crystals could actually be observed in optical microscopy and Raman spectra recorded in the same region and showed fine peaks indicating partial crystallization of the composition. The optical micrograph and Raman spectra recorded on this composition are shown in the Figure 5.10.

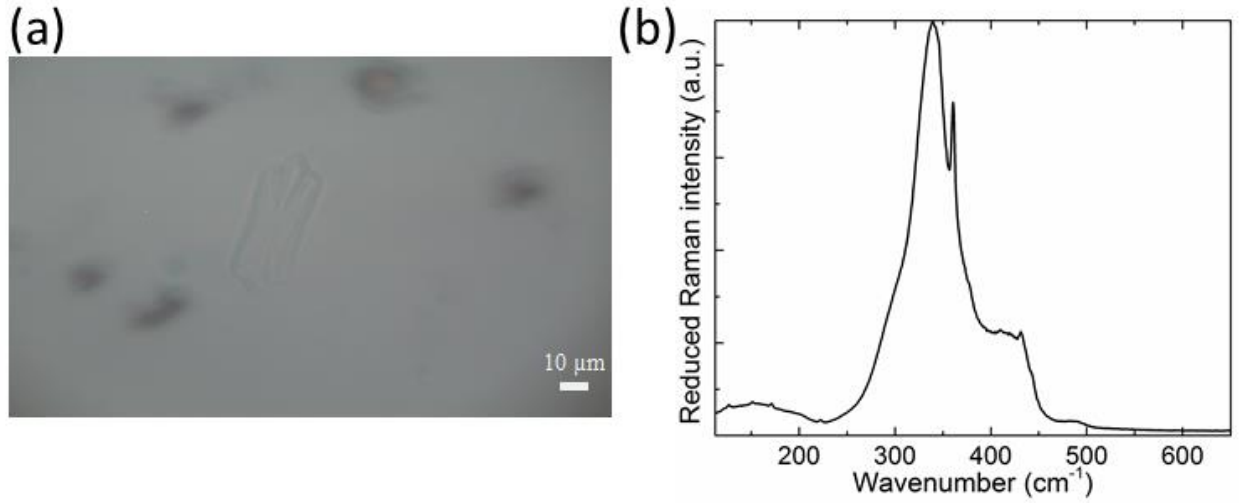

Figure 5.10. Optical micrograph of a crystal present in the composition A -1 % Na_2S (a) and corresponding Raman spectrum (b)

Fine peaks at 127, 170, 360 and 431 appear on the glass spectrum. The presence of these peaks in the germanium sulfide signature region suggests the possible crystallization of germanium disulfide, GeS_2. Due to a lack of experimental Raman spectra in the literature for this crystalline phase, it was not possible to confirm this result.

As no sign of crystallization was found in powder and bulk XRD it is assumed that the size or number density of crystals that precipitated in the glass, were small, making the material appear 'x-ray amorphous'.

5.2 Thermal poling of chalcogenide glasses

5.2.1 Thermal poling of the Na-free glasses

The first part of this work focuses on thermal poling of the Na-free glasses, followed by a discussion on Na-containing glasses. In all experiments, glasses were poled with a DC bias of 3000 V under nitrogen for 30 minutes at 170°C.

5.2.1.1 Maker fringes of thermally poled Na-free glasses

As described in chapter 2, the Maker fringes set-up was used to measure the second harmonic generation and determine the origin of the induced 2nd order nonlinear property. Once poled, Maker fringes were recorded on the poled glasses with the same measurement conditions and then normalized to the incident intensity ($I_{2\omega}/(I_{\omega})^2$).

The first step of the Maker fringes measurements consists in measuring θ-pp scans (incident beam p-polarized and detection collecting only p-polarized signal at the second harmonic). These scans allow to check the homogeneity of the SHG response and to have first insights on the origin of the signal. Figure 5.11 shows the recorded θ-pp scans after thermal poling of the four glass compositions.

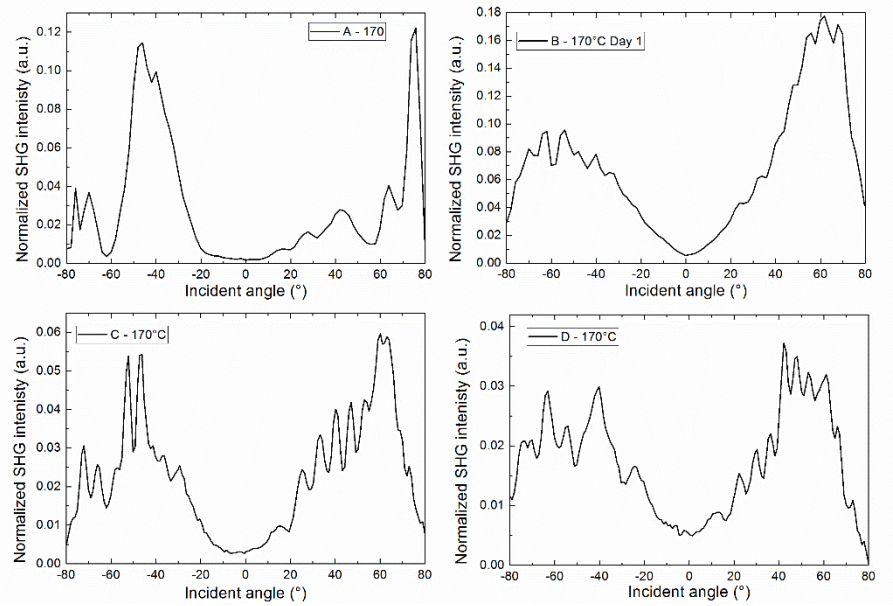

Figure 5.11. θ- pp scans recorded on the freshly poled samples

Several features of these scans should be highlighted. Overall, they present a lack of symmetry which is a sign of a lack of homogeneity in the induced electric field. in the poling process. Indeed, θ-scans vary the optical path inside the sample and therefore allow to probe the homogeneity. Then it is observed that after a slight increase of the maximum intensity of the SHG going from A to B, further addition of sulfur is associated with a significant decrease of the SHG intensity. Additionally, sulfur excess leads to the appearance of additional modulation features on the fringes, especially visible for composition C and D. In a classical thermal poling, the SHG comes from an active zone buried few microns under the anodic surface while the bulk of the glass gives a negligible contribution as compared to the near anodic region. The observed modulation in the spectra suggests that there is a non-negligible contribution from the bulk glass to the signal with a sign opposite to the signal generated in the thin near-anodic layer. In addition, multiple fringes are suggesting that the nonlinear active layer thickness is greater than the coherence length.

A significant change from the classical poling response in glass is observed in this study and needs to be highlighted. As soon as the glass composition deviates from the stoichiometry (decreasing Ge with an increase in S), a SHG signal is recorded at normal incidence. This contribution has not been found to be present in samples which inversion symmetry is solely broken by the frozen electric field along the z direction. This is thus evidence of an additional contribution to the signal. This additional contribution is present in compositions B, C and D with similar intensities. As this signal is present at normal incidence, it is linked to in-plane components of the SHG response of the material.

Following measurements of the Maker fringes, the data are then fitted to a model of an EFISH contribution along a longitudinal direction to validate the origin of the induced SHG signal. The glass is divided in two layers: the first layer is the nonlinear active layer created at the anode and the second one is the remaining bulk. The first layer is usually few microns thick and is SHG active, the second layer has a thickness close to one millimeter and usually has no SHG activity. When over-modulation of the scans such as those observed for compositions C and D are seen, a contribution from the bulk with opposite sign to the fine layer is defined. For a purely EFISH process, the electric field is induced along a longitudinal direction and the $\chi^{(2)}$ is obtained through the combination of the $\chi^{(3)}$ of an isotropic medium and the static electric field:

$$\chi^{(2)}(-2\omega;\ \omega,\omega\ ) = 3\chi^{(3)}(\text{-}2\ \omega;\omega,\omega,0).E_{DC} \qquad (5.5)$$

the $\chi^{(2)}$ tensor can be written as,

$$\begin{bmatrix} 0 & 0 & 0 & 0 & d_{31} & 0 \\ 0 & 0 & 0 & d_{31} & 0 & 0 \\ d_{31} & d_{31} & d_{33} & 0 & 0 & 0 \end{bmatrix} \quad (5.6)$$

Terms of the $\chi^{(2)}$ tensor are constraints as for the case of a purely EFISH system, the ratio d_{33}/d_{31} is equal to 3. The model then allows to determine the thickness of the SHG active layer, the coefficients of the $\chi^{(2)}$ tensor and the value of the induced electric field for compositions of known $\chi^{(3)}$. For the Maker fringes of Figure 5.11, the lack of symmetry and additional contribution to the SHG signal in the plane of the glass surface does not allow to fit the data. The SHG response thus cannot be solely described by an electric field induced along z.

Finally, an important finding in our study and a key outcome from this work, is the measured stability of the induced 2nd order nonlinear properties. To measure post-poling stability of the thermally poled specimens (samples were stored under ambient laboratory conditions, in the dark at room temperature) the Maker fringes of the poled samples were systematically measured over a period of 90 days to assess the stability of the induced optical property modification. For the Na-free glass, fast decay of the SHG was observed and no signal was measured two weeks after thermal poling. The stability of the frozen in charges at the origin of the static electric field is therefore quite poor. This 'benchmark' material response served as a baseline for efforts in other compositionally-modified glasses, where the impact of glass network on the post-poled stability, could be correlated to glass network structure.

5.2.1.2 Study of potential structural changes in Na-free glasses using Raman spectroscopy

In a classical thermal poling experiment, such as the one presented in chapters 3 and 4, the DC bias applied across the glass sample leads to migration of cationic species and structural re-

arrangements of the glass matrix. Chalcogenide glasses are theoretically free of the cationic species found in oxide glasses (mainly alkali and alkaline-earth elements), but it has previously been suggested that some form of cation migration was taking place in chalcogenide upon poling. [4] These cationic species (mainly sodium) were coming from impurities at the ppm concentration level. As part of this study, we aimed to address this conclusion specifically, and evaluate the impact of the addition of known quantifies of cation species to the glass and their migration. Here, we aimed to compare the structural response of these doped glasses via Raman spectroscopy, to that of the alkali free material's response as observed in the prior section. Figure 5.12 shows the Raman spectra recorded for the 4 base glasses and the poled Na-free samples. As a reminder, sample A corresponds to the stoichiometric composition ($Ge_{25}Sb_{10}S_{65}$) while the three other compositions correspond to $Ge_{22.5}Sb_{10}S_{67.5}$, $Ge_{20}Sb_{10}S_{70}$ and $Ge_{17.5}Sb_{10}S_{72.5}$.

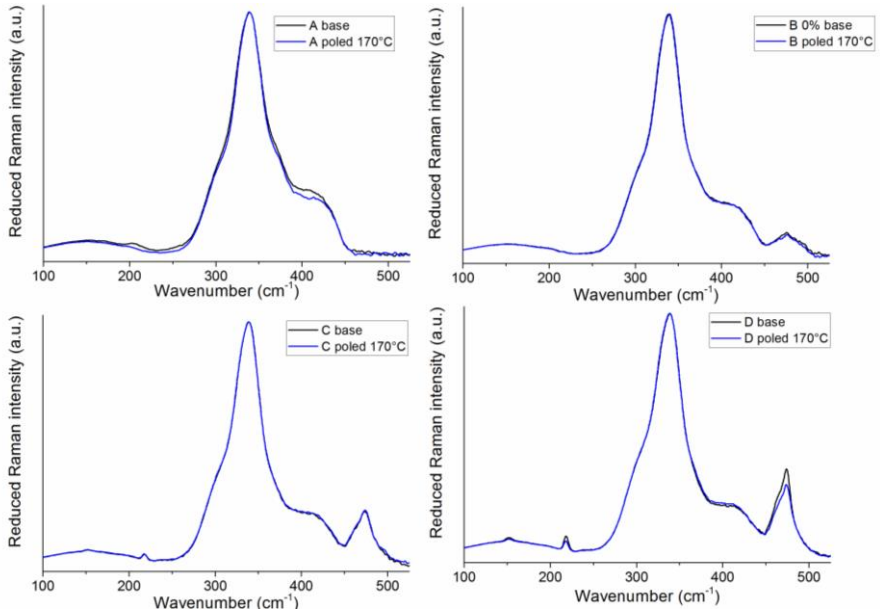

Figure 5.12. Raman spectra recorded on the various glasses before and after thermal poling

The reduced Raman spectra were calculated and all spectra were normalized to the highest intensity band. In glass A, there is a decrease of the band related to corner sharing GeS_4 tetrahedra. Only this composition shows this trend. On the other glasses, the only visible variation is a decrease of the band related to the S-S homopolar bonds at 475 cm^{-1} in glass D. This variation is small but need to be put in perspective with the Raman spectra shown in the Raman section of the base glasses with and without sodium. Indeed, it was observed that addition of sodium to the glass matrix lead to an increase of the sulfur bands especially seen on the band with highest Raman activity at 475 cm^{-1}. We attributed this change to the incorporation of sodium sulfide to the glass matrix which lead to the creation of a non-bridging sulfur in a GeS_4 tetrahedra, the sulfur added to the composition was then thought to link two sulfur together, thus lengthening sulfur chains. Addition of sodium to the glass composition also shifted the main vibrational band related to GeS_4 tetrahedra to higher wavenumber. Here the opposite trend is observed for the sulfur mode while no significant change is observed for the GeS_4 mode. The sulfur mode at 475 cm^{-1} decreases upon poling, if we apply the same reasoning, eventual sodium departure from a near anodic region should be linked to a decrease of the sulfur bands. The Raman spectrum of thermally poled glass D could therefore show the presence of sodium impurities which migrate upon poling but the modifications are overall, small.

5.2.2 Thermal poling of sodium-rich chalcogenide glasses

In classical thermal poling experiments, the role of sodium cations has been highlighted in most glass systems. Even in Na-free chalcogenide glasses, they are thought to play a role through their migration as impurities under the electric field. Sodium was thus added to the glass network through addition of sodium sulfide in the four base glasses and its impact on post-poling properties

was evaluated. All glass compositions were doped, thermally poled and their second harmonic response measured with the Maker fringes. The results being overall comparable, it was thus decided to only present the study of composition B. In addition to the composition doped with 1% of sodium sulfide, a second one was prepared with 3% of sodium sulfide. Glasses with 1 and 3 mol % of sodium sulfide will be treated at the same time as well as the impact of the treatment temperature. For sake of clarity, these two compositions will be referred to B-1% and B-3%. In all cases, the study will focus on the effect of sodium on the induced SHG origin and stability over time. Eventual structuring changes in both cases will be discussed at the same time.

5.2.2.1 Evidence of cationic migration during thermal poling

Upon poling of these glasses, the first difference is that ionic conductivity is non-negligible and that a current can be recorded once the voltage is applied. The activation energy of cationic conductivity is known to vary exponentially with increasing temperature.

Figure 5.13 shows both the evolution of the voltage across the sample as well as the evolution of the current across the sample when subjected to this DC bias. In both cases, the DC bias was applied once a homogeneous temperature was reached on the sample. Due to the high alkali content in the glass, thermal poling could not be performed at 3000 V as conductivity would exceed 1 mA which is the limit we usually set during thermal poling. The voltage was therefore decreased and set up to 1300 V. The impact of poling temperature is clearly observed; an increase of 40°C is accompanied a strong current across the sample. This current curve, similar to the one observed in alkali-rich glasses, is a clear evidence of cationic migration during poling. On the experiment performed at 210°C, a voltage threshold for cationic migration can be observed that is around 200 V. As voltage continues increasing, so does the current which quickly reaches a maximum of 0.11

mA and then gradually drops. This behavior was previously related to the creation of the sodium depleted layer. As sodium migrate towards the cathode, the resistivity of the near-anodic layer increases, resulting in progressive current drop.

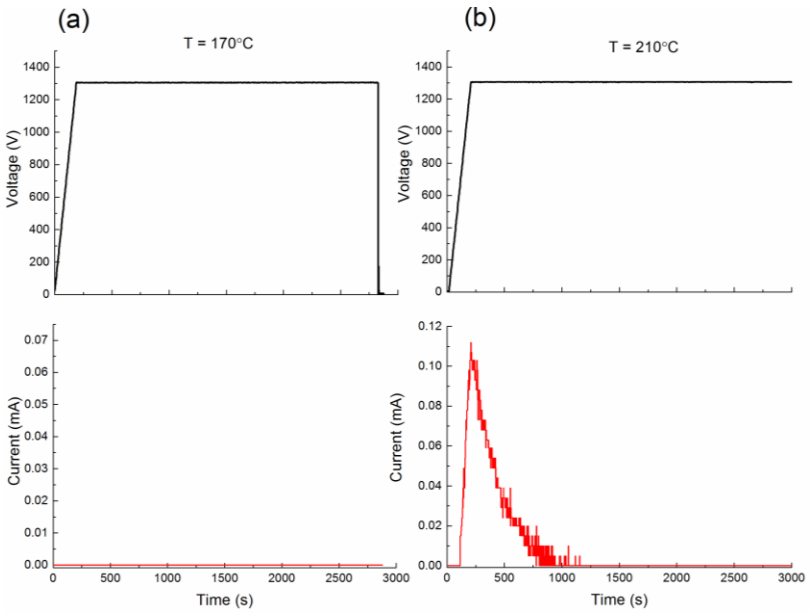

Figure 5.13. Voltage profile (top) and measured current curves (bottom) for B - 1% Na_2S poled at respectively 170°C (a) and 210°C (b)

If the sodium content is increased to 3%, the current measured at 170°C is still too low to be accurately detected but it increases to 0.14 mA at 210°C, as seen on Figure 5.14. The increase of measured current is directly linked to the increase of sodium concentration.

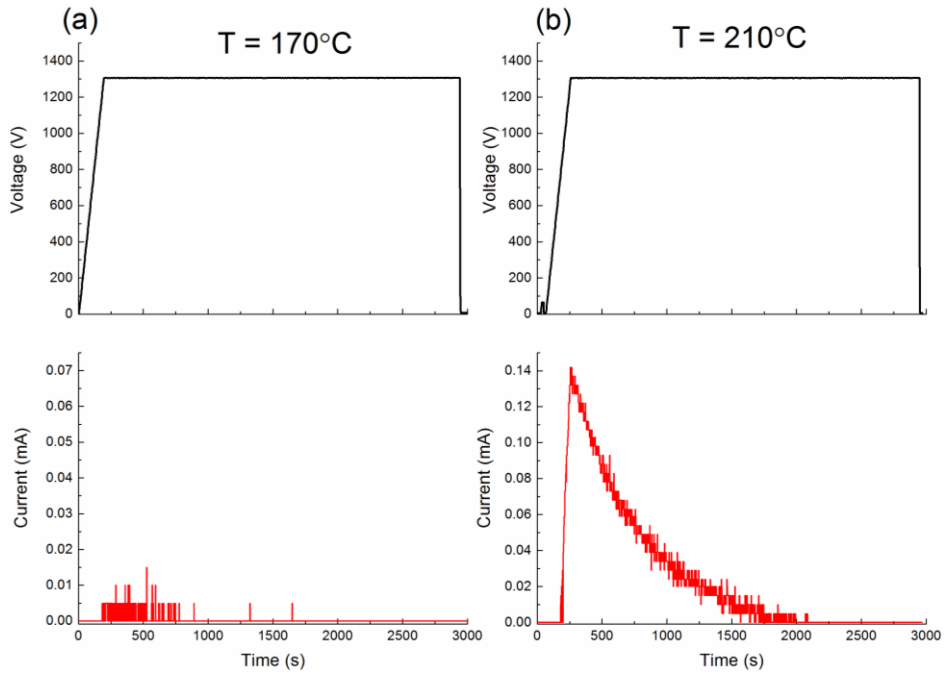

Figure 5.14. Voltage profile (top) and current measured across the sample (bottom) thermaly poled at 170°C (a) and 210°C (b)

5.2.2.2 Evidence of formation of a sodium depleted layer using SIMS

An important material response associated with the application of a strong field, is the resulting ion migration associated with the field, resulting in a spatial region void of the mobile ion. The creation of a sodium depleted layer in a near anodic region was suspected because of the current measured during poling and was evaluated as part of our study. Several samples were selected for Secondary Ion Mass Spectroscopy to probe the distribution of the various glass constituents from the surface going inside the sample.

The SIMS profile in Figure 5.15 illustrates the concentration as inferred as counts per second signal, of each of the glass' four chemical constituents, as a function of depth from the glass' surface. As can be seen, these profiles clearly illustrate the creation of a layer entirely depleted of sodium underneath the anode. Similar SIMS measurements performed on the base glasses prior

thermal poling and on the Na-free glasses after thermal poling can be found in appendix D and show no compositional changes.

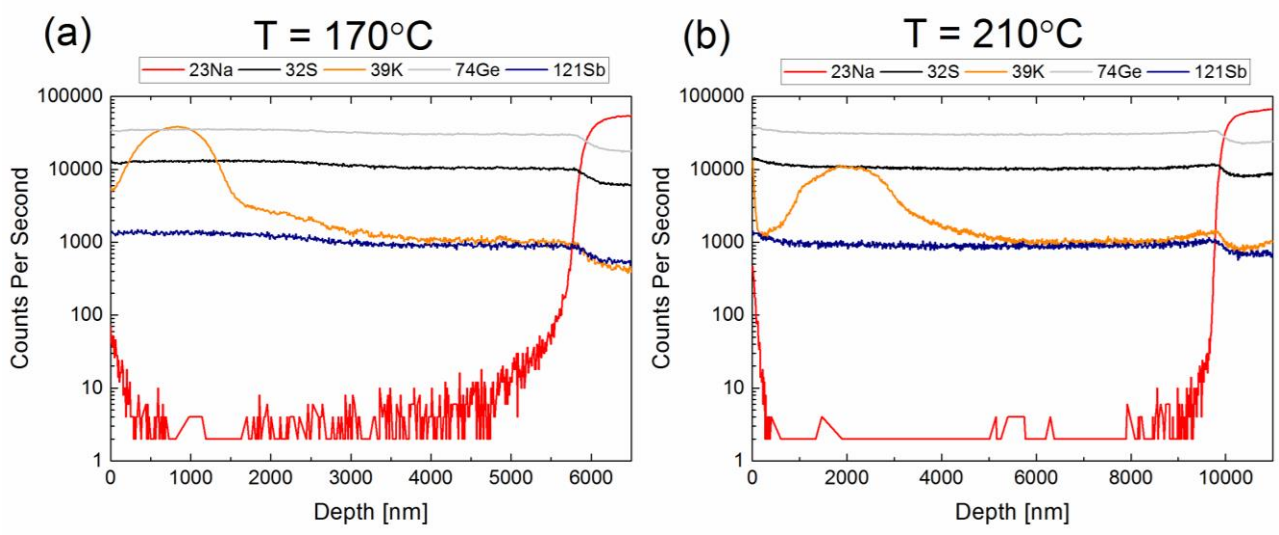

Figure 5.15. SIMS profiling from the anode going inside the glass for composition B-1% Na_2S and a treatment temperature of 170°C (a) and 210°C (b)

In addition, the SIMS data in Figure. 5.15 (b) shows the change (increase) of the thickness of the depleted layer with increasing poling temperature. At 170°C, the thickness is measured at 6.1 µm while at 210°C, it is measured at 10.1 µm if the point at which the sodium level reaches its maximum value is taken as the end of the sodium depleted layer. While not an absolute measure of ion concentration and spatial position, the measurements clearly show that the species no longer is uniformly present throughout the glass, following treatment. It was previously reported that an increase of temperature could lead to thicker sodium depleted region as cations have more mobility to migrate. This was confirmed in these measurements. Additionally, we noted the presence of potassium cations in our sample, suggesting additional alkali are present, perhaps due to impurities. Additionally, one can observe a small decrease of the counts measured after the sodium

reaches its maximum counts (after 6000 nm for profile (a) and 10000 nm for profile (b)). This is believed to be an artifact due to charging of the sample under the electron beam. To highlight this charging effect, the electron beam parameters were re-adjusted and the milling was continued, the counts went back to their original level. The continuation of the SIMS profile performed on sample B-1% can be found in appendix D.

In the glass containing 3 mol% of sodium sulfide, the depletion layer was measured only for the sample poled at the highest temperature and is shown on Figure 5.16. The profile is similar to the two previously shown but the thickness measured is only equal to 6.6 µm and the potassium maximum is present at the limit of the sodium depleted layer, as previously reported in oxide glasses. [28] A small drop in counts of Ge, Sb and S is once again observed as the sodium level reaches higher counts and is due to charging effect. The SIMS result is really similar to the one observed in thermally poled silica glasses with various level of impurities. As the sodium level increases, the sodium depleted layer has to be thinner or the dielectric breakdown would be quickly exceeded. The resulting electric field is usually stronger as it is restricted to a thin region.

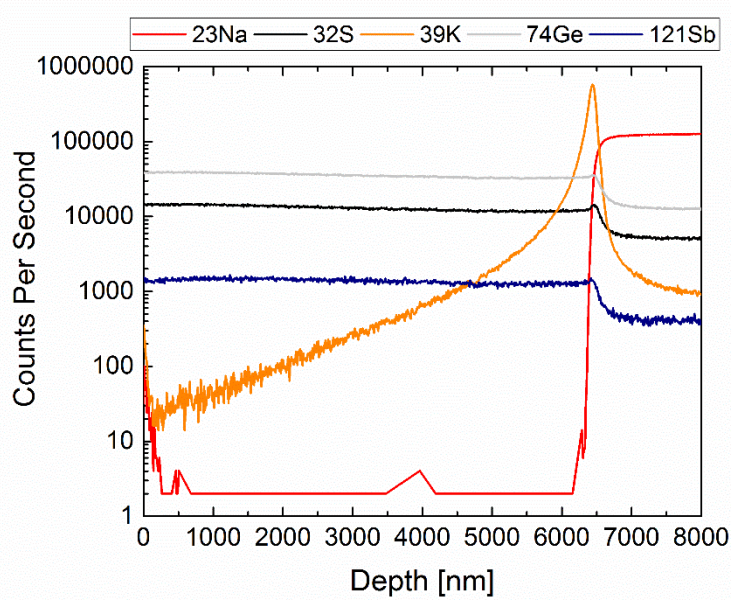

Figure 5.16. SIMS profile measured on B - 3% Na_2S thermally poled at 210°C

5.2.2.3 Study of the induced 2nd order nonlinearity using the Maker fringes

The Maker fringes were measured for both glass compositions following poling under both poling temperatures, 170°C and 210°C, to quantify the magnitude of the SHG induced property and to determine its origin. Figure 5.17 shows the recorded θ-pp as well as the fit (when possible) for both samples and poling conditions.

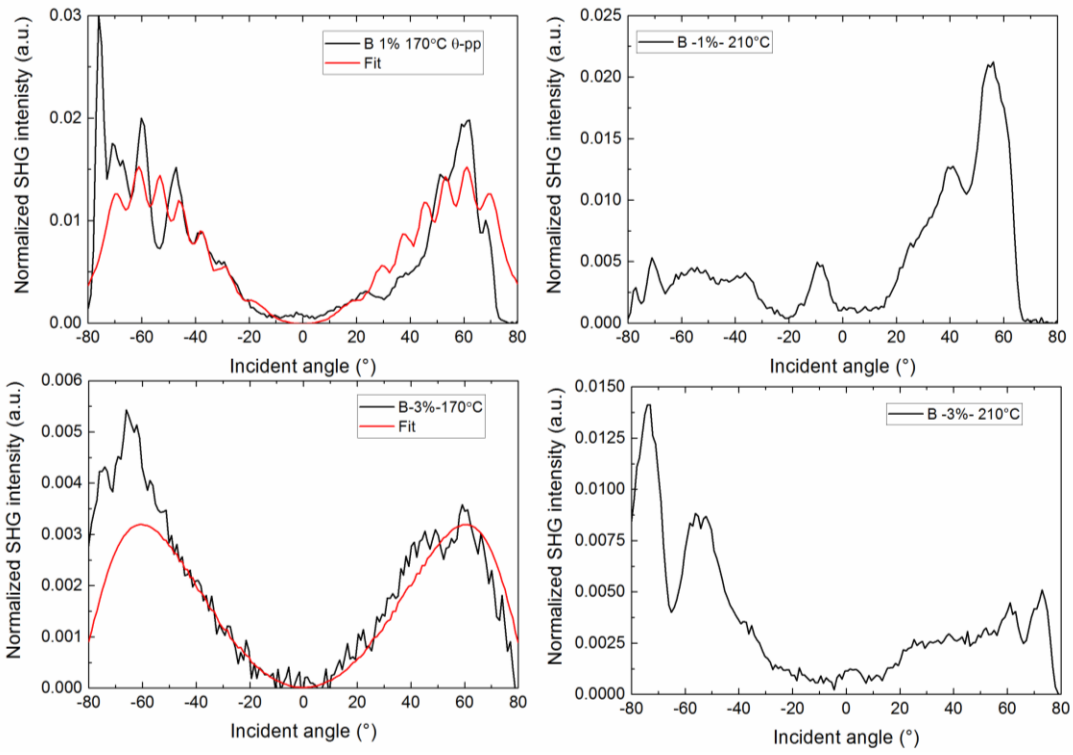

Figure 5.17. θ-scans recorded for glass B-1% Na_2S poled at 170°C and 210°C (top row) and glass B-3% Na_2S poled at 170°C and 210°C (bottom row), fits are presented in red when possible

Compared to the Na-free glasses shown in Figure 5.11, the fit observed for the doped glasses can fairly well describe the measurements made on glasses poled at 170°C. The first fit was obtained by adding a contribution from the bulk glass to account for the overmodulations that can be observed. The overall SHG intensity recorded in these glasses is lower than with the Na-free glasses. Moreover, an increase of the sodium sulfide content from 1 to 3 % further decreases the overall measured SHG intensity.

We have already mentioned that increasing treatment temperature lead to higher cationic conductivity during thermal poling of the Na-rich glasses. However, the fringes measured on samples poled in these conditions are erratic and cannot be fitted with the model of an EFISH

signal along z. Overall, the SHG shows poor homogeneity as the two parts of the measurements are not symmetrical. In addition, a signal at normal incidence is recorded as the temperature increases. This contribution cannot be accounted for with the classical thermal poling model related to centrosymmetry being broken by an induced electric field along z. The presence of signal at normal incidence suggests an additional contribution in the plane of the glass surface instead of along the longitudinal direction. Our ability to show this hypothesis is indeed the case, is discussed below.

5.2.2.4 Study of the overall stability of the induced 2nd order nonlinearity

Similarly as the base glasses, the Maker fringes of post-poled samples were re-measured several times after thermal poling to infer the stability of the induced changes to the glass' optical properties of key interest was degradation of the induced SHG signal.

Figure 5.18 shows the θ-scans recorded on both B- 1% and B- 3% thermally poled at 170 and 210°C, two months after the treatment. For comparison the freshly poled fringe pattern can be found on figure 5.17. The overall SHG also decays over time but as opposed to the base glasses, a SHG signal could still be measured on all thermally poled glasses two months after thermal poling.

As compared to the signal measured on the first day, the overall symmetry is better and the erratic fringes that were visible have disappeared. Fringes recorded for all compositions and temperature can now be well fitted using the model of an EFISH origin induced along the longitudinal direction as in a classical thermal poling. A small contribution coming from the bulk glass was added to the glass containing 1 % of sodium sulfide to fit the overmodulations. Overall, the Maker fringes measured on the Na-containing glasses measured after two months all present the same behavior.

The fringes are smoother and corresponds to the classical model. No signal is ever recorded at normal incidence but all scans show lower intensity. Compared to the Na-free glasses, a better stability is obtained but a decay in SHG intensity still occurs. All fits were done by fixing the thickness of the anodic SHG active layer to the thickness of the sodium depleted layer found with SIMS measurements. The d_{33} could therefore be obtained and its evolution over time is shown in Figure 5.19. As a reminder, the d_{33} parameter provides information on the magnitude of the induced 2nd order nonlinear property. The value of the d_{33} is maximum on day one for the composition with the highest Na content. In addition, increase of the temperature also increases the $d_{33.}$ However, the d_{33} quickly decreases over time and the difference between the two glasses containing different level of sodium decreases. In addition, the difference in recorded SHG between the two treatment temperatures is almost null after two months. It seems that the decay of the d_{33} reaches a plateau and then stabilizes. Such a result supports the notion of a 'fast' initial relaxation mechanism, followed by a more stable (or metastable) permanent modification which maintains the resulting signal.

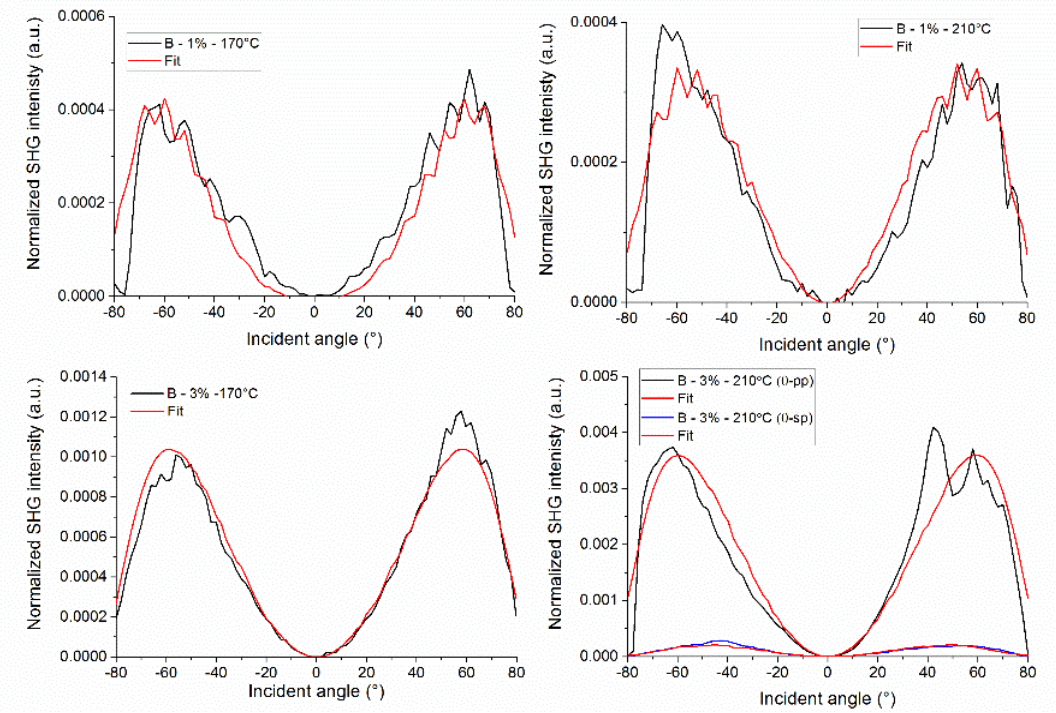

Figure 5.18. Maker fringes measured all Na-rich glasses two months after thermal poling

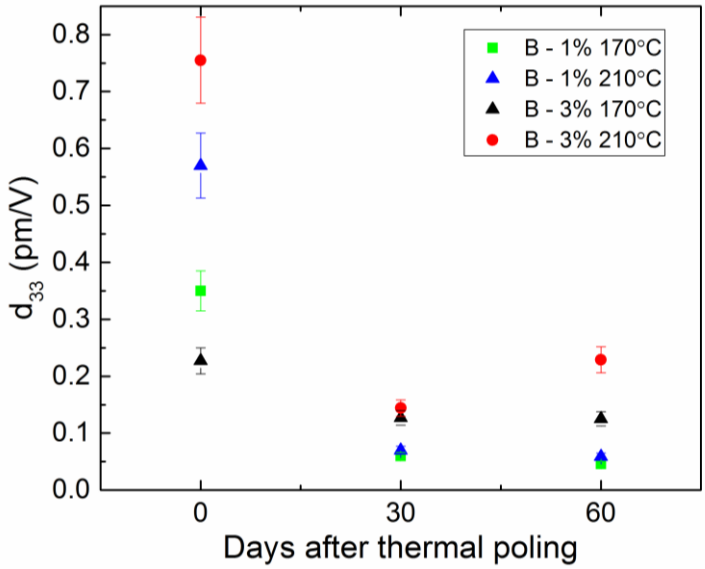

Figure 5.19. Evolution of the d_{33} as a function of time for thermally poled glasses belonging to the Na-rich B series

5.2.2.5 Evidence of structural re-arrangements with Raman spectroscopy

Raman measurements were performed on all Na-containing glasses that were poled at two temperatures. The Raman spectra were measured on the glass sample surface both inside the poled region and outside the poled region. The spectra were then compared to spectra of base glasses with and without sodium. The reduced Raman intensity was calculated for all spectra and they were then normalized to the band of highest intensity. The result of these measurements can be seen in Figure 5.20.

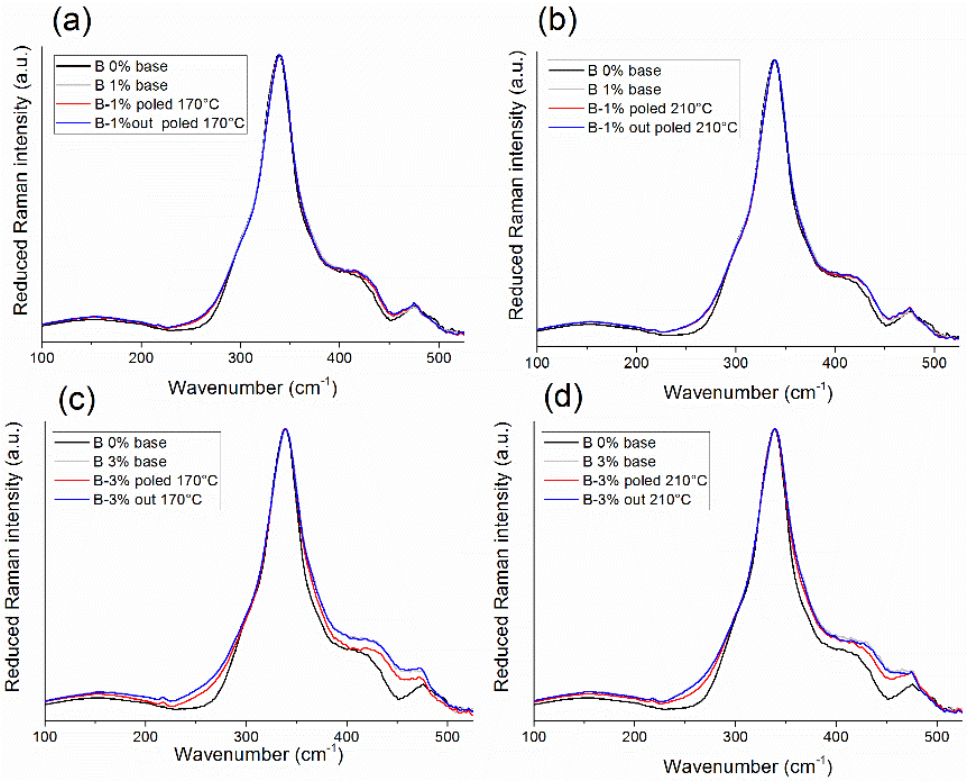

Figure 5.20. Raman spectra of the B series with various sodium content and different thermal poling temperature

Spectra recorded outside the poled area coincide with spectra of their respective sodium containing base glasses indicating no structural changes outside the poled region. Now looking at spectra

taken inside the poled area, deviations in the sulfur bands, mainly at 215, 415 and 475 cm^{-1} are observed and the spectra go towards an intermediate level between that of a Na-free and a Na-rich composition. These changes are more noticeable in the composition containing 3% of sodium sulfide. Possible changes in the frequency of the band of the GeS_4 tetrahedra at 342 cm^{-1} attributed to sodium migration discussed earlier, are still not clear. If there is any change in the position of this band with sodium departure, it might be too small to be clearly resolved.

However, the main structural change regarding the sulfur network and sodium agrees well with what was observed in the treated and untreated base glasses. In the case of the Na-rich glasses, we definitely know that sodium departure occurred thanks to SIMS measurements and Raman spectra confirm the impact of sodium departure on the glass structure. Sodium addition to the glass network had increased the relative contribution of the sulfur bands, a departure of these cations subsequently decreases the contribution of these bands indicating a re-structuring of the glass network.

5.2.3 On the origin and stability of the induced SHG signal

The Maker fringes presented in section 2.1.1 showed that, for the Na-free glasses, an additional contribution to the SHG signal could be found at normal incidence, showing that this signal was in the plane of the glass surface. This same contribution was observed in the Na-rich glasses, especially when increasing the treatment temperature. To conclusively confirm the origin of the induced $\chi^{(2)}$, ψ-scans are most appropriate as they probe the various components of the $\chi^{(2)}$ tensor and they are not impaired by potential inhomogeneity in the treatment as they are recorded at fixed incidence angle. We will first discuss the results obtained for the Na-free glasses. The ψ-scans were measured at the angle of maximum intensity, usually 60°. Figure 5.21 shows scans recorded

for all glasses (black) as well as the corresponding fit from a purely EFISH origin along the z-axis. For the stoichiometric composition, both p and s polarized scans can be perfectly fitted to the response of a $C_{\infty v}$ with $d_{33}/d_{31}=3$. The origin of the signal in this sample can thus be related to an induced electric field inside the sample which breaks the inversion symmetry of the glass along the z-direction. The various scans recorded for the sulfur rich glasses start to show deviation from the model.

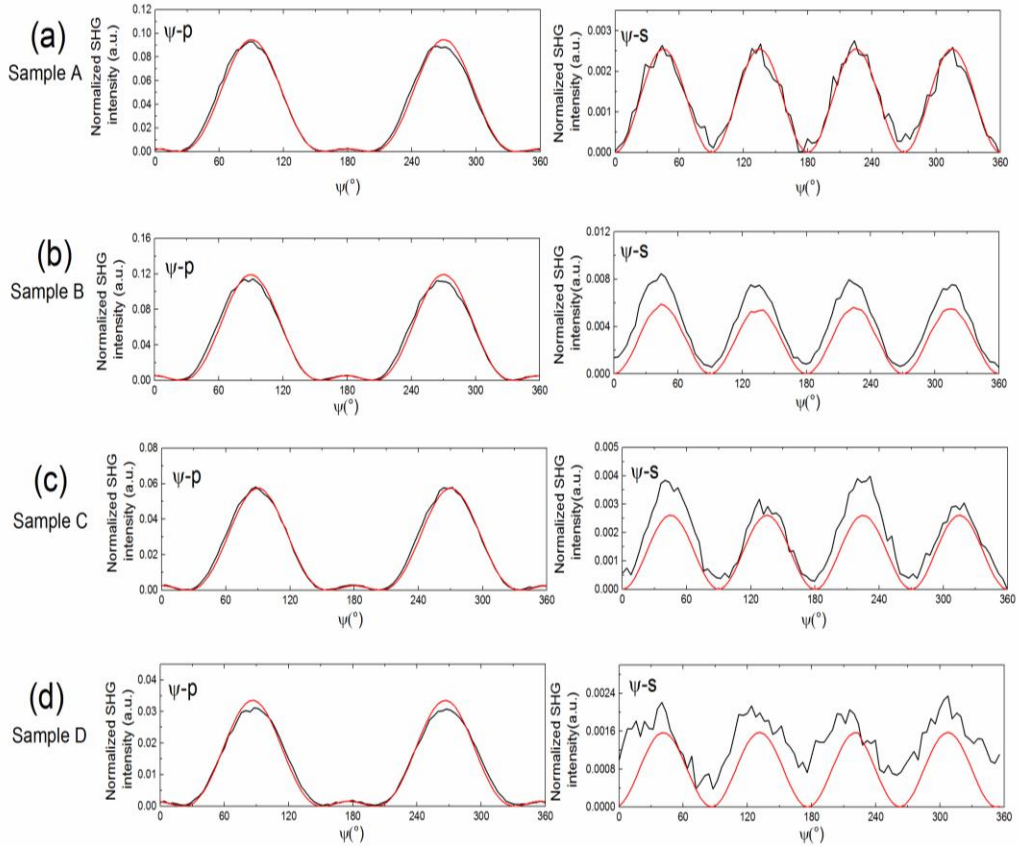

Figure 5.21. ψ- p (left) and ψ- s (right) scans recorded at 60° on samples A, (a), B (b), C (c) and D (d)

On their Maker fringes it can first be observed that the fit and the experimental date do not match. In most cases it is possible to fit the ψ-p scan while in the ψ-s scans, several deviations to the

model can be observed. First of all, the experimental data illustrate that the SHG signatures do not return to a zero intensity at the angle 0, 45, 90, 135 and 180°, as is predicted with a purely EFISH signal along z. It is worth noting that at 60° of incidence, the ψ-p mainly probes the d_{33} term of the tensor, while for a ψ-s measurement's configuration, we are also sensitive to the components in the plane of the glass surface observed at normal incidence.

Similarly with the sodium rich glasses, ψ-scans were recorded and are shown on Figure 5.22 along with the fit of a purely EFISH signal along z to evaluate the origin of the induced SHG.

There is a good agreement between the fit and the measured data for B-1% while differences with the model start to show up in B-3% (the ψ-scans of B-3%-170°C are not presented due to their poor signal to noise ratio). For this last composition, similarities with the Na-free glasses are observed. The signal does not go back all the way to 0 and the maximum intensity is not constant over the entire scan.

From the various recorded ψ-scans, it appears that an additional contribution to the signal can be present which is not solely due to an electric field induced process along the z-direction. Another contribution in the plane of the surface is present and to highlight it, ψ-scans at normal incidence are recorded and displayed in Figure 5.23. By measuring the response of the glass at this angle, it is possible to eliminate all contributions coming from an electric field induced along z as it cannot be probed in this measurement configuration. The scans presented here were measured on the Na-free glass of composition C poled at 210°C on the day of thermal poling and were measured in the same conditions.

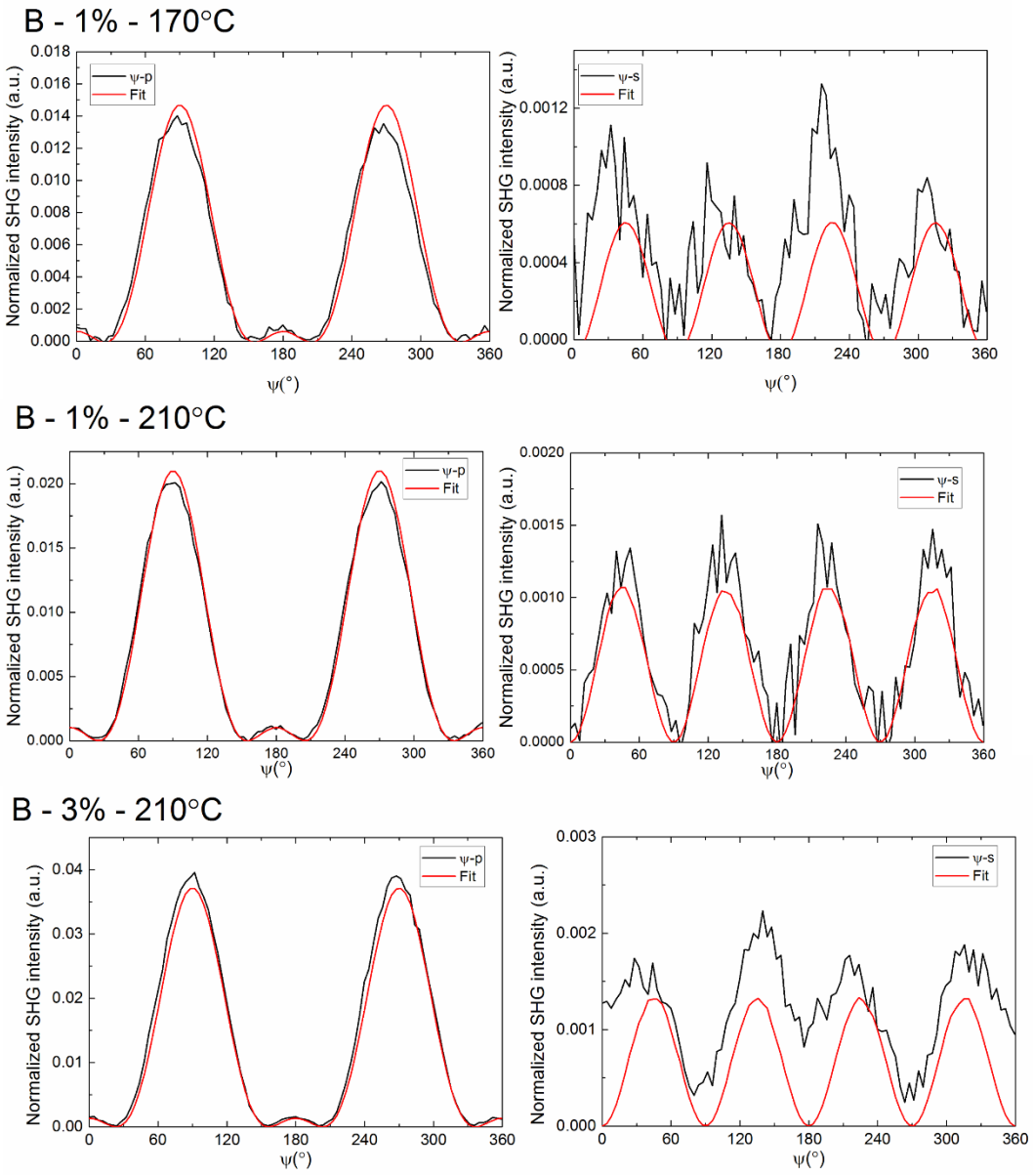

Figure 5.22. Maker fringes (ψ-p and ψ-s) recorded on freshly poled Na-rich glasses

These ψ-scans show contributions at normal incidence which should be absent in a purely EFISH process with an electric field induced along the z-direction. On the ψ-s scan recorded at normal incidence, maxima are at 0, 90 and 180° which corresponds to incident polarization s-polarized. Similarly, for the ψ-p scan recorded at normal incidence, maxima are at 45 and 135° corresponding

to p incident polarization. This shows that a dipolar response is obtained as the maxima are for pp or ss polarization states.

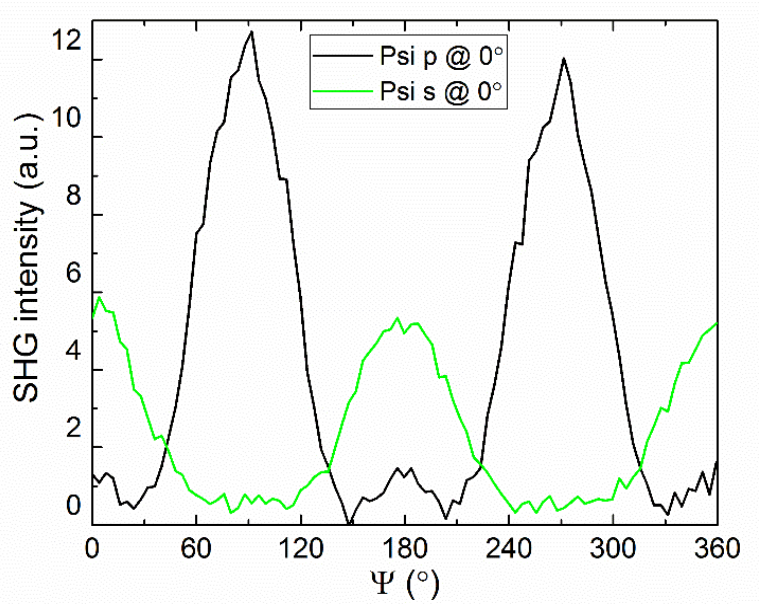

Figure 5.23. ψ- scans recorded at normal incidence for composition C

At least three hypotheses can be proposed to account for the appearance of this contribution in the plane of the glass surface. The first suggests the presence of non-centrosymmetric crystals which would give signal in the plane of the surface. These crystals should grow during thermal poling as no signal was recorded on any samples before poling. This proposition has several limitations. If crystals grow during thermal poling, it is not straightforward that they would grow in the plane of the surface instead of following the applied electric field which gives a strong directionality to the polarizable medium. Moreover, after thermal poling (as shown prior to poling as well), no sign of crystallizations was detected either via Raman spectroscopy or XRD measurements. Finally, we have shown that after poling, the SHG was rapidly decaying over time, reaching a zero value for the Na-free glasses and a plateau for the Na-rich glass. The lack of stability in the SHG signature

demonstrates the impossibility of a SHG coming from crystals. Indeed, if non-centrosymmetric crystals were forming during the process, the SHG signal should actually be quite stable over time as it is really unlikely that crystals would dissolve in the glass matrix at room temperature. A crystalline origin is therefore ruled out.

Another possible explanation could be linked to an electro-mechanical effect which can be occurring. Upon thermal poling, it is known that mechanical constraints can arise in the glass. It could be possible that these mechanical strains locally break the isotropic nature of the glass. The medium would therefore be anisotropic and present contributions in the plane of the glass surface. Upon relaxation of these mechanical constraints at room temperature the abnormal contribution would be expected to progressively disappear.

Lastly, another possibility to the observed behavior lies in that the new contribution to the SHG signal observed at normal incidence comes from an electro-optical effect in the plane of the glass surface. As chalcogenide glasses are more conductive by nature (than their oxide counterparts), it could be possible that in-surface currents are present during poling. It is important to remind the reader that the induced electric field in the thermally poled glass can be seen as the image of the frozen in gradient of charges in the glass matrix. Therefore, if charges are now also moving in the plane of the surface, once frozen in the glass matrix, they could be responsible for the observed additional contributions. The additional contribution would then originate from an electro-optical effect, not only along the z direction but also along the x and y direction. We know that for a purely EFISH process with a longitudinal electric field, the $\chi^{(2)}$ is obtained through the combination of the $\chi^{(3)}$ of an isotropic medium and the static electric field induced along z :

$$\chi^{(2)}(-2\omega;\ \omega,\ \omega) = 3\chi^{(3)}(\text{-}2\ \omega;\omega,\omega,0).E_{DC} \tag{5.7}$$

Only some of the components of the tensor are non-zero as E_{DC} is only along z and the $\chi^{(3)}$ tensor terms of an isotropic medium have the following symmetry properties:

$$xxxx = xxyy + xyxy + xyyx \tag{5.8}$$

$$\text{-yyzz=zzyy=zzxx=xxzz=xxyy=}\ldots. \tag{5.9}$$

$$\text{-yzyz=zyzy=}\ldots. \tag{5.10}$$

$$\text{-yzzy=zyyz=}\ldots. \tag{5.11}$$

The $\chi^{(2)}$ tensor arising from the interaction between the $\chi^{(3)}$ and a static electric field induced along z can thus be written as,

$$\begin{bmatrix} 0 & 0 & 0 & 0 & d_{31} & 0 \\ 0 & 0 & 0 & d_{31} & 0 & 0 \\ d_{31} & d_{31} & d_{33} & 0 & 0 & 0 \end{bmatrix} \text{ with } E_{DC,z} \tag{5.12}$$

Bear in mind that according to the convention used in this thesis, $\chi_{ijk}^{(2)} = 2\mathrm{d_{il}}$. In addition, our hypothesis of an isotropic media with an EFISH origin of the second order optical response imposes the relationship $d_{33}=3d_{31}$.

If we know take the same symmetry requirements but with an E_{DC} along x and y, we obtain two new tensors:

$$\begin{bmatrix} d_{11} & d_{12} & d_{12} & 0 & 0 & 0 \\ 0 & 0 & 0 & 0 & 0 & d_{12} \\ 0 & 0 & 0 & 0 & d_{12} & 0 \end{bmatrix} \text{ with } E_{DC,x} \tag{5.13}$$

$$\begin{bmatrix} 0 & 0 & 0 & 0 & 0 & d_{21} \\ d_{21} & d_{22} & d_{21} & 0 & 0 & 0 \\ 0 & 0 & 0 & d_{21} & 0 & 0 \end{bmatrix} \text{ with } E_{DC,y} \qquad (5.14)$$

In both of these tensors, we have $d_{11}=3d_{12}$ and $d_{22}=3d_{21}$. If we combine the three of them, we obtain

$$\begin{bmatrix} d_{11} & d_{12} & d_{12} & 0 & d_{31} & d_{21} \\ d_{21} & d_{22} & d_{21} & d_{31} & 0 & d_{12} \\ d_{31} & d_{31} & d_{33} & d_{21} & d_{12} & 0 \end{bmatrix} \text{ with } E_{DC\ x,y,z} \qquad (5.15)$$

All terms of the tensor are therefore linked to the orientation of the induced electric field E_{DC} with respect to the laboratory frame. So far mainly θ-scans have been shown but they present the disadvantage of probing different areas of the poled glasses and are consequently dependent on inhomogeneity. However, ψ-scans are recorded at fixed incident angle and thus do not probe inhomogeneities. They present the advantage of probing the various components of the tensor and are therefore more suitable to identify the origin of the recorded signal.

When ψ scans are recorded at normal incidence only the first two lines of this last tensor are probed. These lines are only linked to in-plane components of the induced E_{DC}.

We know that the intensity measured with the Maker fringes is related to the quadratic polarization. It is necessary to rewrite nonlinear polarization term in the lab frame:

$$P_i^{2\omega}(\psi) = d_{i1}(E_x^{\omega})^2 + d_{i2}(E_y^{\omega})^2 + 2d_{i6}E_x^{\omega}E_y^{\omega} \qquad (5.16)$$

And in our particular case, d_{i6} is equal to d_{i1} or d_{i2} (respectively for the first and second line of tensor (11)) and i= 1 or 2 (s or p polarization). It is important to realize that the electric field of equation (5.12) are the components of the *incident light* and not the components of the induced electric field E_{DC}.

In our ψ-scan measurements, the incident electric field components can be written as a function of ψ, the angle of incident polarization

$$E_y^\omega = E_0^\omega \sin(\psi) \cos\left(\omega t + \frac{\pi}{2}\right) \tag{5.17}$$

$$E_x^\omega = E_0^\omega \cos(\psi) \cos(\omega t) \tag{5.18}$$

With E_0^ω being the amplitude of the incident electric field, $\psi/2$ the angle of the half wave plate and the phase shift $\frac{\pi}{2}$ is induced by the quarter wave plate. The expression of the electric field components can then be injected in the expression of the quadratic polarization and after time averaging it, the following expression is obtained for the ψ-p:

$$\begin{aligned} I_{\psi p}^{2\omega} &\propto \left| P_p^{2\omega}(\psi) \right|^2 \\ &= \frac{(E_0^\omega)^4}{8} | d_{21} cos^4(\psi) + d_{22} sin^4(\psi) \\ &+ 2(2(d_{26})^2 - d_{21}.d_{22}) sin^2(\psi) cos^2(\psi) | \end{aligned} \tag{5.19}$$

And for the ψ-s, we have:

$$\begin{aligned} I_{\psi s}^{2\omega} &\propto | P_s^{2\omega}(\psi)|^2 \\ &= \frac{(E_0^\omega)^4}{8} | d_{11} cos^4(\psi) + d_{12} sin^4(\psi) \\ &+ 2(2(d_{16})^2 - d_{11}.d_{12}) sin^2(\psi) cos^2(\psi) | \end{aligned} \tag{5.20}$$

Important relations exist between the various components for an EFISH origin. In the case of a s-polarized scan, the terms d_{11}, d_{12} and d_{16} will be probed and the d_{16} should be linked to d_{21}. In addition, as the tensor was obtained from an isotropic medium with an electric field component

along x, we have $d_{11} = 3d_{12}$. The same relations can be used to constraint terms in the expression of the ψ-p scan.

In the case presented here, the ψ-p scan was first fitted using expression (5.19) and the three coefficients d_{21}, d_{22} and d_{26} were returned. We have already seen that the d_{26} corresponds to the d_{12} (see tensor (5.15)), the terms obtained in this first fit can be directly used to simulate the second ψ-scan. The second scan is thus not fitted but simulated using the terms obtained in the first fit and greatly constraints. The resulting fit are shown along with the measured data on Figure 5.24.

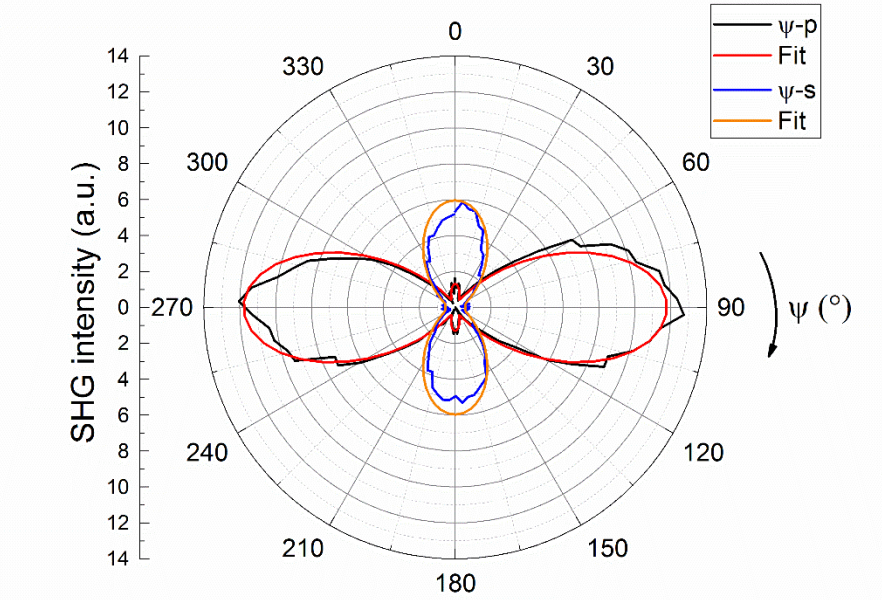

Figure 5.24. Polar plot of ψ-scans recorded at normal incidence along with fit obtained for an electro-optical contribution along x and y

There is a good agreement between the model and the experimental data, which tends to confirm the hypothesis that the contribution at normal incidence is due to electro-optical contributions along the x and y directions. In addition, the ratio between the terms of the two first line of tensor (5.15) can serve to obtain information on the orientation of the frozen in electric field. In our case,

the terms propped with the ψ-p have a higher weight than the terms probed with the ψ-s. To help visualizing this result, both experimental data and fit are shown in Figure 5.24 as a polar plot. The dipolar origin of the contribution is clearly observed as well as the larger weight of terms along the y-axis.

At this point, it is worth summarizing the information obtained from the Maker fringes study. It has been observed that the behavior of the base glasses towards poling at 170°C can be separated in two categories. The stoichiometric composition A, presents a classical EFISH response arising from an electric field induced along the z-direction. On the other hand, the response of glasses with a sulfur excess can be described by an electro-optical effect induced in the glass along several directions. The main contribution of the signal is coming from the classical EFISH process along the longitudinal direction (z). In addition, non-negligible contributions are induced in the plane of the glass surface (x-y).

This additional contribution is usually not observed in classical thermal poling experiments such as poling of oxide glasses. In the case of chalcogenide glasses, their highest electronic conductivity could be promoting surface current which upon return to room temperature would lead to the freezing of charge gradients in the plane of the surface. These contributions are responsible for the additional signal measured at normal incidence. In any cases, the induced SHG presents a poor stability over time with a rapid decay and complete decay of the signal over the first 20 days.

In the Na-rich glasses, the same reasoning can be applied. On the first day, most of the glass compositions present a SHG signal coming from an E_{DC} induced along all directions, responsible for the erratic fringes and the signal at normal incidence. When the signal at normal incidence is

not observed, the fringes can be easily fitted with an E_{DC} solely along z. However, as opposed to the Na-free glasses, over time the SHG signal evolves differently. It also decays but then reaches a plateau. Maker fringes recorded after the SHG decay then show a signal that fulfill all requirements of a symmetry broken through an induced electric field E_{DC} along the longitudinal direction. As both contribution in and out of the plane decay at different rate, we suspect a different nature of the frozen in charges at the origin of the induced electric field.

To explain this particular behavior of the charges and its impact on the resulting SHG signature, it is necessary to draw a parallel with the theory of Shimakawa in photosensitive chalcogenide glasses. [29] As described in the literature review, he has shown that two mechanisms explaining the separation of charges associated with structural units in chalcogenide should be taken into account. As noted, these differing entities would be expected to have different stabilities. The first state corresponds to the creation of excitons, or charged defects. Such defects possess a non-stable level of energy which tend to recombine easily. The second possible state corresponds to the creation of random pairs of charged defects (which through spatial association remain charge neutral). In this case, charges are more effectively separated as they are stabilized through structural re-arrangements. We suggest that the difference in stability between the Na- free and Na-rich glasses can be explained through similar phenomena.

In the Na-free glasses, we suspect that charged defects, similar to self-trapped excitons, are created and recombine easily over time. This theory can also explain the reason behind the more erratic behavior of the sulfur-rich compositions. Indeed, Shimakawa suggested that charged defects could be formed through bond breakage. In the sulfur rich glasses, we have shown that more S-S bonds are present and can even create S_8 entities. In sulfur species containing lone pair electrons,

breakage of such a bond would result in the creation of such charged defects. The abundance of these bonds would make the process more likely to happen. When measuring θ-scans these inhomogeneity of charge repartitions at the surface would be responsible for the erratic fringes. In addition, the Raman spectra have shown almost no structural changes in these glasses following thermal poling. This indirectly indicates the preferential formation of these charged defects which are not stable over time and then quickly recombine.

Regarding the Na-rich glasses, other conclusions can be drawn. The evolution of the Maker fringes over time could be originating from a dual origin of the induced nonlinearity. On the first day, the erratic fringes and presence of signal at normal incidence could be linked to a non-negligible contribution coming from charges trapped along the x-y plane as in thermal poling of the Na-free glasses. This is especially noticeable for glasses poled at higher temperature. As compared to the Na-free glasses, this contribution seems to be minor but could still be contributing to the overall signal on the first day. Over time, we have shown in the Na-free glasses that this in-plane contribution was quickly vanishing. The same phenomenon occurs here and over time the SHG signal evolves and changes its physiognomy. The obtained Maker fringes are then free of any SHG signal at normal incidence, show good symmetry/homogeneity and present moderate overmodulations. The fringes are then comparable to the one recorded in oxide glasses for an induced static electric field E_{DC} purely along the z-axis. This signal seems to be more stable overtime and the reason behind this needs to be determined.

The current curves have shown that, in the sodium rich glasses, the cationic conductivity is no longer negligible. We suspect that the sodium displacement can be linked to the electric field induced along the z-direction, similarly to an oxide glass. Upon thermal poling, cations migrate

towards the cathode and a layer entirely depleted of them is formed under the anode. When the sample is brought back to room temperature, charges are frozen inside the glass matrix which results in an induced static electric field along z. The creation of the sodium depleted layer underneath the anode was confirmed by SIMS measurements. Raman spectra then showed that the poled region was associated with structural re-arrangements involving the sulfur network of the glass. As sodium left the vicinity of the surface, the glass network re-arranged to go towards the structure of the Na-free glasses. The obtained Raman spectra are intermediate between that of the Na-rich and Na-free glasses. Shimakawa has shown that random pairs of charges can be stabilized through structural re-arrangements. The charges are then effectively separated and cannot easily recombine. The stabilization of the charges is indirectly confirmed by the structural changes observed in Raman spectroscopy. By changing its structure, the glass network would stabilize the separated charges thus preventing a complete decay of the SHG. After 30 days, the SHG plateaus and only the contribution along z remains while the erratic contribution has completely vanished. As the charges are now only oriented along the z-direction, the recorded fringes perfectly match the classical model of Second Harmonic Generation being obtained through the interaction of an isotropic $\chi^{(3)}$ and a static electric field induced along z. These findings are consistent with a rapidly relaxing and more stable secondary contribution to the induced SHG in the glass network, and matches the observed material response seen in this effort.

The SHG signal in Na-rich glasses would therefore be due to two contributions which evolves at different rate over time. The smaller SHG intensity recorded on the Na-rich glasses can also be explained by this dual contribution. We have shown that the additional contribution in the plane of the glass is especially visible at normal incidence. During a θ-scan, in addition to the signal

along z, the electric field along x and y also contributes to the overall intensity which could explain the erratic and non-symmetrical fringes. The charges could be inhomogeneously distributed at the surface of the glass and therefore responsible for spikes in some areas. In the Na-rich glasses, the contribution at normal incidence being smaller, when θ changes the contribution coming from the in-plane components is small as compared to the contribution from E_{DC} along z. The relative absence of this additional contribution in the plane could be responsible for the overall lower measured SHG.

5.2.4 Conclusion of section 5.2

This study of the Ge-Sb-S glasses in the sulfur rich region and their potential for thermal poling has allowed us to highlight the importance of the glass structure and of the cations present in the glass for thermal poling.

In the instance of Na-free glasses, it has been shown that a sulfur excess leads to the overall decay of the SHG intensity and to the appearance of additional contributions in the SHG signal. This additional contribution does not correspond to the classical thermal poling model of a symmetry broken through an induced electric field, which indicates *only* a contribution along the z direction. Only the stoichiometric composition has been shown to exhibit SHG originating from an electric field induced *solely* along the z direction. It was necessary to account for additional contributions in the sulfur rich region and for these cases, we suggest that these deviations from the classical model can be linked to charges trapped at the surface of the glass. Charges are separated as in a classical poling mechanism but the direction of the induced electric field does not only follow a longitudinal (perpendicular to the surface) direction. The distribution of these trapped charges give the direction of the induced electric field. In the sulfur rich region, if electro-optical effects not

only along z but also along the x and y directions are considered, the additional contributions can be perfectly fitted, lending credence to our proposal that indeed field effects in all three directions result from poling of non-stoichiometric structures which have suitable glass structural flexibility, to rearrange during poling. The fact that this mainly occurs for sulfur rich glasses might be due to the presence of sulfur chains that could more easily promote creation of charges at the surface of the glass, along the chains. Indeed, this particular behavior seems to be more significant as the sulfur content increases. We have suggested that most of the charges in Na-free glasses originate from the creation of charged defects which are not stable over time and rapidly decay. In arsenic selenide glasses, it was indicated that these charged defects were forming through the breakage of selenium bonds and recombination of broken bonds thus separating charges. If a similar process is taking place in sulfur glasses, the presence of long sulfur chains of smaller (and less sterically hindered) sulfur species, should lead to an ease of creation of such re-arrangements of bonds in the sulfur part of the network. Especially at high sulfur content, we have shown the creation of S_8 molecular units in the glass, the sulfur network could be at the center of the process of defects creation. Overall the induced nonlinearity in the glasses is not stable over time as the trapped charges are neutralize over time. We have shown that structural re-arrangements in the glasses following thermal poling were minimal which would explain the low stability.

To deliberately promote structural re-arrangements associated with cation migration and to evaluate the stability of an induced modification during poling of glass structure, glasses were doped with sodium sulfide and better stability of the induced 2^{nd} order nonlinear optical properties were obtained. Here, the SHG intensity dropped with addition of sodium but the overall SHG was closer to the purely EFISH model that we expect after thermal poling. An increase of poling

temperature however leads to more erratic fringes and a non-negligible contribution at normal incidence. In addition, on the first day, the Maker fringes are not symmetrical showing a poor homogeneity in the treatment. However, as the SHG decays over time, all recorded fringes were found to be smoother and closer to the purely EFISH model of an electric field induced along the longitudinal direction. It was therefore suggested that two types of trapped charges were at the origin of the recorded signal on the first day. The first type of charge signature originated from charge gradient in the plane of the glass surface with a poor stability as we proposed for the Na-free glasses. Overtime, these charges are (more quickly) neutralized and their contribution to the signal progressively disappears. The second contribution, originating from a gradient of charges frozen along the longitudinal direction is then the only one left. We believe that their stability is linked to the sodium migration (as shown with SIMS) which forces the glass network to re-organize (as shown with Raman spectroscopy).

Thus we believe, that the process of charge creation and stabilization in chalcogenide during thermal poling is quite similar to the mechanism was proposed by Shimakawa in photosensitive arsenic-selenide. [29] We have demonstrated that by adding controlled amount of sodium to the glass composition, structural re-arrangements can be promoted during thermal poling. While only noted for two doping levels, to date shown for 1 and 3 mol% Na_2S, with no upper limit defined our findings for both of these glasses support this proposed model. These structural changes allow to stabilize the charges frozen inside the glass matrix. The resulting 2^{nd} order nonlinear optical properties are then more stable over time. While only discussed in this chapter for composition B, the effect of the sodium addition on stability was found to be similar in the other compositions. Other compositions with a sulfur excess (C and D) showed improved stability with sodium

addition and were then easily described by a EFISH system induced along the z-axis after the initial decay of the SHG signal. This effect was not studied on composition A as we showed that sodium addition lead to partial crystallization of the glass matrix.

We believe that this mechanism is primarily responsible for the enhance stability shown in the present work as compared to prior efforts. Regarding the improved longevity of the induced 2nd order nonlinear optical properties, the impact of sodium was clearly demonstrated. However, it was demonstrated that sodium addition was accompanied by an increase in impurities in the glasses as seen on Figure 5.4. The role of these impurities, in some cases charged themselves, has not been explicitly examined. These species undoubtedly play some role in the process and proposed stability mechanism, however as these impurities are largely negatively charged species, they should enhance any electrostatic recombination with the mobile cation. Further purification of the glasses is needed to study the sole addition of sodium on post-poling stability. This might prove to be especially important where the poling (or micro-poling as discussed in the next section) relies on preserving long standing optical function.

Overall, there is still room to improve these results as the overall recorded SHG intensity is rather low. In addition, even if a better stability was obtained in Na-containing glasses, the signal still decays at first before reaching a plateau. The stability at longer term than few months has not been evaluated and further decrease of the induced 2nd order nonlinear optical properties could prevent a use for concrete applications. The reason for this decay could be linked to the progressive neutralization of the trapped charges. Chalcogenide glasses are known to be photosensitive glasses and a photogalvanic effect could be taking place. Upon irradiation with white light or an intense

laser light, charges could be activated and neutralized. Such an effect has been already demonstrated in other glass compositions.

This intrinsic property of the glass could be difficult to overcome and thermal poling for second harmonic generation in chalcogenide glasses might be limited. However, the addition of sodium has shown promising results and it suggests that if the glass is behaving more like an oxide glasses, the stability is enhanced. Thermal poling of oxi-sulfide glasses could be considered, they would still present a fairly good transparency in the infrared region and they could be more appropriate for second harmonic generation. However, the sodium-rich chalcogenide glasses presented here could be suited for the micro-imprinting process that was presented in previous chapters. The following section of this chapter will thus discuss the potential of these glasses for micro-poling.

5.3 Micro-patterning chalcogenide surface properties and optical properties

In the previous section, we have demonstrated the advantage of deliberate (i.e., not solely based on low level impurity levels) sodium addition on the post-poling properties of the Ge-Sb-S glasses. Now that baseline global structural and optical behavior induced by thermal poling of chalcogenide is better understood and the stability of the modification has been quantified and interpreted, we aimed to extend our study to understand the ability to induce such poled glass modification, over small (micro-) length scales. To that end, this section discusses the use of a micro-patterning poling process on these glass compositions. Here, we discuss the application using a patterned electrode, and examine the variation and stability of this process on optical properties.

In chapter 3 and 4, the use of micro-patterned electrodes as stamps to tailor optical properties, surface properties, structure and glass composition was demonstrated. From the beginning, the

micro-patterning was developed to tailor glass' properties at the micrometric scale for application in Photonic Integrated Circuits, sensors and so on. The possibility to apply the same process to chalcogenide is challenging. As we have observed, their behavior upon thermal poling can be more difficult to understand. However, if we manage to induce similar changes using the micro-poling process, it could be possible to tailor the glass' properties in a similar manner. This would be especially relevant for microphotonics applications as chalcogenide's great asset is their good transparency in the infrared.

This section is therefore intended to apply the micro-patterning of a surface during thermal poling on this family of glass. Throughout the section, we will show concrete applications of such an imprinting process on chalcogenide discussing the experimental conditions use, the metrology done to quantify the chemical and optical modification, and the potential property and property stability resulting which lends the methods suitable for extension to future optical components.

5.3.1 Experimental section

For this study one glass composition was selected, that is glass B (nominal composition: $Ge_{22.5}Sb_{10}S_{67.5}$) with varying amounts of added sodium sulfide (0, 1 and 3 mol%). The potential impact of the sulfur content is therefore not studied here, rather we have focused on the role of the mobile cation during the imprinting process. As the sulfur content in the glass is already well within the chalcogen-excess region where the glass network possesses large attributes due to S-S bonding, this minor addition does not significantly impact the expected mobility of the S-rich network.

As presented in the oxide glass work, ITO coated microscope slides were patterned and used at the anode, similarly as discussed in chapter 3 and 4, with the details of the electrode patterning as described in chapter 2. The ITO layer was structured and three types of patterns were inscribed: (i) circular systems (of diameter ranging from 5 to 40 μm) (ii) rectangle features 50 by 30 μm and (iii) lines 5 to 25 μm wide and 125 μm .

The three glasses ($Ge_{22.5}Sb_{10}S_{67.5}$) with varying sodium content were subsequently poled in the same conditions. All electrodes possessed similar patterns with constant surface area such that all glasses were subjected to the same applied electric field. The temperature of the treatment was fixed to 210°C to favor sodium migration based on the results obtain in the previous section and the applied electric field to 1300 V. All thermal poling experiments were performed for 30 minutes in nitrogen atmosphere to ensure blocking anode conditions.

Following thermal poling, all glasses were characterized using optical microscopy, AFM in PeakForce KPFM mode, Raman spectroscopy and EDX. Specifically, these measurements were carried out to examine pattern transferability, potential change in surface topology as well as structural and compositional changes, respectively.

5.3.2 Transfer fidelity of the electrode to the glass: impact of sodium content

Similar structured electrodes were used for all glasses. Upon thermal poling, current curves could be measured for glasses containing sodium. This was demonstrated as a sign of cationic migration in the previous section. Once the poling performed all glasses were first studied to evaluate the transfer fidelity of the patterns on the glass surface.

5.3.2.1 Optical microscopy

Following thermal poling of all three glasses, it was observed via optical microscopy that no pattern was transferred to the Na-free glass. The presence of sodium cations therefore seems to be primordial for an effective imprinting process in these poling conditions. On the Na-containing glasses, the patterns were successfully transferred to the glass surface. The Figure 5.25 shows one optical micrograph of the glass surface after thermal poling glass B-3% using an electrode with circular patterns. Clearly evident are the circles that correspond with the circle patterns of the electrode. Within the ability to measure these features, the deposited electrode features (22 to 25 μm in diameter) yielded patterned glass surface features of 22 μm in size. This similarity in feature size suggests that shaped electrodes can be successfully transferred. The lower limit (size of smallest feature size) and larger limit size have not been yet determined.

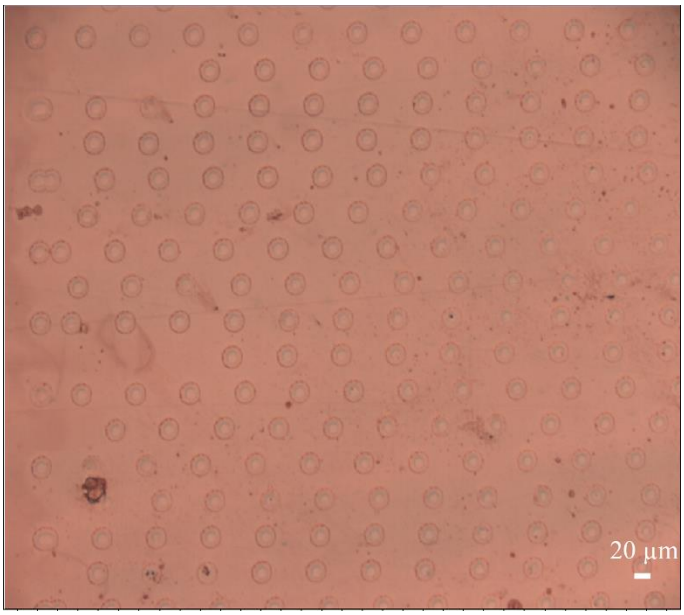

Figure 5.25. Points imprinted on the glass surface using an electric field induced imprinting process on compositions B - 1% Na_2S (a) and B - 3% Na_2S (b)

5.3.2.2 AFM measurements

AFM measurements were then performed on the patterned chalcogenide surface to study a possible change in topology following thermal poling. No AFM measurements were performed on the Na-free glass as it was not possible to find the patterned region. All following measurements will therefore focus on the two other glasses with 1 and 3% of sodium sulfide. Figure 5.26 shows AFM scans recorded on B-1% and B-3% in PeakForce KPFM mode. Only the image of the topology is presented and the change in surface potential will be discussed later on.

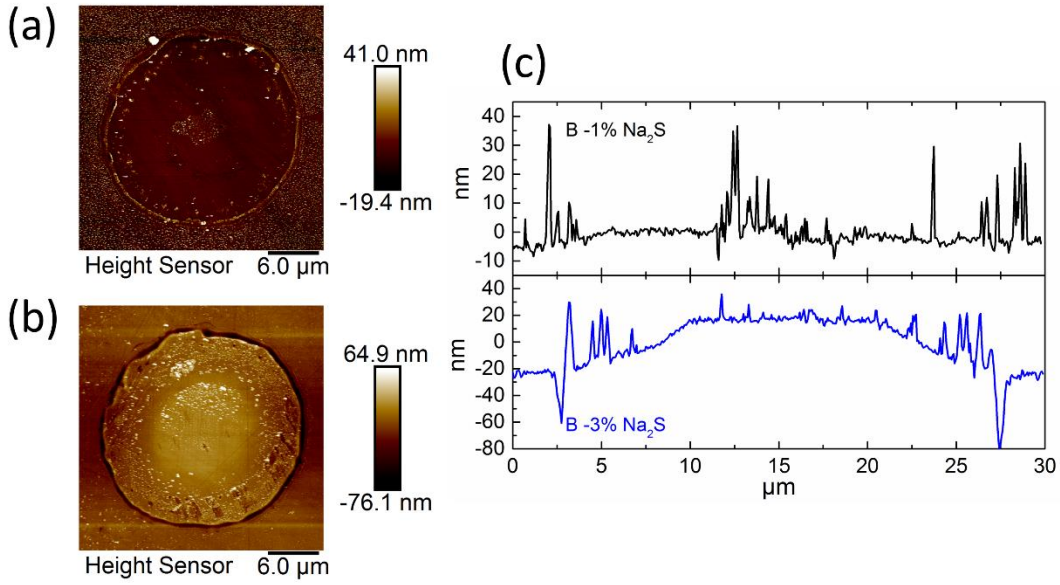

Figure 5.26. AFM map recorded on two points similar in size on sample B containing 1% of sodium sulfide (a) and 3% of sodium sulfide (b) and topology profile recorded across both images (c)

On these two maps, it can be seen that the topology changes are minimal compared to what was observed with the BPN 42 glass in chapter 3. The change of topology here is on the order of tens of nanometers. Some areas in both glasses exhibit sharp peaks with maximum height of 35 nm. Topology changes are more pronounced on the B-3% where a peripheral ring or halo is clearly

imprinted around each dot. The depth of the trench is around 40 µm deep and is present all around the dot. Patterns imprinted on the surface therefore appear with a sharper contrast for higher sodium content. No comparable change is observed on B-1% but the transfer fidelity of the pattern is still excellent as both points presented here are 25 µm wide which is the size of the patterns written on the electrode. This AFM study shows that topological modifications are minimal for both sodium level. The surface can still be considered as rather flat; the impact of topology changes on properties is then minimized.

5.3.3 Study of compositional changes in micro-patterned poled surface: EDX measurements

The possible compositional modification associated with the topological modification shown in section B., were evaluated by SEM-EDX measurements of coated, post-poled patterned arrays. EDX measurements were performed on the structured surfaces to monitor potential changes in composition both in locations in contact with the ITO coating (and cation migration was believed to occur) and in patterned areas where ITO was removed. Maps were recorded on samples B-1% and B-3%. On glass doped with 1% of Na_2S, the EDX measurements were done on the large rectangular patterned area (50 by 30 μm^2) presented in Figure 5.27.

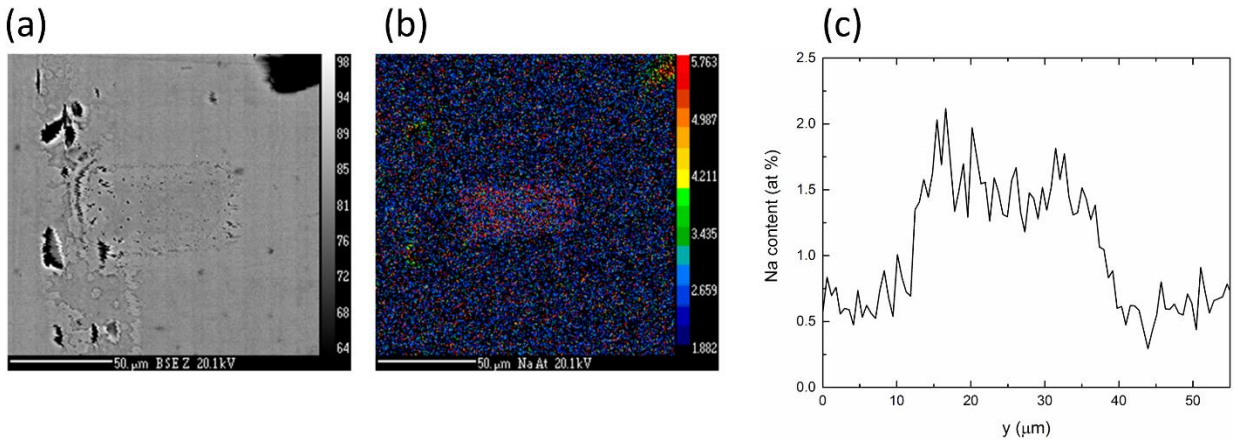

Figure 5.27. Back scattering electron map of a rectangle imprinted on the glass surface (a) and corresponding EDX map of the sodium distribution (b) as well as sodium distribution profile across the square (c) Scale bar in the micrographs correspond to 50 µm

Part (a) of the figure is an image recorded in backscattering electrons and shows in its center the faint impression of rectangle on the surface. Part (b) shows a map of the sodium distribution across the same area. The sodium level greatly decreases outside the pattern while it stays rather homogenous inside of it. Looking at the sodium concentration profile, part (c), it can be seen that the level does not reach exactly 0 outside the pattern and that the level measured within the pattern is close to 1.5-1.9 at %. The glass composition is $Ge_{22.5}Sb_{10}S_{67.5}$ doped with 1% of sodium sulfide. When renormalized to 100%, the composition is then $Ge_{21.85}Sb_{9.7}S_{66.5}Na_{1.9}$. The sodium level measured in the center of the patterned is therefore close to the nominal composition, indicating no or low migration in its center as expected as this position is not in contact with the conductive electrode. In addition, it can be observed that the sodium rich region does not correspond to the full rectangle observed on the BSE image. On the BSE image two distinct regions can be defined. The outer part of the rectangle and a second rectangle inscribed in the first one which corresponds

to a darker region. The sodium rich region observed on the EDX map actually matches the dark region.

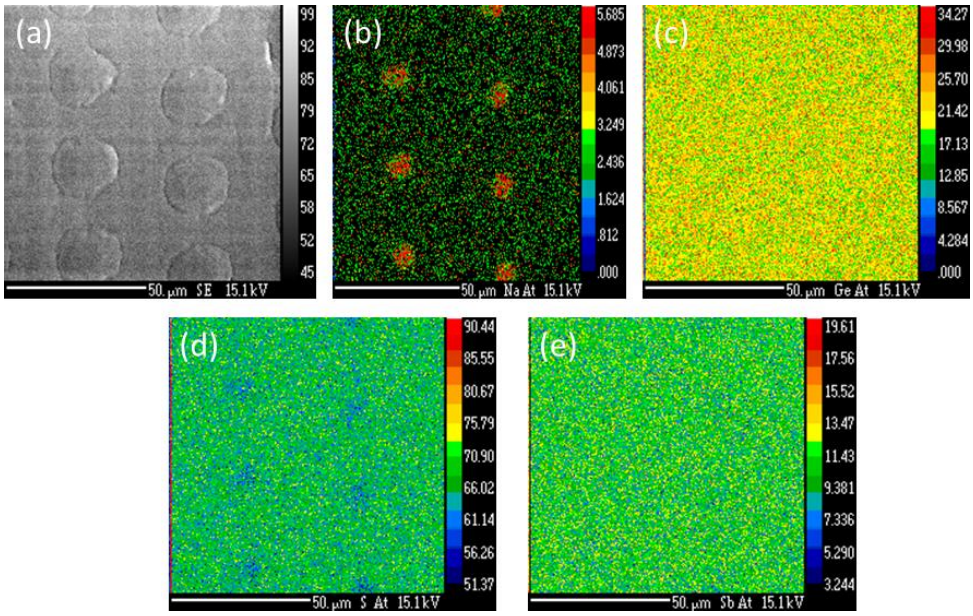

Figure 5.28. BSE map of series of points imprinted on the glass surface (a) and corresponding EDX maps of Na (b), Ge (c), S (d) and Sb (e)

Same measurements were performed on the glass containing 3% of Na_2S on a region patterned with 25 µm wide dots. Figure 5.28 shows the various maps recorded on this sample. There is a large depletion of sodium in the area that was in close contact with the ITO electrode while the sulfur seems to follow an opposite trend. Other elements do not show any variations thus showing that they remain unaffected by the thermal poling process. Overall the measurements are really similar to the one observed on the glass containing 1% of sodium sulfide. The magnitude of the measured changes is just larger.

In addition to elemental mapping, line profiles can be plotted across patterns and are represented in Figure 5.29 with the edges of the circular pattern illustrated as dash dots.

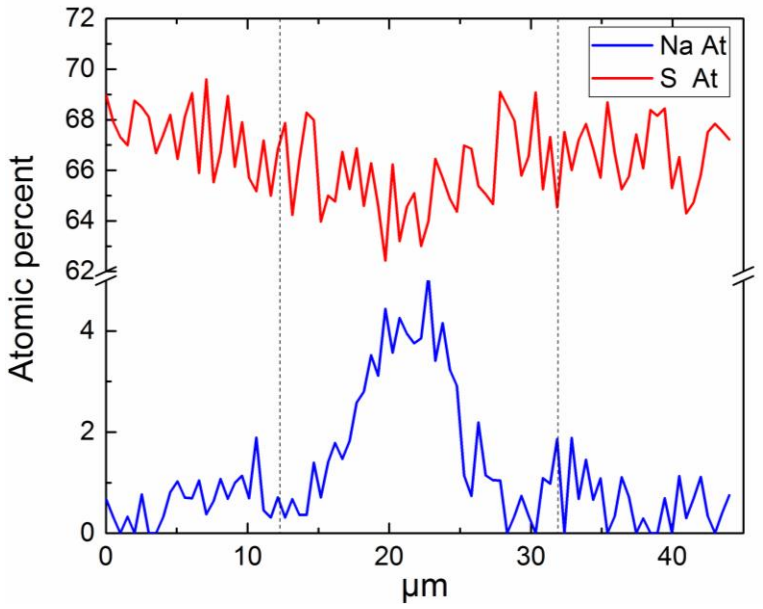

Figure 5.29. Composition profile across one point for sodium and sulfur

In this plot, it is clearly observed that the sodium level starts increasing as we enter the dot while the sulfur content follows an opposite trend. To understand this compositional changes, it is important to come back to the nominal glass composition: $Ge_{22.5}Sb_{10}S_{67.5}$ with 3% of sodium sulfide. If the composition is re-normalized to 100%, we obtain a nominal composition of $Ge_{20.6}Sb_{9.17}S_{64.68}Na_{5.5}$ which is important to remember to explain the obtained maps. The composition at the center of the dots is close to the composition of the glass prior poling indicating that this region was not affected by thermal poling. As we go outside the dots, in regions where thermal poling was taking place, the sodium level decreases and the sulfur level increases. Regarding the composition of the glass in this region, it comes close to the one of the Na-free glass: $Ge_{22.5}Sb_{10}S_{67.5}$. There is thus a progressive change in glass composition across the pattern. The glass composition outside the pattern is however not exactly the one of the Na-free glass. The obtained composition is in between that of the Na-rich and that of the Na-free compositions.

5.3.4 Evidence of localized structural changes with Raman spectroscopy

In the previous section, we were able to measure compositional changes associated with sodium departure after thermal poling. The profiles recorded clearly showed the creation of composition gradients across the pattern. The results were especially noticeable on composition B-3% which was therefore selected for Raman spectroscopy.

As with the EDX measurements, the array of dots imprinted on the glass surface was mapped in Raman spectroscopy. Once mapped, all spectra were normalized to the area under them and a spectrum recorded in the very center of the dot was selected. This spectrum was subtracted from all other spectra to obtain difference spectra highlighting structural changes. The band between 400 and 500 cm^{-1} related to the sulfur mode which had shown variation upon poling was then imaged. The difference spectra as well as the obtained map are shown in Figure 5.30.

The center of the dot, indicated by the red region does not show any structural variations. This region can be spatially correlated to the region where sodium remains in the EDX map which corresponds to a circle centered in the dot. A second region inside the dot can be defined were changes on the sulfur modes start to take place. It is also correlated to the region in EDX where the sodium level starts decrease in the pattern. This region is mainly homogeneous until it reaches the outer ring of the imprinted dot. Finally, the exterior part of the structured region presents the largest deviation from the center which is once again correlated to the EDX map where sodium was totally absent. The obtained spectra outside the circle are closer to the one measured on the corresponding Na-free glass. They are however not completely equal. This is also confirmed with the EDX measurements as the measured glass composition was closer but not equal to the one of the Na-free glass.

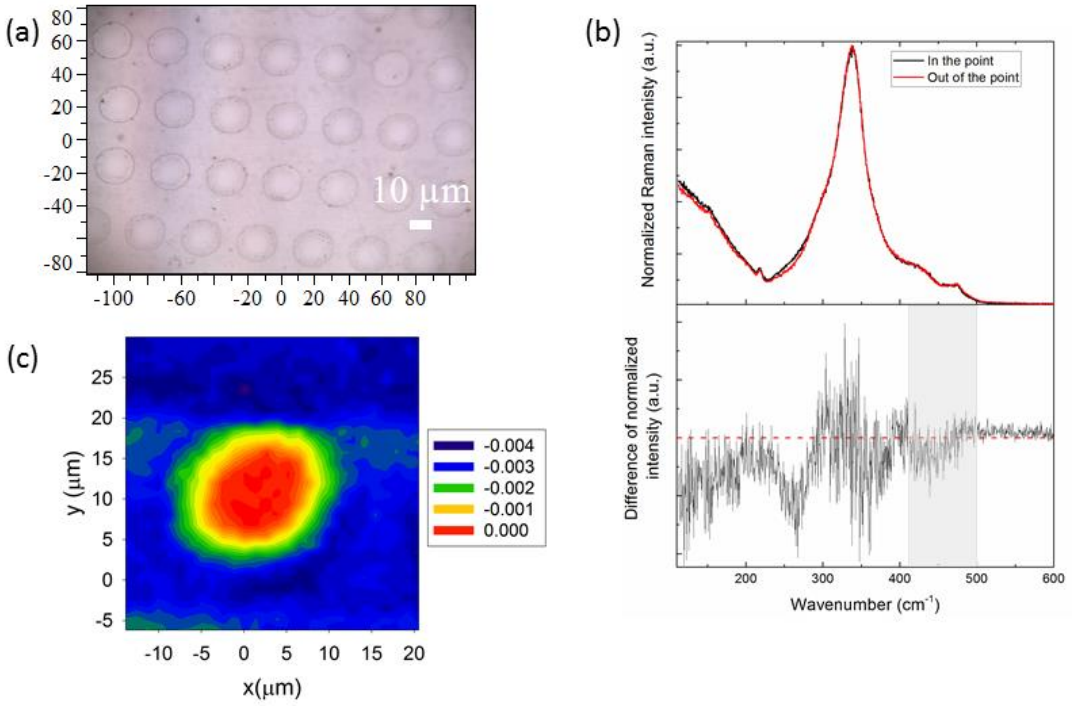

Figure 5.30. Optical micrograph of the glass surface (a), Raman spectra measured inside and outside a point and their difference spectrum (b) Raman image showing spectral variations observed mainly outside the imprinted point corresponding to sulfur modes

All changes presented so far indicate local modification in composition and structure of the glass. The impact of these modifications on surface properties and optical properties (linearly and non-linearly) were therefore studied.

5.3.5 Control and spatial definition of the distribution of induced electric field

In the previous chapters, we demonstrated the use of a patterned electrode to spatially structure the electric field in a near surface region. The presence of a strong electric field in the poled sample can possibly leads to two types of property changes, (i) a change in surface properties (surface potential, electrowetting,…) and (ii) a change in nonlinear optical properties through an electro-

optical effect. Here we discuss the possibility of each of these effects and their possible impacts on the process and resulting properties.

5.3.5.1 Surface properties changes

To evaluate potential surface potential modifications, AFM in PeakForce KPFM mode was used to monitor the surface potential. All measurements were done on the glass containing 1% of sodium sulfide. KPFM measurements can sometimes be dependent on surface topology, where an abrupt topology change is wrongly associated to surface potential change. This composition was chosen for the study as its topological changes were found to be close to zero. Any surface potential changes measured here are therefore trustworthy. Measurements were carried out on freshly poled samples and are presented in Figure 5.31 for two types of patterns: a rectangle and series of dots.

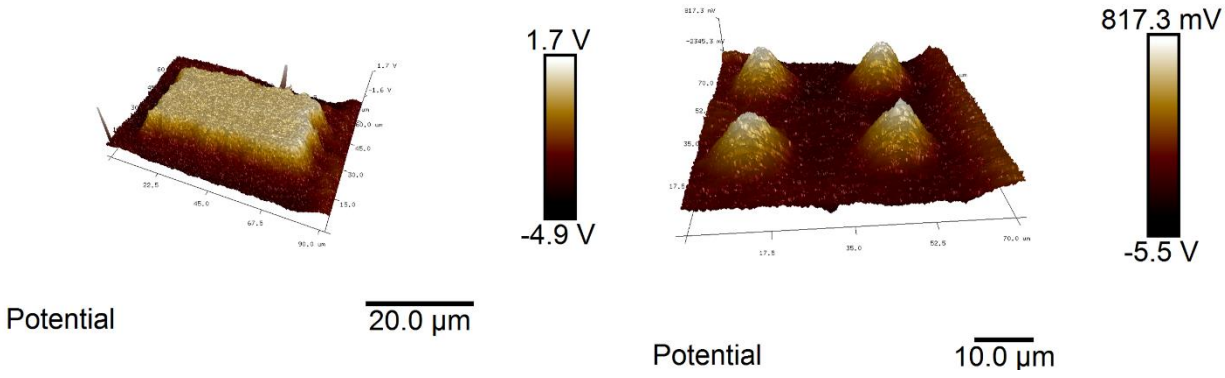

Figure 5.31. Surface potential measured in KPFM mode on an imprinted rectangle (left) and a series of dots (right)

The surface potential measured at the surface of the poled glass is strong and presents a change of sign as it goes inside a pattern. The pattern itself seems to be positively charged while the outer side (the poled region) is negatively charged. The potential measured at the surface of both types of pattern present a really good homogeneity. The inner part of the rectangle presents a

homogeneous potential of approximately 350 mV while the outer part presents a potential of -3.3 V. Results are similar for the dots with a surface potential close to 300 mV inside the pattern and -3.3 V outside of it. The map recorded on the dots is especially interesting. All dots imprinted on the glass surface have the same size and were successfully imprinted on the surface. The resulting image of their potential is identical for all points. Additional measurements were performed on similar regions of the sample and the surface potential change was similar in magnitude.

It is interesting to compare the potential measured at the surface with the work of Palleau et al. on a charged surface. [30] In their work, they positively and negatively charged a polymer surface with an AFM tip. The obtained a patterned area with surface potential change of the order of ± 2 V. They then successfully attracted charged nanoparticles dispersed in a solution by dipping the sample in it. Results presented in our KPFM study of the surface after thermal poling show that the magnitude of the surface potential is comparable to the one obtained by Palleau et al. Such a surface could therefore be used to selectively attract charged particles at its surface. This present a direct application of such a surface, especially as it presents the advantage of being on a substrate transparent in the infrared region. Even if this work represents a good comparison, the potential of a surface potential control at this scale should not be limited to applications for the attraction of charged particles. The change of surface potential is large and could lead to additional surface properties changes and additional investigations are necessary to fully characterize the potential of this finding.

5.3.5.2 Change of nonlinear optical properties

In chapter 3 and 4, it was demonstrated that using patterned electrode during thermal poling resulted in a structuration of the SHG signal. To highlight these effects, µ-SHG measurements

were used and demonstrated the micro-patterning of the induced electric field around imprinted patterns. These effects were thought to be attributed to side effects and a change in charge distribution across the glass' surface.

On Na-rich chalcogenide compositions, it was already shown that changes similar to that seen in oxide glasses were taking place during micro-poling. Following cation migration and structural re-arrangement, the glass properties (surface properties) were modified at the micrometric scale. Regarding the μ-patterning of the SHG response, it is not possible to use μ-SHG measurements to probe for the electric field as the glass is not transparent at 532 nm, 532 nm being the wavelength at 2ω on our μ-SHG setup. However, in chapter III, we have demonstrated that nonlinear refractive gratings could be imprinted on the glass surface and studied using our Maker fringes set-up. We therefore imprinted diffractive gratings consisting in series of lines 6 μm wide and space every 6 μm. The possibility for these gratings to induce SHG diffraction was evaluated with the Maker fringes at 1550 nm. The incident light was linearly polarized perpendicularly to the imprinted lines The recorded diffraction pattern and corresponding fit is presented in Figure 5.32.

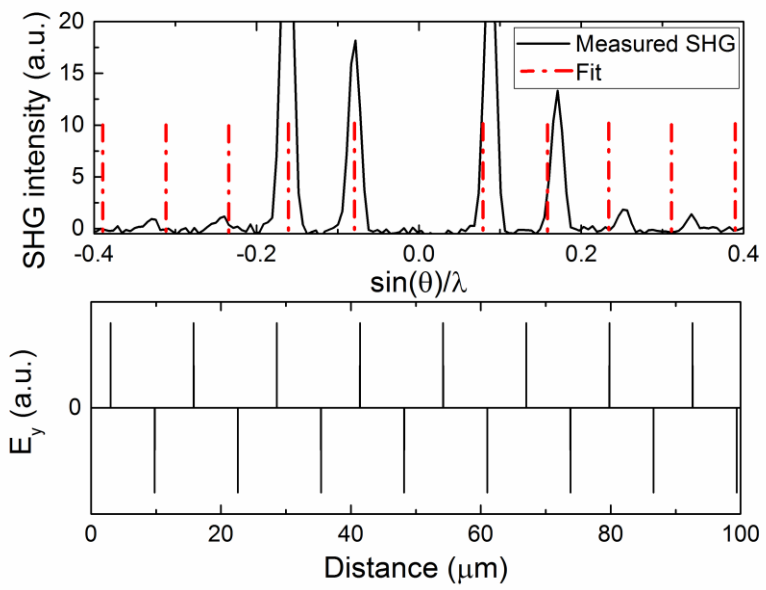

Figure 5.32. Nonlinear diffraction pattern with corresponding fit (top) and electric field component distribution across the surface (bottom)

The gratings can successfully diffract the light nonlinearly. The nonlinear diffraction pattern presents an extinction of the 0 order line and 4 diffraction peaks around it. It was shown on BPN 42 that structuration of the electrode lead to apparition of in-plane components of the induced electric field. When series of lines were written on the glass surface, the in-plane components were controlled and structured. Each edges of the imprinted line gave an in-plane contribution with opposite sign. The same model of the in-plane electric field repartition around the lines was successfully used to fit the obtained diffraction pattern in chalcogenides. However, this simple model does not allow us to fit the intensity of the diffraction peaks. In addition, there are small differences in the diffraction angles between the fit and the experimental data. These differences can be explained by the fact that all imprinted lines had small variations in thickness and pitch from one line to another that the model does not take into account. These inhomogeneities in the

gratings appear during the preparation of the electrode which would require optimization during the preparation step.

The diffractive gratings have allowed us to further demonstrate that the micro-poling process allows one to structure the induced electric field in the plane of the surface in chalcogenide glasses. So far we have only presented results of these procedures on the glass specimens studied. The underlying mechanisms are discussed below for both the imparted changes of micro-patterned poling on the surface properties and linear/nonlinear optical properties.

5.3.5.3 Discussion of observed results

We have shown that the use of a µ-patterned electrodes could serve to imprint structure at the surface of the glass. It was then shown with AFM that the topological change was minimum even if a trench was imprinted on the outer part of the patterns when the sodium content increases. The modification of surface topology was associated with sodium departure and could be monitored using EDX measurements. Raman spectroscopy further confirmed the progressive departure of sodium, observed through structural changes associated with sodium departure. The change in sodium content was proven to be progressive and a gradient of both sodium and structure was then forming across a pattern. The center of the patterned was unchanged while the outside of it underwent the largest changes.

The role of sodium appears to be preponderant in the µ-imprinting process. Indeed, when absent from the composition, no imprinting could take place and when the amount of sodium was increased, so did the magnitude of the property changes. By combining the experimental data

gathered in this section and the electrostatic models presented in chapter 3, it is possible to explain the structuration observed of the surface potential and nonlinear optical properties.

All results can be put in perspective with both compositional changes and structural changes. It is observed that no changes are ever observed in the center of the pattern while a progressive change occur in all measurements. The highest deviation from the center is always found outside the patterns. It is important to note that all of these changes do not occur sharply at the edges of the pattern but that they take place progressively as gradients. The electrostatic models can help to understand this phenomenon. First, structuring the ITO coating was linked to a change in charge distribution at the surface of the glass. To simulate results obtained in μ-SHG in chapter 3, it was necessary to define two neighboring regions of opposite signs, with the patterned area positively charged and the poled area negatively charged. The sign of the surface potential measured in the chalcogenide across a pattern directly confirms the model of two neighboring areas with opposite signs which compensate each other. These two regions follow the sodium distribution across the sample. In effectively poled area, sodium departure leads to an overall negative charged layer which is compensated by a neighboring positively charged layer where sodium has not migrated.

In addition, side effects were considered to be taking place leading to a difference in charge repartition at the surface of the glass. The electrostatic simulations have highlighted the role of in-plane components of the applied electric field; these components are thought to be responsible of additional migration in the plane of the glass surface. The image of these frozen in charges then leads to in-plane components of the electric field. However, we know from the previous section that in-plane components are already present in thermal poling of chalcogenide even without electrode structuration. The structured electrode could hence help to control these components by

changing the distance over which they are effective as well as their magnitude. The nonlinear diffraction experiment help to further confirm this as such effect are based upon control of in-plane components of the electric field. By structuring the electrode, in-plane components are promoted and charges are frozen in the plane of the glass surface. The resulting in-plane components of the E_{DC} field are then patterned across the surface with maxima on each edges of the imprinted lines. The obtained diffraction patterned was successfully described by a strong electric field in the plane of the surface on each edges of the line with opposite direction. In the present experiment, instead of having a random and inhomogeneous distribution of the in-plane electric field, structured electrodes allow to control this effect. We have highlighted the border effects of the structured electrodes, which lead to accumulation of charges close to the pattern. This is also the case here, as the spatial distribution of the diffractive peaks is good showing that the electric field in the plane is present only close to the lines. However, the magnitude of the induced electric field might vary from one line to another as shown by the difference in magnitude of the diffractive peaks between the fit and the experimental values.

5.3.6 Micro-patterning of the linear optical properties

The EDX map and Raman map highlight the creation of a gradient of composition associated with a progressive change of the glass's structure. Potential changes in linear optical properties was therefore evaluated for two properties: (i) the ability to demonstrate optical power to serve as a focusing microlens, and (ii) to utilize the spatial variation as a diffractive optical element (DOE).

5.3.6.1 Capability of the imprinted patterns to function as focusing microlenses

The imprinting process was used to imprint circular pattern on the glass surface. EDX and Raman spectroscopy have shown the formation of a gradient of sodium composition and progressive

structural changes. A progressive change of glass composition could be at the origin of a progressive change of refractive index. The formation of a Gradient of Refractive Index lens (GRIN lens) is therefore possible and was evaluated.

To study the potential to create GRIN lenses with this technique, the capability of these pseudo-lenses to focus light was evaluated. A simple way to verify the focusing capacity of the matrix of lenses was used. The sample to be measured was placed on a microscope stage and illuminated in transmission mode with a collimated light. Light was then collected by a microscope objective. The focus was first made on the surface of the glass; the plane of the surface will be further referred to z=0. The objective was then slowly defocused from the surface until a matrix of illuminated points was observed. If such a matrix is observed, it shows that light is focused by the lenses. Similarly, if one defocuses the assembly, now going inside the sample, the opposite trend should be observed, i.e. a matrix of black dots (blocking the light). The plane of illuminated points is actually the direct image of the image plane, z=x. The focal length can thus be evaluated and is equal to x. This is true in the case of a thin lens approximation.

The measurements were performed on all imprinted lenses and always showed the focusing capacity of the dots. We will therefore subsequently refer to the imprinted dots as µ-lenses. The following figure shows results obtained on glass B – 1% Na_2S for various lens diameters. The top row presents the microscopic image of the lenses (themselves) at the surface of the glass while the bottom row shows the illuminated matrix obtained with the objective focused above the glass surface. These micrographs show that by varying the size of the dots imprinted on the glass surface, the focal length of the resulting patterned array structure changes. The focal lengths were then measured following the procedure described. The evolution of the focal length as a function of

lens sizes is shown in Figure 5.34 for the composition with the lowest amount of sodium and five sizes of imprinted lenses. It can be observed that the increase of lens diameter is directly followed by an increase in focal length.

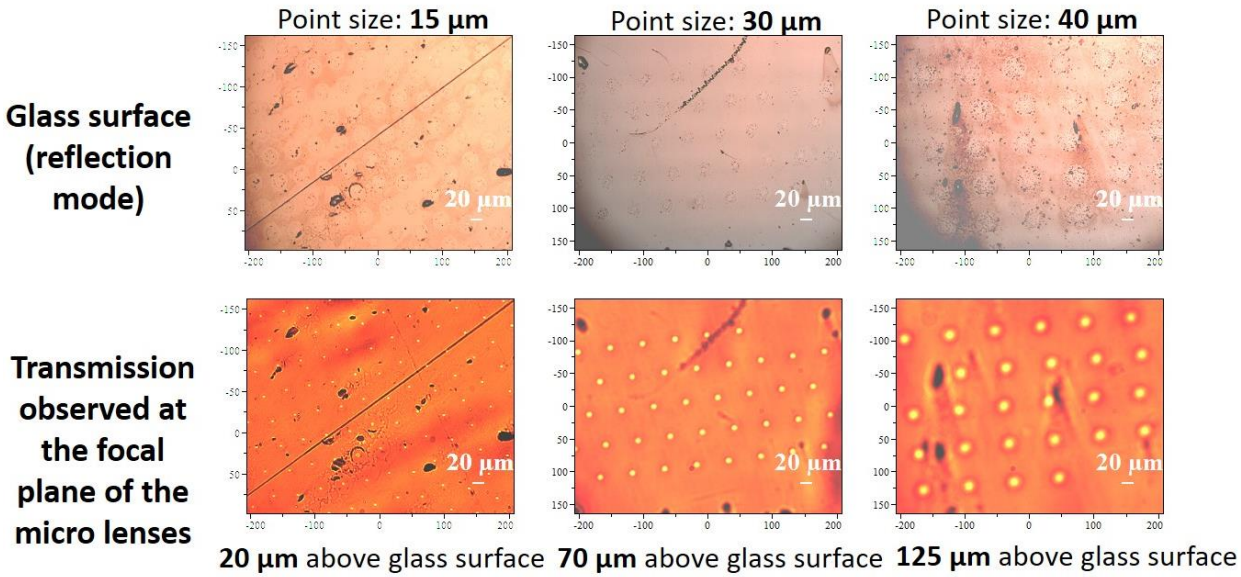

Figure 5.33. Image of various matrices of lens with increasing size (top row) corresponding obtained matrix of illuminated points at the focal plane (bottom)

In the previous section, we showed that nonlinear optical properties induced in the glass following thermal poling were not stable over time. In the case shown here, the focusing capability of the µ-lenses matrix was evaluated several months after they were formed and no change in their focal length was observed. It appears that the change of linear optical properties is stable over time, as opposed to the change in non-linear optical properties.

The capability of the lenses to focus light in their center has been demonstrated. Moreover, it appears that changing the diameter of the lens to be imprinted influences the focal length. It is possible that it affects the curvature of the sodium gradient and therefore the effective refractive

index across the surface. The process of imprinting lenses at a glass surface was demonstrated using a thermal poling approach. The process was proven to be reliable, reproducible and stable over time. An application for a European patent was filled and is awaiting for approval. [31]

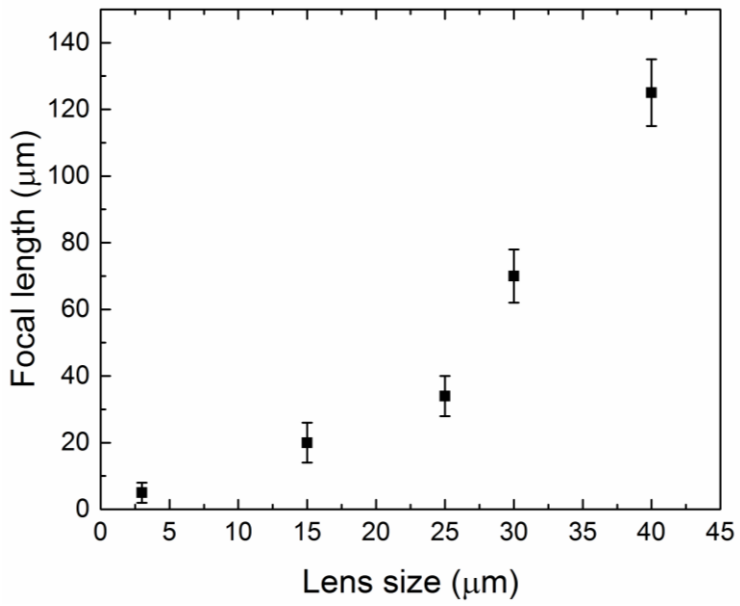

Figure 5.34. Evolution of the focal length as a function of lens size

Finally, in addition to circular patterns, the focusing capability of the pattern was also demonstrated for other shapes, such as lines. Figure 5.35 shows that the center of the imprinted line presents an intense thread of light in its middle when illuminated from underneath. Most patterns showed the capability to focus light except for the rectangle shapes that were of larger dimensions. In addition to this focusing capability, the diffraction capacity of the patterns was also evaluated.

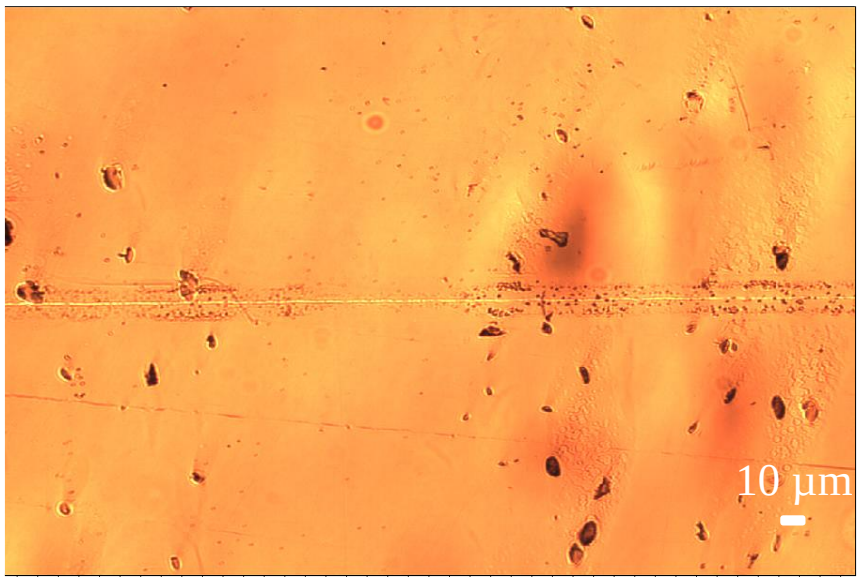

Figure 5.35. Focusing capacity of a line imprinted on composition B-1% Na_2S

5.3.6.2 Linear diffractive gratings

Gratings with various line thickness and pitch between each lines were successfully imprinted on composition B-3% Na_2S. Each grating was 4 mm^2 and could be observed with the naked eye. To evaluate the diffraction capacity of the gratings, the sample was first irradiated with a 785 nm laser to observe visual evidence of diffraction. Figure 5.36 shows this experiment and the presence of various diffraction spots. This simple experiment already indicates the potential of these glasses as diffractive gratings. It is worth noting that diffraction spots could be observed in both transmission and reflection.

To better characterize their potential as diffractive gratings, diffraction figures were then recorded on the Brewster angle set-up presented in chapter 2. The sample was placed at normal incidence and irradiated with a 1550 nm laser. The detection unit was then rotated around the sample to

collect the potential diffraction peaks. The recorded diffraction pattern as well as the grating profile used to fit the diffraction peaks are presented in Figure 5.37.

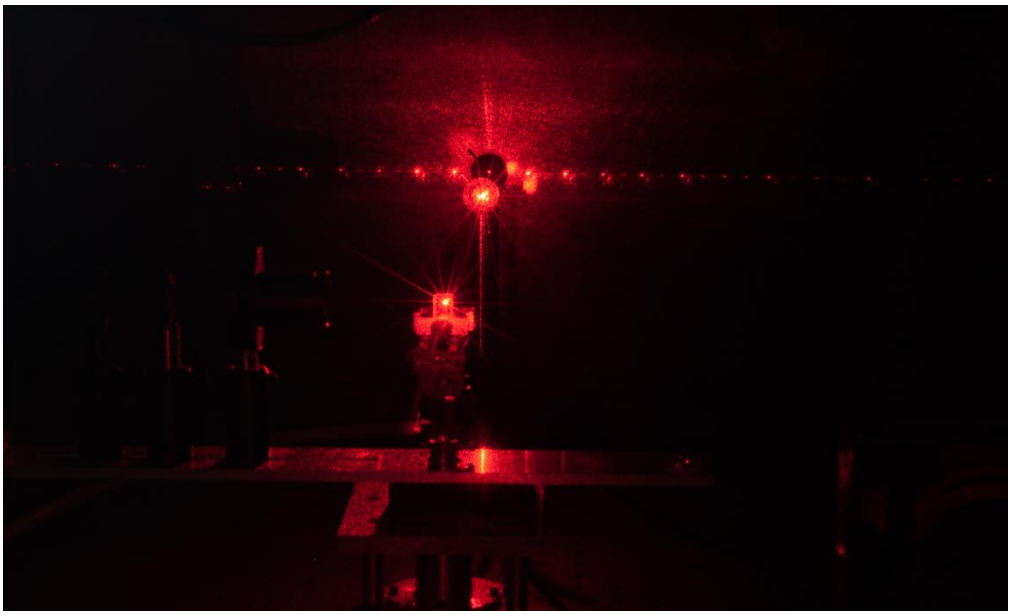

Figure 5.36. Picture of the observed linear diffraction pattern of light at 785 nm

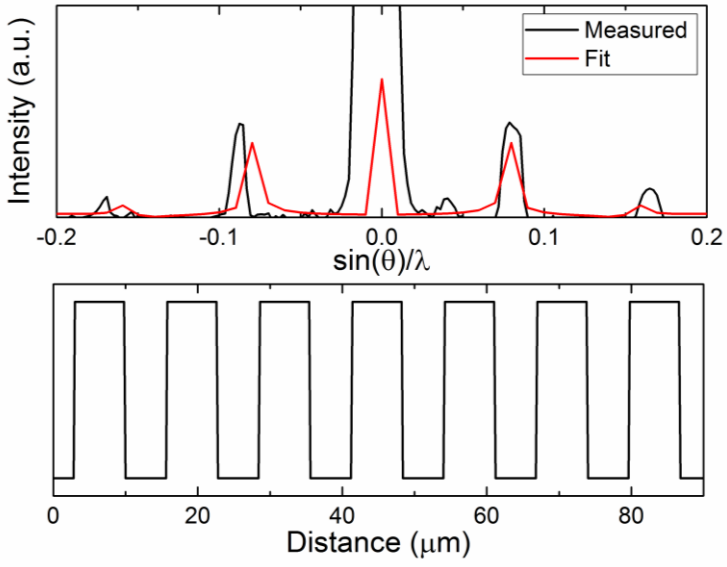

Figure 5.37. Linear diffraction pattern recorded on the grating (top) and profile used to simulate the grating (bottom)

A diffraction grating modulates the phase of the incident wave by a change in topology at the surface of a material. To fit for the obtained peaks, a profile with periodic relief was defined (Figure 5.37 bottom) and peaks were obtained after Fourier transform of this pattern. However, it is important to keep in mind that the topological changes observed after thermal poling are minimal. Similarly as with the nonlinear diffraction grating, the simple model that we have used does not allow us to fit for the amplitude variation from one peak to another. Variations in diffraction angles between the model and the measurement are also due to spatial irregularities in the gratings during the electrode structuration step. Finally, regarding the diffractive gratings, the work presented here is nothing but a proof of concept. Additional characterizations and modeling are necessary to fully characterize them and the impact of pitch, length thickness also necessitate to be studied.

The mechanism responsible for both focusing and diffractive capacity of the patterns need further explanations and will be discussed in the following part.

5.3.6.3 Discussion.

So far, it has been shown that micro-poling of Na-rich glasses lead to changes of surface properties and nonlinear optical properties that could be linked to sodium departure and to the localization of the frozen in charges inside the glass.

Similarly in the change of linear optical properties, the role of sodium appears to be preponderant. The sodium distribution at the surface was found to be gradually increasing as we enter a structured area. It is then easily understood that by changing the size of the features inscribed on the electrode, the curvature of the sodium distribution can be tuned. This change of sodium gradient can also be

linked to surface current especially to the distance over which they are effective. The change of refractive index for both μ-lenses and diffractive gratings is then controlled by the change in composition in a near surface region. This progressive change of refractive index is responsible for the focusing and diffracting properties of the imprinted patterns. The optical properties can then be controlled by tuning the distribution of the composition in the sample. The impact of topology changes is negligible as they were shown to be rather low.

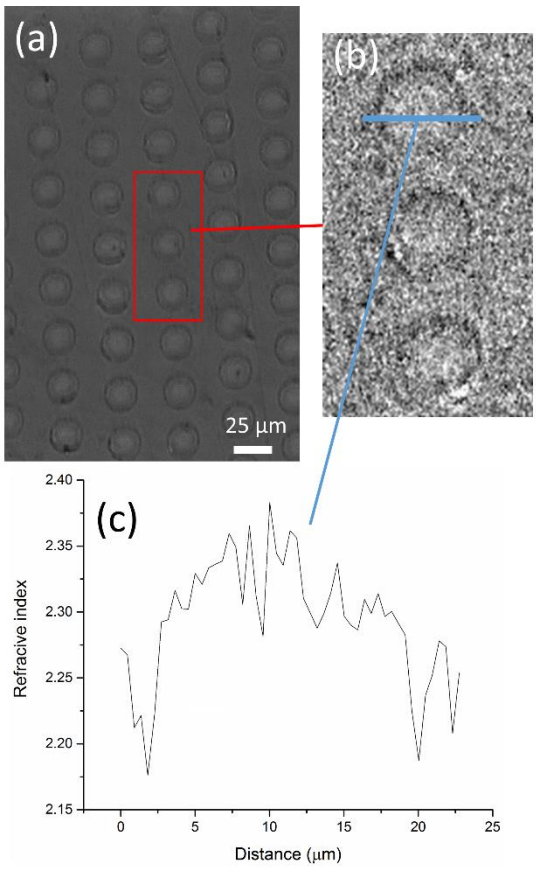

Figure 5.38. Image of the patterned area (a), map of the refractive index change (b) and profile of the refractive index evolution across a pattern (c)

The refractive index is maximum in the center of the pattern and minimum outside of it similarly as the change between Na-free and Na-rich composition. Measurements of the Δn between a poled

area and a neighboring unpoled area is challenging. We lack of good experimental techniques to quantify this change. Trials to quantify the difference using an ellipsometer were attempted and an example is shown on Figure 5.38. The change of refractive index is measured to be as high as 0.09. This measurement needs to be taken carefully as it is strongly model-dependent.

In addition to this first attempt at quantifying the refractive index change, another attempt was made on a thermally poled glass without a structured electrode. The area of refractive index change in such a geometry is homogeneous and thus, it is easier to quantify it through other metrology tools. Micro-IR reflectance spectroscopy was used to measure interference fringes between the poled layer and the rest of the bulk. The refractive index of the bulk should remain unchanged while the sodium depleted layer should present a decrease of its refractive index. Sample B-1% was used for this measurements as sample B-3% presented larger absorption band linked to impurities, rendering the fitting process more difficult. Interference fringes were recorded and a program developed in the Molecular Spectroscopy Group in Bordeaux University was used to fit them. Further details can be found in an article by Dussauze et al.. [32] This model was originally designed to describe multilayers for glass thin films. Simulations were performed in a region which does not present any absorptions and where the refractive index n can be considered as frequency independent and the absorption k as negligible ($\sim 10^{-6}$). The refractive index of the bulk was fixed using the measurements done at $\lambda = 4.5$ μm and the thickness of the bulk was set to 1000 μm. The refractive index and the thickness of the poled layer were the two parameters to be fitted. Figure 5.39 shows both measured fringes and obtained fit using a layer thickness of 13.85 μm and a variation of refractive index of 0.07 between the bulk and the poled layer. As compared to the thickness that was measured with SIMS, there is a fairly good agreement as the difference is within

3 μm and the variation of refractive index is similar to what was measured on sample B-3% with the ellipsometer. There is however room to improve it as it is observed that the periodicity of the fringes changes with increasing wavenumber while the amplitude stays the same. In addition, more samples need to be investigated using this methodology but it could be an interesting tool for us to quantify the variation of refractive index in the poled layer.

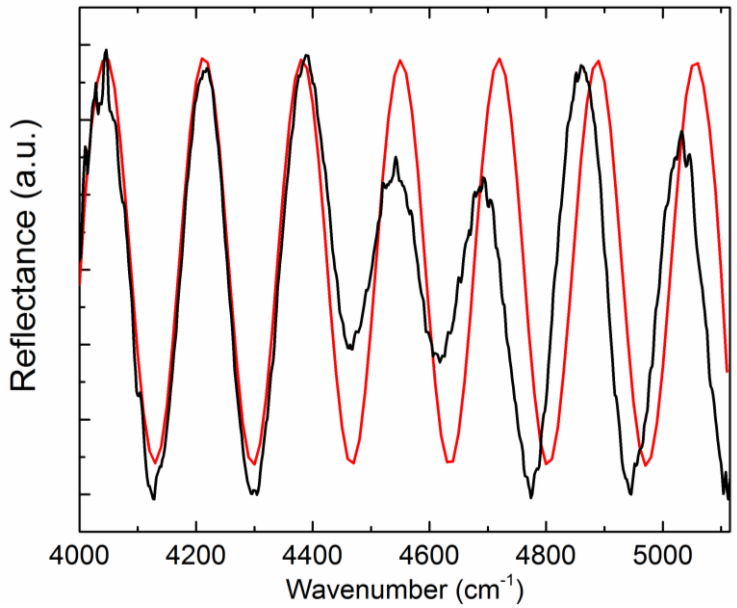

Figure 5.39. Interference fringes measured in IR reflectance spectroscopy on the poled sample B-1% (black) along with a fit (red)

In addition to these two measurements, refractive index measurements performed on both B-1% and B-3% were performed on poled samples using our custom IR Metricon set-up at 4.5 μm. The measurements were done repeatedly on both anode and cathode sides to assess refractive index variations after thermal poling and stability over time. Measurements of both glass samples are reported on Figure 5.40 (once again the error bars are within the data point when not visible). On both samples, measurements were performed on the anode side, which corresponds to the area

where sodium migration effectively takes place, and on the cathode side, which is the opposite side of the glass where no sodium migration was measured (therefore having the composition of the glass prior thermal poling). The first valuable information that can be obtained is that on the cathode side, where the measured refractive index corresponds to that of the glasses prior thermal poling, i.e. 2.2064±0.0002 for B -1% and 2.2073±0.0003 for B -3%. Also, over time, the refractive index on this side of the glass remains the same. However, on the anode side, a large drop in refractive index is observed for both glass samples, respectively by -0.025 and -0.045. For both glass composition, the refractive index on both sides is not varying and remains stable as the sample aged. Larger variations are observed on composition B-3% on the anode side. However, this particular sample was actually partially structured on the anode side which could easily explain this lack of homogeneity. These measurements were performed at the end of our work and are therefore not optimized. In the future, a sample of the same composition will be poled once again without any structuration to have better refractive index measurements. However, these measurements can still be useful to evaluate the magnitude of the refractive index change as a function of sodium content.

Interestingly, the refractive index change in composition B-1% follows the change measured with addition of sodium to the base glasses, where composition B without sodium has a refractive index of 2.1812±0.0002. It therefore appears that for this glass composition, moving away sodium from the anode side is equivalent to going back to the composition of the base glass without sodium. Now looking at the results obtained on composition B-3%, the refractive index change is even greater and after thermal poling, measurements performed on the anode side give value lower than that of the base glass without sodium.

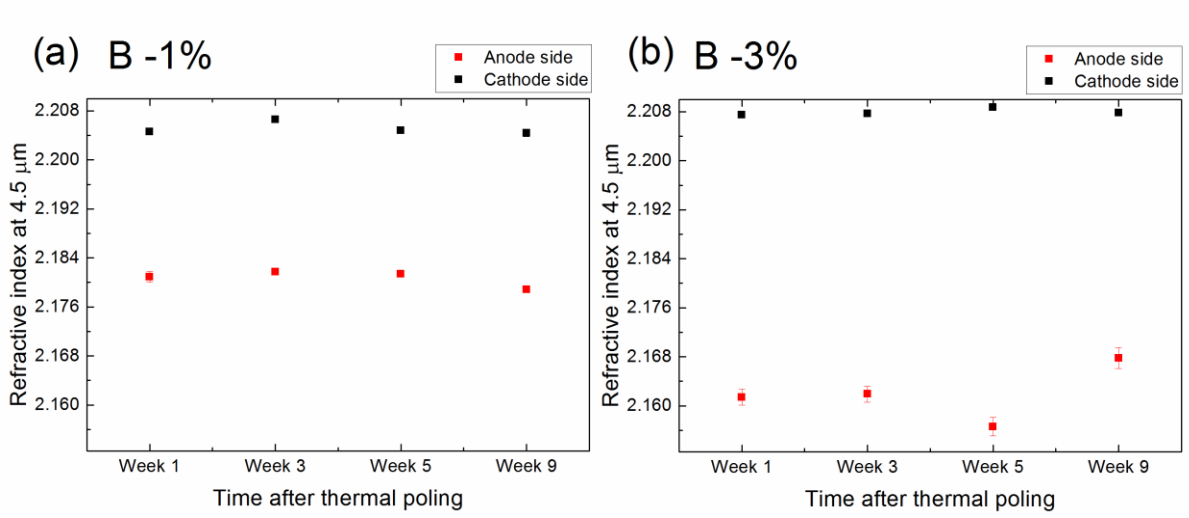

Figure 5.40. Refractive index measurements on thermally poled samples, B -1% (a), B -3% (b)

These three measurement techniques represent ongoing work and efforts are still necessary to calibrate these measurements techniques and to find a reliable way to measure the refractive index change. However, they give us a brief and impressive idea of the magnitude of the induced refractive index change in the poled area that is responsible for the focusing capacity of the μ-lenses and highlight the important contribution of this work, that clearly illustrates selection of the candidate glass composition (and network) can result in not only a meaningful ($\Delta n \sim 0.02$) change in index within the bulk material but one that exhibits retained stability over timescales that are important to potential device applications.

We believe that the gradually changing composition associated with the alkali migration (within the electrode/poled region) is responsible for the formation of a gradient of refractive index creating μ-lenses. In measurements on composition B-1%, the Metricon set-up gives refractive index changes which are comparable to sole compositional changes; for the two other techniques and sample B-3%, the variation of refractive index is far too great to be solely explained by

compositional changes. The refractive index difference between the sodium free (B) and sodium rich glass (B-1%) at 4.5 μm is only of 0.02. The change of refractive index can therefore not be simply explained by a local compositional changes and likely also contains a change in structure (which can impact local density and molar volume, both attributes that impact the polarizability that defines the local refractive index). It is however known that sodium departure can be accompanied by a change in molar volume and density in the poled area which was, for instance, already mentioned in BPN glasses. The combination of these two effects, compositional changes and molar volume changes, could explain for the larger variation in refractive index which is observed. Further investigations and quantifications of molar volume changes are necessary to fully describe the refractive index change measured.

5.3.7 Conclusion of section 5.3

This section has shown through a concrete example that the micro-imprinting process is useful to design optical functionalities and surface properties in glasses. This method is versatile and was proven to be feasible in oxide glasses as well as non-oxide glasses as soon as they present a non-negligible cationic conductivity. In the creation of μ-lenses array, diffractive gratings and patterning of the surface potential, it has been demonstrated that the key element is to control the gradient of sodium in the glass. To do that, we need to control the in-plane component of the electric field associated with the use of structured electrode.

All examples presented here have the main advantage of being transparent in the infrared region and partially transparent in the visible region. All of these elements were successfully created using a μ-poling technique which has the advantage of being versatile, fast and transferable to a variety of glass compositions. The patterns that can be imprinted on the glass surface can be precisely

controlled by the laser ablation of the ITO coating and large surfaces can be patterned at once. As shown, excellent correlation between lenslet shape, gradient index (as quantified by the radial change in refractive index associated with Na ion content) knowledge of a look up table of size, index change, shape change, poling conditions could enable tailored grin structures and profiles to be created. Finally, the method is rather cost-effective as electrodes can be re-used after thermal poling, as long as the ITO layer is not damaged.

5.4 Conclusion of the chapter

This chapter was intended to present a complete study of thermal poling of Ge-Sb-S glasses. The second section was more of a fundamental study to understand the mechanism behind thermal poling of chalcogenide glasses. Even if these glasses have been previously studied in the literature, lots of questions were still unanswered. Especially, the poor stability of the induced 2^{nd} order nonlinearity has always been a drawback. Solutions to improve the stability were therefore needed. At the end of our study, we agree with the vision described by Guignard et al. [7] where charged defects are forming upon thermal poling. These charges then easily recombine at room temperature, especially upon exposure to light, possibly due to a photogalvanic effect. In order to stabilize these charges, we added sodium sulfide to the glass network to promote structural re-arrangements upon cationic migration. The sodium migration and structural changes were highlighted using EDX and Raman spectroscopy as well as the concomitant enhancement of the stability of the induced 2^{nd} order nonlinear optical properties. Even if progress has been made in this study, there is still room to improve the induced SONL as the intensity of the $\chi^{(2)}$ is rather low. Solutions could be found in other glass systems, maybe in oxi-chalcogenide glasses which could combine the stability of an oxide with the transparency and high $\chi^{(3)}$ of a chalcogenide.

Finally, this chapter has also allowed us to confirm the potential of thermal poling as a way to create optical elements such as µ-lenses and diffractive gratings as well as patterning the surface properties of a glass substrate. These applications are only possible through the use of patterned electrodes comprised of a conducting layer on top of an insulating substrate. The structured electrode then allows to locally control the composition of the glass at the micrometric scale. It is therefore possible to create a multiplicity of optical functions on a glass substrate by tuning the refractive index locally. Creation of µ-lens array finds direct applications in the industry. Thermal poling has been now studied for over two decades but this could be the first time that it finds concrete applications and that it could lead to its transfer from the laboratory to the industry. We believe that other applications of thermal poling using patterned electrodes will be found in the near future.

5.5 References

(1) Dussauze, M.; Cremoux, T.; Adamietz, F.; Rodriguez, V.; Fargin, E.; Yang, G.; Cardinal, T. Thermal Poling of Optical Glasses: Mechanisms and Second-Order Optical Properties. *International Journal of Applied Glass Science* **2012**, *3*, 309-320.

(2) Vengel', T. N.; Kolomiets, B. T. Vitreous Semiconductors some Properties of Materials in the System as/Sub 2/Se/Sub 3/-as/Sub 2/Te/Sub 3/. II. *Zhurnal Tekhnicheskoi Fiziki* **1957**, *27*, 2484-2491.

(3) Kolomiets, I. B. T. Vitreous Semiconductors. *Physica Status Solidi* **1964**, *7*, 359-372.

(4) Guignard, M. Verres et vitrocéramiques infrarouge à base de chalcogénures pour l'optique non linéaire du second ordre, Université de Rennes I, Rennes, 2005.

(5) Wang, R. In *Amorphous chalcogenides : advances and applications;* Singapore : Pan Stanford Publishing, 2014]: 2014; .

(6) Koontz, E.; Wachtel, P.; Richardson, K. A. In *In Compositional dependence of structural relaxation behavior in the Ge-As-Se system characterized by length dilatometry;* Classical Optics 2014; Optical Society of America: 2014; , pp OM2.4.

(7) Guignard, M.; Nazabal, V.; Smektala, F.; Adam, J. -.; Bohnke, O.; Duverger, C.; Moréac, A.; Zeghlache, H.; Kudlinski, A.; Martinelli, G.; Quiquempois, Y. Chalcogenide Glasses Based on Germanium Disulfide for Second Harmonic Generation. *Advanced Functional Materials* **2007**, *17*, 3284-3294.

(8) Guignard, M.; Nazabal, V.; Troles, J.; Smektala, F.; Zeghlache, H.; Quiquempois, Y.; Kudlinski, A.; Martinelli, G. In *In Second-harmonic generation improvement in sulfide glasses;* Proceedings of SPIE - The International Society for Optical Engineering; 2005; Vol. 5949, pp 1-9.

(9) Guignard, M.; Nazabal, V.; Troles, J.; Smektala, F.; Zeghlache, H.; Quiquempois, Y.; Kudlinski, A.; Martinelli, G. Second-Harmonic Generation of Thermally Poled Chalcogenide Glass. *Optics Express* **2005**, *13*, 789-795.

(10) Zeghlache, H.; Guignard, M.; Kudlinski, A.; Quiquempois, Y.; Martinelli, G.; Nazabal, V.; Smektala, F. Stabilization of the Second-Order Susceptibility Induced in a Sulfide Chalcogenide Glass by Thermal Poling. *J. Appl. Phys.* **2007**, *101*.

(11) AnonymousREACH: Registration, Evaluation, Authorisation and Restriction of Chemicals. *http://eur-lex.europa.eu/legal-content/EN/TXT/?uri=CELEX:32006R1907* (accessed 7/10, 2016).

(12) Thorpe, M. F. Bulk and Surface Floppy Modes. *J. Non Cryst. Solids* **1995**, *182*, 135-142.

(13) Phillips, J. C.; Thorpe, M. F. Constraint Theory, Vector Percolation and Glass Formation. *Solid State Commun.* **1985**, *53*, 699-702.

(14) Thorpe, M. F. Continuous Deformations in Random Networks. *J. Non Cryst. Solids* **1983**, *57*, 355-370.

(15) Thorpe, M. F. Rigidity Percolation in Glassy Structures. *J. Non Cryst. Solids* **1985**, *76*, 109-116.

(16) Tanaka, K. Structural Phase-Transitions in Chalcogenide Glasses. *PHYSICAL REVIEW B* **1989**, *39*, 1270-1279.

(17) Sreeram, A. N.; Swiler, D. R.; Varshneya, A. K. Gibbs-DiMarzio Equation to Describe the Glass Transition Temperature Trends in Multicomponent Chalcogenide Glasses. *J. Non Cryst. Solids* **1991**, *127*, 287-297.

(18) Vahalová, R.; Tichý, L.; Vl?ek, M.; Tichá, H. Far Infrared Spectra and Bonding Arrangement in some Ge-Sb-S Glasses. *physica status solidi (a)* **2000**, *181*, 199-209.

(19) Linke, D.; Eberhardt, G. Eigenschafts-Korrelationen Bei Chalkogenidgläsern. IV. Relative Spannungsoptische Koeffizienten Und Volumenkompressibilitäten Von Gläsern System GeS -GeS2-Sb2S3 Und GeSe-GeSe2-Sb2Se3. *Zeitschrift für anorganische und allgemeine Chemie* **1978**, *442*, 263-279.

(20) El-Hamalawy, A.; El-Zaidia, M.; Ammar, A. A.; Elkholy, M. M. Density, Differential Thermal Analysis and Direct-Current Conductivity of [Sb.Sub.10][S.Sub.90 -X]Ge.Sub.X Chalcogenide Glasses. *J. Mater. Sci. : Mater. Electron.* **1994**, , 147.

(21) Tauc, J. Optical Properties and Electronic Structure of Amorphous Ge and Si. *Mater. Res. Bull.* **1968**, *3*, 37-46.

(22) Tauc, J.; Menth, A. States in the Gap. *J. Non Cryst. Solids* **1972**, *8–10*, 569-585.

(23) Kavetskyy, T. S.; Kovalskiy, A. P.; Pamukchieva, V. D.; Shpotyuk, O. I. IR Impurity Absorption in Sb2S3-GeS2(Ge2S3) Chalcogenide Glasses. *Infrared Phys. Technol.* **2000**, *41*, 41-45.

(24) Jaffe, H. W. In *Crystal chemistry and refractivity;* Mineola, N.Y. : Dover Publications, 1996; Dover ed: 1996; .

(25) Koudelka, L.; Frumar, M.; Pisarcik, M. Raman Spectra of Ge-Sb-S System Glasses in the S-Rich Region. *J. Non Cryst. Solids* **1980**, *41*, 171-178.

(26) Lucovsky, G.; Galeener, F. L.; Keezer, R. C.; Geils, R. H.; Six, H. A. Structural Interpretation of the Infrared and Raman Spectra of Glasses in the Alloy System Ge1-xSx. *Physical Review B* **1974**, *10*, 5134-5146.

(27) Ward, A. T. Raman Spectroscopy of Sulfur, Sulfur-Selenium, and Sulfur-Arsenic Mixtures. *J. Phys. Chem.* **1968**, , 4133.

(28) Brennand, A. L. R.; Wilkinson, J. S. Planar Waveguides in Multicomponent Glasses Fabricated by Field-Driven Differential Drift of Cations. *Opt. Lett.* **2002**, *27*, 906-908.

(29) Shimakawa, K.; Inami, S.; Elliott, S. R. Reversible Photoinduced Change of Photoconductivity in Amorphous Chalcogenide Films. *Physical Review B* **1990**, *42*, 11857-11861.

(30) Palleau, E.; Sangeetha, N. M.; Viau, G.; Marty, J. -.; Ressier, L. Coulomb Force Directed Single and Binary Assembly of Nanoparticles from Aqueous Dispersions by AFM Nanoxerography. *ACS Nano* **2011**, *5*, 4228-4235.

(31) Dussauze, M.; Lepicard, A.; Bondu, F.; Rodriguez, V.; Adamietz, F.; Cardinal, T.; Fargin, E.; Richardson, K. , 2016.

(32) Dussauze, M.; Kamitsos, E. I.; Fargin, E.; Rodriguez, V. Refractive Index Distribution in the Non-Linear Optical Layer of Thermally Poled Oxide Glasses. *Chemical Physics Letters* **2009**, *470*, 63-66.

CHAPTER 6: CONCLUSION

This dissertation aimed to examine the use of poling for modifying physical and optical properties of glasses. Here, we have examined means to tailor optical properties and surface reactivity of glass substrates at the micrometric scale by mean of a thermal poling treatment where we have optimized treatment conditions in both oxide and non-oxide glass families. Results obtained during this work exceeded our expectations as we were able to apply this to a variety of glasses ranging from oxide glasses (BPN and borosilicate) to non-oxide glasses (chalcogenide).

To obtain these results, we first chose glass compositions that were suitable for such applications. BPN 42 was selected as it was extensively used in Bordeaux and thermal poling's impact on its properties and structure are already well characterized. The study thus focused on controlling the known changes at a smaller scale. For that, we have developed the µ-poling process using structured ITO coated microscope slide as anodes. This new approach has allowed us to control the induced electric field location and geometry. This was an important proof of concept as by mean of a single treatment we were able to control the surface properties at the micrometric scale on distances as long as centimeters long. This possibility was first used to create nonlinear diffractive gratings but could be used for other applications. Once the process fully characterized by mean of µ-SHG/ Raman spectroscopy and electrostatic models, it was possible to apply it to other glass compositions.

On borosilicate glasses, our work focused on finding a way to enhance surface reactivity towards atmospheric water. The first difficulty was to find the appropriate composition which would exhibit that enhanced reactivity only after thermal poling. It was therefore necessary to understand

the glass structure and to predict how it would change upon thermal poling. This is why a glass on the boric oxide anomaly was chosen as its structure, especially through the role of sodium modifiers, could be well controlled. It was then shown that thermal poling in the appropriate conditions could lead to a drastic change of the glass structure which locally changes the arrangements of the borate network towards a more B_2O_3-like structure associated with a strong static electric field. The charged borate structure was stable if stored in vacuum and showed preferential reactivity towards atmospheric water once out of the controlled atmosphere. A leaching process was then identified and responsible for the formation of boric acid. Two approaches were then developed to control similar changes at the micrometric scale, one based on laser induced heating and the second one being the µ-poling approach developed on BPN glasses. The first approach showed limitations as enhance reactivity was not obtained but structuration of the SHG signal was precisely controlled. The second approach allowed to obtain similar properties changes as in the macropoling process but precisely controlled at the micrometric scale.

The work on chalcogenide glasses was overall the most challenging as these glass compositions have always been difficult to thermally pole and exhibited transient stability that was not widely understood. Their high $\chi^{(3)}$ made them attractive for thermal poling for electro-optics as they should lead to large induced $\chi^{(2)}$. While most of the studies done to date had demonstrated poor stability of the induced second order nonlinearity following thermal poling, this work aimed to understand the structural reasons which limited it with the goal of improving the long term stability of post-poling modification.

The first part of the work thus consisted in a fundamental study on thermal poling of chalcogenide glasses. The post-poling properties and structural changes were investigated as a function of sulfur

content and sodium content. Even if sodium is usually not found in chalcogenide glasses, deliberate addition of it was made to study its potential impact. Following thermal poling, the recorded SHG was found to be erratic and not stable for the Na-free glasses. The response of the glass network could not be explained solely by an electric field induced along a longitudinal direction. However, we successfully managed to simulate the obtained fringes with an electric field induced along all directions of the lab-frame. A similar behavior was obtained in the Na-rich glasses but a better stability and improvement of the SHG signal homogeneity was found. It was possible to highlight the similarities with mechanisms of photosensitivity in chalcogenide. and the formation of charged defects under illumination with radiation, as discussed by Shimakawa. The unstable signal was attributed to the formation of charged defects, which can easily recombine at room temperature or under illumination. Such defects would be especially formed in the sulfur rich glasses as they are formed by bond breakage, such as S-S bonds. We attribute the change of stability in the SHG signal of Na-rich glasses to a more stable charge separation through structural re-arrangements which were shown in Raman spectroscopy. A simple way to improve stability of the induced electric field and therefore of the 2^{nd} order nonlinear properties was described. The key element is to promote structural changes to effectively separate charges. The obtained SHG is still rather low and the challenge is still to increase the stability and magnitude of induced changes. Deliberate cation addition could however be part of the answer to a still open question.

In the second part of the chalcogenide work, it was possible to adapt the µ-poling process in the Na-rich glasses. First of all, we showed it was possible to control the magnitude and sign of the surface potential at the surface of the glass at a micrometric scale. This first result is especially promising as surface properties such as electrowettability, reactivity should be enhanced thanks to

the electric field. In addition, a proof of concept of formation of μ-lenses and diffractive gratings (both linearly and nonlinearly) was made in chalcogenides. The presence of sodium which was first intended as a way to improve SHG stability was found to be necessary for the imprinting process to be successful. The refractive index of the glass can then be tailored by controlling the compositional changes in the glass with thermal poling. The formation of such devices was thoroughly studied by a various set of experiments such as Raman spectroscopy, macro-SHG, EDX and AFM/KPFM. All gathered data agreed on the primordial role of sodium migration in all property changes.

I would like to emphasize that all of this work would not have been possible without the first part of the thesis on oxide glasses and the work done in Bordeaux University on thermal poling over the many years prior to this dissertation. The good understanding of the fundamental science behind thermal poling and the evolution of analytical techniques to assess macro- and micro-scale physical and optical properties at both Bordeaux and UCF, has allowed us to quickly transfer the μ-poling technology to non-oxide glasses.

To conclude, it is important to note that the work done during this dissertation opens up new possibilities in thermal poling as one considers its potential in real commercial applications. The technology is now understood deeply enough to enable its consideration in specific commercial applications. Thermal poling as a way to pattern glass surface properties has been shown here and is in the future of this process. During this PhD, the understanding realized in these processes have led to several patents being filed regarding thermal poling for mechanical property changes, 2^{nd} order nonlinear optical properties tailoring and finally the creation of μ-lenses. This proves the potential of this technique in a variety of applications. As an example, we now know how to change

the refractive index of the glass by tuning its composition. This process is feasible in a variety of glass compositions and should not be limited to the creation of μ-lenses. As we have demonstrated, the induced electric field can now be locally controlled which could be useful to improve the 2^{nd} order nonlinear capability of the poled glasses. By controlling the area where thermal poling is effective, phase matching conditions could be obtained therefore greatly improving the usefulness of such poled glasses.

APPENDIX A: COPYRIGHT CLEARANCE

Copyright Clearance Center RightsLink®

Home | Create Account | Help

ACS Publications
Most Trusted. Most Cited. Most Read.

Title: Coulomb Force Directed Single and Binary Assembly of Nanoparticles from Aqueous Dispersions by AFM Nanoxerography

Author: Etienne Palleau, Neralagatta M. Sangeetha, Guillaume Viau, et al

Publication: ACS Nano

Publisher: American Chemical Society

Date: May 1, 2011

Copyright © 2011, American Chemical Society

LOGIN

If you're a copyright.com user, you can login to RightsLink using your copyright.com credentials. Already **a RightsLink user** or want to learn more?

PERMISSION/LICENSE IS GRANTED FOR YOUR ORDER AT NO CHARGE

This type of permission/license, instead of the standard Terms & Conditions, is sent to you because no fee is being charged for your order. Please note the following:

- Permission is granted for your request in both print and electronic formats, and translations.
- If figures and/or tables were requested, they may be adapted or used in part.
- Please print this page for your records and send a copy of it to your publisher/graduate school.
- Appropriate credit for the requested material should be given as follows: "Reprinted (adapted) with permission from (COMPLETE REFERENCE CITATION). Copyright (YEAR) American Chemical Society." Insert appropriate information in place of the capitalized words.
- One-time permission is granted only for the use specified in your request. No additional uses are granted (such as derivative works or other editions). For any other uses, please submit a new request.

If credit is given to another source for the material you requested, permission must be obtained from that source.

Copyright Clearance Center RightsLink®

Home | Create Account | Help

ACS Publications
Most Trusted. Most Cited. Most Read.

Title: Surface Reactivity Control of a Borosilicate Glass Using Thermal Poling

Author: A. Lepicard, T. Cardinal, E. Fargin, et al

Publication: The Journal of Physical Chemistry C

Publisher: American Chemical Society

Date: Oct 1, 2015

Copyright © 2015, American Chemical Society

LOGIN

If you're a copyright.com user, you can login to RightsLink using your copyright.com credentials. Already **a RightsLink user** or want to learn more?

PERMISSION/LICENSE IS GRANTED FOR YOUR ORDER AT NO CHARGE

This type of permission/license, instead of the standard Terms & Conditions, is sent to you because no fee is being charged for your order. Please note the following:

- Permission is granted for your request in both print and electronic formats, and translations.
- If figures and/or tables were requested, they may be adapted or used in part.
- Please print this page for your records and send a copy of it to your publisher/graduate school.
- Appropriate credit for the requested material should be given as follows: "Reprinted (adapted) with permission from (COMPLETE REFERENCE CITATION). Copyright (YEAR) American Chemical Society." Insert appropriate information in place of the capitalized words.
- One-time permission is granted only for the use specified in your request. No additional uses are granted (such as derivative works or other editions). For any other uses, please submit a new request.

Copyright Clearance Center RightsLink®

Home | Account Info | Help | Live Chat

Title: Micro-structuring the surface reactivity of a borosilicate glass via thermal poling

Author: A. Lepicard,T. Cardinal,E. Fargin,F. Adamietz,V. Rodriguez,K. Richardson,M. Dussauze

Publication: Chemical Physics Letters

Publisher: Elsevier

Date: 1 November 2016

© 2016 Elsevier B.V. All rights reserved.

Logged in as:
Antoine Lepicard
LOGOUT

Order Completed

Thank you for your order.

This Agreement between Antoine Lepicard ("You") and Elsevier ("Elsevier") consists of your license details and the terms and conditions provided by Elsevier and Copyright Clearance Center.

Your confirmation email will contain your order number for future reference.

Get the printable license.

License Number	3967540068142
License date	Oct 14, 2016
Licensed Content Publisher	Elsevier
Licensed Content Publication	Chemical Physics Letters
Licensed Content Title	Micro-structuring the surface reactivity of a borosilicate glass via thermal poling
Licensed Content Author	A. Lepicard,T. Cardinal,E. Fargin,F. Adamietz,V. Rodriguez,K. Richardson,M. Dussauze
Licensed Content Date	1 November 2016
Licensed Content Volume	664
Licensed Content Issue	n/a
Licensed Content Pages	6
Type of Use	reuse in a thesis/dissertation
Portion	full article
Format	both print and electronic
Are you the author of this Elsevier article?	Yes
Will you be translating?	No
Order reference number	
Title of your thesis/dissertation	Design of Surface Chemical Reactivity and Optical Properties in Glasses
Expected completion date	Dec 2016
Estimated size (number of pages)	300
Elsevier VAT number	GB 494 6272 12
Requestor Location	Antoine Lepicard Bâtiment A12, Université de Bordeaux 351 Cours de la Libération Talence, 33405 France Attn: Antoine Lepicard
Total	0.00 USD

ORDER MORE | CLOSE WINDOW

Copyright © 2016 Copyright Clearance Center, Inc. All Rights Reserved. Privacy statement. Terms and Conditions.
Comments? We would like to hear from you. E-mail us at customercare@copyright.com

APPENDIX B: UV-VIS TRANSMISSION SPECTRA

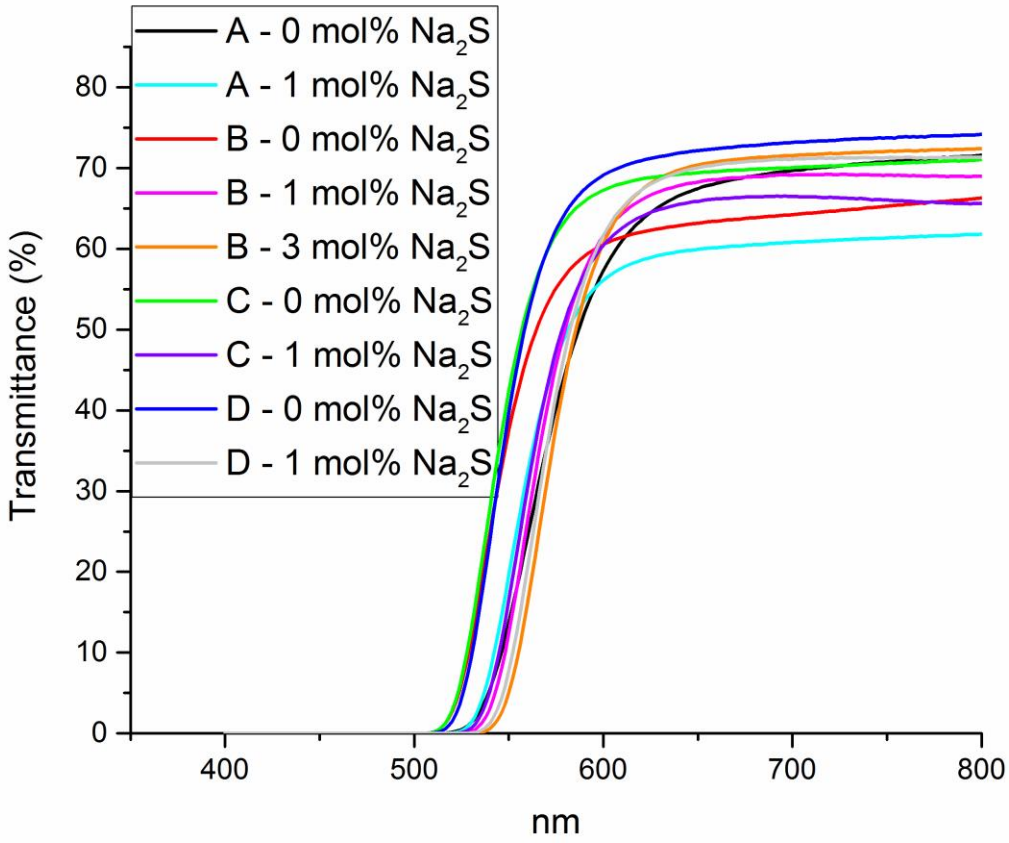

Figure B.1. UV-vis transmission spectra of all glasses prior thermal poling

APPENDIX C: IR TRANSMISSION SPECTRA

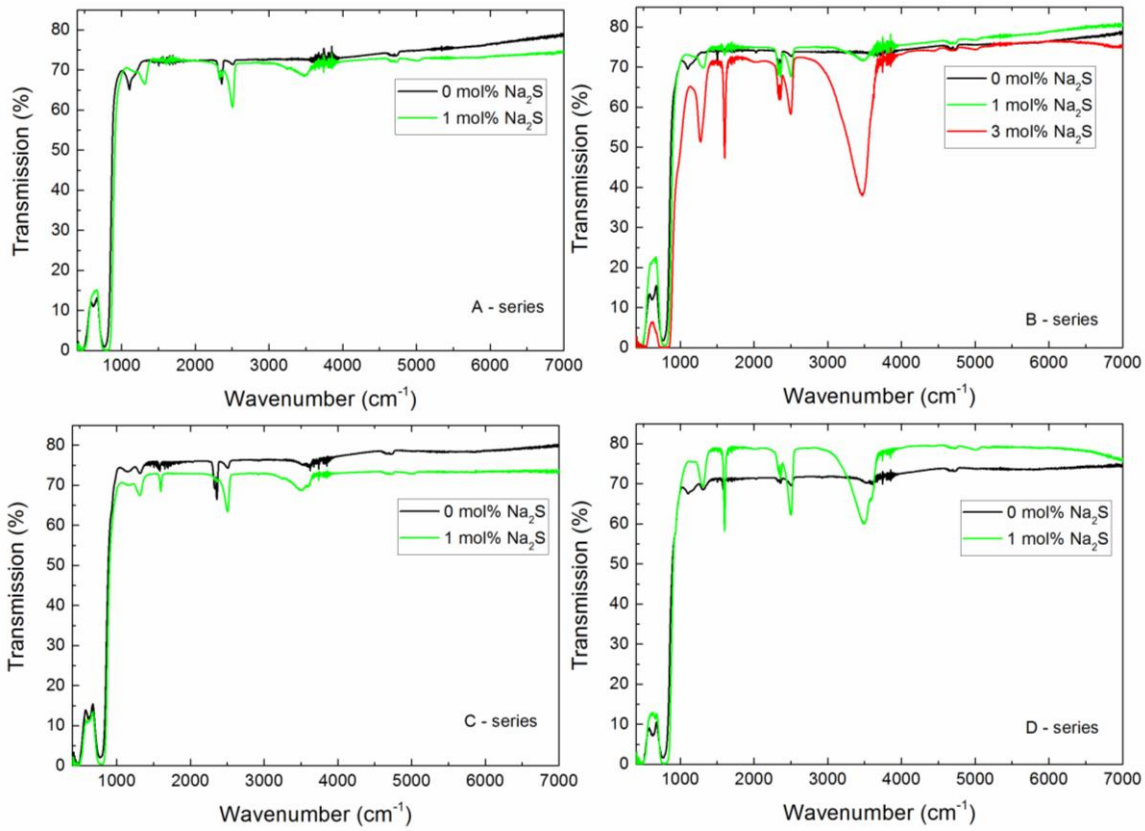

Figure C.1. IR transmission spectra measured on all chalcogenide compositions

APPENDIX D: SIMS PROFILES

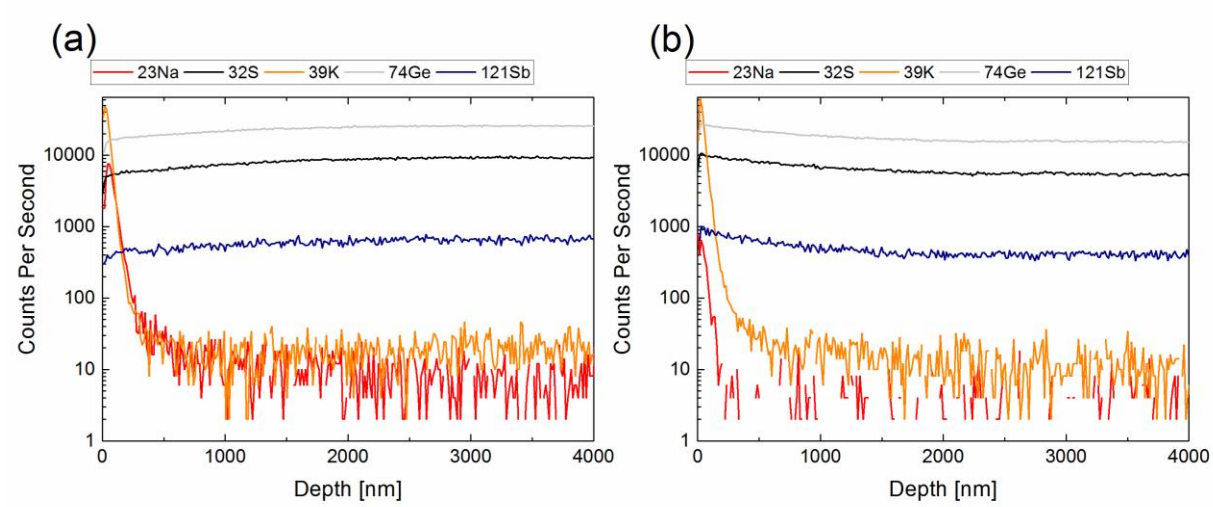

Figure D.1. SIMS profile recorded on base glass of composition A (a) and on a thermally poled Na-free glass of composition A (b)

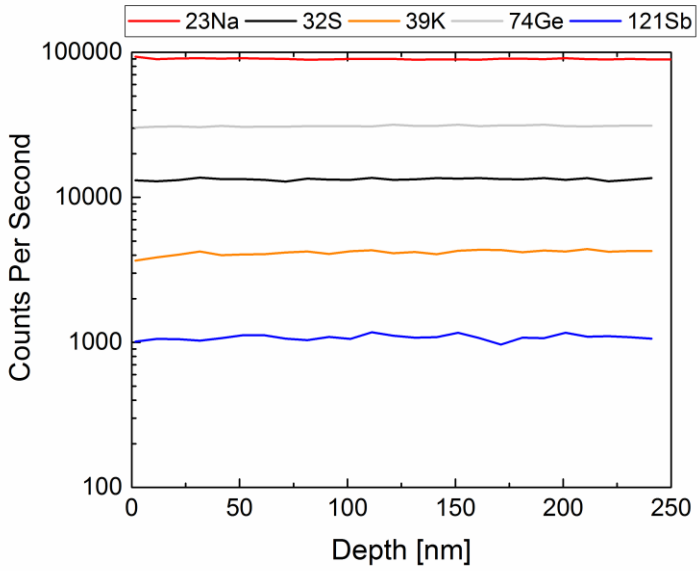

Figure D.2. Continuation of the SIMS profile recorded on B-1% thermally poled at 170°C (Figure 5.15) after adjusting the electron beam conditions

Contrôle de la réactivité chimique de surface et des propriétés optiques dans les verres

Résumé : Le poling thermique est une technique consistant à appliquer un fort champ électrique (DC) à un substrat de verre chauffé. Après traitement, un champ électrique est figé au sein de la matrice vitreuse, brisant sa centrosymmétrie. La présence de ce champ permet d'accéder à des propriétés d'optique nonlinéaire du second ordre, habituellement interdite dans un milieu centrosymmétrique tel que le verre. En plus des propriétés d'optique nonlinéaire, la présence du champ électrique a été associée à des modifications structurelles et compositionnelles mais également à des changements de propriétés de surface. Notre objectif a été d'utiliser cette technique pour modifier les propriétés de réactivité de surface et optique de verres d'oxyde (borosilicate et borophosphate de niobium (BPN)) et de verres de chalcogénures. Après poling, les modifications structurelles ont été caractérisée par spectroscopie vibrationnelle Raman et infrarouge. L'intensité et la localisation du champ électrique ont été caractérisées par des techniques de génération de seconde harmonique (SHG) : une analyse quantitative avec les franges de Maker et une d'imagerie μSHG. Le traitement a permis d'augmenter localement la réactivité de surface du verre borosilicate. Dans les verres BPN et chalcogénures, le traitement a permis de contrôler les propriétés optiques à la fois linéaire et nonlinéaire à l'échelle micrométrique. Ces résultats permettent d'envisager l'utilisation du poling thermique pour des applications en photonique intégrée.

Mots clés : verres d'oxydes, verres de chalcogénures, poling thermique, génération de seconde harmonique, réactivité de surface, gradient d'indice de réfraction

Design of surface chemical reactivity and optical properties in glasses

Abstract: Thermal poling is a technique which consists in the application of a strong DC electric field to a heated glass substrate. Following the treatment, a static electric field is frozen inside the glass matrix, effectively breaking its centrosymmetry. Presence of the electric field allows for second order non-linear optical properties usually forbidden in centrosymmetric medium such as glasses. In addition to nonlinear optical properties, the presence of the electric field has been associated with structural/compositional modifications as well as surface property changes. Our objective was to use this technique to tailor surface reactivity and optical properties in oxide (borosilicate and niobium borophosphate) and chalcogenide glasses. After poling, structural modifications were investigated using Raman and infrared spectroscopy. Strength and localization of the electric field were characterized by Second Harmonic Generation (SHG) techniques: quantitative Maker fringes analysis and μSHG imaging. The treatment has successfully allowed to locally enhanced the surface reactivity of a borosilicate glass. In niobium borophosphate and chalcogenide glasses, the treatment has permitted to control optical properties both linearly and non-linearly at the micrometric scale. These results show that thermal poling could be used to create functional devices for applications in integrated photonics.

Keywords: oxide glasses, chalcogenide glasses, thermal poling, second harmonic generation, surface reactivity, refractive index gradient

ISM, UMR 5255, 351 cours de la libération, 33405 Talence Cedex, France

CREOL, the College of Optics and Photonics, 4304 Scorpius St, Orlando, FL 32816, USA